Study of the processes of layer growth and ion beam etching using specular and diffuse X-ray scattering

Luca Peverini

To cite this version:

Luca Peverini. Study of the processes of layer growth and ion beam etching using specular and diffuse X-ray scattering. Condensed Matter [cond-mat]. Université Joseph-Fourier - Grenoble I, 2005. English. NNT : . tel-00011519

HAL Id: tel-00011519
https://theses.hal.science/tel-00011519

Submitted on 1 Feb 2006

HAL is a multi-disciplinary open access archive for the deposit and dissemination of scientific research documents, whether they are published or not. The documents may come from teaching and research institutions in France or abroad, or from public or private research centers.

L'archive ouverte pluridisciplinaire **HAL**, est destinée au dépôt et à la diffusion de documents scientifiques de niveau recherche, publiés ou non, émanant des établissements d'enseignement et de recherche français ou étrangers, des laboratoires publics ou privés.

Université Joseph Fourier – Grenoble 1
U.F.R. de Physique

THÈSE

pour obtenir le grade de

DOCTEUR DE L'UNIVERSITE JOSEPH FOURIER-GRENOBLE 1

Etude des procédés de croissance de couche et de décapage ionique par mesures de diffusion spéculaire et diffuse de rayons X

Présentée et soutenue publiquement le 25 février 2005

par

Luca PEVERINI

Discipline: Physique

COMPOSITION DU JURY:

J. Chevrier	Université Joseph Fourier	*Président*
C. Boragno	Università di Genova	*Rapporteur*
P. Dhez	Centre d'Orsay	*Rapporteur*
E. Ziegler	ESRF-Grenoble	*Directeur de thèse*
J. Lilensten	Université Joseph Fourier	*Directeur de thèse*
I.V. Kozhevnikov	Institute of Crystallography – Moscow	*Membre Jury*

Optics Group – BM5 / European Synchrotron radiation Facility

THESIS TITLE

Study of the processes of layer growth and ion beam etching using specular and diffuse X-ray scattering

by

Luca Peverini

A thesis submitted to the University Joseph Fourier

Grenoble, 2005

PhD degree

Contents

Contents iii

Acknowledgements 1

Abstract 3

Introduction 4

Chapter 1 Hard X-ray optics 7

1.1 X-ray optics with grazing incidence mirror and multilayer reflectors 8
1.1.1 Total reflection mirrors 8
1.1.2 The X-ray total external reflection phenomena 11
1.1.3 Mirror coatings: thin films and multilayers 12
1.1.4 Specifications for hard X-ray mirrors 18
1.2 Imaging reflective optics 19
1.3 Focusing 24
1.4 Kirkpatrick Baez optics 27
1.4.1 Mirror manufacturing 27
1.4.2 Layer coating 30
1.5 Performance of X-ray reflective optics 31
1.6 Future applications of SR reflective optics 31

Chapter 2 Surface roughness 33

2.1 Surface finish parameters 33
2.2 Roughness characterization techniques 34
2.2.1 Scanning probe techniques 36
2.2.2 X-ray based techniques 38
2.2.3 High resolution angular dispersive diffuse X-ray scattering 40
2.3 Thin film and multilayer characterization 44
2.4 The definition of Power Spectral Density 45
2.4.1 Bandwidth limited PSD measurements 46
2.4.2 PSD and Correlation function 49

2.4.3 2D and 1D power spectra ... 50
2.4.4 PSD models ... 52
2.5 Scaling model ... 54
2.6 Linear stochastic model of growth/erosion of thin film ... 55

Chapter 3 X-ray Scattering theory ... 58

3.1 X-ray reflectometry ... 59
3.1.1 Coherence criteria in X-ray scattering ... 59
3.1.2 Specular reflection ... 60
3.1.3 Diffuse X-ray scattering analysis of a rough surface ... 66
3.1.4 Diffuse X-ray scattering from a rough thin film ... 72
3.1.5 Transition layer model ... 78
3.2 Time-resolved reflectometry ... 80
3.3 Summary ... 85

Chapter 4 Experimental technique and instrumentation ... 86

4.1 Beamline description ... 86
4.2 Apparatus: design strategy and realization ... 87
4.2.1 Sample environment, positioning and X-ray alignment ... 90
4.2.2 Sample Holder ... 92
4.2.3 Sputter gun ... 94
4.2.4 Ion source ... 96
4.2.5 Detection system ... 98
4.3 Instrument control and data transfer ... 104
4.4 Temporal scans ... 106
4.5 Data correction ... 106
4.6 Experimental measurements and normalization ... 109
4.6.1 Specular reflectivity ... 109
4.6.2 Diffuse scattering measurement ... 110
4.7 Instrument performance and application ... 112

Chapter 5 Real-time studies on film growth ... 116

5.1 Substrate characterization ... 116
5.2 Determination of film thickness and optical constants ... 120
5.3 Real time analysis in the case of a thick film ... 124
5.4 Study of tungsten film growth on smooth silicon substrate ... 129
5.5 Roughness analysis: conformity during film growth ... 136
5.6 Alternative approach to extract the PSD ... 147
5.7 Dynamic scaling analysis ... 155
5.8 Critical analysis of the scattering method ... 158

5.9 Minimization of the surface roughness 160

Chapter 6 Real time studies on surface etching 162

6.1 Ion beam sputtering processing 162
6.2 Ion-induced ripple formation 163
6.3 Ion erosion experiments 167
6.3.1 Evolution of roughness conformity during ion erosion 172
6.3.2 TIS and roughness evolution during tungsten ion erosion 174
6.4 Ion beam assisted deposition 182
6.5 Ion bombardment of silicon 185

Conclusion and outlook 189

***Résumé* 193**

Bibliography 202

Acknowledgements

I wish to thank Dr. Eric Ziegler for his constant help and valuable advice throughout this research and for being the initiator of this project. These were the most exciting years of my scientific career. I would also like to thank Prof. Jean Lilensten for supporting and encouraging me during the thesis.

I am honored that Professors Corrado Boragno and Pierre Dhez were willing to judge this work.

Special thanks go to Dr. Igor V. Kozhevnikov for his guidance and for being always willing to discuss and exchange new ideas as well as for his contribution during the analysis of the experimental data. The originality of his theoretical formalism constitutes a unique contribution to this work.

I would like to thank my colleagues Dr. Thierry Bigault and Dr. Joanna Hoszowska whose help and encouragement throughout the experiments, allowed me to obtain new and original experimental results. It was a very good experience to work with them.

I am grateful for assistance and help during the design and the preparation of the setup to Jean-Yves Massonnat, Robert Hustache, Gerard Rostaing, Cyril Ponchut, Marc Dubrulle, Jean-Christophe Peffen, Christine Borel, Philippe Villermet, Jean Pierre Vassalli, Laureant Claustre and Manuel Perez. I am indebted also with all the support groups of the ESRF for their effectiveness in performing any kind of practical work, hardware and software.

I wish to express my thanks to Amparo Rommeveaux from the Metrology Laboratory and Emilie Dubard from the Surface Science Laboratory of the ESRF.

I kindly acknowledge Dr. Christian Morawe and Dr. Andreas Freund for fruitful discussions.

I am thankful to Hélène Rocchiccioli and Manuel Sanchez del Rio for their contribution given to the realization of a very useful data analysis software for X-ray scattering data.

I am indebted with Dr. Gavin Fox for his help during the last moments of the manuscript preparation. He always proved a true friend in troubled times of my life during the last three years.

Many thanks to all those who have contributed to the realization of this works: Alessandro Mirone, Claudio Ferrero, Roberto Felici, Roberto Cerbino, Marco Potenza, Marzio Giglio, Anatoly Snigirev, Irina Snigireva, François de Bergevin, Peter Takacs, Giovanni Pareschi, Mauro Ghigo, Daniele Spiga, Alessandro Patelli, Timm Weitkamp, Bruno Golosio, Finn Christensen and David Windt.

Special thanks to Silvia, Laura, Annamaria, Quinto and in particular to Rosalia for their support, encouragement and immense patience over the course of my time spent at the ESRF.

Abstract

A novel X-ray scattering technique and a dedicated apparatus have been conceived and realized at the optics beamline BM5 at the ESRF. The apparatus permits to study the surface roughness in-situ and in-real time via grazing incidence X-ray scattering. The interaction of X-rays with the surface was analyzed in the framework of the first order scalar perturbation theory expressing the surface's attributes through the power spectral density function. Information on the rms roughness, the correlation length, the roughness conformity and the scaling exponents characterizing the synthesis process could be extracted.

The potential of the method was demonstrated in two particular cases: thin film deposition by magnetron sputtering and surface etching by ion beam bombardment. Finally, the experimental results obtained were discussed in the light of the present models of film growth and ion interaction with solids.

Introduction

Any real surface is marked by the presence of roughness. On a macroscopic level the concept of surface roughness should be familiar to anyone. Most of the light we see is light scattered diffusely from rough surfaces. For instance, objects that are observed under conditions which differ from the specular one are visible. Roughness also induce friction, when one body moves relative to another body with which it is in contact, and this allows, for example, to have grip between shoes and the ground for walking.

A wide variety of surfaces and interface present in nature, possess the characteristic of roughness and can be associated with the fractal concept defined by Mandelbrot [1] in terms of fractional Brownian motion. Many surfaces appear as a self-affine instead of a pure fractal surface. This is often the case of surfaces that are of interest in technology, e.g., in X-ray optics, microelectronics or EUV lithography, when dealing with spatial scale ranging from several μm up to the atomic scale. The concept of self-affine surface has been created to describe a surface that is in-between that of a pure fractal, an object showing the same morphology at different observation scales, and a non-fractal object. In mathematical terms, this is an object that rescales anisotropically at different spatial coordinates (lateral and vertical).

Roughness is a measure of the topographic relief of a surface around a mean plane conventionally taken as zero level. For synthetic surfaces, roughness, and its stochastic nature, arises from the manufacturing process. These processes may involve deposition, grinding, polishing, and etching techniques. At the atomic scale the morphology of a surface is still rough. At this scale, roughness is caused by the action of a stochastic process while the surface morphology is governed by the interplay between several relaxation mechanisms: the dynamics of surface roughening due to the random arrival of particles and smoothing due to material transport induced by surface relaxation [2]. In the analysis of roughness and of the relaxation mechanism that generates it, the fractal concept is powerful because it enables to describe the morphology of a surface with a limited number of statistical parameters. For instance, when dealing with surface scatter

measurements: three statistical parameters are sufficient to describe both the surface topography and the distribution of the scattered radiation.

For any surface, the study of roughness presents both fundamental and practical interests. In the case of coated surfaces, from a fundamental point of view, roughness is related to the kinetics that controls film deposition and therefore studying the roughness evolution may bring insights on the growth mechanisms. Technologically, the study of roughness is important since roughness determines the ultimate performance of the reflective optical elements used, for example, in X-ray optics or EUV lithography.

This thesis is a contribution to the development of hard X-ray optics for synchrotron radiation sources. Almost any application of synchrotron radiation requires optical elements to condition the X-ray beam. The short wavelength in use and the source characteristics (flux exceeding 10^{13} ph/sec and beam divergence below few μrad) impose unprecedented specifications for the reflecting surfaces, which have to satisfy requirements on smoothness and figure finish at the atomic scale, to fully exploit the beam properties. Nowadays, there are three classes of reflective optics used in the conditioning of synchrotron radiation beams, namely grazing incidence mirrors, crystals and multilayers. To optimize the surfacing of these elements, a metrology with accuracy at the atomic spatial scale is needed. This is the primary motivation of this thesis. The objective of the project is to realize a real-time on-line roughness-measuring instrument for surfaces and thin films to be used in synchrotron radiation applications.

Presently, the techniques of investigation of roughness can be divided in two main categories: (i) *Scanning Probe Techniques* such as stylus profilometry, optical interferometry, Scanning Tunneling Microscopy and Atomic Force Microscopy. (ii) *Scattering Techniques,* energy and angular dispersive. As the sensitivity and accuracy of each technique are only satisfactory within limited lateral spatial bandwidth and vertical heights, the combination of several instruments and measurements is essential for a full description of the morphology of a surface. Among these techniques, X-ray reflectometry is widely accepted as a routine characterization for determining thin-film properties such as density, thickness and surface roughness. For these characteristics, X-ray reflectometry was chosen to provide a representative description of the surface analyzed during this work.

The experimental work achieved was performed at the bending magnet beamline BM05 at the European Synchrotron Radiation Facility.

Keeping in mind that the performance of a reflective-based imaging device is eventually related to the various imperfections of the mirrors surfaces, Chapter 1 will present an overview on the general manufacturing issues of the X-ray optics for synchrotron radiation sources. Several reflective optical elements commonly used in synchrotron radiation beamline will be presented together with an overview of the

manufacturing technologies currently employed. Layer coating, figuring, and polishing processes will be discussed and compared with more recent approaches. As the main tool of investigation of this thesis is the scattering of X-rays from surfaces, Chapters 2 and 3 will review the physical and mathematical concepts underlying the scattering phenomenon in the case of a single surface (substrate) and particularly when a film is grown on it. The main roughness parameters and the statistical tools commonly used to describe a surface are presented first. Those parameters are linked to the theory of scattering from a rough surface in Chapter 3 using the first order scalar Perturbation Theory. Emphasis will finally be given to the concept of time-resolved reflectometry showing the potential of the method in contrast to other "post-process" characterization techniques.

The main practical tasks were to design, implement and characterize an apparatus and a technique to perform time-resolved studies on thin films. These are extensively described in Chapter 4. Chapter 5 presents the most representative results obtained experimentally, thus demonstrating the performance of the instrument in terms of spatial and temporal sampling. The comparison of some of these measurements with results obtained with an atomic force microscope complements the findings. On the basis of the experimental observations, a more detailed description of the physics underlying the growth process will then be given. The experimental results are presented in the context of an eventual use of this method for manufacturing mirrors. Emphasis is given to the "real time" advantage of the method for surface roughness optimization. The other important part of this thesis concerns the study in situ of ion beam etching of thin films and of silicon substrates. This is discussed in Chapter 6. The intriguing formation of ripples observed during the experiments is also presented and discussed.

Chapter 1 Hard X-ray optics

Modern synchrotron radiation (SR) sources such as the Advanced Photon source (APS-USA), the European Synchrotron Radiation Facility (ESRF-France) and the Super Photon ring (SPring-8-Japan), deliver photon beams of unprecedented intensity and quality. The size of the source is of the order of a few tens of microns FWHM and the X-ray beam divergence is well below the milliradian. As an example, at the beamline ID01 of the ESRF, the beam divergence is of 0.208 x 0.009 $mrad^2$ and the flux after monochromatization in the order of 10^{13} ph/sec. The available photon energy range for these machines spans from few tenths of kilo electron Volts (keV) to several hundreds of keV. The associated wavelength range is 100 Å - 0.1 Å.

Surfaces almost ideally figured and finished are needed to reflect efficiently X-rays between 0.1 keV and 100 keV through total external reflection from mirrors and Bragg reflection from multilayers (ML) and crystals. Unfortunately, the finite quality of real mirrors will partially spoil the exceptional brilliance of the available photon beam. Local deviations from the ideal reflecting surface, called figure slope errors, should be kept in the 1 μrad rms range over the whole mirror length (~1 meter) and micro roughness should be in the few Å rms range. As traditional mechanical polishing techniques have remarkably evolved over the last few years, these requirements can nowadays be achieved over a relatively wide range of materials. However, this is still a remarkable challenge, especially when a full exploitation of the partial coherence of the source is needed, e.g., in phase contrast imaging, X-ray fluctuation spectroscopy or X-ray interferometry applications.

The large variety of SR optical elements can be categorized in 4 families: crystal monochromators, grazing incidence mirror reflectors (focusing or not, with or without coating), compound refractive lenses and Fresnel zone plates. For all of them the surface imperfections give rise to diffuse scattering which degrade their optical performance. However, in this thesis only the reflective optics is presented. Additional information concerning the other optical components have been recently reviewed by Dhez (see [3] and reference therein).

1.1 X-ray optics with grazing incidence mirror and multilayer reflectors

1.1.1 Total reflection mirrors

Grazing incidence X-ray mirrors are nowadays widely used as energy low pass filters, focusing and imaging devices. Usually, the mirrors of a reflective optics are made of a super-polished light material substrate, such as Si, SiC or glass, coated with either a high-density (high-Z) metal, a few tens of nanometer thick, or with a multilayer (ML) coating. When coated with ML, reflective mirrors can be used as an energy band pass filter or as a low-resolution high-flux monochromator as compared to single crystals. Here, thanks to the small grazing angle, the thermal load per surface unit is reduced, as it is spread over a large area keeping a spectral purity $\Delta E/E$ in the order of few percent.

The grazing incidence mirror exploits the phenomenon of total external reflection (TER). As for any electromagnetic wave and material, the reflectivity of a photon beam shining onto a material increases as the grazing angle of incidence gets smaller. However, for sufficiently short wavelengths, typically less than a few nanometers, an abrupt increase in reflectivity, known as total external reflection, occurs when the grazing angle of incidence becomes smaller than a value known as the critical angle, see, e.g., Figure 1-1. This is because the refractive index of materials is slightly smaller than unity for short wavelengths. In other words, passing from air (n= 1) to the reflecting material (n < 1), it is possible to totally reflect the beam if the incident angle θ (angle between the surface of the sample and the incident beam) is small enough. This occurs when the incident angle is smaller than the critical angle θ_{cr} given by the Snell/Descartes law, $\cos(\theta_{cr}) = n = 1 - \delta$. Since n, in the X-ray domain, is very close to unity, this angle is very small and a Taylor approximation in θ_{cr} yields

$$\theta_{cr} \approx \sqrt{2\delta} \qquad (1.1)$$

At the same time the constant δ is related to the bulk density of the reflecting material according to the following equation:

$$\delta = \frac{r_0}{2\pi}\lambda^2 \mathrm{N}_{at} f \qquad (1.2).$$

The quantities in (1.2) are, r_0 the classical electron radius, λ the wavelength of the radiation in use, N_{at} the atomic density of the material and f is the atomic scattering factor. Formula (1.2) suggests that the best candidate materials to achieve the widest reflection band pass in the X-ray are high-density materials, such as Pt, Au, Ir and W.

To understand the TER phenomenon[1] in a simple way we can imagine the reflection phenomenon considering X-ray photons as particles and associate to the reflecting material a critical momentum perpendicular to the surface plane. The critical momentum can be written as $q_{cr} \sim \sqrt{n_e}$ where $n_e = N_{at} f_1$ is the effective electronic density. Particles with a perpendicular projection of the momentum higher than this critical momentum will penetrate while others will be reflected. Notice that the defined momentum does not explicitly depend on the photon energy. However, as the optical constant (and in turns n) depends on the X-ray energy, θ_{cr} is expected to change as well. A practical equation can be written to relate the value of the critical angle of TER and X-ray energy in use:

$$E[keV] \times \theta_{cr}[\deg] \sim 4.4 \cdot keV \cdot \deg \quad (1.3)$$

Eq. 1.3 is valid in the absence of absorption edges and for high-Z materials.

As the penetration depth is small in TER condition, the mirror reflectivity can be further tailored by coating a bare substrate of density ρ_{sub} with a material with a different density, ρ_{layer}. Let us limit ourselves to the case of $\rho_{layer} > \rho_{sub}$. In this case the critical angle is increased by a factor $\sqrt{\rho_{layer} / \rho_{sub}}$. This is a consequence of the relation that exists between density and critical angle. Figure 1-2 shows the reflectivity curve of a silicon mirror coated with three different materials and assuming ideally smooth interfaces. As one can see, the critical angle of TER can be further increased by a factor 2-3 if the coating is done with a high-density material. The reflectivity is less than 100% because of absorption, which is greater for high-Z materials. To account for it, one must describe the film using a complex refractive index. Due to the finite thickness of the coating layer, interference effects may be present. These effects appear as oscillations on the reflectivity curve above the TER region and are called Kiessig fringes, after the name of the scientist who first discovered and explained this effect [4].

Let us discuss the reflectivity of a tungsten mirror at different energies (Figure 1-1) and grazing angle of incidence (Figure 1-2) of an X-ray beam. As one can see, to achieve an efficient reflection (TER) over a wide energy range one needs to reduce dramatically the angle of incidence. In this region the mirror behaves as a low pass filter.

From the above consideration, one can understand why normal incidence mirrors cannot be used in the X-ray domain as efficiently as in the visible light region: the region

---

[1] This effect can be understood with the analogy with the launch of a stone onto the surface of a lake: the stone will only bounce at the water surface if the momentum projection is short enough, i.e., if the stone is thrown at sufficiently grazing angle.

of angles and energy where reflection occurs efficiently is indeed limited to grazing angle only[2].

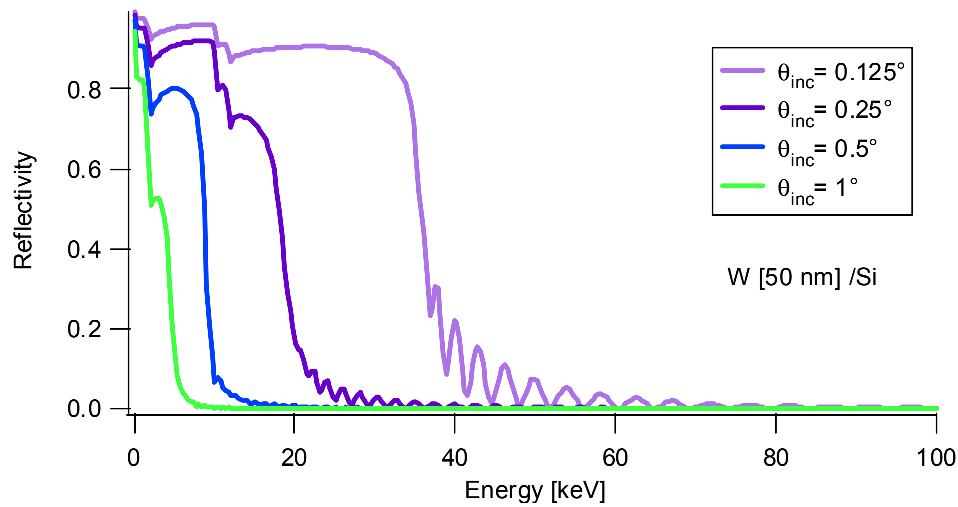

Figure 1-1: Reflectivity of a tungsten-coated silicon mirror at different glancing angles of incidence.

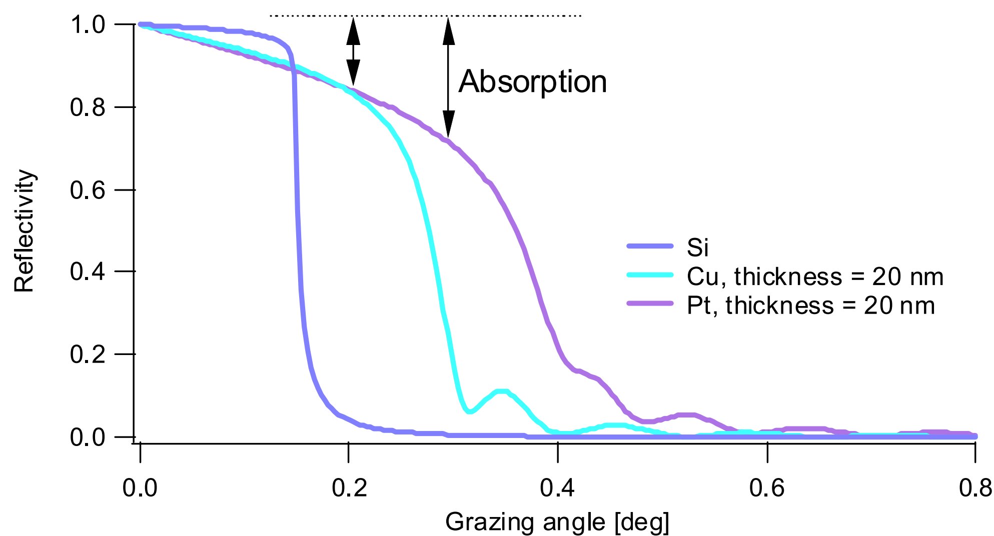

Figure 1-2: Reflectivity versus angle of a silicon substrate coated with materials of different density, namely Si, Cu and Pt. The curves are calculated using a radiation wavelength of 0.1 nm.

---

[2] Strictly speaking, using mirrors coated with short period ML, the use of normal incidence is technologically possible and can effectively used up to about 200 eV. This conditions are typical in EUV lithography.

1.1.2 The X-ray total external reflection phenomena

The first X-ray experiment on TER from flat and smooth surfaces was reported by Compton in 1923 [5]. The TER phenomenon was only discovered about 30 years after the discovery of the X-rays (Roentgen). His discovery has been one of the most important scientific events of this century as it opened up many new areas of modern science. Within a few years, this discovery was awarded the Nobel Prize, a clear confirmation of its importance.

It was found that the beam could be reflected by the surfaces of a polished glass and of silver inclined by angles of several minutes of arc at ~8 keV (Cu-Kα). By studying the spectrum of the reflected beam, the critical glancing angle was found to be approximately proportional to the wavelength (see Eq. (1.3)).

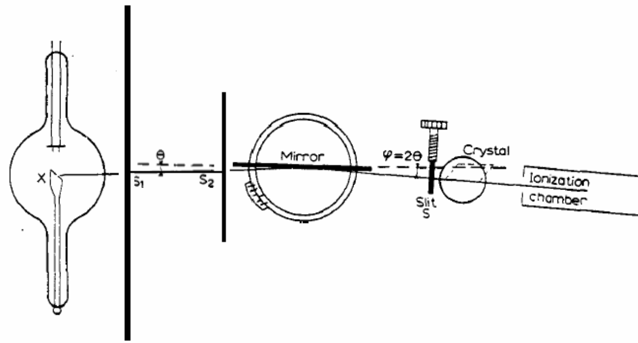

Figure 1-3: The apparatus used by Compton for studying the total reflection of X-rays (taken from his Nobel lecture[3]).

For X-rays whose wavelength is one half of an Ångström, the critical glancing angle from crown glass was found to be about 4.5 minutes of arc (0.075 deg), implying a reflective index differing from unity by less than one part in a million. The experimental difficulties encountered before the Compton discovery were due to the fact that the polarizability δ for common materials at X-ray wavelengths is extremely small, typically $10^{-5}\div10^{-6}$, thus generating deviations from the direction of the incoming beam that were very small and difficult to be recorded with the equipment available at that time.

Furthermore, for X-rays, the refractive index of a material n is slightly less than unity. This means that concave rather than convex lenses and very large radius of curvature would have to be used for an X-ray beam to converge. Recently [6], this possibility was proved technologically realizable by stacking behind each other several concave lenses in linear array of a low-Z material to form a compound refractive lens (CRL).

1.1.3 Mirror coatings: thin films and multilayers

In SR radiation optics mirrors are frequently coated with the materials that help matching the requirements of a specific application, e.g., in terms of reflection within a given range of angles or energy. As previously stated, the most common way to achieve efficient reflection at grazing incidence is to use, either mirrors coated with a high-Z material, e.g., Ir, Pt or Au, or multilayer-coated mirrors.

Total external reflection can provide usable grazing angles up to a few tens of keV (see Figure 1-1). However, above this energy range total external reflection would occur at very small angles and long mirrors would be needed to allow a usable acceptance. This

---

[3] http://nobelprize.org/physics/laureates/1927/compton-lecture.html

would lead to tighter constrains in terms mirror alignment and handling. An interesting solution was pioneered by Spiller in the seventies for extreme ultraviolet region (EUV)[7]. He understood first that, by layering two materials with dissimilar densities, a spacer made of a low-Z material and a high-Z as a "reflector", it was possible to fabricate a 2d crystal-like structure capable of diffracting an X-ray beam with an excellent efficiency. Since then, metallic multilayers have been successfully employed for a variety of applications from the EUV to the hard X-ray range, where substitute solutions are rare.

As first explained by Spiller [7], the use of synthetic multilayers instead of a single layer can finally lead to the largest angles of incidence accessible with a synthetic structure. Here, the reflection occurs due to the Bragg reflection phenomenon, i.e., the waves partially reflected at each interface add in phase when constructive interferences occur.

The reflectivity curves for three material systems, namely a Si substrate, a Si coated with a W layer and a periodic ML, are shown for illustration in Figure 1-4, at a grazing angle θ_{inc}=0.25°. The curves show that, by stacking together two materials with dissimilar densities, one can access regions where the reflectivity for a single material would be negligibly small. Figure 1-5 shows the dependence of the reflectivity on the number of layers present in the stack. The ML structure is the same in the three cases. The saturation occurs for different number of bi-layers due to the variation of the absorption with the X-ray energy. As one would expect, absorption becomes less effective when the radiation energy increase.

As shown in Figure 1.4 the reflectivity is sharply peaked around angles fulfilling the Bragg condition as for perfect crystals. The reflectivity of a ML can be further tailored through an a-periodic design of the stack. With such a variation of the periods along the stack the ML can be employed as a wide band reflector in the angle or the energy ranges.

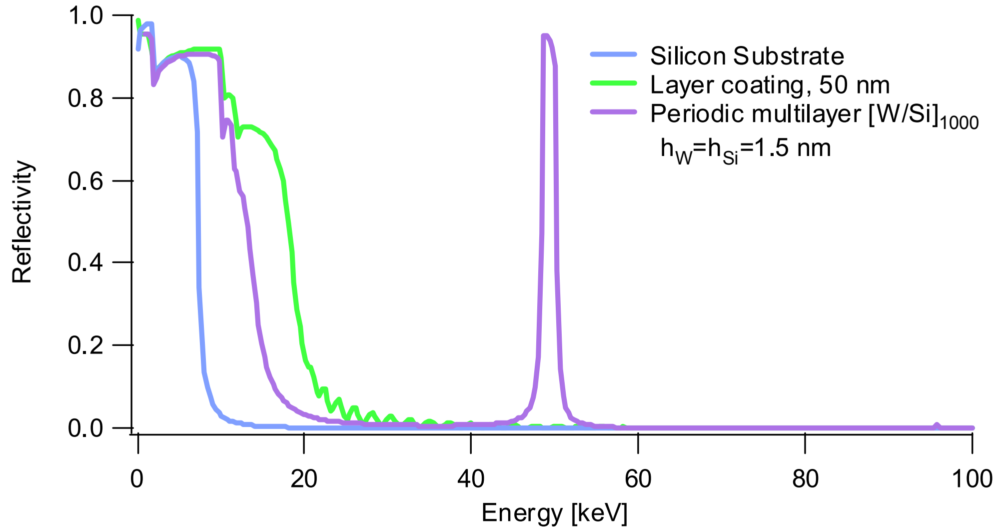

Figure 1-4: Reflectivity versus energy for grazing incidence mirrors for different systems: Si substrate, substrate coated with Pt, 50 nm thick and with a periodic W/Si multilayer. The curves are simulated assuming smooth interfaces. The multilayer comprises 500 bi-layers with thicknesses τ_{Si}=1nm and τ_W =1nm.

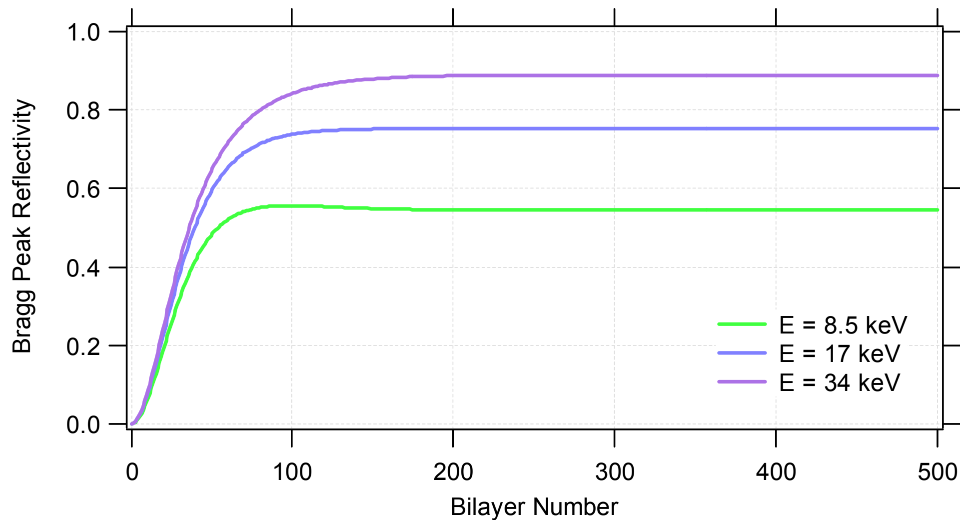

Figure 1-5: Variation of the reflectivity of a multilayer as the number of bi-layer is varied along the stack at three different energies.

The general principle of these structures can be easily understood by discussing the reflection in the energy domain. This is schematically shown in Figure 1-6: if a white beam is illuminating such a mirror shorter wavelengths will penetrate deeper into the structure while others will be reflected by the upper layers. If the bi-layer periodicity is varied continuously, the Bragg law will be fulfilled locally along the stack with the results that many Bragg peaks will overlap over the energy range and result in wide band-pass reflection.

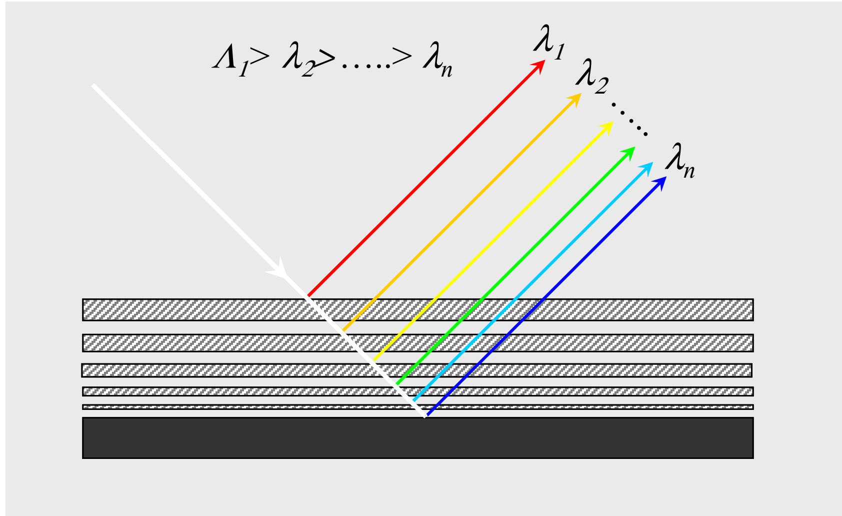

Figure 1-6: Principle of production of a broadband reflection using a multilayer with variable d-spacing. A white X-ray beam is partially reflected at the various interfaces.

Figure 1-7 shows the reflectivity versus energy of several layered materials systems. Two of them are multilayer mirrors with a different layer distribution along the stack and assuming ideally smooth surfaces. The sharp Bragg peak corresponds to a periodic multilayer with constant spacing while the wide peak represents the spectral response of an aperiodic ML. The latter case corresponds to the combination [Si/W] with N=1000 periods for which the thickness of each bi-layer period is varied according to the following power law:

$$z(i) = \frac{a}{(b+i)^c} \tag{1.4}$$

To obtain a wide reflection band the Si layer thickness was varied using the following parameters a=42.18, b=0.24 and c=0.25 which lead to a variation of the thickness from 4.0 nm to 0.75 nm. The W layer was varied using a=42.19, b=1.11 and c=0.25, i.e., varied from 3.50 to 0.75 nm. Notice that the oscillations are nothing but the effect induced by a smooth variation of the film thickness along the stack. It has been shown that[8], with local random variations of film thickness modulated by the function defined in Eq. (1.4), these oscillation can be reduced. These multilayer structures are now becoming popular in SR applications because of the large flexibility in contrast to the use of traditional crystals and mirrors.

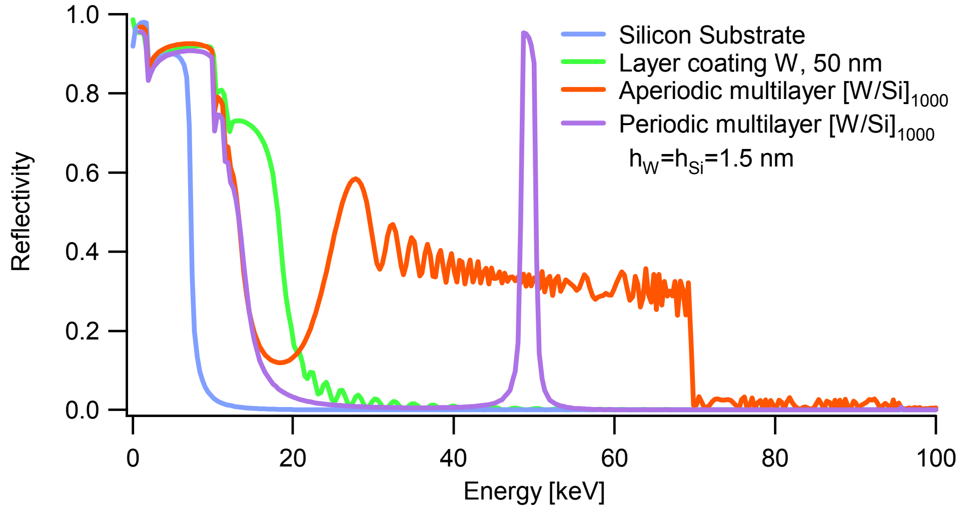

Figure 1-7: Reflectivity versus energy for grazing incidence mirror coated with different materials systems. The aperiodic multilayer structure was calculated using the "a b c" model parameters which are in given in the text and a grazing angle θ_i*=0.25°.*

The design of a multilayer can be done for the reflection to occur within well-defined spectral range and shape of the reflectivity curve. Moreover, ML can be routinely grown on any kind of shaped substrate, using techniques such as sputtering, evaporation and ion beam assisted depositions. However, the fabrication of short periods ML and the mastering of more complex structures such as aperiodic ML, requires the availability of a dedicated metrology capable of accuracy at the picometer spatial scale. The testing method should be fast enough to allow a short deposition-testing loop to improve the performance of the coating. These were the two important requirements that motivated the work carried out during this thesis: the development of an X-ray scattering technique and the realization of an apparatus for real-time on-line roughness measurements on surfaces and thin films.

The ultimate efficiency of a reflecting ML mirror is eventually determined by the absorption of the spacer material and by the surface errors (figure and finish). The former is minimized by employing low-Z materials. The latter requires highly specialized technological procedures to polish the surface at the desired level (see section 1.4).

The effect of interfacial roughness on the ML mirror reflectivity is illustrated in Figure 1-8. The figure shows the reflectivity of a ML coating for different interfacial roughness values, 0 nm, 0.2 nm and 0.4 nm. The effect of roughness is much pronounced at larger angles, up to one order of magnitude when the roughness is varied from 0.2 nm to 0.4 nm. This example shows once more the importance of reducing roughness when high mirror acceptance, and in turn, flux or throughput are needed.

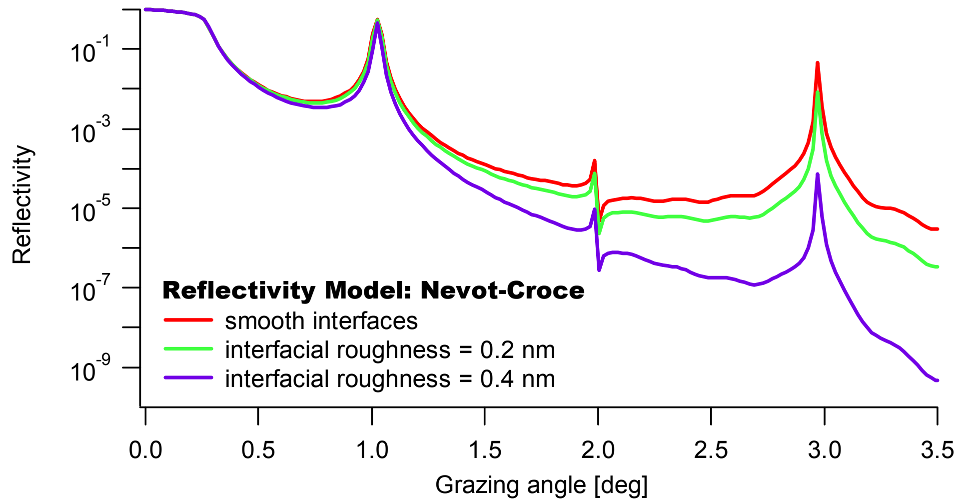

Figure 1-8: Reflectivity of a multilayer mirror [W(1.5)/Si(1.5)] versus grazing angle for three different interfacial roughness values.

The advances in film thickness measurements are generally important in the advanced technological processes implicated in the fabrication of layered devices. When fabricating ML mirrors, the individual layer thickness must be tailored for the boundaries to be close to the correct positions. The positioning of the absorber material (high-Z) should be in correspondence with the nodes of the wave field produced by superposition of incident and reflected field and spacer material (low-Z) in the remaining space. For the required exact period thickness control, a sputtering rate monitor with a sensitivity better than 0.001 nm is usually needed (1 pm). This sensitivity is not readily available by any commercial methods applicable for sputtering. Several techniques can be used as an in situ thickness monitor. *The quartz microbalance* is probably the most widely used since it is rather cheap and easy to use in comparison with the others. This is a resonance-frequency method that is based on the property of quartz, i.e., on the change in the resonance frequency with the change of mass. In principle, the thickness measurements performed with a quartz microbalance require knowledge of the film density and viscoelastic properties. The latter depend on the material and crystal structure or molecular arrangement in the film. The major drawback of this method is its sensitivity to thermal drift which may occur during deposition and can provide relative errors up to 20 %. *In-situ tracking ellipsometry*, is an optical method based on the measure of the changes in polarization of a monochromatic light , usually in the visible range, reflected from matter. The changes are related to the film thickness, the angle of incidence, the wavelength and the optical constants through an optical model of the film (accounting for film inhomogeneities, film structure and roughness). Therefore, the suitability of the method for a specific case depends on the validity of the model used. *In-situ reflectivity* is a method that will be discussed extensively throughout this thesis work

1.1.4 Specifications for hard X-ray mirrors

Current (third-generation) SR sources deliver photon beams with high brilliance and moderate coherence. Full exploitation of coherence and brilliance preservation have required the use of grazing-incidence mirrors typically 1 m long or more, with surface figure errors below 3 μrad rms and surface micro-roughness errors less than 0.3 nm rms. These requirements, along with others concerning high heat loading and ultra-high vacuum-compatibility materials, have imposed stringent specifications for the mirror manufacturing process. Successful collaborations between synchrotron radiation beamline scientists and mirror vendors have resulted in the production of mirrors with a quality that is sufficient to meet the challenges of third-generation beamlines. Special fabrication tools were created, in particular, the long trace profiler (LTP) [9]. They were developed to measure surface figure and curvature of long aspheres. Standard commercial instruments were adapted to evaluate the figure and finish of these large optics.

The impressive improvement of micro roughness and slope error of mirrors used at ESRF over the last 10 years is shown in Figure 1-9[10]. The best achieved values at present settle at 0.07 nm and 0.15 - 0.17 μrad, for mirrors with a perfect area with a length of 160 mm and 400 mm, respectively. Typical figure errors obtained currently on SR mirrors are of the order of 2 μrad or less, depending on the mirror material, size and shape.

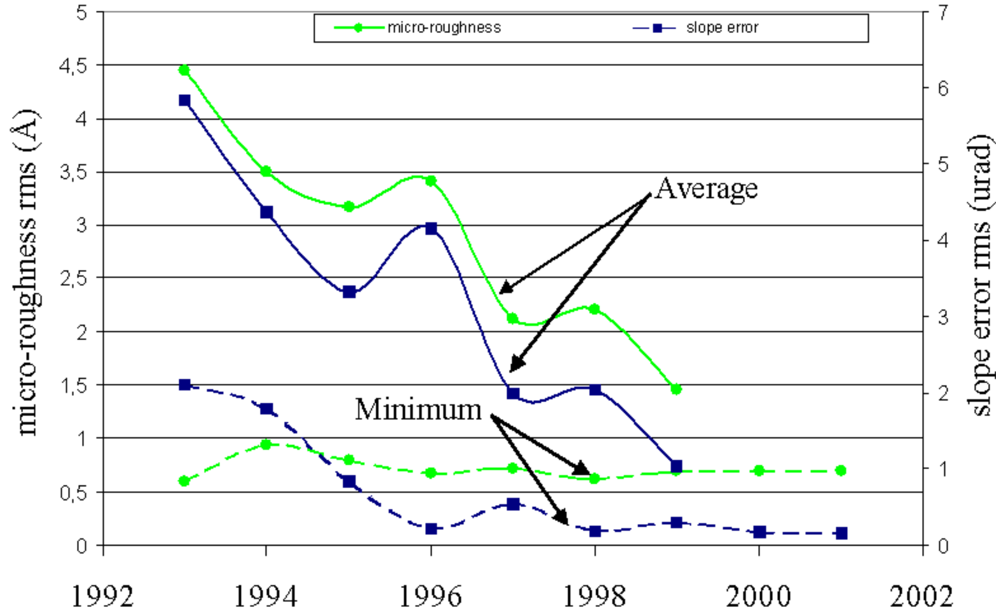

Figure 1-9 Improvement of micro roughness and slope error of mirrors used at ESRF over the last 10 years. The best-achieved and measured values settle at rms values of 0.07 nm and 0.15 -0.17microrad, respectively, measured over a length of a perfect mirror area of 160 mm and 400mm.

Despite the remarkable results achieved technologically, the production of a high quality figured mirror remains a challenge. Only two techniques, namely differential deposition[11] and Elastic Emission Machining [12], are presently being developed for figuring and polishing elliptical mirrors to x-ray quality surface roughness. In these cases, only few test models have been produced and alternative solutions are still wanted. These optical devices are of interest for imaging applications and when X-ray focusing is needed. These issues shall be discussed in the next two sections.

1.2 Imaging reflective optics

When using grazing incidence mirrors, two reflecting surfaces are at least necessary to produce an extended image without residual aberrations. One can understand that by considering an ellipsoidal reflector. In this case, one can only focus a point source. Notice that this is not the case for an extended source. This is because the magnification of an image changes along the surface of the ellipsoid. The rays reflected closest to the source are demagnified while the ones reflected closest to the focus are magnified. For a reflecting surface working at grazing incidence the magnification changes linearly with the position, and only a short section should be used. This situation does not occur in normal

incidence optics for which the magnification changes only slightly. In geometrical optics the requirements for constant magnification can be expressed by the *Abbe sine condition*:

$$\frac{\sin(u)}{\sin(u')} = \frac{y'}{y} = \text{constant} \tag{1.5}$$

where *u* and *u'* are the aperture angles of rays on the side of the object and image, and *y'/y* is the magnification. This condition defines for each optical system the shape of the effective surface as the intersection between the input ray and its corresponding output ray.

There are three different configurations for objectives, which are potentially suitable for grazing incidence imaging systems. These are called (i) Kirkpatrick-Baez (KB) type (ii) Wolter types and (iii) focusing collimator or "*Lobster-eye*" systems. All these configurations can fulfill the previous conditions and generate a constant magnification.

Among them the KB system is the imaging device the first most used in SR applications. Kirkpatrick and Baez obtained the first two-dimensional images ever obtained in a laboratory with grazing incidence reflection[13]. At that time they used two Pt coated cylindrical mirrors to image simple objects with a resolution of 1-2 μm over a field of view (FOV) of about 10 μm. The KB systems used today utilize two successive reflections to focus a source in two dimensions. They combine two elliptically shaped mirrors rotated 90° from each other, and having a common focus at a distance *F*. A representation for such a system is given in Figure 1-10. The main concept is the following: sagittal rays, weakly focused by the first mirror, become the tangential rays for the second and vice versa.

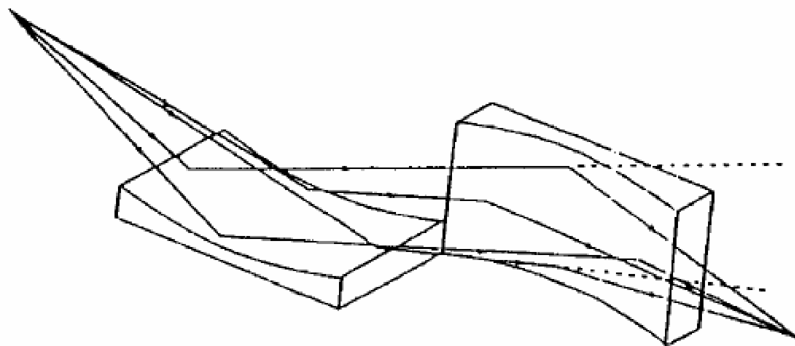

Figure 1-10: Kirkpatrick-Baez focusing system.

The focusing properties of such a mirror are described by the Coddington equations, that is:

For tangential rays

$$\frac{1}{p}+\frac{1}{q_t}=\frac{1}{f_t}=\frac{2}{R_t\sin(\theta_0)} \tag{1.6}$$

and for sagittal rays:

$$\frac{1}{p}+\frac{1}{q_s}=\frac{1}{f_s}=\frac{2\sin(\theta_0)}{R_s} \tag{1.7}$$

where p is the source object distance, q_t is the distance of the tangential line focus from the mirror pole and R_t and R_s are the mirrors radii of curvature in the two orthogonal directions (meridional and sagittal).

If the mirror is spherical ($R_t = R_s$), the two focal lengths differ by a very large factor and the mirror is clearly a poor image-forming device. In 1929 [14] Jentzsch pointed out that a toroidal mirror having a sagittal radius R_s smaller than the meridional radius R_t by a factor θ^2 would bring the two set of rays at the common focus. Therefore, the ideal shape for KB mirror, to reduce astigmatism, is the toroidal one [15]. If so, only two mirrors could be used to image an extended source. However, because of technological difficulties in manufacturing such a mirror, and because the focusing along the sagittal rays is very weak, the mirrors are often prepared flat along this direction, i.e., with $R_s = \infty$. Here, an extended source could be imaged with minimum aberrations only if two pairs of crossed mirrors are used (i.e. four reflections)[16]. In this case aspheric surfaces are needed to remove the coma aberration completely and to ensure a good image quality.

When ML mirrors are employed two additional constraints must be added to the design, which is dictated by the choice of the d-spacing of the multilayer (if periodic). The requirement to achieve a certain magnification M is given by the following relation:

$$\frac{R_1 d_1}{R_2 d_2}=\left(1-\frac{s}{u_1}\right)\left(M-\frac{s}{u_1}\right)M \tag{1.8}$$

where d_1 and d_2 are the multilayer periods, u_1 is the distance between the object and the first mirror and s is the distance between mirrors centers. The ML periods should also fulfill the following relation for the Bragg angles θ_1 and θ_2:

$$2d_1\sin(\theta_1)=2d_2\sin(\theta_2)=n\lambda \tag{1.9}$$

We see that the mirrors must be specifically tailored to achieve a specific value of M.

For extreme focusing, the Kirkpatrick-Baez has proven recently to give the best focusing results (~90 nm, ESRF). This result was obtained with a KB coated with a ML to filter the incoming white beam.

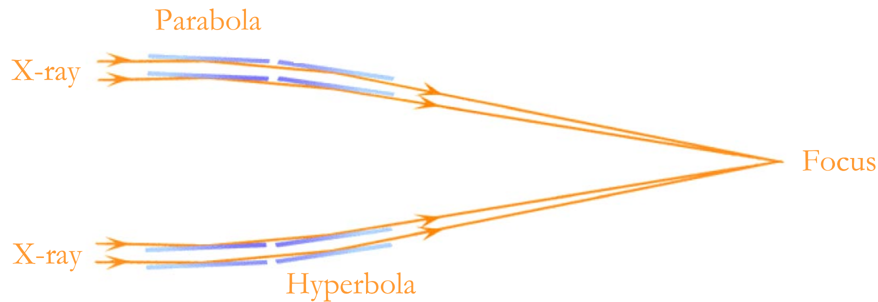

Figure 1-11: Schematic principle of a Wolter type imaging system

Figure 1-12: Wolter type mirror proposed for the fourth-generation SR sources, external diameter ϕ~.01 m (left), the Free Electron Laser. Wolter I mirror shells for Chandra mission (NASA), ϕ~1 m (center). Artistic impression of the ambitious project XEUS (ESA), the X-ray telescope having ϕ~10 m will be linked at 50 m with another detectors satellite with the helps of an auto-tracking system (yellow box).

Wolter types and Lobster eyes [17] have been often proposed for hard X-ray telescopes (HXRT) as they can easily achieve a large effective area. An interesting application of the Wolter geometry has been also proposed for SR application and for the next FEL source, at the Linac Coherent Ligth Source (LCLS)[4]. With a replication technology derived from the experience accumulated over many years in HXR astronomy, miniature Wolter type mirrors have been realized for SR application as focusing or collimator devices. The operating principle is the following: X-rays enter on one end, undergo a single reflection at the interior surface, and exit at the other end with a different direction of travel. The optics is composed of truncated paraboloidal or ellipsoidal shells of revolution depending whether they are used as collimator or as focusing devices. Other authors have proposed the use of Wolter type mirrors for

[4] http://www-ssrl.slac.stanford.edu/lcls/lcls_x-ray-optics_fotos01.html

imaging purposes and, in particular, to image extended objects at SR sources[18]. In this case, as for the KB system, two reflections are needed to fulfill the *Abbe sine condition*.

These optical devices are made of layers with materials deposited onto a supersmooth mandrel[19, 20]. When the mandrel is separated from the mirror shell, for example by thermal dilatation, the innermost layer replicates the mandrel smoothness and serves as the reflecting surface. One of the advantages of using this type of optics is that their cylindrical geometry is adapted to sustain high heat load, as it will be the case for FEL source. Moreover, it can image extended sources without residual aberration. By nesting several confocal mirrors shells it is possible to obtain a largest effective area. This feature is fully exploited when designing an X-ray telescope whose scope is to collect extremely weak flux or to image an extended source such as rest of a Supernova. Their major drawback is that the slope errors induced by the replication process are often too large to be used as optics for advanced SR applications.

Typical optics systems fabricated have a length of approximately 10 cm, a large end diameter of 3-4 cm and a small end diameter of 2-3 cm. A photograph of a large-diameter mandrel and its associated replicated optic is shown in Figure 1-12 (left). On the same figure, similar Wolter type mirrors for HXR astronomy are shown for comparison purpose.

Note that, while the KB geometry was first introduced for X-ray telescopes, the Wolter type mirrors were first designed for microscopy purpose. The reverse finally occurred: KB systems are used in SR source as microscopes and Wolter type mirrors in HXRT!

The lobster-eye[5] design was proposed by Angel in 1979 [17]. The optical geometry consists of a series of micro channels disposed over a plate slightly curved. A ray passing through these micro channels is then either reflected once or transmitted. Rays reflected will be focused in a way which is determined by the plate geometry while rays that pass straight through, will contribute to a diffuse background. The finite height of the tubes will also produce some defocusing in the image, while the angle subtended by each tube at the detector will limit the resolution of the system. Despite of these drawbacks, the great advantage of this design is an almost unlimited field of view. This makes it ideal for imaging and particularly as an all-sky X-ray monitoring device. However, to date, no X-ray telescopes have been built using lobster-eye optics, principally due to the difficulty in

[5] The lobster eye shows a remarkable geometry not found elsewhere in nature. The eye focuses light by reflection, unlike most other eyes that focus by refraction (bending of light) by a lens.

constructing the reflective tubes. Improvements in multi-channel plate technology are expected to lead to a further advance of this technology[6].

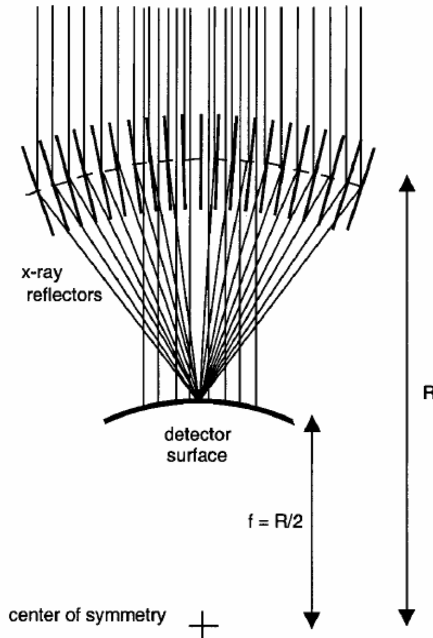

Figure 1-13: Lobster eye imaging system

1.3 Focusing

A very important application of mirrors in X-ray optics is in beam focusing[21]. For this purpose, the mirrors should have an ellipsoidal shape to fulfill the requirement for constant magnification along the beam footprint thus reducing residual aberration and the number photons spread off-axis. If the mirror is coated with a ML, the requirement for constant magnification is translated in a lateral thickness gradient Δx to fulfill the Bragg law along the mirror length while an additional depth gradient Δz is designed according to the required spectral bandwidth.

In the TER geometry the small angle value complicates the optical design, the main aberrations being astigmatism and field obliquity [22]. When using Bragg diffraction from multilayers, the reflected intensity at the peak is less than in the TER case. However, this loss is recovered by the increase of aperture (larger angles). Therefore, this geometry is very efficient for achieving high magnification (large f-number) and throughput.

[6] See for example, http://www.src.le.ac.uk/projects/lobster/

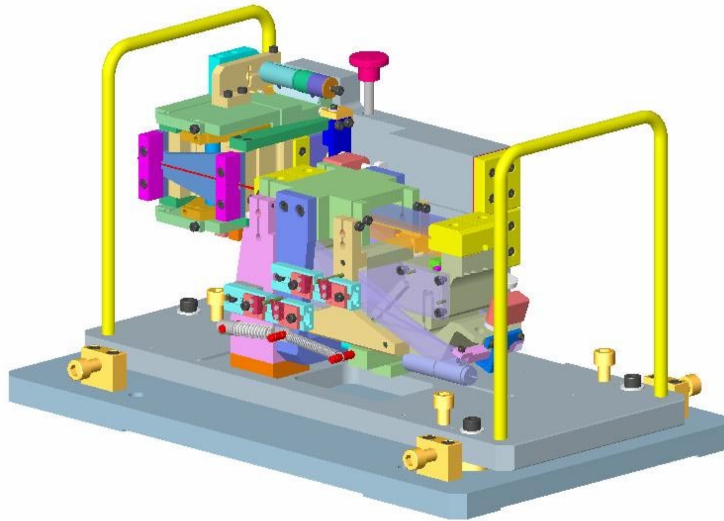

Figure 1-14: Kirkpatrick Baez mirror system fabricated at ESRF[23].

Their use is typically involved when ones need: i) to increase the flux density at the sample position, ii) to obtain a demagnification of the source or iii) in projection imaging geometries.

The performance of a focusing system is typically given in terms of flux and gain in as compared to an equivalent slit geometry. The reflectivity of each individual mirror is also important: in double-reflection geometry the reflectivity of each individual mirror contributes in a multiplicative way. This is particularly important for mirror systems working out of the TER condition because the reflectivity is intrinsically lower than in the TER region.

Let us illustrate this discussion with a practical example: consider a double multilayer mirror $[W/Si]_{200}$ with a 3-nm period and thickness ratio γ=0.5 whose reflectivity is shown in Figure 1-8. We assume the interfacial roughness to be fully correlated and with a constant value of σ_{rms}= 0.2 nm throughout the stack. As seen in Figure 1-8, an increase of interfacial roughness by a factor 2, i.e., when passing from 0.2 nm to 0.4 nm, the reflectivity of a single mirror would decrease from 60% to 47 % and from 36% to 22% after two reflections.

At higher order Bragg peaks this reduction can reach several orders of magnitude. Therefore, to increase the Bragg angle, excluding an operation at the (higher) angles of the harmonics, the preferred solution would consist in reducing as much as possible the multilayer periodicity. Notice that, presently, the minimum usable ML periodicity is settled to about 1-2 nm [24]. The major limitations in fabricating smaller periods are

technological: presence of coating inhomogeneities, use of lateral gradients along the mirror, layer intermixing and difficulty of controlling/monitoring the film thicknesses.

An important figure of merit to evaluate the performance of a focusing device is the *gain* factor *G*. It can be defined as the ratio between the flux at the focal point and the one achievable with a slit that would lead to an equivalent spot size, that is

$$G = \frac{\Phi(\text{Focus})}{\Phi(\text{slit})} = \frac{R^2 A_{eff}}{A_{slit}} = \left[\frac{RL\sin(\theta_0)}{M\sigma}\right]^2 \qquad (1.10)$$

where $M=q/p$ is the mirror magnification, R the mirror reflectivity, L the mirror length, and σ the vertical source size assumed to be 80 μm. Let us consider different KB mirrors configurations, namely, an uncoated silicon system, and a device coated with two ML with dissimilar periods. We consider a typical distance from the source to the mirrors of p = 50 m and a focal length q = 1 m. The gains will be compared assuming mirrors 0.30 m long. The results in terms of G are summarized below. The former case leads to a grazing angle of the order of θ_0*=0.2 deg.*, and reflectivity $R\sim 1$. These numbers provide a GAIN = 4 10^5. The gain is increased if we now consider a ML to increase the usable angles to some degrees. We consider first a ML W(1 nm)/Si(1 nm) such that the first Bragg peak is at θ_t~1 deg and another one with shorter periods, say a ML with W(.5 nm)/Si(.5 nm), for which the angle is increased by a factor 2. Their reflectivity, R=0.6 and R=0.5, respectively, leads to an increase of the gain of G= 2.5 10^6 and G= 2.4 10^7. If now we consider the last example and a focal length of 15 cm, which is possible to achieve with ML-coated KB we arrive to a gain of $\mathbf{10^9}$ (10^8 if we include .2 nm roughness when modeling the reflectivity), a remarkable result in contrast to a TER mirror: a factor 10000 more.

The roughness is probably the ultimate effect limiting ML devices. Its effect is illustrated by the example given in Figure 1-15 and Figure 1-16 showing the variation of the reflectivity at the first Bragg peak of a periodic ML with progressive roughness.

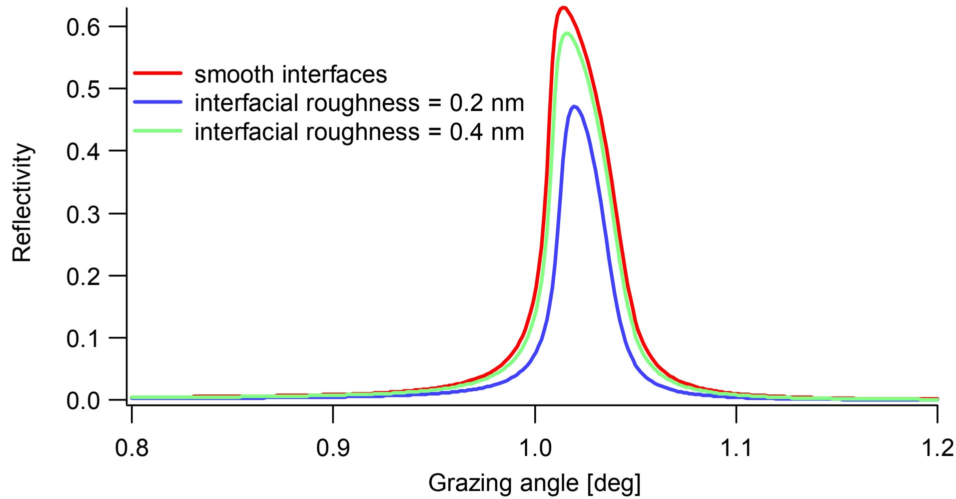

Figure 1-15: Reflectivity of the first Bragg order for different roughness values: 0, 0.2 nm and 0.4 nm.

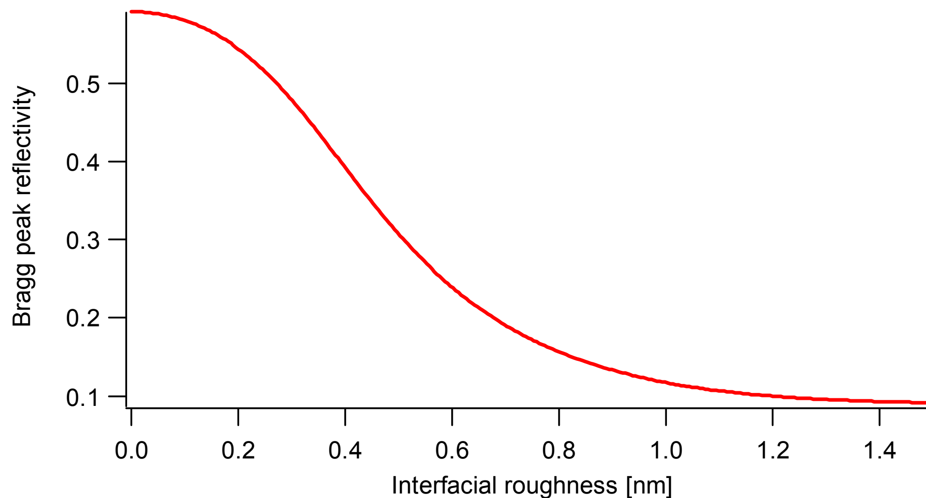

Figure 1-16: Variation of the intensity at the first Bragg peak as a function of the interfacial roughness (Nevot Croce model).

As one can see in Figure 1-16, rms roughness values at each interface should be kept less than 0.3-0.4 nm if one wants to achieve a reflection above the 50% and therefore advantageous gain values.

1.4 Kirkpatrick Baez optics

1.4.1 Mirror manufacturing

Advances in mirror manufacturing have been recently made, and now it possible to fabricate x-ray mirrors with a few Ångstroms rms roughness and with sub-microradian deviations from the ideal spherical or flat figure. Only two techniques are presently

existing for polishing elliptical mirrors to x-ray quality surface roughness. The alternative to the fabrication of monolithic mirrors is to induce the desired shape by bending a flat mirror.

The techniques employed to reach the desired mirror shape are briefly summarized below:

Dynamical Shaping. Here, sophisticated bending techniques are used to shape an x-ray quality flat to an ellipse[21]. This method has successfully produced submicron x-ray beams, the best focus measured to date being 90 nm. However, the focus size is very sensitive to the bender adjustment and is complicated when compared to monolithic mirrors. Because of their additional complexity, benders become increasingly less attractive with stronger demagnification and decreased focal length (large f-number). On the other hand, a fixed shape is only optimized for a fixed energy, i.e., reducing the tenability performance.

Differential deposition. This recent approach allows to realize monolithic mirrors for elliptical K–B system [11]. With this approach, a high density Au layer is differentially deposited onto a cylindrical substrate to get the elliptical shape. Here the desired shape is obtained by mastering the reciprocal speed of the sample and/or sputtering target. This looks relatively easy, in comparison with other figuring techniques (see below). On the other hand the deposited thickness needs to be large, which typically results in the development of intrinsic roughness (columnar growth, crystallization).

Elastic emission machining. Several highly sophisticate techniques can presently be used to reach a good figure up to the nm scale. Yamauchi et. used the fabrication methods of elastic emission machining (EEM) and plasma chemical vaporization machining (CVM) as ultra-precise figuring and polishing methods to prepare both flat and figured X-ray mirrors [12, 25]. EEM is a chemical machining method utilizing reactivity of the surfaces to ultrafine powder particles. Digitally-controlled EEM was proved to create atomically and crystallographically non-damaged surfaces with a figuring accuracy in the 0.1 nm r.m.s range. The main inconvenience of this technique is that the removal rate is low compared with other figuring techniques (ion-milling, diamond turning, etc). Plasma CVM, developed as a precise and effective preprocess of EEM, is a chemical-plasma process with an r.m.s. figure accuracy close to 1 nm, having a high removal rate comparable with conventional grinding. A combined process of plasma CVM and EEM in series was also proposed to enable the manufacturing of the ultra-precise X-ray optical components in a reasonable time. However, only a couple of test mirrors have been produced to date. Therefore, its implementation for intensive mirror production is far from being realized.

Ion milling and diamond turning. Two techniques are well known since the seventies for fabricating high quality mirrors: diamond turning [26, 27] and ion milling[28-30]. The former consists in making a mass replication master or in direct production, as in high precision aspherical optics. In such a case, a single diamond crystal cuts the surface of the metal or glass master into an arbitrary 3D surface with nanometer precision. A sub-nanometer position measurement system is thus required to control the motion of the diamond cutter. This technology was successfully employed for visible and infrared reflective optics because the residual surface roughness is extremely low compared to the wavelength in use. However, there are residual imperfections arising in this process: relevant periodic components appear at spatial scales determined by the removal rate of the tip in the order of several nanometers. This leads inevitably to an enhancement of the X-ray diffuse scattering, which in contrast is extremely sensitive to these spatial frequencies. As a results the diamond turning could only be employed in combination with a polishing technique adapted to polish curved surfaces.

In summary, in terms of gain and spatial resolution, a monolithic system seems to be preferable. Moreover, higher grazing angles can be accessed by coating the mirror with a ML. At large grazing angles dynamical shaping is not suitable due to mechanical constrains. Larger grazing angles would lead to larger beam acceptance, and in turn, to higher flux and lower residual aberrations, coma and field of obliquity. On the other hand, dynamical shaping guarantees a certain flexibility and the possibility of obtaining energy tunability [21]. Its use seems to be complementary and dictated mainly by the final application of the mirror optics.

Among the various solutions to obtain an elliptical mirror, the Optics group of the ESRF proposed first the dynamical shaping [21]. The dynamic shaping has been proved flexible and effective for its optical performance in term of focusing. To achieve X-ray focusing a bender shapes a flat mirror to an elliptical shape. The mirror can be made of a light-weight material as a silicon crystal substrate coated with a high-Z material or a multilayer coating to further tailor the X-ray reflectivity. Anyhow, a flat surface with atomic scale roughness has to be prepared. The details concerning the procedure adopted at ESRF can be found at the page reported below[7]. The best surface finish presently achieved is about 1Å (rms) while the best figure (flatness) for a thick specimen is around 1 μrad (rms).

[7] http://www.esrf.fr/UsersAndScience/Experiments/Optics/CrystalLab/

1.4.2 Layer coating

Numerous materials can be deposited on substrates and various types of techniques of deposition have been used. The sputtering technique is probably the most widely used for coating metallic films.

The sputtering involves knocking an atom or molecule out of a target material by accelerated ions from an excited plasma and condensing it on a substrate either in its original or in a modified form. The sputtering can be achieved by a number of ways, including accelerating the plasma ions by a d.c. field, or with a d.c. field combined with a magnet (to direct the high velocity emitted electrons away from the substrate), with r. f. (with its self induced bias) as well as with ion beams. Hence, names such as magnetron or reactive r.f. sputtering reflect the process that has been used for the deposition.

The technique used in this study involves magnetron sputtering in an Ar+ plasma. This method has the reputation of providing good uniformity and sharp interfaces. Parameters known to influence the quality include sputtering pressure, pre-conditioning, film thickness and dc power. A detailed description of the system used in this dissertation is presented in Chapter 4.

There are many other ways to create complex layered structures. The traditional techniques are listed in the following items:

1. *Evaporation* –Thermal evaporation is the oldest technique, it involves vaporizing a solid by heating the material to sufficiently high temperatures and recondensing it on a cooler substrate. The high temperature can be achieved by resistively heating or by an electron-beam hitting the boat containing the material to be evaporated.

2. *Ion Beam Assisted Deposition (IBAD)* – The interfacial roughness of film deposited by e-beam evaporation can be further improved by making the film thicker and removing the exceeding material by ion bombardment or by parallel ion irradiation of an ion beam. These two processes are generally called IBAD. Here, smoothing occurring is though to be due to preferential removal of weaker bounded surface atoms.

3. *Pulsed Laser Deposition* – A pulsed infrared or ultraviolet laser beam is focused onto a target material at a power density sufficient to vaporize it but not to form a hot plasma. Its main advantage in contrast to the previous methods is the possibility of choosing a wider range of materials, including, carbon, platinum, gold, tungsten, rhenium and tantalum.

Several authors have tested alternative deposition methods for microelectronic industry applications. However, they have not yet been used to produce ML synchrotron

optics. Examples of these techniques include, cluster deposition, atomic layer-by-layer growth, and ion beam deposition.

1.5 Performance of X-ray reflective optics

Although real surfaces have a continuous spectral range of error periods, the traditional way of specifying mirror quality is to divide their shape errors into two main groups: figure and finish. These two extreme regimes are distinguished only by their spatial wavelengths (or frequency). The figure errors are those left by the shaping process. They are generally in a spatial frequency scale range from 10 cm^{-1} down to the macroscopic scale of the mirror. They are measured by interferometry and are usually expressed in terms of Zernike polynomials. At smaller spatial scales, surface imperfections are called finish errors. Finish errors are imperfections left by the finishing process and cover the overall spatial-wavelength spectrum from the near-atomic dimension up to the macroscopic scale. However, as polished surfaces exhibit a fractal spectrum (or fractal-like), i.e., their power spectrum is a power law of the spatial frequency, their finish is only characterized below few hundred of μm (see chapter 2) and finally combined to figure measurements. All those errors can be described in terms of their power spectral density.

The light scattered from the surface irregularities degrades optical performance in several different ways. First, it reduces the optical throughput because some of the scattered radiation will not even reach the focal plane. Second, the wide-angle scatter will produce a veiling glare that reduces the image contrast or the signal-to-noise ratio at the detector. Finally, the intensity scattered at small angle will decrease resolution by producing an image blur.

A detailed description of these effects is beyond the scope of this work. Therefore, we will limit ourselves to mention two references, [9, 31], illustrating the way surface finish and figure errors affect the performance of an optical system. With the approach described in these works it is possible to describe the intensity in the image plane of an imaging optics in terms of the Power Spectral Density of the surface roughness. Eventually PSD measurements, available through surface metrology, can be used to predict the optical performance of X-ray optics.

1.6 Future applications of SR reflective optics

The two main tasks for future applications involved in the third and fourth generations of SR are: i) to preserve the high degree of spatial coherence and ii) to obtain extreme focusing down to the diffraction limit. For extreme focusing surface roughness and angular errors will have to be further decreased, depending on the specific

application. The development of fabrication processes controlled in-situ using SR itself is believed to achieve these two objectives.

Among the most promising applications envisaged for the near future, imaging techniques play an important role. They can be classified as full field or scanning. The full-field techniques include absorption radiography, tomography, phase-contrast tomography, phase contrast imaging. Depending on the level of resolution, the techniques use either direct illumination of the sample or additional magnifying optical elements (projection imaging). The diffractive optics promises to reach a resolution of 10 nm for 10 keV radiation, compared to the 90-100 nm limit at third generation synchrotron sources. Very promising is imaging for time-resolved studies of processes. Scanning methods, on the other hand, require focusing optics to provide a small beam cross section at the sample position and micro stages for mechanical movements of the sample.

There are wide prospects of combining scanning imaging techniques with other methods of X-ray analysis (chemical mapping, trace element mapping, magnetic diffraction). The full transverse coherence of the beam will allow the development of novel methods for the investigation of crystalline and non-crystalline matter. Many of these methods are already known from the domain explored by optical lasers, but the use of short-wavelength radiation in the Å regime will improve the resolution and expand the range of applications. Methods to be mentioned here are off-line holography, interferometry methods and speckle interferometry. Moreover, the use of coherent beams will enable the development of new techniques like lens-less imaging, where the information about the wavefront form and the intensity distribution provides phase information and allows the image of the object to be reconstructed with holographic methods.

However, even with the present advances in mirror fabrication technology, residual imperfections on mirrors (as well as on other optical X-ray SR components) will be found to degrade the quality of X-ray beams. This raises new challenges on mirror polishing and metrology and strongly motivates the subject of this dissertation.

Chapter 2 Surface roughness

As already pointed out, the finish of optical surfaces is an important issue in Hard X-ray optics because roughness leads to scattering thus leading to performance degradation of an imaging device. In this chapter, the main parameters affecting the surface finish are discussed by introducing the power spectral density (PSD) function. As mentioned previously, the optics performance can be expressed in terms of the parameters used to describe the PSD, i.e., the rms roughness, the correlation length and the roughness exponent.

In this chapter, the characterization techniques giving access to these finish parameters and the surface topography are presented in comparison with scattering methods and in relation to their spatial sensitivity. The scaling theory and the linear model of film growth are finally discussed. These approaches show that a parametric description of the roughness (through a physical model of the surface) combined with a scattering theory (see Chapter 3), enable one to make a detailed description of a surface morphology both in the spatial and temporal domains in a unique descriptive frame.

2.1 Surface finish parameters

The parameters describing the finish of a surface are usually defined from the surface $Z(x,y)$ referenced to the zero mean surface plane. Let us consider for simplicity a 1D profile as schematically shown in Figure 2-1. The relevant statistical quantities about a surface topography can be defined in accordance to the following identity:

The root mean square (rms) roughness, σ:

$$\sigma^2 = \lim_{L\to\infty} \frac{1}{L} \int_{-L/2}^{L/2} Z^2(x)dx \tag{2.1}$$

The rms profile slope, m:

$$m^2 = \lim_{L\to\infty} \frac{1}{L} \int_{-L/2}^{L/2} \left(\frac{dZ}{dx}\right)^2 dx \tag{2.2}$$

The rms profile curvature, c:

$$c^2 = \lim_{L\to\infty} \frac{1}{L} \int_{-L/2}^{L/2} \left(\frac{d^2 Z}{dx^2} \right)^2 dx \tag{2.3}$$

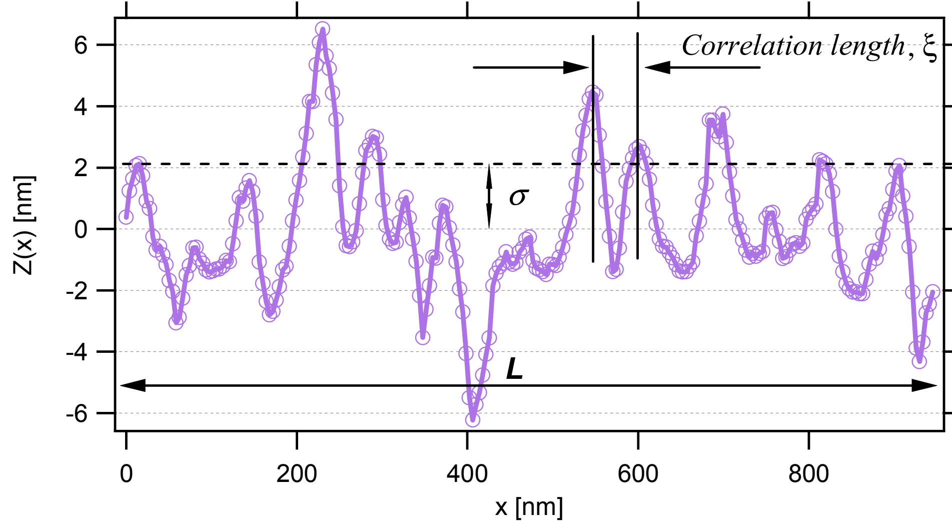

Figure 2-1: Typical sampled profile, measured with an Atomic Force Microscope, after the flattening procedure (profile -line fit). The notation used in the text are illustrated on the profile.

The above definitions are written using the notion of infinite limits for the scanning length (or window) L. However, any real measurement can only be performed within a limited bandwidth. This leads to the well-known Nyquist theorem (also called sampling theorem). The theorem states that any real roughness measurement can be performed only in a discrete bandwidth of spatial frequency determined by:

$$f_{\min} = \frac{1}{Nd} \quad f_{\max} = \frac{1}{2d} \tag{2.4}$$

where N is the number of sampled points and d is their sampling distance. The longest measurable wavelength is essentially the trace length and the shortest is twice the sampling interval, $2d$, the reciprocal of the Nyquist frequency. For a profile roughness measurement, these limits arise from the fact that low frequencies are filtered out of the measured profile by the flattening procedure to remove tilt effects introduced by the measurement process, and high frequencies are removed by a mechanism involved in any realistic measurement, such as the finite lateral resolution.

2.2 Roughness characterization techniques

The various measurement techniques can be classified by the range of spatial wavelengths they can reach when measuring mirror imperfections. They can be divided in two main families: the ones measuring shape errors, generally based on optical

interferometry and/or slope errors and those measuring the finish, which, have sub-micron resolution. The former will not be discussed along this thesis as they involve the analysis of spatial periods that do not influence the diffuse scattering phenomenon. Notice, that even though shape errors are not responsible for scattering, during scatter measurements, they can lead to significant experimental difficulties, e.g. due to geometrical deflection of the specular beam. Therefore, their characterization is preferable before to carrying out X-ray measurements.

Scanning Probe Microscopy (SPM) and X-ray reflectometry are the experimental techniques which are most commonly employed for sub-micron lateral resolution characterization of surface roughness. The performances of these two characterization methods are illustrated in Fig. 2.2 in comparison to other techniques. As one can see, when synchrotrons are used as radiation sources, the scattering method provides the largest spatial frequency range covering more than five orders of magnitudes.

SPM techniques as Scanning Tunneling Microscopy (STM) and Atomic Force Microscopy (AFM) became popular in the early 80's for their capability of providing accurate topographic area profiles at nanometer length scale vertically and laterally on both conducting and non conducting surface. They can probe surface topology over many orders of magnitude (>5 order of magnitude in the vertical and lateral extent) by simply changing the scanning size.

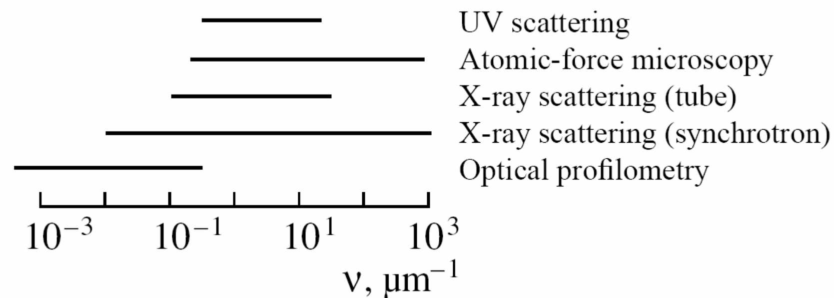

Figure 2-2: Typical spatial frequency ranges accessed by presently existing methods of investigation of surface roughness.

The X-ray reflectometry method (specular and diffuse X-ray scattering) will be presented extensively in a dedicated chapter (Chapter 3). In contrast to SPM methods, it cannot provide a topography image of the surface but only statistically averaged information over a large area of the surface investigated (~cm^2), namely, the rms roughness (from specular reflectivity), the PSDs of external and buried interfaces and their correlation (form diffuse X-ray scattering), and the density profile distribution (from reflectivity). On the other hand, strictly speaking, not even SPM methods yield 2D topographs: the electronic signals measured by SPM are translated, through processing in

height variations. Evidently, the correctness of the processing depends on many instrumental effects, e.g., tip deterioration and/or setup stability, as well as factors that may result in image artifacts, e.g., presence of oxidization affecting the tunnel current measurements (STM) or presence of thin water layers during AFM measurements.

Three advantages of the X-ray scattering (XRS) testing method are worth being mentioned. First, the x-ray method gives a unique possibility to investigate a buried interface and, particularly, to establish the degree of vertical correlation (conformity) of roughness between the substrate and the external surface of a film. Second, it can be easily adapted for in situ investigations. Third, the small angle in use (large footprint), allows a reliable and representative measurement of the entire surface, avoiding in particular the statistical oscillations that arise frequently during the PSD analysis. These points are extremely delicate especially for measuring the scaling exponents[32, 33].

2.2.1 Scanning probe techniques

In the early 1980's two IBM scientists, Binnig and Rohrer, developed a new technique for studying surface structure - Scanning Tunnelling Microscopy (STM). This invention was quickly followed by the development of a whole family of related techniques that, with STM, may be classified in the general category of Scanning Probe Microscopy (SPM) techniques. The most important of these later techniques is Atomic Force Microscopy (AFM). The development of these techniques has without any doubt been the most important event in the field of surface science in the last decades, and has opened up many new areas of science and engineering at the atomic and molecular level. Within five years, this invention was awarded the Nobel prize, a clear confirmation of its importance.

Like all scanning probe microscopes, the AFM utilizes a sharp probe moving over the surface of a sample in a raster scan movement. In AFM, the probe is a tip made of few atoms built on the end of a cantilever that bends in response to the force between the tip and the sample. The first AFM used a scanning tunnelling microscope at the end of the cantilever to detect the bending of the lever, but now most AFMs employ an optical lever technique.

The diagram in Fig. 2.3 illustrates how this works; as the cantilever flexes, the light from the laser is reflected onto the split photo-diode. By measuring the difference signal, changes in the bending of the cantilever can be measured. Since the Cantilever obeys Hooke's Law for small displacements, the interaction force between the tip and the sample can be found.

The movement of the tip or of the sample is performed by an extremely precise positioning device made from piezo-electric ceramics. The scanner is capable of sub-angstrom resolution in x-, y- and z-directions. As a usual convention, the z-axis is chosen to be perpendicular to the sample surface.

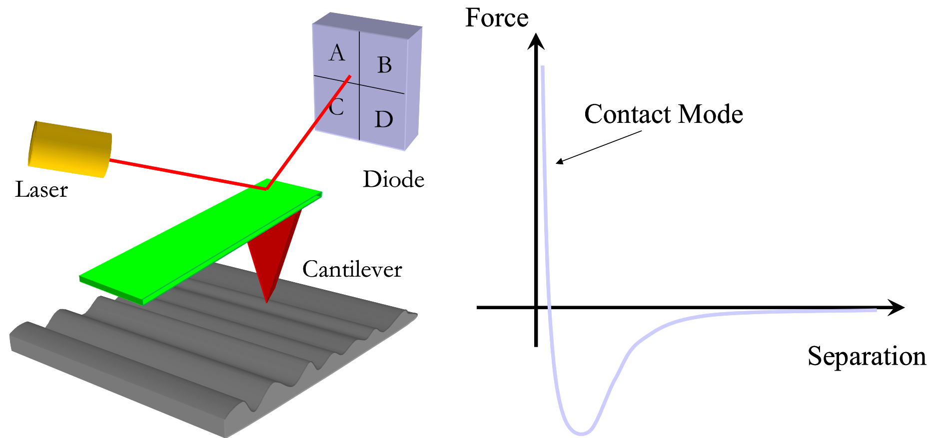

Figure 2-3: (left) Schematic principle of an atomic force microscope. (rigth) General behavior of the force as a function of the separation between tip and sample.

The AFM can be operated in three principal scanning modes:

The contact mode is the most common method of operation of the AFM. As the name suggests, the tip and sample remain in close contact as the scanning proceeds. Here "contact" means that the intermolecular force between the tip and the sample is in a repulsive regime (see figure 2.3, right).

The tapping mode is the second most commonly used mode. When operated in air or other gases, the cantilever is oscillated at its resonant frequency (often hundreds of kilohertz) and positioned above the surface to only tap the surface for a very small fraction of its oscillation period. This is still a contact mode, in the sense defined earlier, except that with very short time over which this contact occurs, the lateral forces are dramatically reduced as the tip scans over the surface. Other methods of obtaining image contrast are also possible by tapping mode. An interesting one is the constant force mode, where the feedback loop adjusts so that the amplitude of the cantilever oscillation remains (nearly) constant.

The non-contact operation is another method for getting an image of the sample. Here, the cantilever is oscillated above the surface of the sample at a distance sufficiently large to leave the repulsive regime of the inter-molecular force. At ambient conditions this mode is very difficult to operate because of the contamination with a thin layer of water present on the surface of the sample, which will invariably form a small capillary bridge between the tip and the sample and cause the tip to "jump-to-contact".

2.2.2 X-ray based techniques

Information about the spatial distribution of the roughness from X-ray scattering measurements is generally obtained by inspecting the distribution $I(\theta_0, \theta_S)$ with a point detector placed at the angle $\theta_0 + \theta_S$ around a specular position θ_0. The scattered intensity can be probed by employing different detector-sample scanning geometries. The main type of scans in the plane of incidence, defined by the surface normal and the beam projection on the surface, are the following:

1. *Specular scan* or $\theta / 2\theta$ scan: it corresponds to maintaining $\theta_0 + \theta_S = 2\theta_0$. This scan is used to measure the specular reflectivity as a function of the grazing angle θ_0. The scan after data modeling, allows probing thickness, density and roughness.
2. *Detector scan* or 2θ-scan, in this case θ_0 is kept constant and $\theta_0 + \theta_S$ is varied. By scanning the detector around the specular reflection position one probes the lateral distribution of the surface roughness directly, i.e., one measures the PSD of the surface "directly". Since θ_0 is constant, the field inside the sample remains constant during a scan. Therefore, the interference effect that may be observed is only due to the superposition of the waves scattered at the interfaces that contribute to the measured intensity.
3. *Rocking scan* or sample scan: while the detector is maintained fixed in a direction such that $\theta_0 + \theta_s = const$, the sample is scanned by a relative movement of $\pm\theta_0$. As in the previous case, the scan gives access to the PSD. However, the interpretation is more complicated because the interference may be not a property of the sample but partially due to the interference between incident and scattered beams.

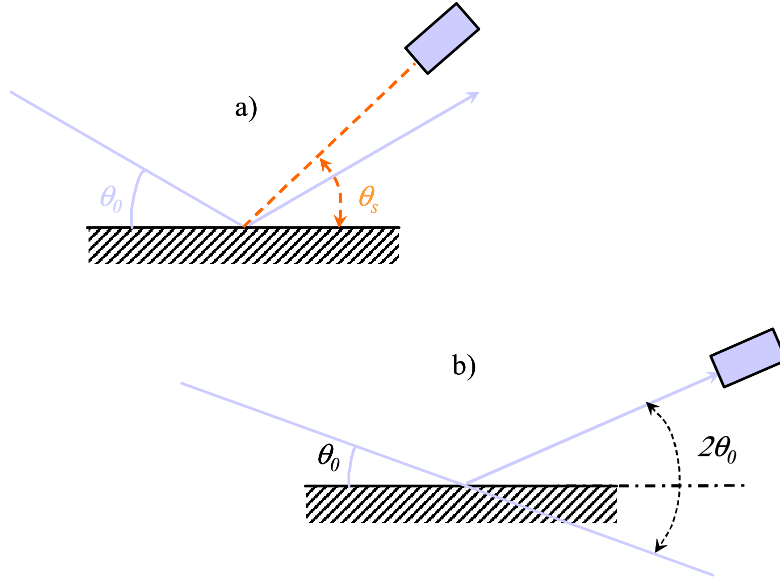

Figure 2-4: Scattering geometry commonly employed for surface roughness characterizations: (a) 2θ scan (or detector scan) (b) $\theta/2\theta$ scan. The blue lines represent the specular beam direction assumed to be a monochromatic plane wave.

Another experimental approach was recently proposed by Salditt [34]. It consists in the off-plane detector-scan through the azimuth angle φ at fixed grazing angle θ.

In a sense, the different scans are equivalent, because all of them allow one to obtain similar information about the sample, namely, the PSD-function in a certain range of the spatial frequencies. Nonetheless, the range of measurable spatial frequencies is quite different for different scans.

The upper and the lower frequency limit of detector scanning in the incidence plane is estimated by Taylor expanding the cosines in $f = |\cos(\theta_s) - \cos(\theta_0)|/\lambda$, as:

$$f_{\max} = \frac{\theta_{\max}^2}{2\lambda}; \qquad f_{\min} \sim \frac{\theta_0 \delta\theta}{\lambda}; \qquad \delta\theta = \frac{d_{vert}}{D} \tag{2.5}$$

where θ_{max} is the maximal measurable scattering angle, d_{vert} is the height of a primary beam and D is the sample-detector distance. In case of the rocking-scan we obtain the same maximal frequency as for detector scanning if the incidence angle $\theta_0 = \theta_{\max}/\sqrt{2}$, where θ_{max} is the maximum detectable angle in detector scan geometry, i.e., typically $\theta_0 >> \theta_{cr}$.

However, there are several crucial points inherent in the rocking-scan. In particular, large grazing angles result in a deep penetration of an incident beam into a matter, i.e. up to several micrometers instead of several nanometers in case of detector scanning (in total

external reflection region). Hence, an uncontrollable contribution of scattering from volume inhomogeneities into the total scattering diagram is much larger for the rocking-scan. Moreover, the intensity decays as $\sim 1/\sin^4(\theta_0)$ at large θ, thus reducing the counting statistics. At the same time the effect of a near surface (oxidized or adhesion) layer on the reflectance and scattering of X-rays is more pronounced in this region and this makes difficult the extraction of the information about the sample. Besides, the theory describing the X-ray scattering from a surface becomes more complicated (see next chapter).

For the off-plane detector scanning we have:

$$f_{\min} \cong \frac{\varphi \cos\theta_0}{\lambda}, \tag{2.6}$$

where φ is the fixed azimuth angle. The expression (2.6) shows that, although the angle φ is small, the minimal registered frequency will be larger than that available in detector scanning by a factor $\varphi/(\theta_0\delta\theta) \sim 1/\delta\theta$.

So, it is possible to conclude that the detector scanning in the incidence plane permits the determination of the PSD-function in a widest range of the spatial frequencies, and only this scanning will be used in the experiments described hereafter. Furthermore, among the X-ray scanning modes presented above only the detector scan characterization allows the sample to be in a stationary position. Experimentally this is an important feature, and the characterization technique we developed will benefit from it.

2.2.3 High resolution angular dispersive diffuse X-ray scattering

As observed at the beginning of this section, the scattering methods can provide information on a surface over a spatial frequency range that is more than 5 orders of magnitude large. Full exploitation of this performance requires the development of relatively sophisticated setups to achieve the smallest beam divergence and a relatively high signal to noise ratio. The performance of a scattering experiment in terms of spectral bandwidth is actually imposed by the width of the primary beam (i.e., the smallest detectable spatial frequency), the spatial resolution of the detector convolving the scattering image, and by the minimum flux detectable at large scattering angles (corresponding to the largest detectable spatial frequency). The limitation to the maximum detectable scattering angle can be due to several factors: the X-ray background present during the experiment, an asymmetric shape of the primary beam with pronounced wings at large angles or by limits imposed by mechanical impediments to the propagation such as X-ray windows after the sample. Developing an experimental station for scattering measurements that maximize the usable angular range turned out to be an

extremely delicate and laborious task. For example, to reduce the background inside the experimental hutch, it is necessary to operate either in vacuum or in a low absorbing environment to reduce scattering along the beam path. Scattering from windows in the angular region of interest should be reduced as much as possible, while operating with extremely long beam lines is favorable to reduce the angular width of the primary beam. The angular width of the primary beam generally depends on the size of the last slit present before the sample. The slit size determines the beam divergence only if the following condition is verified:

$$\Delta z \leq \sigma + L \cdot \tan(\Delta\theta_{source}) \tag{2.7}$$

where Δz is the slit size, σ is the source size and $\Delta\theta_{source}$ is the angular divergence of the source, see e.g. in Figure 2.5.

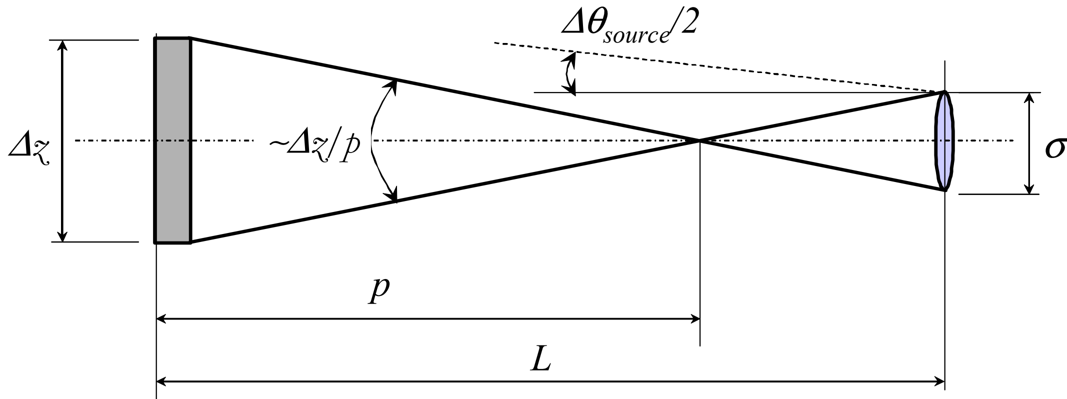

Figure 2-5: Sketch illustrating the slit-source geometry

Another solution consists in using multiple reflections in a channel cut crystal to reduce as much as possible the angular width predicted by the Darwin theory. This solution enables an accurate measurement of the specular peak where the intensity typically varies very quickly. On the other hand, this is done at the expense of the flux, therefore limiting the maximum scattering angles usable.

As an example results showing measurements performed with a high-resolution setup are presented. This setup makes use of an angular dispersive setup to analyze highly polished Si crystals from two different manufacturing companies.

The measurements were performed using a set of channel cut crystals in a scheme with multiple reflections (three for each crystal) to reduce as much as possible both the beam divergence of the primary beam and the angular acceptance of the detector (both less than 0.4 μrad). This experiment allowed us to characterize the sample over more than five orders of magnitudes. In this experiment, after monochromatization, the probing beam was reflected by a Si crystal set at a working energy of 17.5 keV delivered by a ML

monochromator ($\Delta E/E \sim 10^{-2}$). Figure 2.6 presents a sketch of the setup used to determine both the instrumental resolution and the scattered intensity. The setup is shown in Fig. 2.7.

The results obtained from the measurements of the two samples are finally shown in Fig. 2.8 (samples obtained from SESO company) and Fig. 2.9 (Sample from GENERAL OPTICS). The wings observed on the scattered beam are wider than for the direct peak, which proves that the scattered signal is well above the instrumental response. A comparison between XRS and instrumental resolution shows that one could evaluate the PSD function over more than 5 orders of magnitude. On the other hand, a wide peak in Fig. 2.9 (green curve) was proved to be present even under different grazing angle and slit apertures. Although the two surfaces were extremely smooth, the roughness was proved to be σ_{rms}<0.3 nm, this peak was always present during the measurements. Its origin is probably caused by the presence of edge effects and/or relevant figure errors at low spatial frequencies. Therefore, diffuse X-ray scattering measurements are probably impossible on this sample. The two silicon samples were polished with different technologies, resulting in different slope errors, despite similar small-scale roughness.

The above considerations show both the advantages and the limits of using a high-resolution XRS setup.

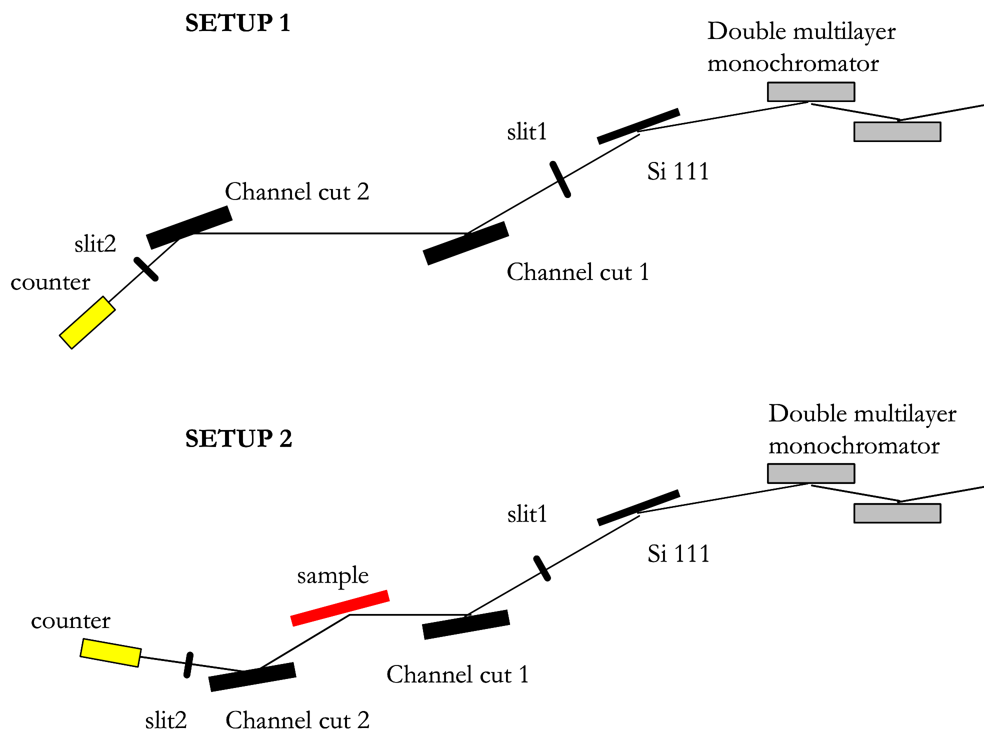

Figure 2-6: Setup for the measurement of the instrumental resolution (top) and a high-resolution setup for angular dispersive XRS measurements (bottom).

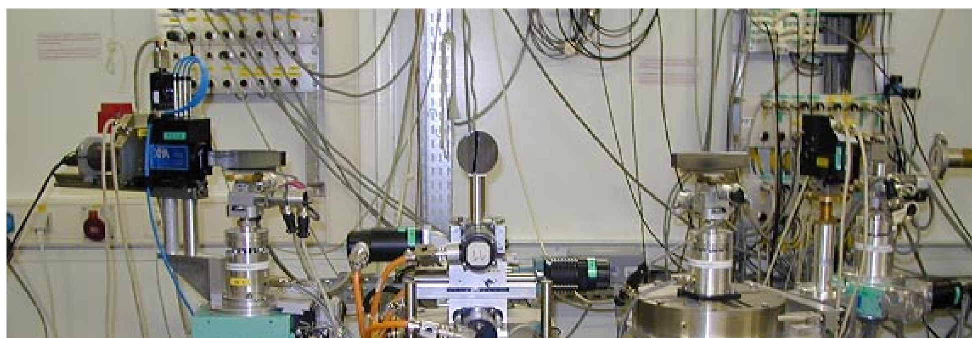

Figure 2-7: Experimental setup for angular dispersive measurements; the black box facing the detectror is a set of filters with calibrated thicknesses used for the measurements over several orders of magnitude of the radiation intensity.

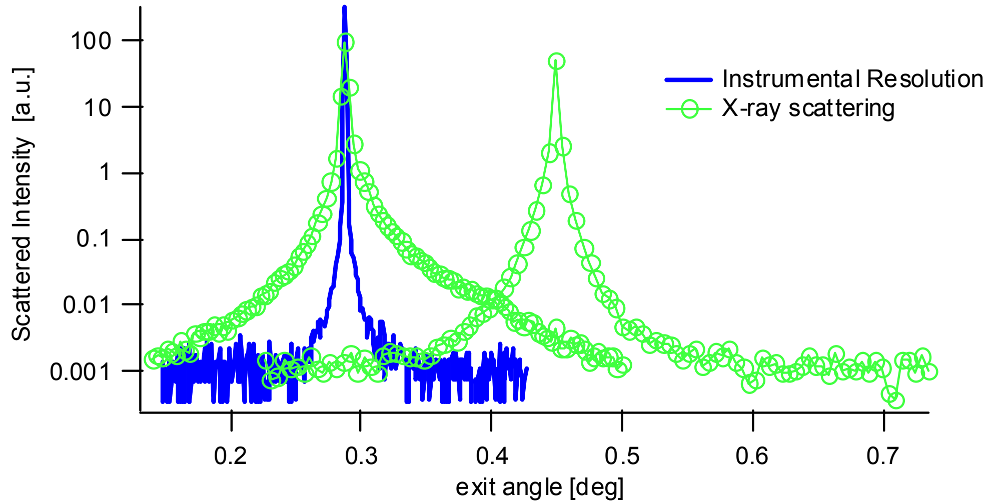

Figure 2-8: High resolution XRS measurements at two different grazing angles performed with the setup depicted in the previous figure. The sample analyzed was a super-polished Si (111) crystal from SESO.

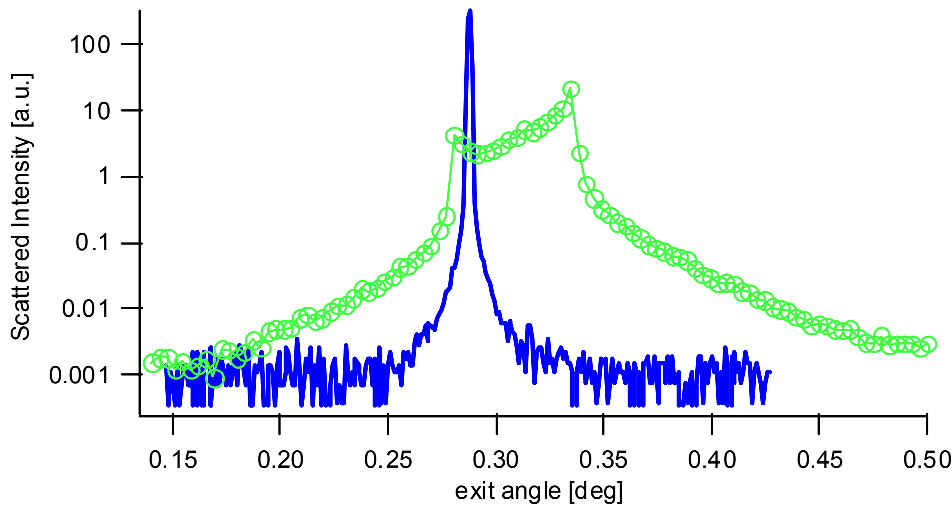

Figure 2-9: High-resolution XRS measurements performed on super-polished substrate from General Optics in comparison with instrumental resolution.

2.3 Thin film and multilayer characterization

In the first chapter, we have described the potential of synthetic layered structure in comparison with perfect crystals. Their technological development implies the availability of a testing method enabling a quantitative analysis of these layered structures not accessible with standards SPM. For the manufacturing of layered coatings it is extremely important to have a short feedback loop between the measurement of the performance of a coating obtained in a deposition run (calibration) and the next one (fabrication of the final structure). The test methods should yield sufficient information to improve the next

deposition run and hence improve the final performance. A typical technological issue is the control of the boundary positions along the multilayer stack. The small thickness of the layers involved, of the order of few nanometers, and the requirements on their position regarding the standing wave field, require a picometer control of the thickness. Other sources of imperfections include boundary roughness, mixing of the materials and contamination. A characterization technique capable of distinguishing between all imperfections is highly desirable.

The deposited films are often very thin and interference between the boundary interfaces cannot generally be neglected. A scattering theory that is more general than the one used in the case of a simple substrate is necessary to quantitatively analyze these structures. It requires an accurate modeling of solid-X-ray interactions.

A unique theory describing any kind of surface does not exist yet. Various models exist, although none is fully satisfactory to describe the problem, see, e.g., The Rayleigh, DWBA and PT Theory [35]. For all of them, in the first order approximation only surface and interface in the smooth surface limit can be described. Rougher surfaces require the development of cumbersome formulae, which lack physical interpretation, and lead to problems of numerical nature requiring sophisticated computing procedures. When the first order of approximation is sufficient to describe the problem, the X-ray scattering method through a modeling of scattering data, gives the unique opportunity of investigating each boundary quantitatively providing information in a non-destructive way. Then, the experimental techniques have used the scanning geometry schemes presented in the previous sections.

Hereafter, we shall discuss how to obtain quantitative information about a surface introducing the formal definition of PSD function and presenting its version used in case of bandwidth-limited measurements. This is done considering only 1D and 2D profiles data onto a surface, while the spectral analysis from the inspection of the scattering data will be introduced in the following chapter.

2.4 The definition of Power Spectral Density

Most of the roughness characterizations techniques presented so far measure the fluctuation along a linear surface profile rather than over an area, and area-measurements data are often composed of series of parallel line traces. Therefore, it is natural to define the profile power spectral density $PSD_{1D}(f)$ first and then to relate it to the area spectrum $PSD_{2D}(\vec{f})$. The profile power spectral density is then expressed as the expected value of the Fourier transform of the profile Z(x) over an ensemble of profiles (or surfaces). That is [36],

$$PSD_{1D}(f) = \lim_{L \to \infty} \left| \frac{2}{L} \int_L dx \cdot e^{i2\pi f \cdot x} \cdot Z(x) \right|^2 \tag{2.8}$$

where f is the surface spatial frequency, L is the trace length and $Z(x)$ is a surface profile. The two-dimensional (area) spectrum can be defined in the following way:

$$PSD_{1D}(f) = \lim_{A \to \infty} \left| \frac{1}{A} \int_A d\vec{r} \cdot e^{i2\pi \vec{f} \cdot \vec{x}} \cdot Z(\vec{r}) \right|^2 \tag{2.9}$$

where $\vec{r} = (x, y)$ and $\vec{f} = (f_x, f_y)$ are vectors in the surface plane and A is the area considered on this surface.

Despite an apparent similarity, the two spectra (2.8) and (2.9) are quite different. They have different dimensions: the $PSD_{1D}(f)$ is measured in cubic length units, while its 2D version has a fourth power length unit. As we shall see later on (Sec. 2.6), they are connected by a simple manner (see sec. 2.4.3).

2.4.1 Bandwidth limited PSD measurements

The spectra defined in (2.8) and (2.9) are given for an infinitely long profile. However, any real instrument can measure it in a limited spectral bandwidth with a limited number of sampling points following the Nyquist criteria. We shall discuss first how the PSD is obtained from a limited set of sampled points. Processing discrete data points to obtain a 1-D PSD involves specific algorithm procedures. The most commonly used is called estimator or periodogram[36-39], in which the PSD is calculated using a finite number of finite-length profile through an FFT algorithm.

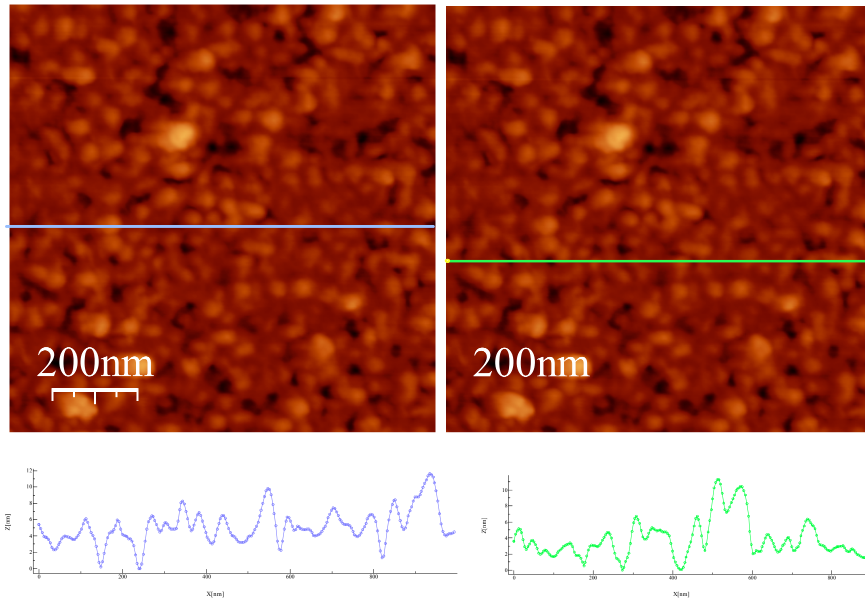

Figure 2-10: Two sampled profiles extracted from 2 different regions of the same sample area. The topography of an Iridium sample was measured by AFM using $L = 1\,\mu m$ *and* $N = 256$

The use of this procedure leads to some statistical effects: let us consider the two profiles shown in Figure 2-10. These profiles are taken from the same surface area. However, due to the random nature of roughness, these two 1D statistical realizations are different and large fluctuations are observed between adjacent frequencies on their estimated power spectrum (Figure 2-11) as well as from profile to profile, which is analog to speckle phenomena in fluctuation spectroscopy [36]. Notice also the raising of the fluctuation amplitude when the spatial scale approaches the largest dimension. This is due to the limited number of periods contributing to the counting statistics during the calculation of the PSD. These fluctuations are smoothened out if one considers as many realizations as possible or when considering unbounded profiles[8]. To illustrate this effect, let us compare the power spectrum obtained from a single linear profile to its corresponding bi-dimensional PSD, see Figure 2-12. Here, the ensemble averaging is increased by a factor N^2 and this results in a strong reduction of the fluctuations. From an experimental point of view, this means that one should perform as many profile measurements as possible in order to have reliable statistics for the surface investigated.

8 An infinitely long profile will have thus an infinite (integer) number of spatial frequencies contributing to the PSD calculation.

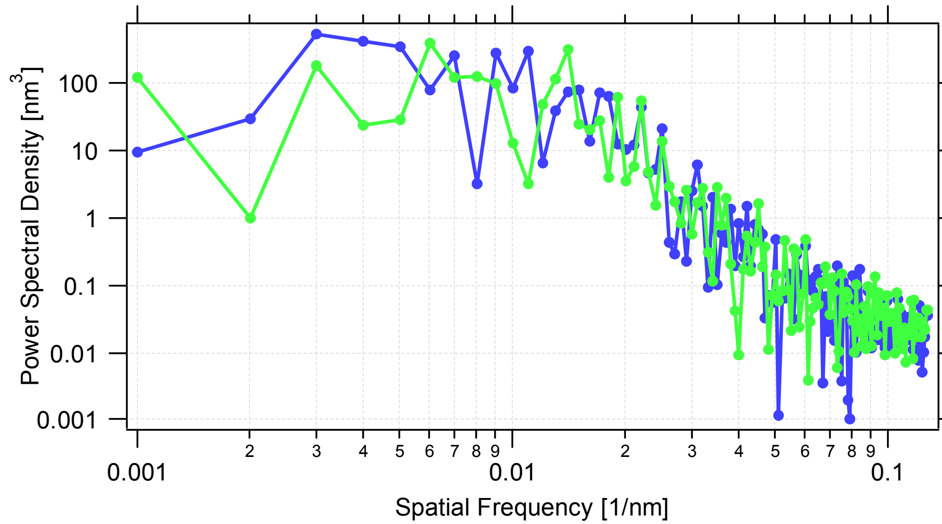

Figure 2-11: 1D PSD obtained from the previous profiles. The large fluctuation is an artifact caused by the finite size of the measurements.

Another effect of the finite size of the PSD might arise during the detrending procedure, i.e. the subtraction of the tilt from original data, consisting in the appearance of a characteristic length where the PSD saturates (*knee* point)[40]. This is just an artifact that can be removed using windowing [37] during the periodogram estimator procedure or combining the measurement to another one, e.g. obtained from another characterization technique, sensitive in a spectral bandwidth extending before the roll-off spatial frequency. If the roll-off frequency is present also after the PSD corrections, one can conclude that the PSD reflects a property of the sample, i.e. the saturation of the roughness at small spatial frequency. The wavelength at which the saturation occurs is called the correlation length of the surface roughness.

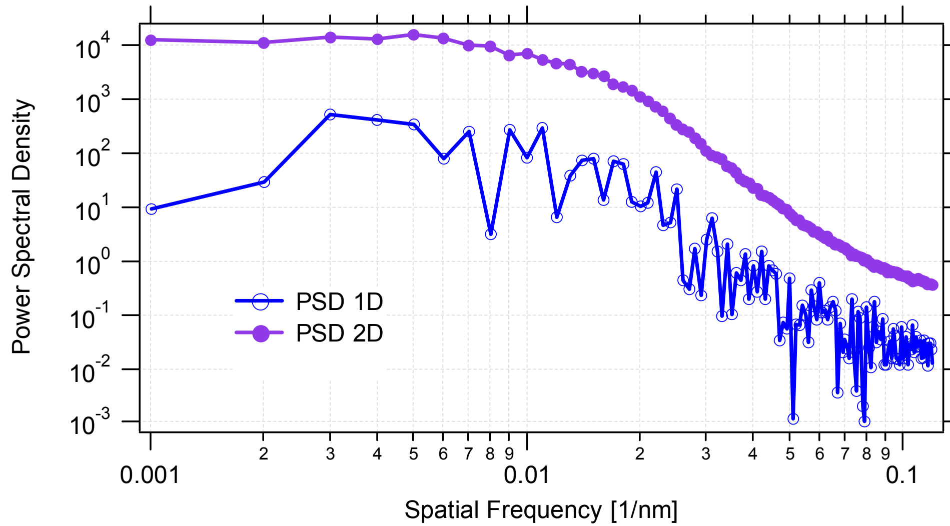

Figure 2-12: Comparison between area spectrum and profile spectrum. Evidently the reduction of the fluctuation has to be attributed to the improved sampling and not to the sample itself.

2.4.2 PSD and Correlation function

Several metrology procedures based on the use of the PSD function have been incorporated by metrology associations as standard characterization method for the surface roughness, see, e.g., the American Society for Testing Materials[9]. Nevertheless, some authors use the correlation function instead of the power spectral density to characterize a rough surface. This is in principle equivalent since the correlation function is just the Fourier transform of the PSD [41]. However, the Fourier transform can only be calculated if the PSD is known for all spatial frequencies from 0 to ∞, while real measuring instruments have limited bandwidth and spatial resolution. As each measurement gives the PSD over a limited range of spatial frequencies, the instrumental resolution described by the modulation transfer function of the instrument, enters as a multiplication factor in the PSD that can thus be easily corrected. Measurements performed with different instruments can then be combined by superimposing the PSDs in the region where the spatial frequencies overlap. In addition, surfaces often have a fractal behavior and their PSD could be described by a power law without any characteristic length. Here, the notion of correlation length introduced when dealing with correlation functions, would only describe the measurement tool[42]. The power spectra, still described in this case by a power law in the measurable range of spatial frequencies, remain meaningful. As we shall see in the next chapter, the scattering into a specific

[9] See e.g. http://www.astm.org/cgi-bin/SoftCart.exe/DATABASE.CART/WITHDRAWN/F1811.htm

direction in the smooth surface limits, will be shown to be uniquely determined by the PSD at one single spatial frequency ($I(\theta) \Leftrightarrow PSD(f)$) according to the grating equation relating them uniquely. In contrast, the evaluation of the scattered intensity from the correlation function would require information over the entire range from 0 to ∞ [10].

2.4.3 2D and 1D power spectra

The 1D spectrum is the natural statistics of profile measurements, while the area spectrum (2D) appears in the description of the scattering and other area dependent properties of the surface, e.g., during the description of film growth evolution[43]. The two are related by the following relation:

$$PSD_{1D}(f_x) = \int_{-\infty}^{\infty} PSD_{2D}(f_x, f_y)\, df_y \tag{2.10}$$

Although related, the two spectra are quite different quantities, with different units. The PSD_{1D} has length cube unit while the 2D spectra have length to the fourth power. Together with (2.10), this leads to the interesting consequence that the area under the two spectra should be the same, i.e., the root mean square profile roughness must equal to the rms area roughness.

Generally, Eq. (2.10) cannot be inverted to give the area spectrum in terms of the profile spectrum. There are only two special cases of interest where this operation can be carried out: i) a grating-like surface and ii) a random surface statistically isotropic. In the former case, and considering a profile taken across the grooves, the Eq. (2.10) will yield $PSD_{2D}(f_x, f_y) = PSD_{1D}(f_x)\delta(f_y)$. The second case consists of an isotropically rough surface that can be defined as $PSD_{2D}(f_x, f_y) = PSD(f)$, where $f = \sqrt{f_x^{\,2} + f_y^{\,2}}$. In this case the variable in the integral (2.10) can be changed with $f_y = \sqrt{f^2 - f_x^{\,2}}$ and the differential df with $df_y = 2f_x / \sqrt{f^2 - f_x^{\,2}}\, df$. The equation (2.10) can be rewritten in the following way:

$$PSD_{1D}(f_x) = 4\int_{f_x}^{\infty} \frac{f}{\sqrt{f^2 - f_x^{\,2}}} PSD_{2D}(f)\, df \tag{2.11}$$

$$PSD_{2D}(f) = -\frac{1}{2\pi}\int_{f}^{\infty} \frac{df_x}{\sqrt{f_x^{\,2} - f^2}} \frac{dPSD_{1D}(f_x)}{df_x} \tag{2.12}$$

---

[10] The arguments for the use of PSD are similar to those, which make the noise spectrum in frequency space the preferred tool in many fields, e.g. from the description of the noise in an electronic channel as well as to represent the density fluctuation characteristics of the large scale clustering in the Universe.

which allows to pass from 1D to 2D power spectra. The integrals in (2.11) and (2.12) contain upper limits which go to infinity. To carry out the integration one should know the PSD beyond the fundamental limits imposed by the Nyquist theorem, 1/2d, which in turn means to perform additional assumption about the system itself.

One way to overcome this problem consists of fitting the experimental data, see, e.g., Figure 2-13, with an analytical function, such as the ABC model (see next section) or a fractal-like power law. When substituted into the integrals the unknown PSD can be solved. This procedure does the following things simultaneously:

1) it smoothes the statistical oscillation in the spectrum

2) it condenses the finish information in few fitting parameters

3) it adds, through the physical content of the model, the a priori information required for realistic extrapolation of data outside the bandwidth of the measurement.

The latter point will be discussed in details in section 2.6, where a model of roughness in terms of its power spectrum will be connected to a stochastic model of film growth/erosion. In this case, the model deals with 2D spectra while typically XRS measurement provides 1D PSD. Thus, one should transform the 2D PSD to 1D to interpret the data correctly.

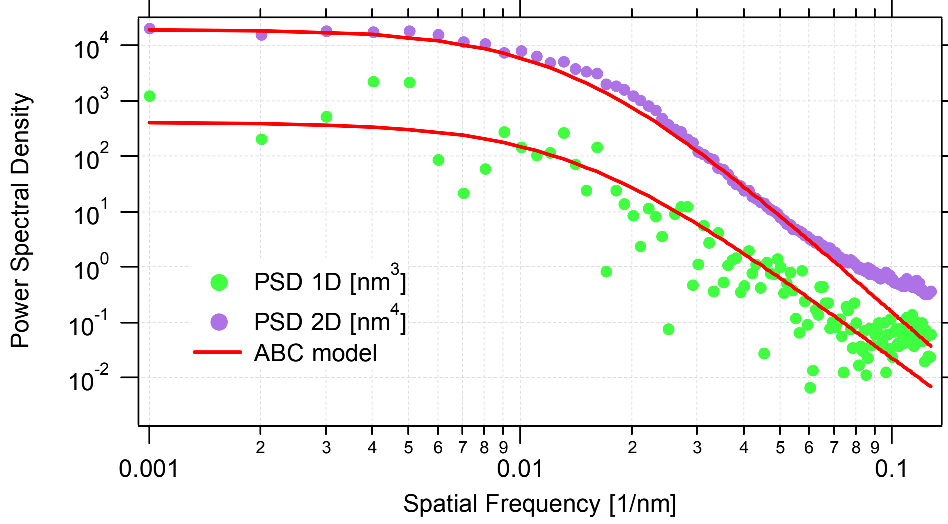

Figure 2-13 Comparison between power spectra determined by a profile and area measurements and interpolation obtained using the same PSD model

2.4.4 PSD models

A model of a surface enables one to either extrapolate the PSD out of the finite bandwidth measurement or to fit a measured power spectrum with this model. The common model used for this purpose is the ABC model or K-correlation model[38]:

$$PSD_{1D}(f) = \frac{A}{\left[1+(Bf)^2\right]^{\frac{C}{2}}} \qquad (2.13)$$

where A, B and C are adjustable finish parameters. By inserting Eq. (2.13) into (2.12), the corresponding expression for the two dimensional power spectrum can be obtained:

$$PSD_{2D}(f) = \frac{\tilde{A}}{\left[1+(Bf)^2\right]^{\frac{C+1}{2}}} \qquad (2.14)$$

where

$$\tilde{A} = \frac{1}{2\sqrt{\pi}} \frac{\Gamma(\frac{C+1}{2})}{\Gamma(\frac{C}{2})} AB \qquad (2.15)$$

in which $\Gamma(x)$ is the Gamma function evaluated at the point x.

Eqs. (2.13) and (2.14) reduce to white noise when B=0, pure fractals when $B=\infty$, to the Lorentzian (exponential correlation function) when C=2 and Gaussian when $C=\infty$. Let us discuss now some properties related to this PSD model. At large

spatial frequency, the model shows an inverse power law or Fractal-like character and the expressions (2.13) and (2.14) become proportional to $1/f^{C}$ and $1/f^{C+1}$.

The fractal form is expected to break down at a high spatial frequency due to the presence of atoms of finite dimensions and at low spatial frequency due to the finite size of the sample. However, some surfaces show a spectral flattening at the highest spatial frequency. This is due to the presence of an intrinsic spatial scale or "correlation length" ξ, induced by the fabrication process. This can be included into the model by assigning a value $\xi=B$.

Eqs. (2.13) and (2.14) can then be rewritten in terms of roughness parameters rms σ, correlation length ξ and fractal parameters α (or roughness exponent, see section 2.5) in the following way:

$$PSD_{1D}(f) = \frac{2}{\sqrt{\pi}} \frac{\Gamma(\alpha+1)}{\Gamma(\alpha)} \frac{\sigma^2 \xi}{\left[1+(\xi f)^2\right]^{\alpha+1/2}} \tag{2.16}$$

and

$$PSD_{2D}(f) = \frac{\sigma^2 \xi^2 \alpha}{\pi\left[1+(\xi f)^2\right]^{\alpha+1}} \tag{2.17}$$

where f in the last equation denotes the modules of a 2D spatial frequency. The additional factors in (2.16) and (2.18) arise from the normalization of the integral of the PSD to give a value equal to σ^2. The effective roughness in a spectral region defined by the Nyquist criteria, can be calculated using the following expression:

$$\sigma_{eff}^2 = \int_{f_{\min}}^{f_{\max}} PSD_{1D}(f)df \tag{2.19}$$

$$\sigma_{eff}^2 = \int_{f_{\min}}^{f_{\max}} PSD_{2D}(f) 2\pi f df \tag{2.20}$$

Similar equations, involving the even moments of the PSD, can be written to calculate both the average slope error and the curvature:

$$m^2 = \int_{f_{\min}}^{f_{\max}} PSD(f)(2\pi f)^2\, df \tag{2.21}$$

and

$$c^2 = \int_{f_{\min}}^{f_{\max}} PSD(f)(2\pi f)^4\, df \tag{2.22}$$

In these equations $f_{\min}$ and $f_{\max}$ define the spatial bandwidth over which the surface statistic is calculated. These limits can be changed to allow comparison between measurements systems with different bandwidths.

2.5 Scaling model

In the last twenty years it has been observed that roughness of many natural surfaces would follow rather simple scaling experimental laws, which could be quantified using scaling exponents. This approach has some advantages in comparison with other empiric approaches that limit their analysis to an estimation of the roughness value.

To illustrate the basic idea of the scaling model, let us consider a two-dimensional surface characterized by the height function *Z(x, y; t)*. The morphology and dynamics of a rough surface can then be quantified by an interface width, or defined by the rms fluctuations in the height Z(x; y; t),

$$\sigma(L;t) \equiv \sqrt{\frac{1}{L^2} \sum_{x,y=1,L} \left[Z(x,y;t) - \bar{Z} \right]^2} \qquad (2.23)$$

where L is the linear size of the sample and $\bar{Z}$ is the *mean surface height* of the surface

$$\bar{Z}(t) \equiv \frac{1}{L^2} \sum_{x,y=1,L} Z(x,y;t) \qquad (2.24)$$

Instead of measuring the roughness of a surface over the whole sample size L, we can choose a window of size l, and measure the local roughness, $\sigma(l)$. A general property of many rough surfaces is that the roughness $\sigma(l)$ depends on the length scale of observation. This can be quantified by plotting $\sigma(l)$ as a function of l. There are two characteristic regimes one can distinguish: (i) For length scales smaller than $l_\times$, the local width increases as:

$$\sigma(l) \sim l^{\alpha} \qquad (2.25)$$

where α is the *roughness exponent*. If we are interested in surface phenomena that take place at length scales shorter than $l_\times$, then we cannot neglect the roughness of the surface. In this regime the roughness is not simply a number, but it depends on the length scale accessible to the method probing the surface. (ii) For length scales larger than $l_\times$, the surface appears smooth. In this regime we can characterize the surface roughness with the saturation width $\sigma_{sat} = \sigma(l_\times)$.

If we are interested in the dynamics of the roughening process we will follow σ as a function of time. At the beginning of growth roughness increases as $\sigma(L,t) \sim t^{\beta}$, where β is the *growth exponent*. However, for finite systems, after a crossover time $t_\times$, the width saturates, following the Family-Vicsek scaling function[44]

$$\sigma(L,t) \equiv t^{\beta} g\left(\frac{t}{L^{z}}\right) \tag{2.26}$$

where $z = \alpha / \beta$ is the dynamic exponent and $g(u \ll 1) \sim 1$, while $g(u \gg 1) \sim u^{-\beta}$ and d is the dimensionality of the PSD.

Scaling relations such as Eq. (2.26) allow one to define *universality classes*. The concept of a *universality class* is a product of modern statistical mechanics, and encodes the fact that there are but a few essential factors that determine the exponents characterizing the scaling behavior. Thus systems, which at first sight may appear to have no connection between them, behave in a remarkably similar fashion. The values of the exponents α and β are independent of many "details" of the system, and they are uniquely defined for a given universality class. In contrast, other quantities, such as $l_{\times}$, or σ_{sat}, are non-universal, i.e. they depend on almost every detail of the system.

As the experiments described along this dissertation aimed at measuring surface PSDs, it is useful to examine how the dynamic scaling relation (2.26) is modified in the Fourier space. In this case it can be translated to the following relation for the PSD [2]:

$$PSD(f,t) = f^{-d-2\alpha} g(t / f^{-z}) \tag{2.27}$$

where now $g(u) \sim u^{\frac{(2\alpha+d)}{z}}$ for $u \ll 1$, and $g(u) \rightarrow const$ for $u \gg 1$.

This suggests an alternative way to establish the scaling exponents of a random system. If one can have access to the temporal evolution of the PSDs of a surface at different time of the growth, e.g. from a scattering measurement, the scaling exponents can thus be probed in a simple way. By rescaling the PSDs in accordance with (2.27) one can obtain the scaling exponents in a simple way. The methods known as "data collapse", consist of collapsing the measured spectra into a single master curve using (2.27) with the right scaling exponents. The advantage of this approach is that each single harmonics gives a separate contribution, while using the standard scaling, i.e., Eqs. (2.26), only long spatial wavelengths contribute mainly to the roughness values and thus to the scaling. An example of this approach will be presented in section 5.7 using PSDs obtained from the scattering measurements during the deposition of a tungsten layer.

2.6 Linear stochastic model of growth/erosion of thin film

In this section the linear model of thin film growth of films with isotropic surfaces is analyzed. This model was first developed by Stearns and is detailed in several publications [43, 45-47]. One of the main advantages of this model is that it can be easily implemented to analyze the variation of roughness at different time of growth and to model the evolution of scattered intensity during real time reflectometry experiments. The

model assumes the variation of the Fourier harmonics amplitude $\zeta_f(\vec{\nu},h)$ of a film surface with increasing film thickness to obey the following linear equation:

$$\frac{d\zeta_f(\vec{\nu},h)}{dh} = -b(\vec{\nu})\zeta_f(\vec{\nu},h) + \chi(\vec{\nu},h) \tag{2.28}$$

where the function $\chi(\vec{\nu},h)$ is the Fourier transformation of the fluctuating part of an arriving flux of particles.

The general solution of Eq. (2.28) is written in the form:

$$\zeta_f(\vec{\nu},h) = \exp[-b(\vec{\nu})(h-h')]\zeta_s(\vec{\nu}) + \int_0^h dh'\exp[-b(\vec{\nu})(h-h')]\chi(\vec{\nu},h') \tag{2.29}$$

where the function $\zeta_s(\vec{\nu})$ is the Fourier transform of a substrate relief. If we assume that the film and substrate surfaces are stationary in space and that the incoming flux is stationary and delta correlated both in space and time, i.e. $\left\langle \eta\left(\vec{f},h\right)\eta\left(\vec{f}',h'\right)\right\rangle = \Omega\delta\left(h-h'\right)\delta(\vec{f}-\vec{f}')$, one can find from Eq. (2.29) the following relations between the PSD functions of the film and the substrate roughness:

$$PSD_f(f,h) = \exp(-2b(f)h)PSD_s(f) + PSD_i(f,h) \tag{2.30}$$

$$PSD_i(f,h) = \frac{\Omega}{(2\pi)^2}\frac{1-\exp(-2b(f)h)}{2b(f)} \tag{2.31}$$

$$PSD_{sf}(f,h) = \exp(-b(f)h)PSD_s(f) \tag{2.32}$$

where the spatial frequency of the surface is $f = |\vec{\nu}|$. The first term in (2.30) describes the contribution of the substrate roughness, where the function $b(f)$ characterizes the relaxation processes of a film surface, the second term in (2.30) describes the intrinsic film roughness arising during film deposition, Ω being a constant parameter representing the volume of a growth unit (atom, molecule or cluster)[48]. The relaxation function is represented typically as a polynomial of the fourth degree in the spatial frequency:

$$b(f) = \sum_{j=1}^{4} c_j f^j \tag{2.33}$$

where each summand corresponds to one relaxation mechanisms of a surface (viscous flow, re-deposition, volume and surface diffusion).

Using (2.30), (2.31) and (2.32) it is possible to inspect the variation of the PSDs and in turn σ with the film thickness both on rough and ideally smooth substrates (i.e. PSD_f=PSD_i). Simulations obtained assuming an ideally smooth substrate and using the model (2.30) are shown finally in Figure 2-14 and Figure 2-15.

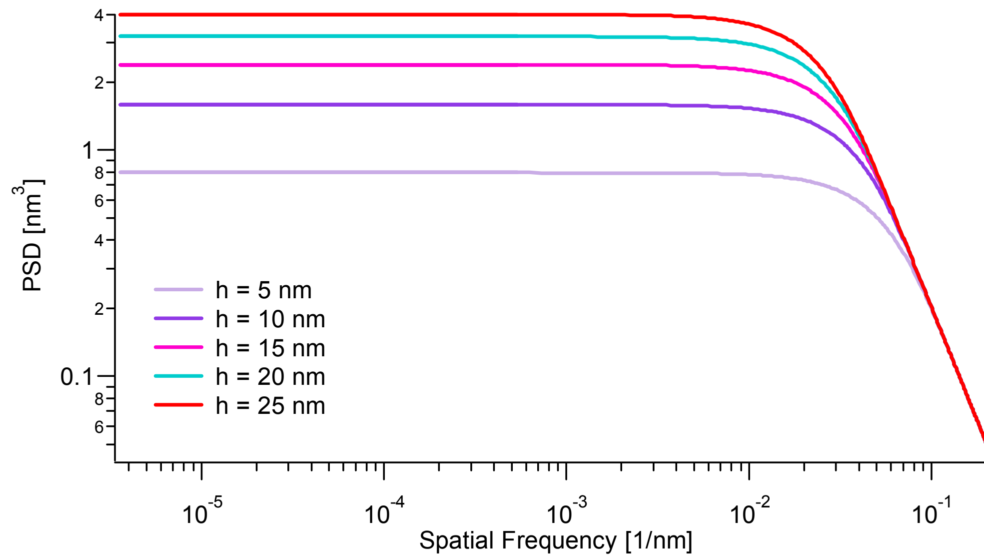

Figure 2-14: Variation of the external film's PSD according to the model proposed by Stearns. The growth parameters for a tungsten layer are Ω=0.015 nm^3 and ν=1 nm while the substrate was considered ideally smooth..

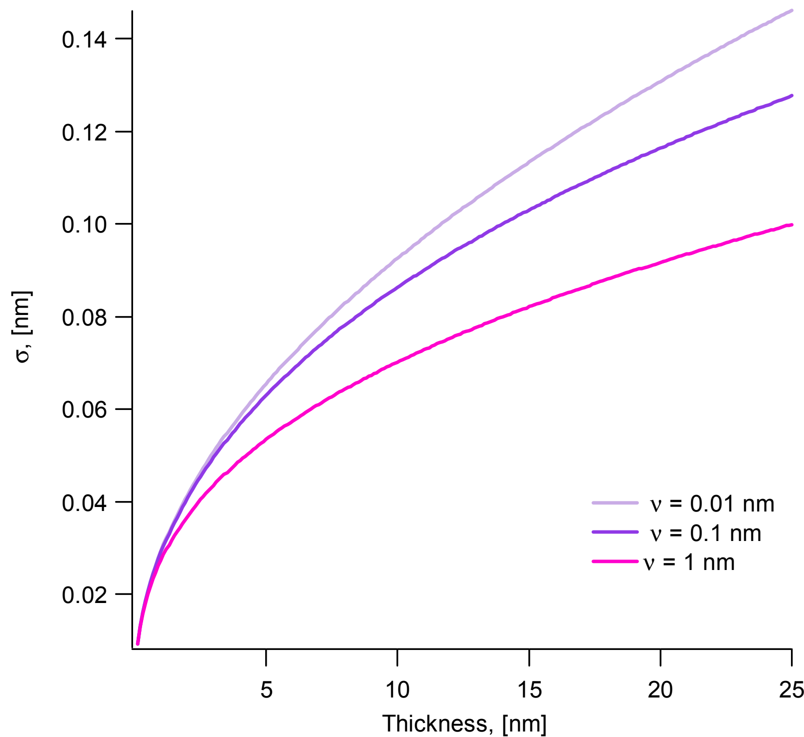

Figure 2-15 Variation of the external film's roughness obtained from integration of the PSD as a function of the film thicknesses for various relaxation lengths. The substrate is considered ideally smooth.

Chapter 3 X-ray Scattering theory

The earliest recorded scientific studies on the optical behavior of thin films were made in the seventeenth century. They appear, with the results of a wide range of other optical experiments, in Sir Isaac Newton's treatise "Optiks" [49]. Although, at that time the mechanism of the propagation of light was not yet clear, the observation made on the colors of thin films in relation to their thickness proved to be very useful. Nowadays, these findings still form the basis of some of the methods of thickness measurement we use, including the principle and the apparatus described in this work. The basic idea of Newton's observations was that films with dissimilar thicknesses could diffract colors in accordance with their thickness. This experimental method is what is called today an energy dispersive scattering measurement.

The optical properties of thin films are also intimately related to the surface roughness, which is inevitably generated during the synthesis process. The X-ray Scattering (XRS) technique presented along this work deal with angular dispersive measurement with a monochromatic and collimated X-ray beam. Although both angular and energy dispersive methods are extremely different experimentally, their concept is always the same and is based on the theory of interaction of X-rays with inhomogeneous interface.

The following section will present the interaction of a monochromatic X-ray beam with a rough surface for a bare substrate and for the particular situation where a film is grown on it. The requirements in terms of coherence of the radiation at the sample position are discussed first. Then, specular (Fresnel formulas) and diffuse XRS are presented. The theoretical approach discussed in the following paragraphs is based on the Perturbation Theory (PT) considering the scattering amplitude as a power series in the roughness height. This theory represents the theoretical basis for all the analysis performed in this dissertation. The PT is widely used for the analysis of light scattering and was demonstrated applicable to many cases of interest in the X-ray domain by Kozhevnikov and co-workers over the last 20 years [35, 50-53].

3.1 X-ray reflectometry

In thin film material research, the trend is to design films which provide specific properties (optical, electrical, mechanical etc.) depending on the technical applications. The perfection of layered structures is defined both by the quality of the interfaces and by the reproducibility that can be achieved during the deposition of the layers (control of thickness, crystallinity or various defects, which may appear during the growth process). In particular, the roughness of the interfaces is of crucial importance for many technological applications connected to the X-ray optics fields, e.g. see chapter 1. Therefore, this is an important parameter to be determined if one wants to assess the quality of the interfaces. Optically, the access to this quantity is possible when the coherence onto the sample surface is present and interference patterns appear. The next paragraphs present the theory of specular and diffuse X-ray scattering in this light and show through various examples how density, thickness and roughness influence the interaction between an X-ray beam and a solid surface.

3.1.1 Coherence criteria in X-ray scattering

As it is known in visible light optics, the interference pattern appears under certain coherence conditions [54]. The coherence of the light source means the capability of the various partial waves to interfere. It also requires that the coherence on the sample surface. To describe it one uses the notion of coherence length, physically defined as the distance between two scattering centers for which the scattered waves interfere. A diffraction experiment usually probes the smallest of the two types of coherence and results in broadening of the scattering diagram approximately given by ~ $\lambda / \xi \sin(\theta_0)$, where ξ is the correlation length of the surface and θ_0 is the grazing angle of a probing X-ray beam and λ the radiation wavelength [54]. To make sure the broadening observed is due to the sample, it is necessary to estimate the coherence length of the incoming X-ray beam and verify that the correlation length of the surface is less than the coherence length of the radiation source.

On the scattering plane two types of coherence can be defined, in the spatial and temporal domains:

The *transverse coherence length* - which is related to the source size r_s and the distance between sample and detector R by $l_t = \lambda R / 2r_s \approx \lambda / \delta\theta_i$, and $\delta\theta_i$ is beam divergence.

The *longitudinal coherence length* - which is related to the wavelength used and the spectral purity $\Delta\lambda$ as $l_l = \lambda^2 / 2\Delta\lambda$.

In the case of a scattering process on a surface illuminated under grazing angle θ_0, it is the projection of the two coherence lengths that matter:

$$L_t = \frac{l_t}{\sin(\theta_0)} \tag{3.1}$$

$$L_l = \frac{l_l}{\cos(\theta_i)} \tag{3.2}$$

It is clear that L_t becomes very large under grazing incidence. Let us consider a typical Bending magnet radiation source with a vertical source size of 80 μm and a distance source - sample of 50 m. For an incidence angle of 0.5° and a wavelength of λ = 0.07 nm we obtain a value L_t = 2.5 mm using (3.1). This value is much higher than the typical correlation length of a surface, in the order of several μm.

3.1.2 Specular reflection

When the previous experimental hypotheses are fulfilled, it is legitimate to use X-ray reflectometry as a tool to investigate the physical properties of a surface in the directions parallel (from specular measurements) and perpendicular to the surface normal (from diffuse scattering measurements). We shall consider first an ideally smooth surface, as it is assumed in the Fresnel theory, and then the case of a thin film grown on it.

When an X-ray beam impinges onto the surface of a material, part of the incoming intensity I_0 is reflected and part is transmitted. If the surface is flat, the reflected intensity will be confined in a direction symmetrical to the incident with respect to the surface normal: we will call it specular intensity.

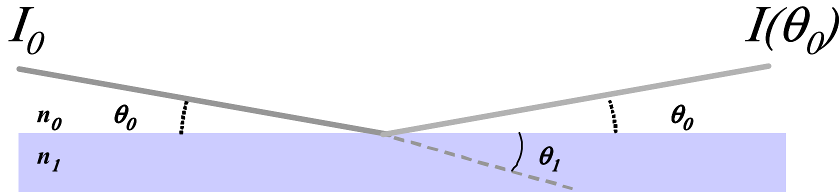

Figure 3-1: Illustration of the reflection phenomenon using the notation in the text. The refracted wave is represented by a dashed line.

The specular reflectivity is conventionally defined as the ratio

$$R(\theta_0) = |\tilde{r}(\theta_0)|^2 = I(\theta_0)/I_0 \tag{3.3}$$

where $\tilde{r}(\theta_0)$ is the complex[11] amplitude reflection coefficient and $I(\theta)$ is the reflected intensity at angle θ_0. The domain of validity of X-ray reflectivity is limited to small angles of incidence where it is possible to consider the electron density as

[11] Hereafter, tilde sign will denote complex numbers.

continuous. In this approximation, this is the classical problem of reflection of an electromagnetic wave at an interface and the reflected amplitude is obtained by writing the continuity of the electric and magnetic fields at the interface. This leads to the *Fresnel* relationships from which the reflection and transmission amplitude for the (s) and (p) polarizations can be derived. However, in the Hard X-ray domain these are practically coincident since the angle θ_0 is small and only the formula for (s) polarization will be considered hereafter. A formal treatment of this subject can be found in the classical work of Born and Wolf [55]. Let us consider now the reflectivity and transmission of a perfectly smooth substrate; these are given by the square modulus of their respective coefficients:

$$R(\theta_0) \equiv |\tilde{r}(\theta_0)|^2 = \left| \frac{n_0 \sin(\theta_0) - \tilde{n}_1 \sin\left(\tilde{\theta}_1\right)}{n_0 \sin(\theta_0) + \tilde{n}_1 \sin\left(\tilde{\theta}_1\right)} \right|^2 \tag{3.4}$$

$$T(\theta_0) \equiv \left|\tilde{t}(\theta_0)\right|^2 = \left| \frac{2 n_0 \sin(\theta_0)}{n_0 \sin(\theta_0) + \tilde{n}_1 \sin\left(\tilde{\theta}_1\right)} \right|^2 \tag{3.5}$$

where n_0 and $\tilde{n}_1$ is the complex refractive index, respectively for vacuum ($n_0 = 1$) and the reflecting material, respectively.

The formulas can also be rewritten more conveniently, in a form where only the measurable angle θ_0, and not the angles inside the material[12], appears. To do that another relation, the Snell-Descartes law, should be used:

$$n_0 \cos(\theta_0) = \tilde{n}_1 \cos\left(\tilde{\theta}_1\right) \tag{3.6}$$

the notation used here and in (3.4) and (3.5) are shown in Figure 3-1.

By squaring the two terms and using trigonometric identities, the terms $n_1 \sin(\theta_1)$ can be written in terms of θ_0 and put into the equations to obtain a function of the external angle only:

$$\tilde{r}(\theta_0) = \frac{\sin(\theta_0) - \sqrt{\tilde{\varepsilon}_1 - \cos^2(\theta_0)}}{\sin(\theta_0) - \sqrt{\tilde{\varepsilon}_1 - \cos^2(\theta_0)}} \tag{3.7}$$

$$\tilde{t}(\theta_0) = \frac{2\sin(\theta_0)}{\sin(\theta_0) - \sqrt{\tilde{\varepsilon}_1 - \cos^2(\theta_0)}} \tag{3.8}$$

[12] For the reflection and refraction of X-ray from a solid material the angle inside the material, from a mathematical point of view, is a complex number. Thus, as usual when dealing with complex numbers, they cannot represent the physical quantities.

where ε_1 denote the dielectric permittivity which is related, for isotropic material, to the refractive index by $\tilde{n} = \sqrt{\tilde{\varepsilon}}$.

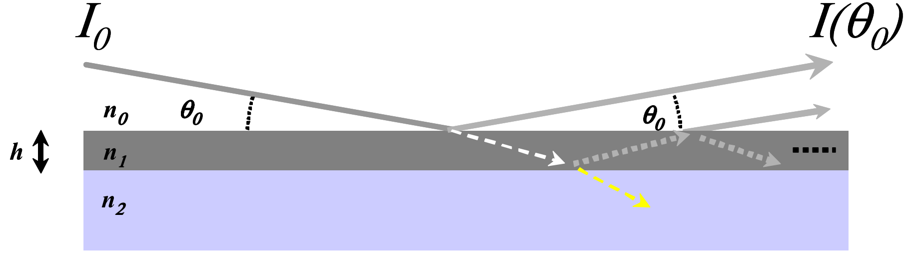

Figure 3-2: Schematization of the reflection geometry for a thin film of thickness h onto a substrate wit refractive index n_2.

Let us now consider a thin film layer on a substrate (see Fig. 3-2). To evaluate the reflectivity of this type of material system we need the reflection coefficient at the two interfaces: *vacuum-layer* (subscripts 0-1) and *layer-substrate* (subscripts 1-2). These can also be calculated using a similar procedure as the ones presented earlier. By defining the following set of functions:

$$k_i(\theta_0) = k\sqrt{\varepsilon_i - \cos^2(\theta_0)},\ \text{i=0,1 and 2} \tag{3.9}$$

where $k = 2\pi/\lambda$ is the wave number. The reflectance and transmittance at the various interfaces can then be written as:

$$\tilde{r}_{i,j}(\theta_0) = \frac{\tilde{k}_i(\theta_0) - \tilde{k}_j(\theta_0)}{\tilde{k}_i(\theta_0) + \tilde{k}_j(\theta_0)} \tag{3.10}$$

$$\tilde{t}_{i,j}(\theta_0) = \frac{2\tilde{k}_i(\theta_0)}{\tilde{k}_i(\theta_0) + \tilde{k}_j(\theta_0)} \tag{3.11}$$

Here, as it was shown before, only the real measurable angle θ_0 appears.

The exact formula describing reflectance and transmittance for a thin film was obtained by summing together all the partial reflections occurring between the two interfaces. This is done through an infinite series summation. For details see the references [48, 54, 56]. The result is:

$$\tilde{r}(\theta_0, h) = \frac{\tilde{r}_{01}(\theta_0) - \tilde{r}_{12}(\theta_0)\exp\left[2i\tilde{k}_1(\theta_0)h\right]}{1 - \tilde{r}_{01}(\theta_0)\tilde{r}_{12}(\theta_0)\exp\left[2i\tilde{k}_1(\theta_0)h\right]} \tag{3.12}$$

$$\tilde{t}(\theta_0, h) = \frac{\tilde{t}_{01}(\theta_0)\tilde{t}_{12}(\theta_0)\exp\left[i\tilde{k}_1(\theta_0)h\right]}{1 + \tilde{r}_{01}(\theta_0)\tilde{r}_{12}(\theta_0)\exp\left[2i\tilde{k}_1(\theta_0)h\right]} \tag{3.13}$$

Notice the dependence on the film thickness h inside the phase factor $\exp(ik_1(\theta_0)h)$, which is responsible for the appearance of *Kiessig* [4] fringes on the reflectivity.

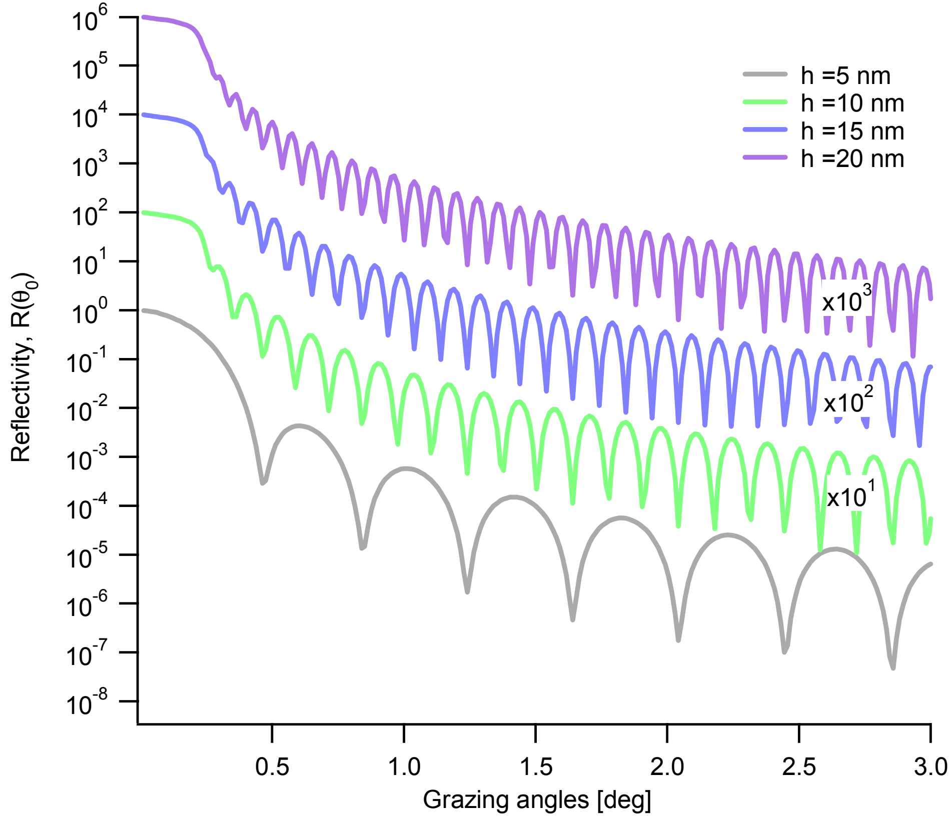

Figure 3-3: Reflectivty curves at 17 keV calculated at four W film thicknesses versus grazing angles. The curves are shifted vertically for clarity.

To illustrate the dependence of the reflectivity on the angle and film thickness, Figure 3-3 shows such curves calculated for a W layer at an X-ray energy of 17 keV.

The dependence of $R(\theta_0, h)$ on the film thickness h is finally given in Figure 3-4 for three different grazing angles, namely θ_0 =0.125°, 0.25° and 0.5° (E=17 keV). Notice that the critical angle for W at this energy is given by θ_{cr} ~ 0.2°. As one can see in Fig. 3-3, the oscillations disappear when approaching the region of total external reflection for tungsten and when the thickness increases. This is due to a unique property: the penetration depth is reduced thus preventing the creation and the interference of waves partially reflected at the two interfaces. By looking at the variation of $R(h)$ in Figure 3-4 another feature, visible at small thicknesses (less than ~5 nm), can be seen: $R(\theta_0, h)$ increases quickly with increasing thickness. This is due to the rapid reduction of the X-ray penetration depth, related to θ_{cr}, when passing from the OTER region for silicon to the TER region for tungsten.

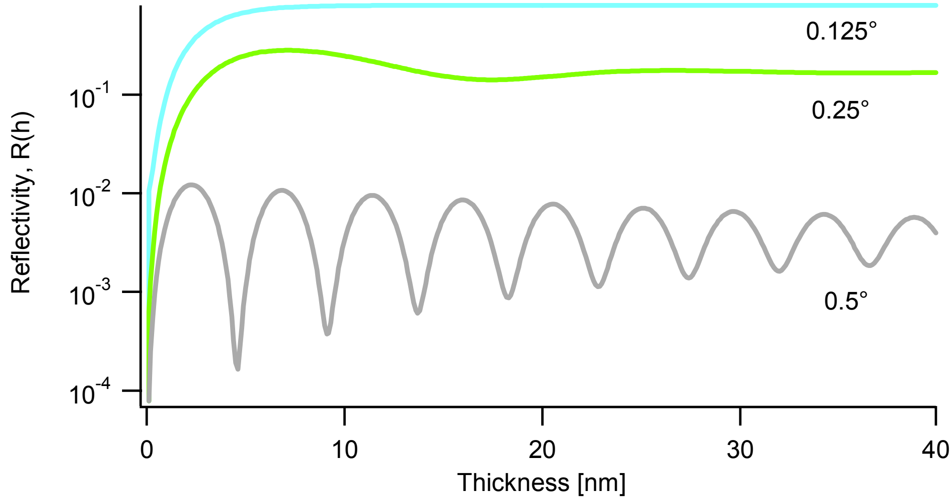

Figure 3-4: Reflectivty curves calculated at three grazing angles as a function of the W film thickness, respectively θ_0=0.125°, 0.25° and 0.5°.

Several authors [54, 57, 58] have reported expressions in which the Fresnel coefficients have modified forms and in particular, $r(\theta,h)$ is multiplied by a factor accounting for the reduction of the reflectivity due to the presence of roughness. The most used expressions are due to Debye-Waller[59] (DW) and Nevot-Croce[60] (NC). In the first case, the result is the so-called DW factor $\exp(-2k_0{}^2\sigma)$ where k_0 is perpendicular component of the wave vector of the incident radiation, $\vec{k}_0$. The NC factor is equal to $\exp(-2k_0k_1\sigma)$. Here k_1 is the perpendicular component of the wave vector of the incident radiation inside the material, after refraction. The NC factor is used in vicinity of the TER region and small correlation length, whereas at large k_0 and large correlation length the DW form gives a better description. A formula which interpolates these two results has also been reported by De Boer[58].

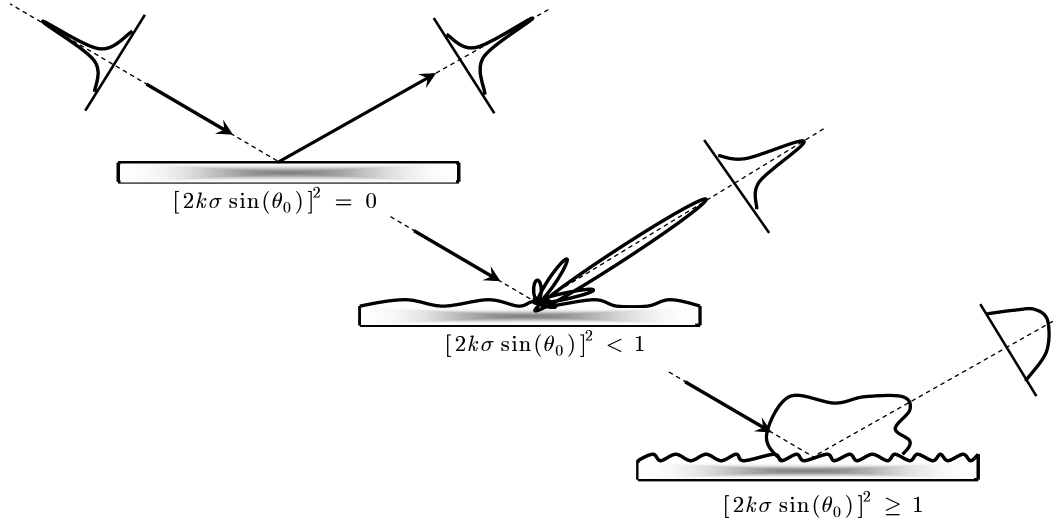

Figure 3-5: Transition from specular reflection to diffuse scattering. The surfaces are in sequence: smooth, slightly rough and very rough. The intermediate case leads to a dominant specular beam that can be approximated with the Fresnel formula, as the beam is not redirected inside the bulk.

However, there is an interesting case where the effect of roughness on the measured reflectivity becomes negligible and the Fresnel theory can be applied: that is, when measuring the sum of the specular reflected and diffuse scattered intensities. Then, the effect of a surface roughness on the measured reflectance is minimal. Actually, the total reflectance can be written in the following form $R_\Sigma = R_F - \delta R + TIS$, where R_F is the reflectance from a perfectly smooth sample, δR is the decrease in the specular reflectance due to radiation scattering by roughness, and TIS is the total integrated scattering into vacuum. The dependence of specularly reflected beam on the parameter $[2k\sigma \sin(\theta)]^2$ is illustrated in Figure 3-5. If the rms roughness is not too large (Figure 3-5, center), then both the reflectance and the total integrated scattering can be described by the Debye-Waller factor $\delta R \cong TIS \cong R_F \cdot (4\pi\sigma \sin\theta / \lambda)^2$. Thus, the total reflectivity can be accurately described by the Fresnel formula and $R_\Sigma \cong R_F$, i.e., roughness does not increase the amount of flux directed into a substrate but redistributes the reflected intensity between the specularly reflected and the diffusely scattered components. In this situation the extraction of the film thickness and density is simpler than in the case of the specular reflectivity (effect of roughness). Such approach has been used to analyze the data obtained from the experiments presented in Chapter 5.

Specular reflectivity is commonly measured using a narrow slit in front of a point detector [54]. For a review about the standard experimental techniques see [48, 54]. Here also, it is implicitly assumed that all the radiation should not be redirected inside the sample, i.e., the surface must be only slightly rough, otherwise erroneous roughness estimation, whatever the model used (NC or DW), would inevitably occur.

From the above considerations, it results that the information about roughness contained in the specular beam is poorly available. On the contrary, information about roughness can be gained by inspecting the differential distribution of the XRS intensity around the specular peak.

3.1.3 Diffuse X-ray scattering analysis of a rough surface

In the previous paragraph we assumed the ideal case of a semi-infinite substrate with a flat and smooth surface. Any real surface, from the atomic scale up to the macroscopic scale, exhibits roughness. A surface is characterized by at least three parameters, namely, rms roughness, correlation length and a roughness exponent (see Chapter 2). Let us now consider a case of great interest in X-ray optics: the very smooth surface regime. We are then, in the smooth surface limits (SSL) for which the following inequality holds:

$$(2k\sigma\sin(\theta))^2 \ll 1 \tag{3.14}$$

Here $k = 2\pi/\lambda$ denotes the wave number and σ the rms roughness. This inequality shows that for a given value of the roughness the smooth surface regime may be obtained by working either at small grazing angles or at long radiation wavelength. This explains the large range of validity of the scattering theory from radio waves [59] up to X-ray domains.

A rough surface can be thought as a superposition of diffraction gratings, with spatial periods or frequency extending from the atomic scale up to its macroscopic dimension, with random phase and amplitude [59, 61, 62]. The net effect of this structure is to scatter part of the reflected beam out from the specular direction, the angle of scatter θ_s (with respect to the surface) being related to the spatial frequency f, by the grating equation at grazing incidence:

$$f = \frac{|\cos(\theta_s) - \cos(\theta_0)|}{\lambda} \tag{3.15}$$

where λ is the radiation wavelength and θ_0 is the incidence angle, see Figure 3-6.

This equation associates a specific direction θ_s to a specific lateral surface periodicity, while information about the vertical scale can only be obtained by analyzing the intensity of the scattered radiation at that angle. This is done invoking perturbative approaches that approximate the exact scattering amplitude and describe the relation between the X-rays scattered out of a surface and its microtopography. The simplest one uses the first-order scalar perturbation theory, where the scattering amplitude is represented by the first term only of a power series in the roughness height z.

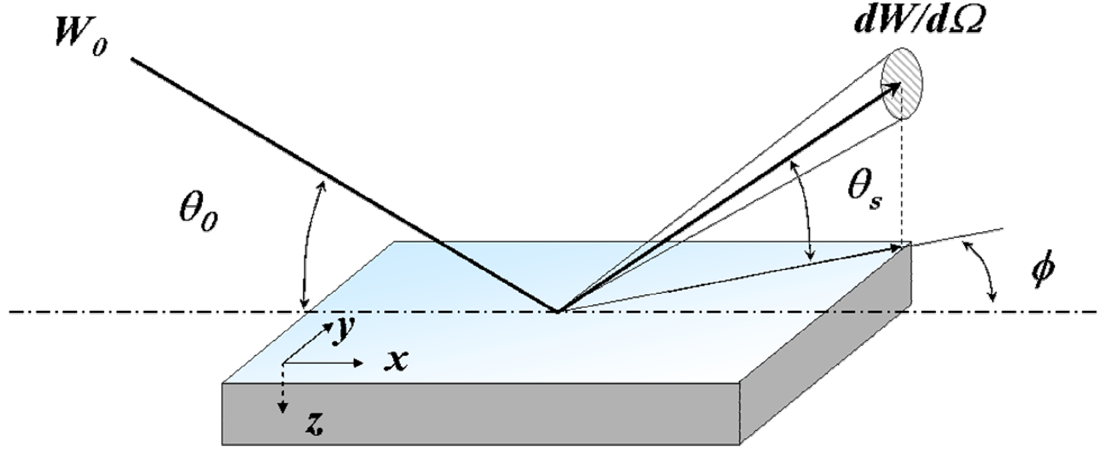

Figure 3-6: Scattering geometry.

The expression for the scattered intensity (or scattering diagram) in the first-order scalar perturbation theory has the following form

$$\Phi(\theta,\varphi) = \frac{1}{W_0}\frac{dW_{scat}}{d\Omega} = \frac{k^4}{16\pi^2 \sin\theta_0} \cdot Q(\varepsilon,\theta,\theta_0) \cdot PSD_{2D}(\vec{\nu}) \qquad (3.16)$$

$$PSD_{2D}(\vec{\nu}) = \int C(\vec{\rho})\exp(2\pi i \vec{\nu}\vec{\rho})\, d^2\vec{\rho} \qquad (3.17)$$

$$\vec{\nu} = \vec{q} - \vec{q}_0 = \frac{1}{\lambda}\{\cos\theta\cos\varphi - \cos\theta_0\,;\, \cos\theta\cos\varphi\} \qquad (3.18)$$

where (see Figure 3-6) W_0 is the power of radiation incident onto a surface; dW_{scat} is the power of radiation scattered within the solid angle $\delta\Omega$, θ_0 is the grazing angle of a probe beam; θ and φ are the grazing and azimuth scattering angles; the random function $z = \zeta(\vec{\rho})$ describes the roughness height. The vector $\vec{\rho} \equiv (x, y)$ lies in the plane of a perfectly smooth surface; $C(\vec{\rho})$ is the correlation function of the roughness and, σ is the rms roughness; $PSD_{2D}(\vec{\nu})$ is the 2D power spectral density of the surface; ν is the spatial frequency; $\vec{q}_0$ and $\vec{q}$ are the projections of the wave vectors of the incident and scattered waves onto the XY-plane.

As typical in a perturbation theory results, Eq. (3.16) can be separated in different terms representing the physics of the problem [61]. The fourth power of the magnitude of the wave vector k (the *Rayleigh Blue Sky factor*) accounts for an inherent factor $1/\lambda^2$ due to the dimensionality of the problem ($1/\lambda$ in the 1D case) and for an additional factor $1/\lambda^2$ due to topographic scatter (since the radiation *sees* the height fluctuations in terms of wavelengths). The sinus factor accounts for the projection due to the grazing scattering geometry and $Q(\varepsilon,\theta,\theta_0) = |1-\varepsilon|^2\,|t(\theta_0)\,t(\theta)|^2$ is an electrodynamics factor which accounts for the properties of the material, namely, the dielectric permeability ε and the

transmission $t(\theta)$ at the angles θ_S (scattered) and θ_0 (incident) and polarization (in visible optics only).

The last term, $PSD_{2D}(\nu)$, represents the power spectral density of the surface and describes the morphology of the object interacting with the radiation.

The 2D grating equation (3.18) shows that, in the framework of the first-order perturbation theory, only the harmonic with frequency $\vec{\nu} = \{\nu_x, \nu_y\}$ is responsible for scattering in the direction $\vec{q}$, if a primary beam falls onto a rough surface in the direction $\vec{q}_0$.

For an isotropic surface, the PSD-function depends only on the absolute value of spatial frequency (the norm of $\vec{\nu}$), that is:

$$PSD_{2D}(\nu) = 2\pi \int_0^\infty C(\rho) J_0(2\pi\nu\rho)\,\rho\, d\rho$$
$$\nu = |\vec{q} - \vec{q}_0| = \frac{1}{\lambda}\sqrt{\cos^2\theta_0 + \cos^2\theta - 2\cos\theta_0\cos\theta\cos\varphi} \quad (3.19)$$

Note that the angular distribution $\vec{q}_0$ of the scattered radiation is generally characterized, by two scattering angles. However, the small incidence angle θ_0 leads to a diagram with a large width in the incidence plane $\delta\theta \sim \lambda/(\pi\xi \sin\theta_0)$ and much narrow width in the azimuth plane, being independent on θ_0, $\delta\varphi \sim \lambda/(\pi\xi) << \delta\theta$, where ξ is the roughness correlation length. Therefore, in the experiment the scattering diagram is usually integrated over the azimuth angle. The 1D version of Eqs. (3.16) can be found in Ref. [63] for an isotropic surface and reads:

$$\Pi(\theta) = \frac{1}{W_0}\frac{dW_{scat}}{d\theta} = \frac{k^3}{16\pi\sin\theta_0\sqrt{\cos\theta_0\cos\theta}} \cdot Q(\varepsilon, \theta, \theta_0) \cdot PSD_{1D}(p) \quad (3.20)$$

$$PSD_{1D}(p) = 4\int C(\rho)\cos(2\pi p)\, d\rho \quad (3.21)$$

$$p = \frac{1}{\lambda}|\cos\theta - \cos\theta_0| \quad (3.22)$$

where dW_{scat} is the power scattered within an angular range $d\theta$; $PSD_{1D}(p)$ is the 1D power spectral density of surface roughness, and p is the spatial frequency connected with the angles θ_0 and θ through the 1D grating equation.

Expression (3.20) was deduced under the assumptions that the incident and scattering angles are small *(θ, $\theta_0 << 1$)*, and the roughness correlation length is large as compared to the radiation wavelength *($\xi >> \lambda$)*. These assumptions are generally valid for X-ray experiments.

The scattering diagrams $\Phi(\theta,\varphi)$ and $\Pi(\theta)$ are directly proportional to the PSD-function, the factor of proportionality being independent of the roughness parameters. Despite its apparent simplicity, Eq. (3.20) can explain many phenomena including the anomalous surface reflection or Yoneda effect [64]. This effect, nowadays well described by several theoretical approaches, consists of an enhancement of the intensity in correspondence of the angle θ_{cr}. In Eqs. (3.20) and (3.16) it is caused by the shape of the transmission function contained in the factor $Q(\varepsilon,\theta,\theta_0)$. In the more complex formulae obtained in the framework of the DWBA[13], the physical interpretation is less straightforward. On the contrary Eq. (3.20) is easy to be implemented for data modeling. Several examples of calculation are illustrated in Figure 3-7 to show the dependence of the scattered intensity from the PSD parameters, namely σ, ξ and α.

---

[13] where the intensity is described through an integral equation in the unknown correlation function.

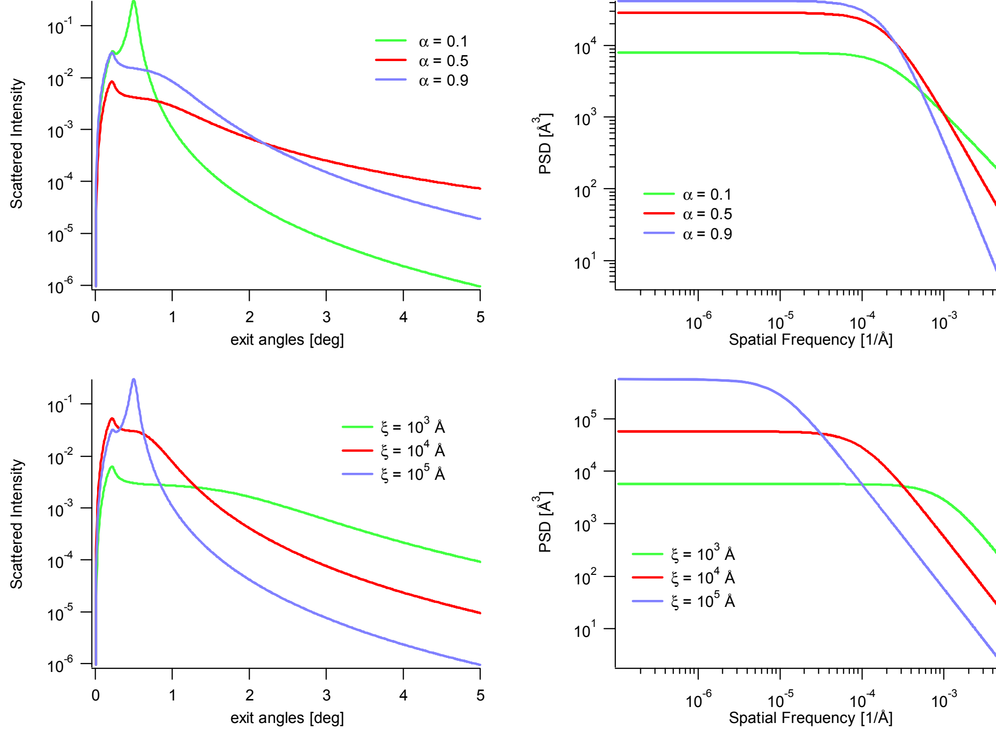

Figure 3-7: Calculated scattering diagrams for thick W films using the ABC model. The various colored curves show the dependence of the correlation length ξ and the roughness exponent α on both PSDs and XRS intensity.

The approach presented allows the study of a surface in a very simple way. It consists in direct determination of 2D or 1D PSD-function from the experimental X-ray scattering diagram via expression (3.16) or (3.20).

The conditions of applicability of the PT are discussed in detail in ref. [35]. In summary, the PT is valid, if the rms roughness is small and the scattering angle θ in small enough, i.e. if they satisfy the following inequalities:

$$\begin{aligned} k\sigma \sin(\theta_0) &< 0.3 \\ k\sigma \sin(\theta_{cr}) &< 0.3 \\ k\sigma \sin(\theta) &< 0.3 \end{aligned} \tag{3.23}$$

In these conditions, the direct determination of the 2D or 1D PSD function from the X-ray scattering diagram, via expression (3.16) or (3.20), is easy and the accuracy on

the PSD function determination is better than 8-10%[14]. The analysis of the different factors resulting in systematic errors on PSD-function measurements has been recently analyzed by Kozhevnikov in the Ref. [65]. The most important artifacts originate from the finite width of the detector slit (or from the channels of a CCD detector), the width of the primary beam, the beam divergence, the spectral purity, the possible error of the zero grazing angle determination and finally the asymmetry of the primary beam profile.

The last inequality in Eq. (3.23) limits the range of the spatial frequencies where the PSD-function can be reliably determined. Notice that, if the radiation wavelength reaches the value

$$\lambda \sim \frac{2\pi\sigma}{0.3} = 20 \cdot \sigma \qquad (3.24)$$

the PT applies for any scattering angle. The expression (3.24) also determines the optimum wavelength value to study roughness. For rms surface roughness of 0.1 – 1 nm this optimum belongs to the soft X-ray (EUV) spectral region.

As shown in section 2.4.4, there is an important case in practice, for which the PSD-functions decrease with increasing spatial frequency in accordance with the following law

$$\begin{aligned} PSD_{1D}(p \to \infty) &\cong \frac{K_1}{p^{1+2\alpha}} \\ PSD_{2D}(\nu \to \infty) &\cong \frac{K_2}{\nu^{2+2\alpha}} \end{aligned} \qquad (3.25)$$

where α $(0 < \alpha < 1)$ is the fractal parameter characterizing the dimensionality of a rough surface D = 3-α. The asymptotic form of these PSD is found for super-polished substrates made of various materials[65].

When the PSD function demonstrates a fractal-like behavior, the last inequality of (3.23) can be then neglected, i.e. the PT is valid for any scattering angle. Then, taking into account the natural condition $\theta_0 \le \theta_c$ and the typical value of the critical angle θ_c[15], we conclude that the PT can be used for processing experimental data dealing with samples with rms roughness not exceeding 1÷2.5 nm, and somewhat larger for light materials.

The formulation of the scattering theory in terms of the PSD has several distinct advantages, in contrast to other approaches (e.g., DWBA): i) The PSD is directly

---

[14] The systematic error of the PSD-function determination does not exceed 10% at small spatial frequencies and is much less at the largest one, all other systematic errors included.

[15] which is proportional to the wavelength and is larger for heavier materials

measurable by (real) instruments having finite bandwidths. ii) The knowledge of the PSD within a limited bandwidth is sufficient to model scattering in the corresponding angular range (determined by Eq. (3.15)). In contrast, the complete autocorrelation function would be required to describe the scattering within the same angular range. iii) The scattering problem can be inverted to determine the PSD of a surface from the angular distribution of the scattering.

3.1.4 Diffuse X-ray scattering from a rough thin film

The formulas (3.20) and (3.16) can be extended to the case of a single film deposited onto a substrate which then contains two interfaces, each with a roughness profile described by random functions $z = \zeta_s(\boldsymbol{\rho})$ and $z = h + \zeta_f(\boldsymbol{\rho})$. Here *h* is the average film thickness and $\boldsymbol{\rho}$ the vector lying in the plane of the surface. The optical properties of a thin film are determined by three correlation functions defined as $C_s(\rho) = \langle \zeta_s(\rho)\zeta_s(0) \rangle$, $C_f(\rho) = \langle \zeta_f(\rho)\zeta_f(0) \rangle$ and $C_{sf}(\rho) = \langle \zeta_s(\rho)\zeta_f(0) \rangle$. The autocorrelation functions $C_s(\rho)$ and $C_f(\rho)$ describe the statistical properties of the substrate and the external surface of the film, whereas the cross-correlation function $C_{sf}(\rho)$ determines the statistical relationship, namely, the degree of conformity between these two interfaces. However, the quantity measured effectively in scattering experiments is the PSD function (which connected to $C(\rho)$ by Fourier transform [42]). It is characterized by the presence of interference effects, the contrast of which depending on the degree of conformity between film and substrate topography. In the framework of the first-order scalar PT the scattering diagram integrated over the azimuth scattering angle is written in the following form:

$$\Pi(\theta,h) = \frac{1}{W_{inc}}\frac{dW_{scatt}}{d\theta} = \frac{k^3}{16\pi\sin\theta_0}\left[A_f PSD_f(p,h) + A_s PSD_s(p) + A_{sf} PSD_{sf}(p,h)\right] \quad (3.26)$$

in which A_f, A_s, and A_{sf} have the following expressions:

$$\begin{aligned} A_f &= \left|(1-\varepsilon_f)[1+r(\theta_0,h)][1+r(\theta,h)]\right|^2 \\ A_s &= \left|(\varepsilon_f-\varepsilon_s)t(\theta_0,h)t(\theta,h)\right|^2 \\ A_{sf} &= 2\,\mathrm{Re}\left\{(1-\varepsilon_f)(\varepsilon_f-\varepsilon_s)^*[1+r(\theta_0,h)][1+r(\theta,h)]t^*(\theta_0,h)t^*(\theta,h)\right\} \end{aligned} \quad (3.27)$$

The dielectric constants of the substrate and of the film are noted as ε_s and ε_f and the * denotes a complex conjugation. The amplitude reflectance and transmittance of a perfectly smooth film of thickness h are noted $r(\theta,h)$ and $t(\theta,h)$, respectively (see 3.1.2). $PSDf(p,h)$ is the 1-dimensional PSD-function of the external film surface and $PSDsf(p,h)$ describes the statistical correlation between film roughness and substrate roughness.

When modeling real scattering data the PSDs in Eq. (3.26) could be entered by using a model of a surface. An easy way is to implement the model proposed by Stearns [43] and described in 2.6. However, this model assumes 2D PSDs while the scattering diagram described in (3.26) requires their 1D forms. This can be done by integrating eq. (2.30) (2.28) and (2.29) with the formulas (2.8) that enable translating a 2D spectrum into a 1D one. Figure 3-8 shows an example of three PSDs obtained using the Stearns (2D) model and the corresponding 1D PSDs obtained by integration. The substrate was described using the ABC model with parameters σ=0.35 nm, ξ=1.8 10^3 nm and α=0.2. The considered film (W) had a thickness h=24.6 nm while the relaxation function was calculated considering only diffusion mechanism, i.e., n=2 (see Eq. (2.33)). Another parameter necessary to the modeling of the film is the volume of a single growth particle Ω (in this case atoms) and the relaxation distance ν. The former is given by:

$$\Omega[\dot{A}^3] = \frac{AW \cdot 10^{24}}{N_{av} \cdot \rho[gr / cm^3]} \tag{3.28}$$

where AW denotes the atomic weight. For tungsten the result is $\Omega \sim 15.3\ A^3$. The relaxation distance, generally a free fitting parameter, has been set to ν=30 A. As one can see the cross correlation is reduced at a large spatial frequency and fully conformal at the lowest one, i.e. practically coincident to the starting spectrum PSD_s. The development of intrinsic roughness is observed by comparing the PSD_f (red curves) with the PSD_s (green one: the PSD_f is higher at high spatial frequency and this trend is expected to increase PSD_s with progressive thickness (see, e.g., Figure 2-15). The scattering diagram was calculated using these three PSDs (Figure 3-9). As the intensity oscillations are related to the degree of conformity, their amplitude is expected to reduce at large scattering angles (i.e., large spatial frequencies).

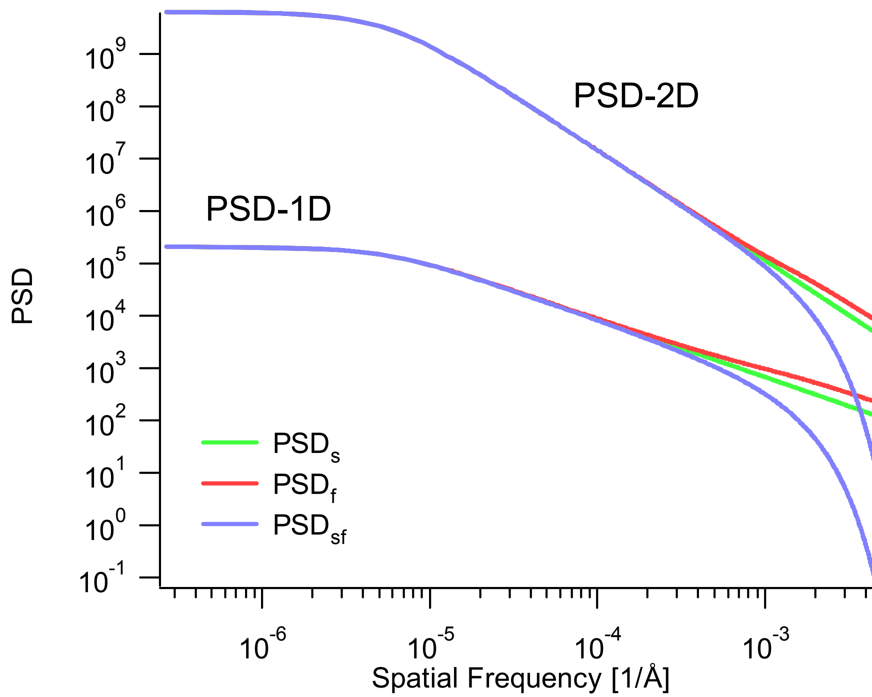

Figure 3-8: PSDs modeling using the Stearns model. The substrate is modeled using the ABC model with the following parameters σ=0.35 nm, ξ=1.8 10^4 nm and α=0.2 and a film thickness h=24.6 nm.

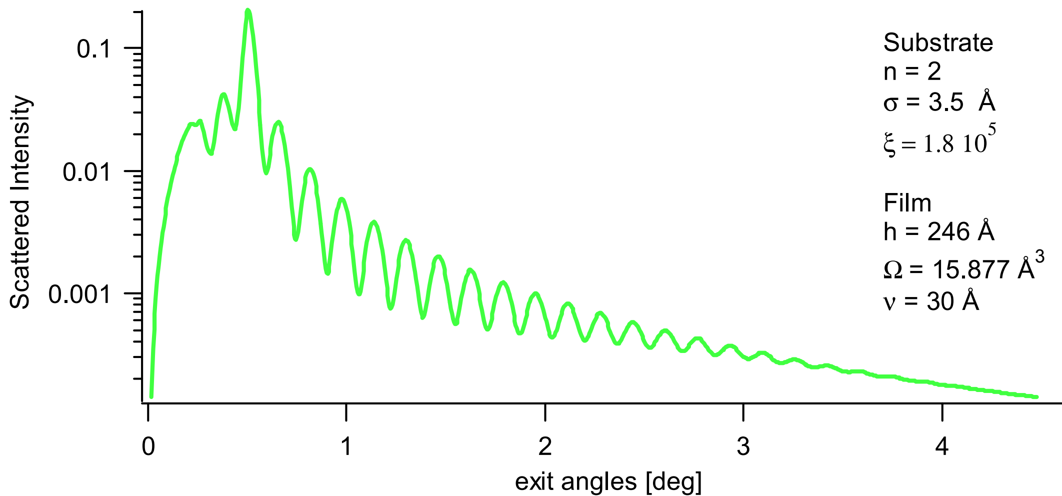

Figure 3-9: Scattered Intensity calculated using the Stearns model (Chapter 2), E=17 keV.

The curves presented in Figure 3-10 show the effect of the substrate (through its PSDs) on the scattering diagram. They use the same structure model as the previous figure except that the roughness exponent of the substrate was varied: α=0.2, 0.5 and 0.9. The correlation length ξ and the roughness σ were kept identical.

As one can see conformity decreases quickly for high roughness exponents α. This means that a surface with large α will be well replicated at small spatial frequencies, where it appears to be smoother. On the contrary, jagged surfaces (low α), see Figure 3-11, will be better replicated on a widest spectral range.

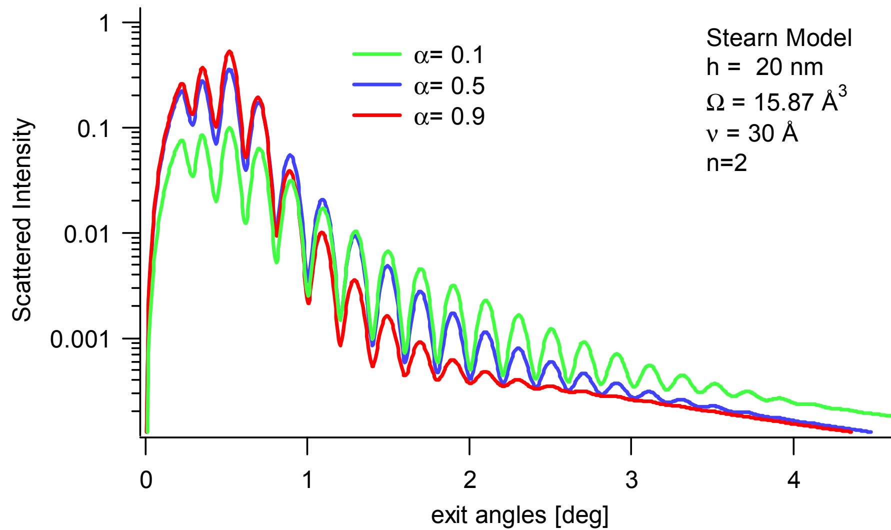

Figure 3-10: Effect of the substrate PSDs on the resulting scattering diagram. The three curves use the same structure model of the previous figure except for the roughness exponent of the substrate, α=0.2, 0.5 and 0.9, σ=0.5 nm and ξ=20 μm.

Figure 3-12 shows, in the framework of the same surface model, the predicted evolution of roughness conformity with increasing film thickness, i.e. starting from 5 nm up to 150 nm. Here also conformity is shown to decrease exponentially with the film thickness, and as expected, the fringes disappear as the film topography "loses the memory" of the substrate topography.

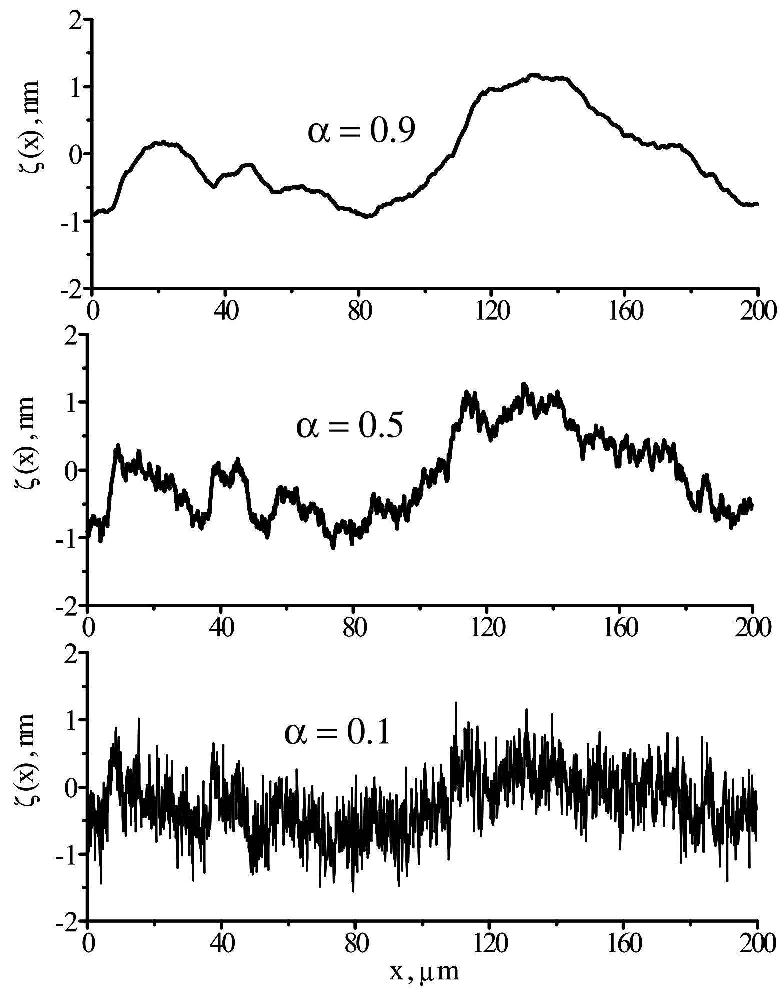

Figure 3-11: Rough surfaces of the same rms height σ *= 0.5 nm and the same correlation length a = 20* μ*m but of different roughness exponent* α*, see ref. [65] .*

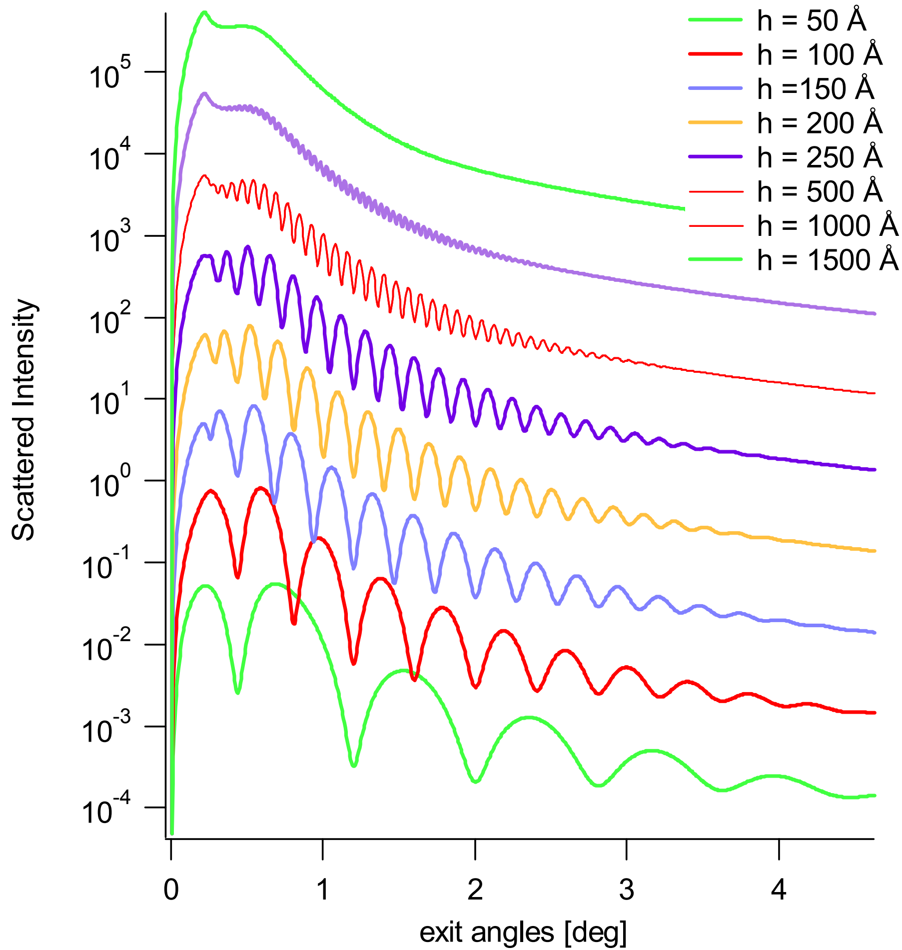

Figure 3-12: Evolution of the scattering diagram with progressive thickness in accordance with the Stearns's model. The model parameters are the same as in Figure 3-9.

Formula (3.27) suggests that, by measuring the scattering diagram at three or more angles or energies, one could solve an algebraic system of linear equations with the three PSD-functions as unknown. This would solve the problem without using a model. A detailed discussion of this approach is reported in a recent publication[66]. In principle the same approach could be used to determine a greater number of interfaces, N (case of a multilayer mirror).

However, when dealing with multilayer films consisting of N interfaces, the situation gets more complicated. In this case the analysis of the diffuse scattered intensity is generated by the summation of the scattering at each boundary and there are many ways to obtain the same sum because of the many different contributions. The knowledge of all N+1 roughness autocorrelation functions, one for each boundary and of the N(N+1)/2 cross-correlation functions is required. It is clear then, that an experimental determination of all these function is impracticable. To accomplish this job it is common

to analyze the structure of the as-deposited multilayer mirror [67, 68] and considering each interface to a different time of growth [43]. Here, the analysis is performed by fitting the scattering measurement with a model that accounts for the roughness evolution and postulates the form of the correlation function at each interface.

An alternative approach is probably to develop a realistic model for the evolution of roughness along the stack on the base of measurements of simplest material systems, e.g. a film on a substrate, and using a physical modeling to extrapolate more complex layered structures. At first glance this approach may appear too simple. However, the validation of growth models even for the simplest material systems is already an important issue largely debated. A detailed comparison between theory and experiment seems to be the first step for reasonable extrapolations to complex layered devices.

3.1.5 Transition layer model

The simplest optical model of a surface is an ideal plane of a vacuum–material interface, with the dielectric function having a step like profile varying from 1 in vacuum to ε inside the material depth (see Figure 3-13, left),

$$\varepsilon(z) = 1 - (1 - \varepsilon) H(z) \tag{3.29}$$

where the function $H(z)$ is the step-like Heaviside function given by:

$$H(z) = \begin{cases} 0, & z<0 \\ 1, & z \geq 0 \end{cases} \tag{3.30}$$

In the framework of this model the reflection of an electromagnetic wave with a surface is described by the Fresnel formulas. However, this description proves to be an abstraction. One of the first to observe deviations from the Fresnel reflection behavior was Lord Rayleigh [69]. The natural extension of this model is to consider a rough surface with profile defined by a stochastic function $z = \zeta(x, y)$ while the dielectric constant is still kept of the step-like type $H(z)$. That is,

$$\varepsilon(\mathbf{r}) = 1 - (1 - \varepsilon) H[z - \zeta(x, y)] \tag{3.31}$$

As already discussed, despite of its simplicity this approach can explain a large number of phenomena. However, in the model described by Eq. (3.31), surface inhomogeneities are associated only with the interface relief itself. A further development of the theory would have to account for inhomogeneities associated with the variation of the dielectric constant in the volume of the material near the surface. These inhomogeneities may be formed through a number of fundamental conditions, including the oxidization, implantation of atoms in the near surface region during deposition, variation of density induced by a polishing process. As a result, transition layer with

modified properties is formed near the interface. In order to describe scattering of electromagnetic radiation from such a surface, it is natural to assume that the dielectric-constant distribution has the following general form:

$$\varepsilon(z) = \begin{cases} 1 & \text{if } z \to -\infty \\ \varepsilon & \text{if } z \to +\infty \end{cases} \quad (3.32)$$

Let us consider a special case of eqs. (3.32), that is,

$$\varepsilon(z) = 1 - \frac{1-\varepsilon_0}{2}\left[1 + \tanh\left(\frac{z}{2L}\right)\right] \quad (3.33)$$

where L represents the extent of the transition layer (see Figure 3-13, right). Notice that inside the distribution (3.33), the inhomogeneities caused by surface roughness are separated from those caused by the electron-density variation over the material depth.

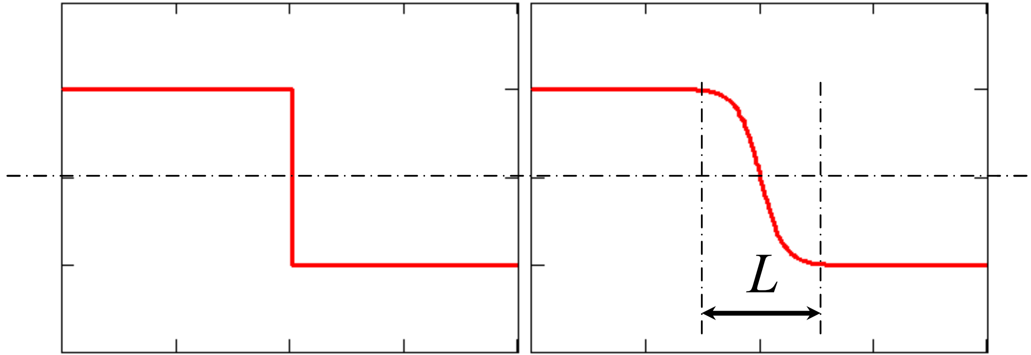

Figure 3-13: Ideally smooth surface with a step-like dielectric function profile (left) and an interface with a transition layer of length L*(right).*

It is now possible to generalize the formulas for both the specular reflectivity and differential scattered intensity using a more general formalism for the interaction of X-rays with a sample. This theoretical approach was first developed by Kozhevnikov and co-workers[70]. In the first retained order of the scalar perturbation theory the expression of the scattering diagram, has the form:

$$\Phi(\theta,\varphi) = \frac{k^4}{16\pi^2 \sin(\theta)}\left|\int \psi_0(z,\theta)\psi_0(z,\theta_0)\frac{d\varepsilon(z)}{dz}dz\right|^2 PSD_{2D}(\mathbf{f}) \quad (3.34)$$

which is valid for an arbitrary layer-inhomogeneous rough surface described by Eq.(3.32). Here $\psi_0(z,\theta)$ is a solution of the 1D unperturbed wave equation:

$$\frac{d^2\psi}{dz^2} + k^2\left[\varepsilon(z) - \cos^2(\theta)\right]\psi = 0 \quad (3.35)$$

which has the following asymptotic expression:

$$\psi_0(z,\theta) = \begin{cases} e^{ik_0(\theta)z} + r(\theta)e^{-ik_0(\theta)z} & at\ \mathrm{z} \to -\infty \\ t(\theta)e^{ik_1(\theta)} & at\ \mathrm{z} \to \infty \end{cases} \quad (3.36)$$

with the same notation for k_0 and k_1 as in paragraph 0.

On the other hand, since the most general formula for the specular reflectivity is rather complicated, only its asymptotic at large angle $\theta_0 > \theta_{cr}$ is given:

$$R_L(\theta_0) = \frac{k^2L^2\delta^2\pi}{16\cdot\sin^2(\theta_0)}\exp[-4\pi kL\sin(\theta_0)] \quad (3.37)$$

Here, δ is real part of the complex refractive index. Formula (3.37) shows the exponential dependence of the reflection coefficient on the grazing angle θ_0 in contrast to the power function of the Fresnel formula. The exponential decrease is a general property of an arbitrary finite analytical function $\varepsilon(z)$, model (3.33). For a continuous, but not analytical function $\varepsilon(z)$ the function $R(\theta_0)$ becomes a power law of θ_0. For example if the *n*th derivative of the function $\varepsilon(z)$ is discontinuous ($n \geq 1$), i.e, the $\varepsilon(z)$ has discontinuity of *n*th order, then $R(\theta_0 > \theta_c) \sim 1/[\sin(\theta_0)]^{2n+4}$. Therefore, the points of discontinuity of the function $\varepsilon(z)$ can be obtained from measurements of the asymptotic behavior of $R(\theta)$ at large θ. The analysis of $R(\theta_0)$ through Eq. (3.37) can finally provide the spatial extent L of a transition layer [70-72].

3.2 Time-resolved reflectometry

The use of an in situ and real time control of the process of layer growth or ion beam etching can improve the potential of inspection in contrast to standard X-ray reflectometry and to other post process characterization methods in general. We call this type of analysis *Time resolved reflectometry*. *Time resolved* refers to the possibility of following a process with a temporal sampling of the order of the time needed to grow/remove a monolayer of material. *Reflectometry* recalls that the analysis is based on the measurement of the radiation reflected by a surface, specular and diffusely scattered.

Numerous studies on the evolution of thin films have been performed by interruption of the growth process followed by post-growth ex-situ characterization using scanning probe microscopy SPM, including AFM and STM. These methods can also be applied for studies of thin film growth without the perturbing effect of exposure to atmosphere, i.e., in-situ. However, interruption of the growth process was still required. A smaller number of techniques monitor the growth process in real time, but often, methods giving complete information, if existing, are difficult and laborious. In addition to the complexity and limited availability of such instruments, these analysis techniques

may also put restrictions on the type of growth that can be performed (see [73] and references therein).

Real-time in-situ X-ray scattering can overcome the shortcomings listed above, by performing a measurement without interrupting the process. A necessary condition to perform a real time experiments with X-rays is to operate with a setup that is stationary in space while the object under study, the processed film, is evolving at an average rate v, see *Figure 3-14*. Indeed, during a synthesis process, not only the film thickness is varied but also the topography, the film density, the degree of crystallinity and the intermixing may a priori undergo changes that will affect on the optical properties of a film and a suitable characterization technique should be able to distinguish between these effects.

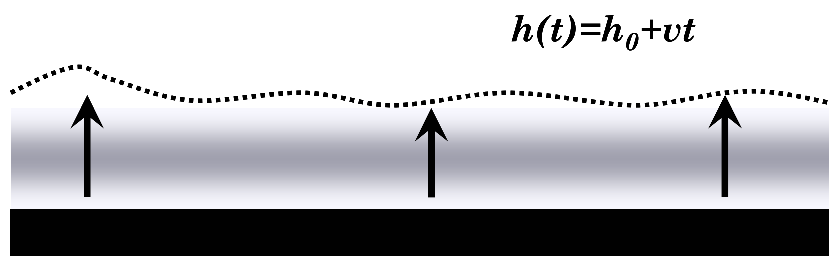

Figure 3-15: Schematic view of a surface profile evolving with constant speed of growth v.

We have chosen to perform X-ray scattering measurements in the detector-scan mode (or 2θ-scan) because it allows the sample to be stationary. This geometry enables one to have access to the lateral structure of the film. In particular the surface is described through its PSD, i.e. in terms of the following parameters: correlation length, roughness exponent and rms roughness (ABC model). Moreover, if other interfaces, located underneath, contribute to the scattering process, their contributions can be separated through an appropriate data analysis (see end of 3.1.4).

Generally, information about the film thickness and the density cannot be accessed with a detector scan measurement. They are accessible performing the so-called $\theta_0/2\theta_0$ scan, i.e. scanning simultaneously the sample and the detector. Ziegler et al., see also the ref. [74], have proposed a new type of X-ray reflectometer that measures the grazing incidence reflectivity at an energy of 8 keV for a series of angles from 0 - 2.5 degree(s), simultaneously. This is done using a curved crystal that sends a fan of X-ray beams on the surface, i.e. containing different grazing angles. With an acquisition time of a few seconds, they analyzed the layer growth during a deposition process with a thickness accuracy in the sub-nm range. However, the analysis of the measurements was complicated by the presence of diffuse scattering mixed with the specular contribution, which was extremely difficult to differentiate. Their reflectometer used an X-ray tube as a source which is, of course, much less intense than a synchrotron. The typical beam size

was few mm wide and several μm high to improve the statistics. Today, a remake of this experiment could probably benefit from the use of intense μ-beams available in modern X-ray sources. The interest today in such a technique would be its ability to measure and differentiate in real-time the reflectivity versus angle and the diffuse scattering. One could study the variations in depth of matter of the dielectric permeability during oxidization or interdiffusion, re-mix of liquids, phase transformation with temperature, to name just a few.

In this dissertation, we discuss another possible way to extract information both in the specular and the off-specular directions, which consists of fixing the grazing angle of incidence and monitoring the specular and diffuse scattered intensities simultaneously. In this case, the reflected and diffuse intensities are expected to behave differently depending on the magnitude of the angle θ_0 with respect to θ_{cr}. The detailed description of the technique will be given in the next chapter.

We have presented previously a description based on the analysis of the PSDs. Here, we will limit ourselves to another type of analysis, found in the literature, which consists in measuring the total integrated scattering, TIS. As shown before, see, e.g., 3.1.2, one special case of interest is realized when the reduction of total reflectivity R_Σ, due to small scale roughness, is negligible. Then, the total reflectivity can be accurately described by the Fresnel formula and $R_\Sigma \cong R_F$, i.e., roughness does not increase the flux directed into the substrate but redistributes the reflected intensity between the specularly reflected and diffusely scattered components. A TIS measurement provides only the vertical roughness parameter, i.e., the rms roughness, of the surface. The information on the lateral scale is not available from TIS. However, this is also an important result as the analysis of the TIS signal during a dynamic process can provide information about the dynamic exponent that defines the variation of roughness with time t.

Thus as $R_F(t) \sim R_\Sigma(t)$ and since only R_Σ can be measured exactly during a real experiment[16], to the relation for the roughness obtainable with measurable quantities, TIS and R_Σ:

$$\sigma(t) \sim \frac{1}{2k\sin(\theta_0)}\sqrt{\frac{TIS(t)}{R_\Sigma(t)}} \tag{3.38}$$

Hence, a simple TIS measurement can gain information about the dynamics of film growth yielding $\sigma(t)$.

[16] Due to the finite width of the detector aperture, the specular and the scattering peaks mixed up and cannot be resolved.

The concept of this type of measurement is very close to a standard technique used in light scattering for the analysis of surface roughness in many practical applications [62]. In light scattering, the measurements make use of TIS integrating sphere, called Coblentz sphere, placed around the sample to measure the amount of diffuse scattered light. With X-rays the radiation diffusely scattered by a rough surface, is concentrated in a much narrower width, approximately given by $\Delta\theta \sim \lambda / \xi \sin(\theta_0)$, where ξ is the correlation length of the surface roughness [62]. Therefore a relatively small detecting area, few cm^2 large is sufficient to record the overall TIS intensity.

Note that, with the approximation used above, TIS can be put equal to the integral of differentially scattered intensity measured out of the specular peak while R_Σ is a quantity measured with a large area detector placed around the specular peaks. In this case, the roughness will be defined in a spectral bandwidth defined by the range of scattering angles integrated.

The following figures Figure 3-16, Figure 3-17 and Figure 3-18, show calculations, at an energy of 17 keV, on the evolution of TIS and σ for two different grazing angles, in TER and OTER conditions with different starting roughness.

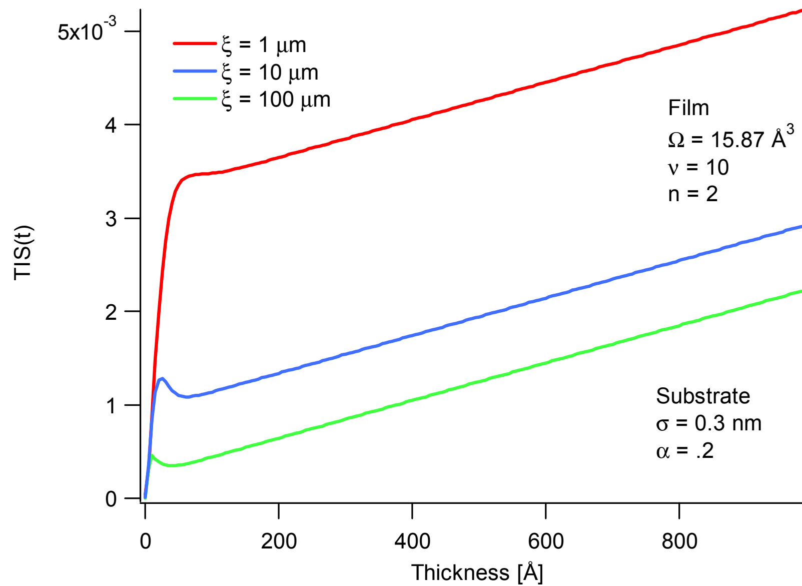

Figure 3-16 Calculated TIS as a function of the film thickness in the TER region assuming three different correlation lengths for the substrate (ABC model) and using the model of Stearns for the film. The grazing angle is θ_0 = 0.15 deg and the energy is set to E = 17keV

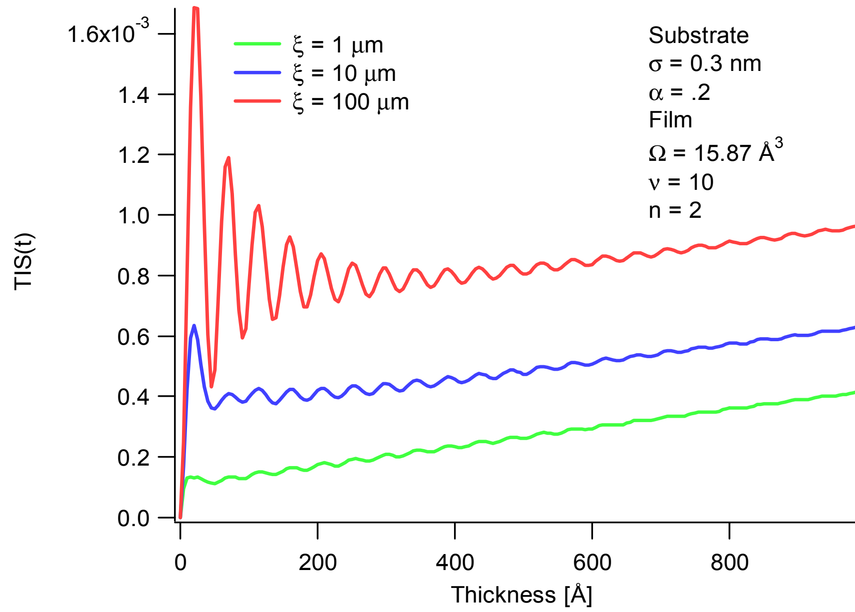

Figure 3-17: Calculated TIS as a function of the film thickness in the OTER region with θ_0=0.5 deg. Other parameters are the same as for Fig. 3-16.

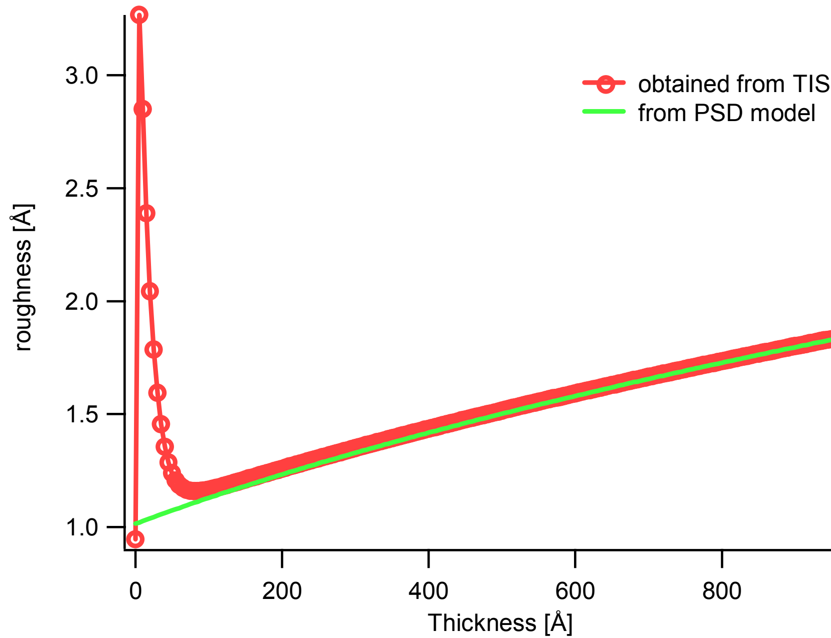

Figure 3-18: Variation of the roughness obtained from TIS calculations compared to that entered in the model of the PSD. The sharp peak is an artifact due to the transition between the silicon substrate and the tungsten layer, i.e. $\theta_{cr}(Si)<\theta_0<\theta_{cr}(W)$. The agreement between the two curves is valid asymptotically for large thicknesses.

The curves presented in Figure 3-18 show again the limitation to obtain the roughness when the films are too thin because of the presence of interference effects. Therefore, the analysis in this region can only be performed through a fitting procedure invoking a growth model describing the evolution of a film [2].

3.3 Summary

In this chapter we have discussed the role of X-ray reflectometry as a tool for studying thin films. The method is shown to be adequate to describe the structure of a film in both the perpendicular and the parallel direction with respect to the surface normal. Several theoretical approaches have been mentioned as possible candidates for the interpretation of the scattering data, i.e. the Perturbation Theory and the DWBA. However, a formal proof of the suitability of one approach over the others has not been found in the literature. To verify the superiority of one model on the others it would be desirable to compare the abilities of these theories at predicting the behaviour of an *exactly solvable* object. A grating structure might be an appropriate object, as it is possible to model exactly the interaction of an X-ray beam with a periodic surface. To date these issues remain open and are expected to feed new lively debates in the field.

Among the various approaches the PT has been selected as the most appropriate for the analysis discussed hereafter for the following reasons: its domain of applicability matches the case of slightly smooth surfaces. This case is also of relevant technological interest, as in many fields, including X-ray optics, microelectronics and EUV lithography where the devices have very smooth surfaces. The use of the PT does not require special fitting procedure and can be directly implemented to extract the statistical information about a sample surface without using a model of film growth or of correlation function. Finally, the method has been shown to be applicable to the interpretation of real time scattering data.

The interest in performing real time analysis has several advantages over the standard X-ray reflectometry, including: i) The necessity for the thin film evolution to be studied without any interruption of the growth process. ii) The ability to determine the film thickness and roughness in-situ and in real time, providing a unique opportunity to optimize processing conditions while they are occurring. iii) The possibility to follow the evolution of the film morphology. Therefore, real time data can follow the history of a processed film, thus, simplifying the analysis of the process.

In the fabrication of a coating, these points enable one to have a short feedback loop providing data on the performance of the coating in one deposition run, giving, in turn, a guide on how a deposition run should be modified or corrected to optimize the optical performance.

Chapter 4 Experimental technique and instrumentation

The main tasks of the experimental part of this dissertation have been the design, realization, characterization and finally the application of a new apparatus for time resolved reflectometry on thin films at the Optics beamline BM05 at the ESRF.

The general layout of the beamline and a description of the optical elements conditioning the synchrotron beam will be presented. The apparatus developed during this dissertation will then be described, including its calibration. Finally, the new experimental method will be presented with emphasis at its performance in terms of spatial and temporal sampling.

4.1 Beamline description

The experiments described in next sections, were performed at the optics beamline (BM5) at the ESRF. An extended description of the beamline is given in a recent publication [75]. It is mainly composed of an optics hutch containing beam conditioning optics such as slits, monochromator and filters, followed by two experimental hutches (EH).

The x-ray beam accesses BM05 from a wall located at 23 m from the source. In this optics hutch (see Figure 4-1) we successively find an aperture selecting a 3 mrad horizontal fan of hard X-rays (bending magnet radiation at 0.8 T), a set of attenuators, and a pair of primary slits.

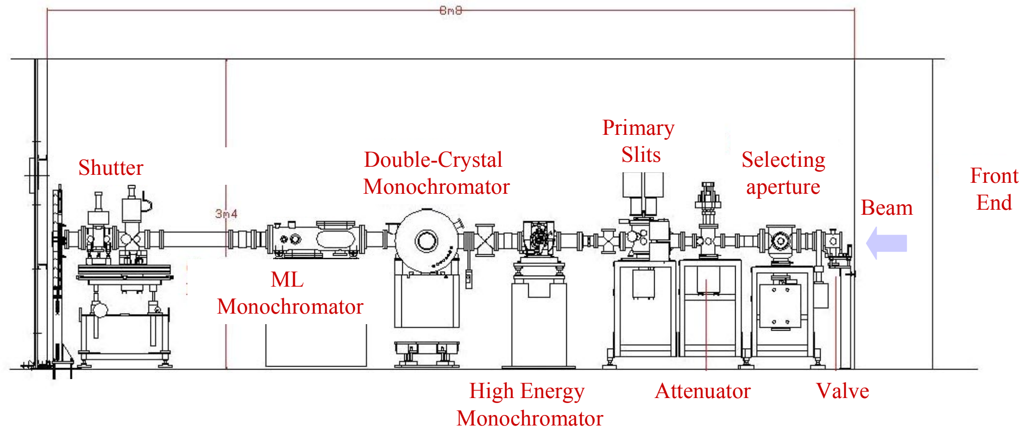

Figure 4-1 Side view of the optics hutch of BM05.

The following components are a channelcut hard x-ray monochromator (40 keV-100 keV), a standard double-crystal monochromator (6 keV- 60 keV), and a double-multilayer monochromator (6 keV- 30 keV). Each of these elements can be inserted or removed without breaking the vacuum of the beamline. When none are used, white beam is propagated. When inserted into the beam, these elements are deflecting the beam vertically and filter it to obtain monochromatic radiation.

At the end of the optics hutch (OH), a shutter controls the transfer of the beam into the experimental hutch (EH1) physically separated from OH by a lead wall. In the first experimental hutch one successively finds a flipping fluorescent screen, a vertical-geometry reflectometer, a pair of secondary slits, and a high-resolution horizontal-geometry multiaxis platform used for various purposes: diffractometry, optics tests tomography, etc... As before, a shutter controls the entry of the beam into the next experimental hutch (EH2) through a shielded tunnel.

The experimental equipment presented in this dissertation is installed in EH2 at ~55 m from the source. At this distance of 55 m, the source is seen with an angular vertical divergence of 1.4 μrad (half-angle). The hutch is equipped with a pair of slits to define the beam, an optical table for micro focusing tests and other characterization, and finally the novel apparatus that was entirely developed during this thesis period. It is composed of two stages mounted on air cushions: one to hold a vacuum chamber, one to hold the detection system. The floor is made so that the instruments can be easily moved around or set aside to allow other experiments.

4.2 Apparatus: design strategy and realization

The first issue appearing during the design of the apparatus was the choice of the scattering geometry for the real time scan. We already discussed in Section 2.2.2 that only

the detector scan allows one to fix the sample in a stationary position. However, detector scanning is time consuming and that makes impossible its use to study the evolution of a surface, unless a systematic set of samples prepared at different time of growth is analyzed under identical condition. This procedure may introduce a number of additional errors during the analysis, e.g., effect of oxidization if measurements are performed in air, presence of systematic errors when realigning the samples and/or resulting from slightly different process conditions.

Some authors [73, 76, 77] proposed the use of energy dispersive techniques to avoids the above limitations because sample and detector remain fixed while measuring the scattered intensity. As a result, they either measure specular intensity as a function of the perpendicular wave vector, k_0, or diffuse scattering as a function of the parallel projection of the vector $\overrightarrow{k_0}$.

However, it is possible to conceive an angular dispersive setup that will preserve the advantages of a stationary sample and detector. To this end, for the sample to be stationary a 2θ-scan should be performed, and for the detector to remain stationary a CCD detector covering the angular range of the experiment should be employed. One practical advantage over the energy dispersive mode is the possibility to optimize the optical layout of the beamline to maximize the flux and the beam stability. Another advantage concerns the data analysis, where the optical constants are the same for all data points as opposed to the energy dispersive mode.

Using this angular-dispersive technique it has been possible to characterize the surface during many sample treatments always keeping a full monitoring of the reflected X-ray beam during a sample process. A sketch of the experimental setup is shown in Figure 4-2.

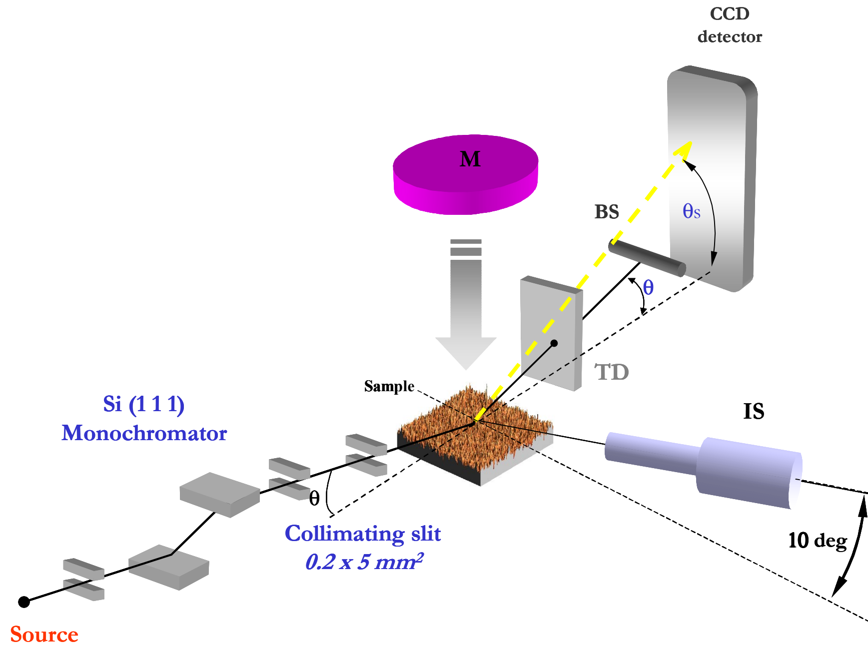

Figure 4-2: Sketch of the set-up, sputter source M, ion source IS, beamstop BS and transmission detector TD.

The setup integrates two schemes: sample processing and x-ray detection. A vacuum chamber with a base pressure of 10^{-7} hPa is equipped with a magnetron sputter source for film deposition and an ion source for etching studies. Facing the sputter target the sample is rigidly fixed inside the chamber. Thanks to a custom sample manipulator, the angles between the incoming flux of particles (atoms/ions) can be set between 0 deg. to 90 deg. while keeping the sample horizontally aligned with the X-ray beam (see 4.2.1 and 4.2.2). Then, once the sample is aligned[17], the whole setup remains stationary during film deposition. Two polyamide windows, 150 μm thick, allow the x-ray probe beam to pass through the chamber. The first detection system, consisting of a semitransparent transmission detector, monitors the total intensity of the reflected beam, i.e., $R_{\Sigma}(t)$. The second one, composed of a 2D detector, collects the scattered beam, i.e., $\Pi(\theta_s, t)$. A beamstop, placed in front of the detector, blocks the intense beam reflected in the specular direction and prevents the detector from saturation. In the experiments described hereafter, the sample–detector distance was always set at ~1 m. This distance was found to be a good compromise between the range of scattering angles accessible in a single detector frame and the angular resolution, typically less than 0.005 deg. The energy

[17] The alignment procedure follows the same procedure used in standard reflectometry [34], with the difference of scanning the primary beam instead of the sample. This is due to the absence of a further step motor in vacuum for movement along the Z axis to preserve the vacuum quality.

was set to 17.5 keV with a spectral purity of $\Delta E/E=10^{-4}$ using a double-crystal monochromator. The divergence in the vertical direction was 3 10^{-6} rad.

The need of performing measurements simultaneously with two detectors is due to the limited dynamic range (2^{16}, at best[18]) of the 2D detector, thus preventing the simultaneous acquisition of both specular and diffuse signals, which have very different magnitudes. For instance, when dealing with very smooth samples, the specular and different intensity could differ by several orders of magnitude.

Thus, our real time data acquisition process consists of monitoring two signals at equal time intervals (parallel recording).

4.2.1 Sample environment, positioning and X-ray alignment

The vacuum chamber shown in *Figure 4-3* is located at 55 m from the X-ray source. It is composed of a monolithic stainless steel block designed to be space effective, i.e., its geometry was designed to accommodate the maximum number of view ports, 26, for a given chamber volume. All ports (internal diameter ranging from 16 mm to 150 mm) face the baricentre of the chamber where the sample is located. Some of them are presently used for vacuum preparation, vacuum diagnostic and sample synthesis (sputter source and ion source). The chamber is pumped with a group composed of a 400 l/sec magnetic turbo-pump and a dry pump. The base pressure, when using the polyamide windows, is of 2 10^{-7} hPa. The magnetic pump enables operation without parasitic vibrations and the possibility of operating at any angle.

The X-ray beam can pass through the chamber from two flanges onto which polyamide windows 150 μm thick, have been glued. The probe beam enters the chamber through a first window, is reflected by the sample, then transmitted through a second X-ray window that is wider in the vertical plane to give access to a maximum scattering angle of 6.7 degree. The polyamide thickness and the surface area were empirically chosen accounting for the lowest base pressure reachable (connected to their surface area and thickness) and mechanical strength (dependent on the thickness) necessary to sustain the shock of the primary pumping. By reducing their total surface by a factor ~3 the base pressure was reduced by an order of magnitude, i.e., from ~10^{-6} up to ~10^{-7} hPa[19].

---

[18] This value can be improved to values exceeding 6 orders of magnitude by changing the integration time.

[19] A better vacuum quality could be obtained using Be windows, but when highly polished they are very expensive and are know to degrade the quality of the primary beam, due to the presence of bulk inhomogeneities.

The experiments performed along this dissertation were performed with two different versions of the same instrument, for the positioning of the sample and the 2D detection system. In the first step, a setup was built using existing equipment until encouraging results on the potential of the method would be observed. The vacuum chamber was mounted on top of an X-ray diffractometer via a custom mechanical interface, so that the alignment of the sample surface with respect to the incident x-ray beam (3 translations and 2 tilt angles) was obtained by moving the chamber itself (sample integral to the chamber). This apparatus was combined to a detection system composed of a DELFT image intensifier, a PRINCETON CCD camera and an optical transfer system in-between. It had a poor performance because of the aging of the intensifier resulting, in particular, in strong image inhomogeneities due to damages on the fiber taper and a degraded spatial resolution. In addition, the optical system was designed for another CCD so that the magnification did not match the effective dimension of the CCD chip. Another drawback was the heavy load of the chamber on the diffractometer and the difficulties to perform the sample alignment. The range of movement available for the sample alignment was limited to +/- 1° for angular tilting and few mm for translation along X and Y directions, making difficult the routine alignment procedure.

After promising pilot experiments, an improved and dedicated setup was designed and manufactured, while continuing the experimental work parallel on the prototype system. Despite several weaknesses, the first setup was successfully used for a long time (about ½ thesis period). It allowed us to demonstrate, the scattering technique and the data acquired could still be used to present the method in papers submitted recently [66, 78].

The setup accommodated a specifically designed stage and an in-vacuum goniometer for sample alignment and manipulation, as well as a new custom designed image intensifier that had a resolution 3-times better than previously (line spread function, LSF=170 μm) and an optimized field of view (72.6 x 18.2 mm). The improved apparatus is presented in *Figure 4-3*, and will be detailed hereafter.

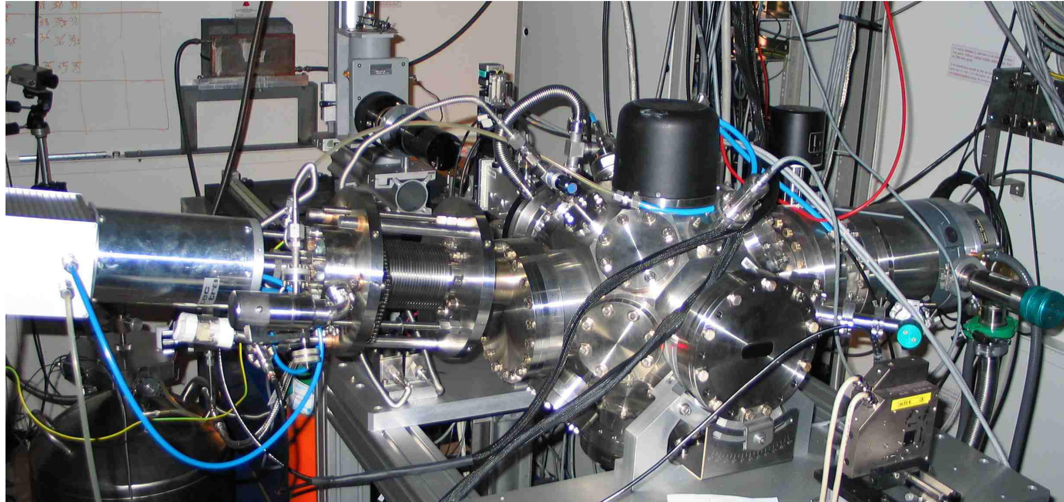

Figure 4-3: Experimental apparatus developed for real-time in-situ studies on thin films

The present chamber is integrated into an aluminum frame with a rolling mechanism that allows the whole chamber to tilt around the X-ray beam axis, θ_X. This mechanism combined with the sample manipulator rotating around the same axis (see next paragraph), allows to adjust the tilt of the sample surface with respect to the direction of particles generated by either a sputter or an ion source while maintaining the sample surface horizontal, i.e., parallel to the X-ray beam sheet. For a given position of the particles source, the angular displacement is about +/- 15 deg. By installing the source on two other view ports the overall angular range can go up to 90 deg. This mechanism was designed to study ion beam etching and deposition as a function of the incidence angle, which is crucial in several developments, e.g., for ion induced nanostructures (ripples and nanonodots [79-81]) and for the optimization of the surface roughness under grazing incidence conditions. For the experiments described hereafter the ion source was set at a 10° grazing angle and the sputter source at normal incidence. Grazing angle ion bombardment is indeed expected to induce surface smoothing[20] as reported by Kimura et al. [82].

4.2.2 Sample Holder

In contrast to our previous setup, the X-ray alignment of the sample does not require anymore changing the position of the whole chamber. It is now performed using a custom designed sample holder and an in-vacuum goniometer. It is composed of an

[20] The authors observed that the rms roughness could be reduced to the order of a single atomic step height if the ion incidence angle is only a few degrees respect to the surface plane. Under these conditions, ions are completely reflected from planar surface due to the low sputtering yield.

aluminum arm fixed onto the internal face of a flange connected to rotating feedthrough. Figure 4-4 (top) shows a perspective view of the sample holder that is mounted on a CF 150 flange with a Lesker® rotating feedthrough. It constitutes the basis of the mechanism our sample manipulator.

The arm is holding the sample stage and can rotate it, using the rotating feedthrough, at any angle respect to the incoming particles (atoms/ions). At the sample stage a linear actuator will translate linear motion in angular tilt of the sample respect to the incoming X-ray beam (grazing incidence angle), see Figure 4-4 (bottom), i.e., by pushing a lever integral to the substrate carrier, that can swing around θ_y and is axially bound. This motor, vacuum compatible, is presently the only one installed inside the vacuum. The accuracy for its angular positioning is better than 10^{-3} deg. The calibration from the linear translation movement to the rotation (step per degree) was obtained by measuring the angular distance between two Bragg peaks of a multilayer with known period. The measurements demonstrated that the mechanical design allowed generating rotation with accuracy better than 0.001°.

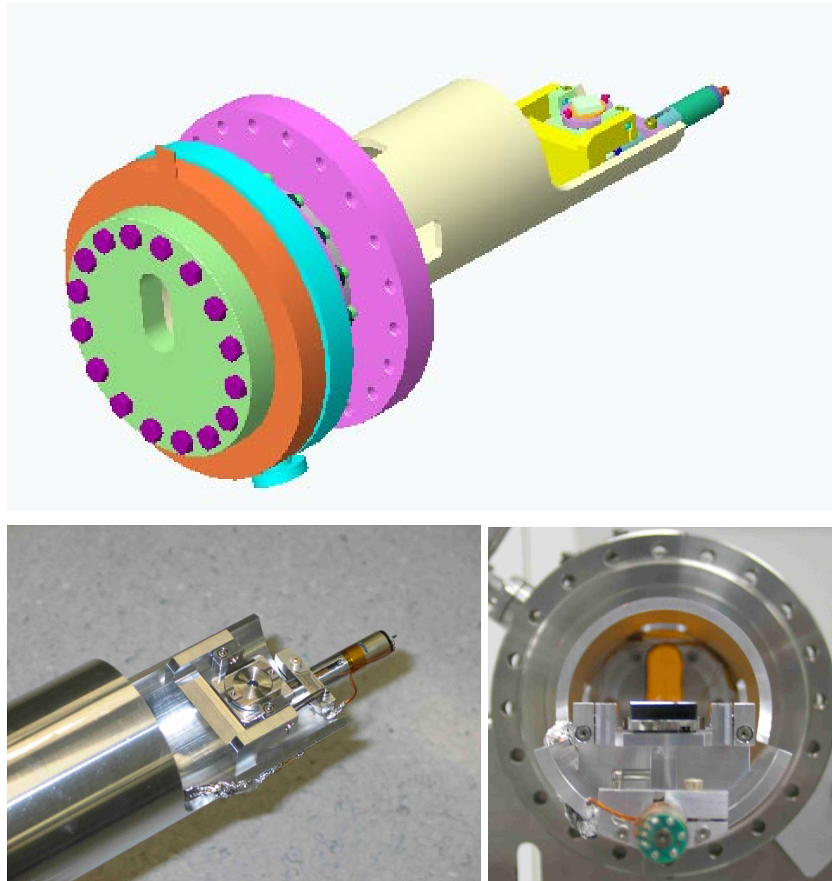

Figure 4-4: Sample Holder (top) and two views (bottom) of the in vacuum goniometer with two degree of freedom θ_Y and θ_X.

Finally, the sample is positioned on a three-point magnet carrier allowing a reliable repositioning (see Figure 4-4, bottom). To change the sample, one only needs to disconnect the sample carrier unit and to move it from a lateral flange of the chamber while the goniometer and the chamber itself remain fixed.

The sample surface is adjusted mechanically at the center of rotation that is fixed at the nominal position within an accuracy better than a micrometer. The sample is fixed on its holder with colloidal graphite (AGAR – vacuum compatible). This product was a good compromise between its capability to sustain the sample during manipulation and the minimum residual stress it would create with the holder.

4.2.3 Sputter gun

The thin film preparation is performed using a DC magnetron sputter gun. The gas discharge is operated at constant power and biased in the range 300-400 V, while the target current could change in the range 20-100 mA (W target). Thin films are deposited

on Si (100) substrates. The sputtering target is a disk, 73 mm in diameter and 3 mm thick, of W (purity 99.95%) placed 150 mm from the substrate. Before deposition, the background pressure of the sputtering chamber is less than 3.6×10^{-7} hPa. The sputtering is conducted with a pure (99.999%) Ar gas with a working pressure of $9.3\ 10^{-3}$ hPa. The gas flow is supplied from another view port placed few cm close to the target and controlled by a mass flow meter (MKS). The chamber pressure was also regulated during deposition by looping a butterfly valve, facing the turbo-pump, with a capacitive gauge (BARATRON). The target bias as well as the pressure set point is computer controlled and tuning is made remotely from the control room of the beamline.

To initiate the plasma, the gas pressure is set to $13.3\ 10^{-3}$ hPa. Once the plasma has ignited, it quickly settles to a steady state. The pressure is then reduced at the value desired for the film deposition experiment. The typical experimental conditions used a bias voltage of 370 V and a total ion current of 30 mA. The pressure level was achieved by fixing the gas flow rate to 3 sccm. In Figure 4-5, the characteristics of a dc glow-discharge are shown for three target currents. When plotting the product (*Pressure-Distance*) versus discharge voltage one obtains the Paschen curves, characteristic of the plasma. These curves where measured by varying the opening of the butterfly valve located in front of the turbo pump from open to closed position while a constant Ar flow of 3 sccm would enter the chamber.

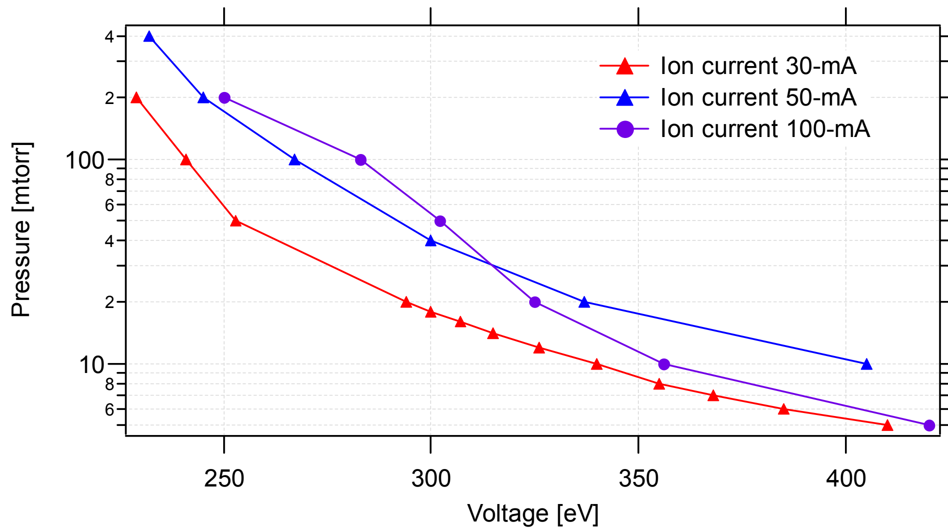

Figure 4-5 Paschen curves obtained for different target current.

To calibrate the deposition system we have measured the relation between deposition rate and target current. The deposition rate was calculated from the analysis of

three reflectivity curves as a function of time[21] for a tungsten film growing at different target currents, namely 30 mA, 50 mA and 100 mA (value displayed on the controller). The deposition rate, resulting from the analysis is shown as function of the target current in Figure 4-6. As one can see, this relation has a linear dependence and demonstrates a picometer sensitivity of both the deposition and the monitoring systems.

The speed of growth can be used to evaluate the flux of particles arriving at the sample surface. This flux can be estimated from the ratio between volume grown on the area S per time unit, given by S times the speed of growth v_g, and the volume of a deposited particle Ω, that is:

$$\Phi\left(\frac{\#}{s \cdot cm^2}\right) = \frac{S \times v_g}{\Omega} = S\left[cm^2\right] \cdot \frac{N_{av}\rho\left[gr/cm^3\right]}{AW \cdot 10^{10}} \cdot v_g\left[pm/\sec\right] \quad (3.39)$$

Where, N_{av} is the Avogadro number, AW is the atomic weight and ρ is the film density. This formula yields fluxes spanning between 3.1 10^{13} and 1.1 10^{14} particles per second and per cm^2.

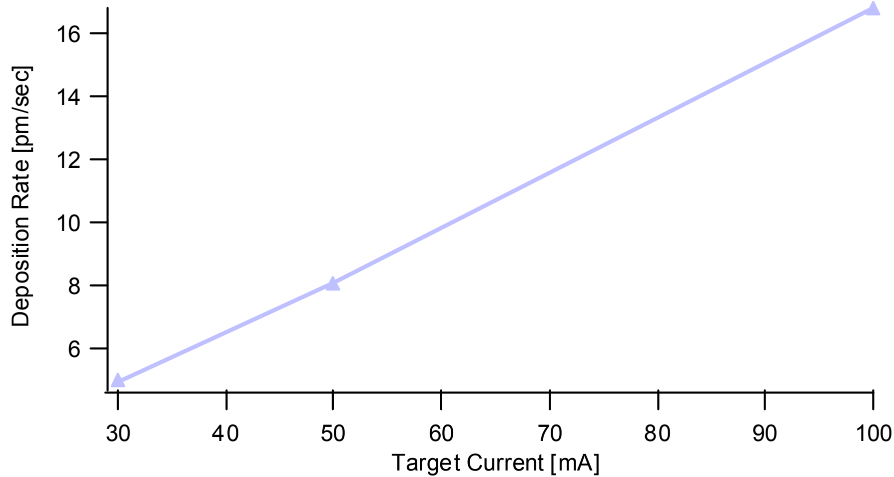

Figure 4-6: Relation between deposition rate and target current obtained from real time in-situ reflectivity measurements (see Chapter 5) at three target current, 30 50 and 100 mA and Ar+ Mass Flow 3 sccm.

4.2.4 Ion source

The ion source we used is producing low energy ions. The specifications are given in table 1 while a detailed description can be found in reference[83]. The principle of operation is based on the electron cyclotron resonance (ECR) effect. The plasma is

---

[21] During the same experimental session, i.e. subsequently growing W onto a unique silicon substrate.

generated by evanescent coupling of microwaves at 2.45 GHz using a 250 W power supply, in presence of an inert gas confined inside an alumina cup. The plasma is further enhanced by the action of a magnetic quadrupole placed around the alumina cup. Ions are finally accelerated by a set of grids (anode and extractor), to provide a broad beam with a divergence of +/- 15 deg.

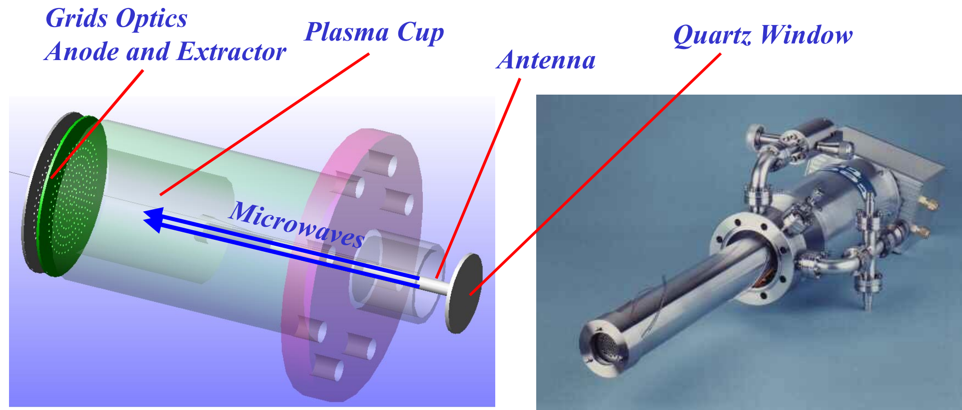

Figure 4-7: Schematic view (Left) and photo (right) of the plasma source.

The source can be configured to operate in several distinct modes: atom source, ion source and atom/ion hybrid source. However, we only used the ion source mode. Besides delivering different species (atoms, ions, radicals) the plasma source covers a complete energy range from neutral thermal atoms to ions above 1500 eV. The shape of the beam and the current density can be altered with several ion beam optics. The experiments were performed using Molybdenum ion grids with an anode voltage of 1000 V and an extractor voltage of –200 eV, corresponding to a total ion current of 15 mA. The flux was estimated in the same way we did for deposition. For simplicity we assumed a sputtering yield equal to 1, leading to a flux of $\Phi = 3.7\ 10^{13}$ particles per second, per cm². The typical working distance *d* was 150 mm. However, it could be varied by 100 mm (bellows system), resulting in a variation of the flux density by a factor 4. A large range of combinations of ion current, energy, and flux could be reached, therefore, allowing a systematic study of the ion bombardment process ($\Phi \propto 1/d^2$).

Microwave power:	250W max at 2.45 GHz
Beam diameter:	~25mm at the source
Plasma cup:	Alumina
Gas flow rate:	0.01-100 sccm
Working pressure:	mTorr
Working Distance:	150 mm typical
Grids sets	Molybdenum and Graphite

Table 4-1: Ion source features

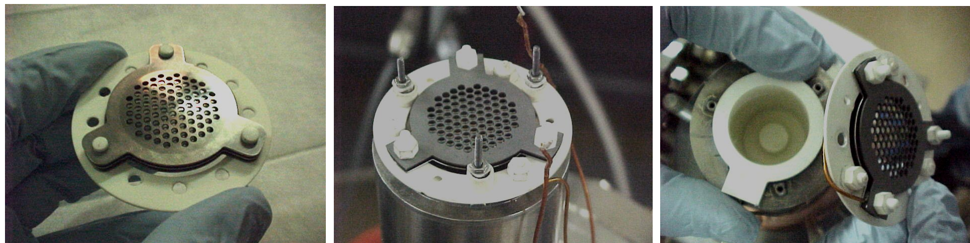

Figure 4-8: Ion grid optics of the TECTRA plasma sources, for beam collimation (left) and for broad beam (centre). The alumina cup is placed behind the grids (right).

4.2.5 Detection system

Over the last 10 years charge-coupled devices, or just called CCD detectors, have enormously improved in terms of quality and speed of x-ray data acquisition [84]. X-ray CCD detectors are typically composed of a sequential cascade of components, which consist of a relay of electro-optical elements, see Figure 4-9. Their function is to stop the x-rays and to generate a primary signal that is amplified and eventually coupled to a CCD. CCD detectors are distinguished one from each other by the components that perform these functions. Therefore, their design requires an analysis of the five functions performed by the signal relay components (see Figure 4-9):

1. The *X-ray conversion* stage absorbs the x-ray in, for example, a phosphor or semiconductor layer and converts the x-ray photons into visible light or electron quanta.
2. An *Intensification* of the resultant signal may be required for weak signals.

3. The *coupling* is done by various methods, e.g., lenses, fiber optics, micro channel plate MCP.
4. The *reading out* of the resultant signal is finally obtained using a CCD array collecting visible light.

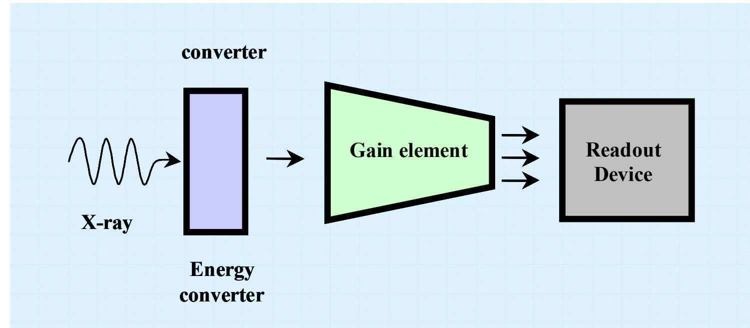

Figure 4-9: Schematic principle of an X-ray detector

The detection system used in our experiments is a custom one designed for specular and diffuse X-ray scattering measurements and was developed in collaboration with the detector group of the ESRF. It consists of a 2D detector to acquire the scattered intensity and a semitransparent detector to monitor the total intensity of a reflected beam.

Figure 4-10: Photo of the LN/CCD camera from Princeton mounted on its stage. The yellow nut is placed on the inlet for the liquid nitrogen (LN).

The 2D detector is a cryogenically cooled CCD camera (1024 × 256 pixels of 19 μm size each) coupled to an image intensifier. The front window made of vitreous carbon is followed by P43 phosphor screen[22], 40 μm thick. Between these two components, a foam layer ensures a good contact between phosphor and entrance of the image intensifier. The X-ray photons stopped by the phosphor screen are converted to visible light a then fiber coupled optically with the entrance window of a reducing image intensifier (demagnification 2.72). The image intensifier consists of a Micro Channel Plate (PROXITRONIC) that is finally lens-coupled to a 16-bit Princeton LN/CCD.

[22] The thickness of the phosphor screen was chosen to work with an X-ray energy peaked around 17-20 keV

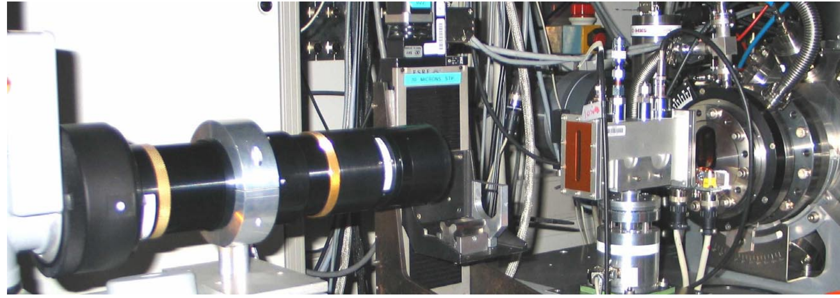

Figure 4-11: 2D detection system based on a reduced (5:1) image intensifier coupled to a 256x1024 CCD camera. The equivalent pixel dimension was 110 μm

At the maximum recording speed, frames of size 256 x 1024 pixels can be acquired with a gap between the frames in the millisecond range. At the maximum gain of the MCP, single photon detection is achievable. To improve the signal to noise ratio the intensifier output is imaged by a lens system onto the CCD detector that is cryogenically cooled with liquid nitrogen supplied externally with an automatic refilling system. The CCD camera is cooled at –90 °C; its thermal stability was contained within +/- 0.050 °C thanks to a servo control system ensuring the thermal regulation during the experiments. The liquid nitrogen is stored in a Dewar that is enclosed in a vacuum jacket to minimize the consumption. Because of the low operating temperatures, the CCD is operated under high vacuum condition (10^{-6} hPa).

A beamstop placed in front of the detection system avoids overexposing the images. To ensure shading of the specular beam, whose angular width is of the order of ~0.057° at 1 m from the sample, the beamstop had 1 mm diameter and a thickness of ~5 mm. For the reflectivity monitor the distance sample-detector was 0.5 m. The spatial resolution, see the resolution pattern images in Figure 4-12 and Figure 4-13, was checked using an X-ray energy of 17 keV (working energy). Line spread function measurements yield a spatial resolution of the system of 170 μm. At the same energy the sensitivity of the system was also tested (gain calibration, Figure 4-14) changing linearly the high voltage applied to the MCP from 460 Volt to 660 Volt and measuring the ratio between measured signal in analog digit units (ADU) and the number of X-ray photons (X). The last two quantities can be used for defining the gain G as G=ADU/X.

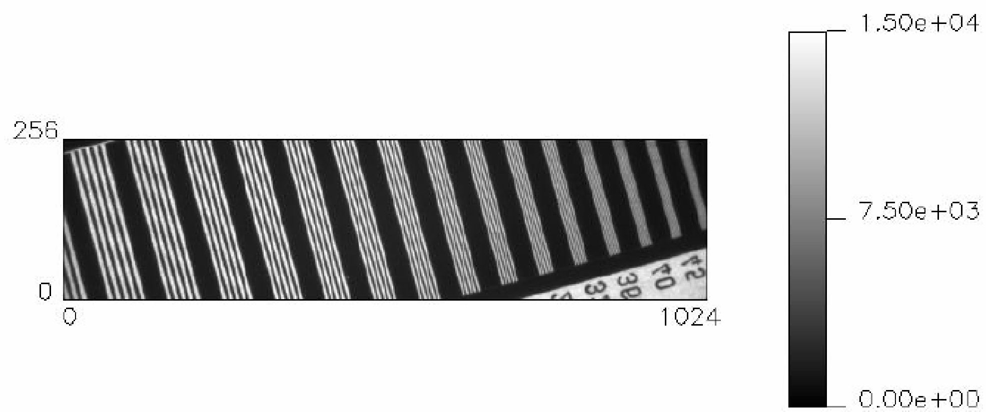

Figure 4-12: 2D resolution pattern image

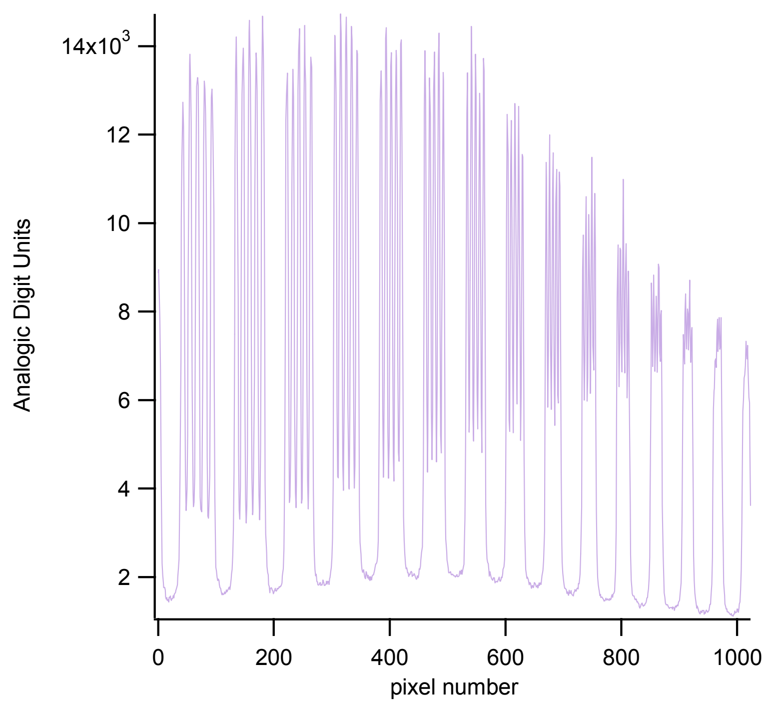

Figure 4-13: Resolution pattern profile obtained with the 2D detector

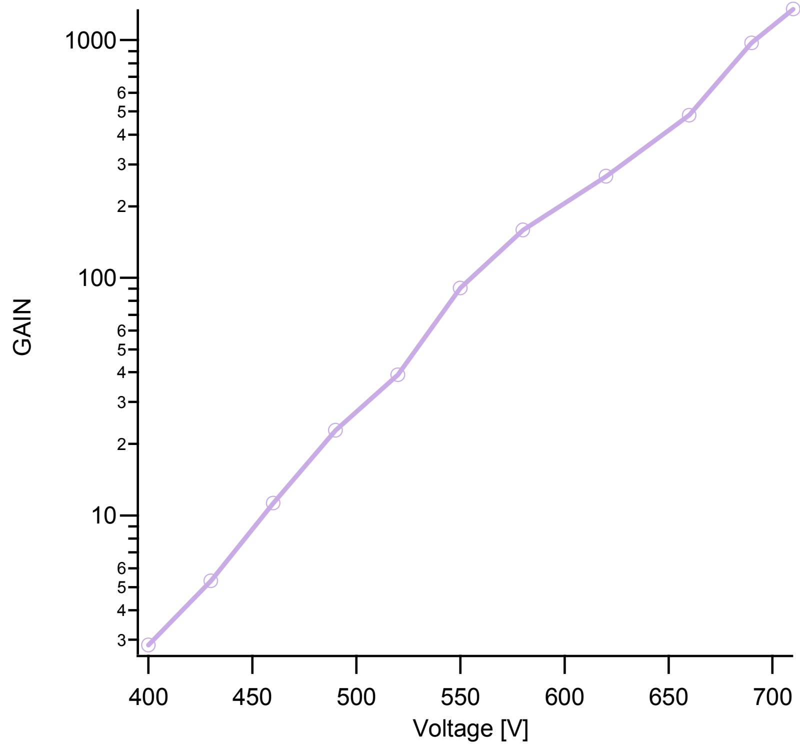

Figure 4-14 Gain calibration at 17.4 keV of the Proxitronic image intensifier coupled to the LN_2-cooled CCD camera

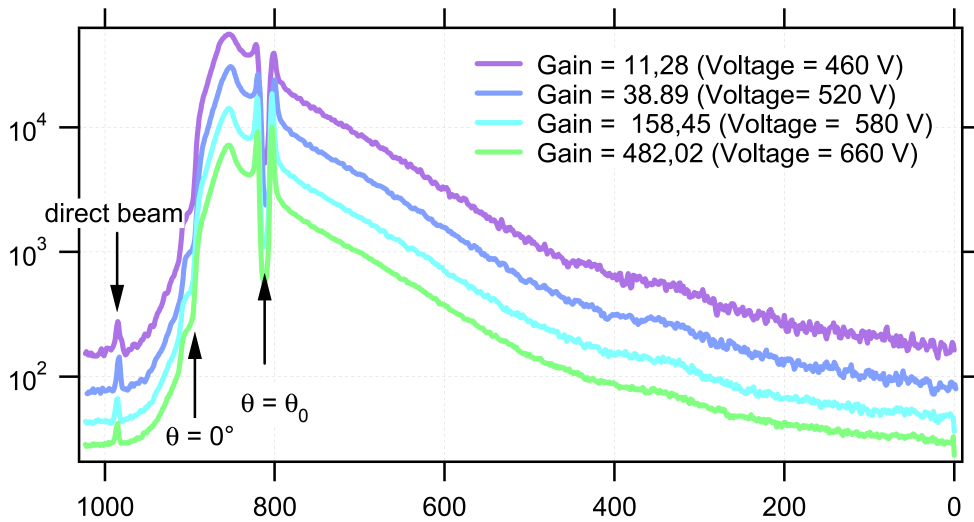

Figure 4-15: Influence of the gain on the scattering data. The three measurements were performed using different integration times (the horizontal axis is reversed).

A summary of the specifications is given in Table 4.2, while Fig. 4.17 shows the effect of the gain on the X-ray scattering patterns. As one can see, large gain values result,

on the one hand, in higher counting statistics, and on the other hand, in low signal-to-noise ratio in the regions of weak signal is (i.e., at large scattering angles).

Image and pixel size	72.6 mm x 18.2 mm, pixel size 70.9 μm 1024 x 256 pixels Total demagnification: 2.72
Line Spread Function	170 μm FWHM
Gain	2.8-1350 ADU/X
CTF	50% at 2.6 lp/mm
Readout noise	1.9 ADU/pixel (HT=0, τ_{exp} = 0.07 sec) 2.4 ADU/pixel (HT=4, τ_{exp} = 1 sec)
DQE	0.71 at 17.4 keV, HT=4, τ_{exp} = 1 sec, level = 23000 ADU
Dynamic range	15 bit

Table 4-2: Specification of the 2D detection system

As transmission detectors we used either a PIN-diode or an ionization chamber either with a mixture of 90% Ar and 10% Kr at a pressure of 1 mbar or in air (for TER measurements, i.e., with high signals). The PIN diodes is made of silicon 300 μm thick and 22 mm in diameter resulting in a transmittance T=71 % at 17.5 keV. The silicon sensor was enclosed inside an aluminum box with an Al window on each side to prevent the detector from seeing parasitic light. The ionization chamber is composed of a box of 150 mm long sealed with two polyamide windows, 0.05 mm thick, and of two electrodes to allow a discharge voltage of 1 keV. The current of both detectors was measured using a KEITHLEY pico-Ampere meter.

4.3 Instrument control and data transfer

For safety reasons the user cannot access the beamline experimental hutch when an experiment is performed, i.e., when in presence of X-rays. Therefore, the instrumentation located in the experimental station needs to be remotely controlled through a control software (called SPEC) installed on the main computer in the control room of the beamline, a SUN workstation. SPEC is a commercial, UNIX-based, software package for instrument control and data acquisition, that is widely used for X-ray diffraction experiments. The most recent developments were done in collaboration with the ESRF

computing staff (BLISS group). The communication between the central workstation and the main instrumentation is performed through VME communication cards, which enable to control almost any component needed during an experiment, providing driver routines have been written.

The CCD camera we used is connected to an interface card mounted in a PC located in the beamline control room. It can be controlled either from the PC using the PRINCETON's WINVIEW software or from the beamline workstation using SPEC or from both platforms. There are advantages for each case. As a general rule the PC and WINVIEW should be used when speed is important, i.e., when the integration time is below the msec range. The main reason is that, the data transfer to the workstation slows down the acquisition time. The use of SPEC is necessary when the CCD is operated in combination with the motion of a motor, e.g., to perform a scan or a macro and to allow the CCD image to be correlated with the monitor count (the transmission detector and/or the direct beam monitor). This is frequently the case during the experiments performed.

The simultaneous access to motors and counters required the development of a specific server (TACO device) to allow the control from the SPEC interface. This architecture allowed recording all the experiment parameters in the header of the image files.

Current detectors, such as PIN diode and ion chamber, are linked to the KEITHLEY 486 pico-Ampere meter connected to the central workstation via a GPIB interface and the Ethernet network. This is an extremely sensitive instrument capable of measuring weak currents (detection limit of 10 fA). When the silicon PIN diode is used, it is connected directly to the current input of the pico-Ampere meter without applying any voltage. In this way, the photocurrent is proportional to the photon flux over typically 9 orders of magnitude or more. When the ion chamber is used, a voltage of 1000 V is supplied externally, leading to flux sensitivity over 2-3 orders of magnitude.

A particular SPEC session was implemented for remote controlling the vacuum, the deposition and the erosion processes. Since the control of the other instruments, including the detectors, is done by independent SPEC sessions, the real time data acquisition and the deposition/etching process can be switched on and off independently. Generally, this is useful when a problem occurs in the chamber, e.g., when the plasma goes off and needs to be restarted, in case of CCD saturation when passing from substrate to film (overestimation of the integration time), or when the position of the beamstop needs to be corrected (tungsten growth).

Finally, two individual measurements ($R_{\Sigma}(t)$ and $\Pi(\theta_s, t)$) are controlled and stored on the hard disk of the main workstation.

4.4 Temporal scans

One of the most important parameters for a successful time scan is the choice of the integration time. Its value is determined by the synchrotron filling mode, the bandwidth of the monochromator, the chosen gain for the image intensifier, and by the counting statistics needed. Generally, the change of density when passing from the Si substrate to the film leads to a variation of the intensity up to 2 orders of magnitude at the beginning of growth. Thus, it is important to estimate the final average intensity reaching the CCD detector before launching the measurements, otherwise, the images will progressively get overexposed and the scan will have to be interrupted. The integration times are ranging from 0.1 s to 1 s in the TER region and from 5 s to 30 s in the OTER region, when the multilayer monochromator is used in combination with a double Si crystal monochromator ($\Delta E / E$ ~ 10^{-4}), with a gain G= 483 and when the ESRF ring current is 200 mA. When using a beamline equipped with an insertion device such as an undulator, the intensity can be higher than for a BM source by three orders of magnitude, leading to integration times in the millisecond range. That would open up the possibility of studying details of the deposition process at the onset of growth. One could also study the sputter growth of films the way it is done for industrial applications, i.e., at rates more than nanometer per second.

4.5 Data correction

There are several factors [85], that need to be taken into account to correct the reflectivity and scattering data before performing a quantitative analysis. First, the intensity of the synchrotron X-ray beam decreases gradually between subsequent re-injections due to the decay of the electron beam in the storage ring. Therefore, we use an additional transmission detector placed downstream the collimating slits at the entrance of the vacuum chamber. In this way, the intensity of a primary beam is monitored continuously. Then, the signals of the detector measuring the reflectivity and the 2D CCD camera measuring the angular distribution of the scattered radiation are normalized by the monitor. Second, the response of CCD camera varies over the entrance aperture. To illustrate this effect we show, in Figure 4-16 and Figure 4-17 flat field images obtained with two different image intensifiers, under uniform illumination of the CCD field of view (FOV). Two line profiles along the horizontal are also shown in Figure 4-18 (i.e., along the scattering plane). As one can see, the response of the detector can be quite different depending on the optical design. It is crucial to correct the scattering data for it. On the other hand, the newest intensifier showed an excellent uniformity over the entire FOV.

The flat field measurements were performed following a standard method, described in ref. [86]. The method consists of recording the fluorescence signal induced by the interaction of an X-ray beam with a Zr sample having an X-ray emission line at 17.66 keV ($K\beta_1$)[23]. The fluorescence was proved to be a good way of obtaining a uniform and flat illumination over a wide FOV [86], particularly if the distance between the sample and the detector is large. In practice, a compromise on the distance is to be found since the exposure time increases quickly with the distance. The high sensitivity of the CCD setup allowed us to fix this distance to 1.5 m. We have carried out the measurement placing the detector perpendicularly to the beam direction to avoid the recording of the primary beam.

Figure 4-16: Flat field obtained with the DELFT image intensifier: the illuminated area is limited due to an inadequate optical coupling.

Figure 4-17: Flat field image with the PROXITRONIC image intensifier. The design of the optical coupling allows the image to illuminate the whole CCD.

[23] The energy used in our experiments is very close to this value, i.e., E=17.5 eV.

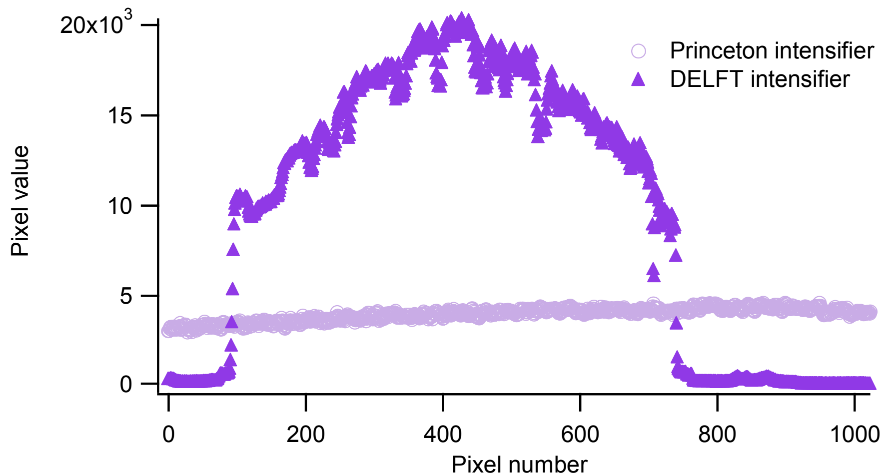

Figure 4-18: Flat field response over a line profile from the image of Figure 4-17 and Figure 4-18.

Finally, the dark image, corresponding to the noise of the CCD camera, was recorded[24] before and after each experiment, and subtracted from the experimental data.

The last unwanted contribution to the experimental data is the effect of the polyamide windows interposed between the sample and the detector/source. When illuminated with X-rays the amorphous structure of the polyamide foil diffracts sharp peaks that enhance the intensity along a diffraction ring. This intensity is registered by the CCD superimposed to the scattering from the sample. This effect is called Small Angle X-ray Scattering (SAXS). Tests were carried out to determine the effect of all windows present in the beam. It turned out that only the polyamide preceding the sample was affecting our data, the net effect being a local increase in the scattering intensity. A series of exposures was performed by adding polyamide foils, each 0.05 μm thick, to evaluate the effect on the scattered intensity. The results shown on Figure 4-19 indicate that this effect is simply additive with the Kapton thickness, and stationary as a function of time. A simple algebraic subtraction of this contribution from the CCD spectra was finally performed.

It is important to notice that such an effect is only visible when the scattered intensity is extremely weak. During our experiments, that case was realized only for highly smooth silicon substrates measured in the OTER region. When depositing a high-density film, this effect becomes negligible, as the overall scattered intensity increases proportionally to the layer reflectivity. One way of avoiding this problem would be to install a pair of slits inside the vacuum in-between the window and the sample. Such an option is envisaged for implementation in a near future.

[24] The dark image is obtained by recording an image without sending the X-ray beam on the CCD.

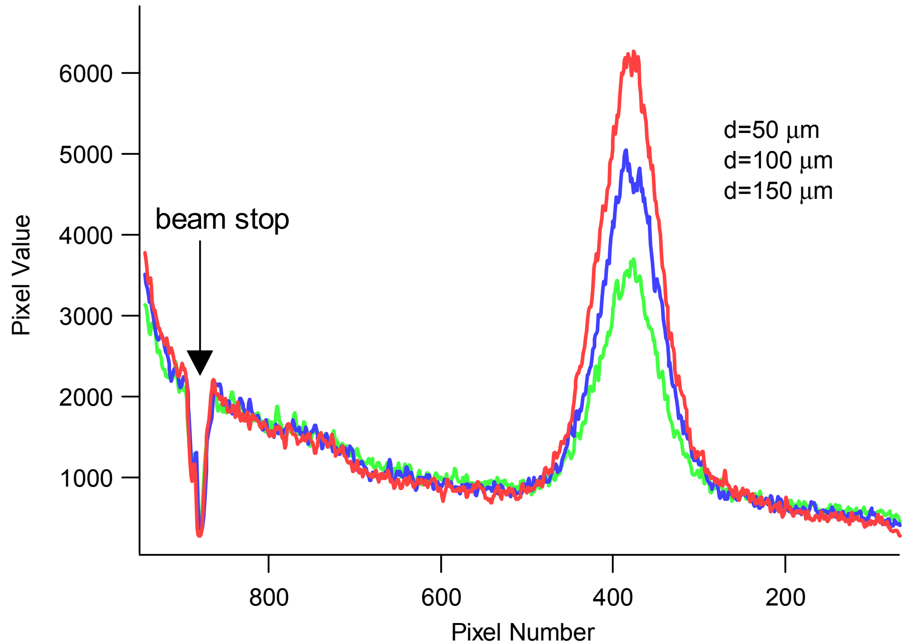

Figure 4-19: Influence of the polyamide SAXS signal on the XRS intensity for a Si substrate, for polyamide thicknesses varying from 50 μm to 150 μm.

4.6 Experimental measurements and normalization

To study the effect of a given process on a surface, we perform a scattering experiment that consists of monitoring the full profile of diffuse scattered intensity as a function of time. A first semi-transparent detector monitors the total integrated reflected intensity while a 2D detector measures a 2D scattering diagram simultaneously.

To avoid experimental artifacts, the effects described in section 4.5 are removed in a normalization procedure. The following sections will now describe the way the data correction (to remove the artifacts) and normalization (to obtain R_Σ and $\Pi(\theta_s, t)$) are carried out.

4.6.1 Specular reflectivity

The reflectivity of a mirror is defined as the ratio between specular reflected intensity and primary beam intensity. The measurement of the primary beam is performed before and after any time-scan to avoid any effect due to misalignments during the scan. The data acquired during a real time scan is also corrected to compensate for the gradual decrease of the incoming beam. For this purpose, an additional transmission detector (ionization chamber) is placed between the collimating slits and the sample to monitor the intensity of the primary beam. At any time *t* during the scan, the monitor measures a

current $I_m(t)$ (*m* standing for *monitor*), while the transmission detector placed after the sample measures the total reflected beam intensity $I(t)$. The normalized total reflectivity can then be obtained by the following operation:

$$R_\Sigma(t) = \frac{I(t)/I_m(t)}{I_0(\tau_0)/I_{0m}(\tau_0)} \tag{3.40}$$

Here, $I_0(\tau_0)$ is the current corresponding to the primary beam normalized to its monitor $I_{0m}(\tau_0)$ at time τ_0. The latter is measured before and after each time-scan. In the usual case the average value is used.

4.6.2 Diffuse scattering measurement

To extract information about surface roughness it is necessary to determine the diffuse scattering diagram. Experimentally, this is not as evident as it may appear at the first glance.

The bi-directional scattering profile $\Phi(\theta,\varphi) = (1/W_{inc})(dW_{scat}/d\Omega)$ describes the power of radiation dW_{scat} scattered within a small solid angle $d\Omega$ and normalized to the power of the incident beam W_{inc}. The scattering diagram depends on the two scattering angles: the angle θ referencing angles in the scattering plane (vertical in our case) and the azimuth angle φ referencing angles in the plane of the sample surface. Let $(\delta I)_{i,j}$ be the signal detected by an individual pixel with coordinates (i,j) during exposure time τ. The radiation power corresponding to this signal is $(\delta W)_{i,j} = K(\delta I)_{i,j}/\tau$, where K is an unknown, normalization coefficient, although supposed to be identical after flat field correction, for all pixels. Then, the scattering diagram is written in the following form:

$$\Phi(\theta_i,\varphi_j) = \frac{K}{W_{inc}\tau}\frac{(\delta I)_{i,j}}{\delta\Omega} \tag{3.41}$$

The main problem of application of Eq. (3.41) is that we do not know the acceptance aperture of the individual pixel $\delta\Omega$, because the CCD camera is a rather complicated device consisting of several consecutive transmission channels. Hereafter we describe a simple approach to find $\delta\Omega$ directly from scattering data that is not limited to the CCD camera, but could be applied to any detecting system.

Suppose we measure, an angular distribution $\Phi_0(\theta,\varphi)$ of the reflected beam intensity without a beamstop, i.e., the sum of the specular reflected and the diffusely scattered components. Evidently, the integral of the total intensity distribution over a solid angle is nothing but the total reflectance, i.e., $\int \Phi_0(\theta,\varphi)d\Omega = R_\Sigma$. Thus, we obtain the following normalization condition:

$$\frac{K}{W_{inc}\tau_0} \cdot \frac{\sum_{m,n} (\delta I_0)_{mn} \cos\theta_m \Delta\theta \Delta\varphi}{\delta\Omega} = R_\Sigma \tag{3.42}$$

Where the summation is over all the detector pixels, τ_0 is the exposure time, and $\Delta\theta$ and $\Delta\varphi$ are the angular distances between neighboring pixels in the vertical and horizontal planes. The values of $\Delta\theta$ and $\Delta\varphi$ are known, because the number of pixels and the total size of entrance aperture are known. Using Eq. (3.41) and (3.42) we can express the scattering diagram in terms of quantities measured in the scattering experiment:

$$\Phi(\theta_i, \varphi_j) = \frac{R_\Sigma}{\sum_{m,n} (\delta I_0)_{mn} \cos\theta_m \Delta\theta \Delta\varphi} \cdot \frac{\tau_0}{\tau} \cdot (\delta I)_{ij} \tag{3.43}$$

Recall that $(\delta I_0)_{ij}$ is the signal detected by an individual pixel during an exposure time τ_0 in an experiment without using beamstop, while $(\delta I)_{ij}$ and τ are the same quantities in an experiment with a beamstop. First, we perform real-time in-situ measurements of the scattering distribution during film growth or erosion with the use of a beamstop. The beamstop blocks the intense specular reflected beam and allows the long exposure time τ necessary for detecting the far wings of the very low intensity of the scattering diagram. Then, we measured the scattering distribution without beamstop with exposure time τ_0 sufficiently short to avoid overexposing the CCD. This data are then used to normalize the previous scattering diagram. The detector signals δI_0 and δI must also be corrected for the decay of the primary beam, flat field, and dark image as described above.

Since the width of the scattering diagram is much narrower in the azimuth plane, we can increase the scattered intensity by using a rather wide beam in the horizontal plane. This permits to decrease the exposure time down to practicable values. Hence, the scattered intensity was integrated over the azimuth scattering angle $\Pi(\theta) = \int \Phi(\theta, \varphi) d\varphi$. Therefore, instead of Eq. (3.43), we obtain the following expression for the integrated scattering diagram

$$\Pi(\theta_i) = \sum_j \Phi(\theta_i, \varphi_j) \Delta\varphi = \frac{R_\Sigma}{\sum_{m,n} (\delta I_0)_{mn} \cos\theta_m \Delta\theta} \cdot \frac{\tau_0}{\tau} \cdot \sum_j (\delta I)_{ij} \tag{3.44}$$

Where the summation over j means a summation along the horizontal pixel direction. This is the expression we used for experimental data processing.

4.7 Instrument performance and application

The apparatus described here has been used over more than a year to study sputter growth and ion beam etching. Some of the most significant measurements are presented in this section to illustrate its performance in terms of spatial and temporal sampling.

Figure 4.20 shows the temporal evolution of the specular reflectivity as a function of time of a W film growing over a Si substrate. Two measurements are presented. One is performed at an angle of incidence of 0.15°, i.e., in the region of total external reflection (TER) and the other one at an angle of 0.5°, i.e., out of it (OTER). The curves always proved deposition rates in the pm/s range, therefore demonstrating a pm sensitivity of the apparatus. The X-ray intensity was measured at equal time intervals of 1 s and 10 s, in the TER and OTER regions, respectively (in both cases the gain was 483). The reflectivity function was modeled assuming a linear relation between layer thickness and time. The excellent linearity measured also indicated an excellent stability of the deposition system within the time of the measurement.

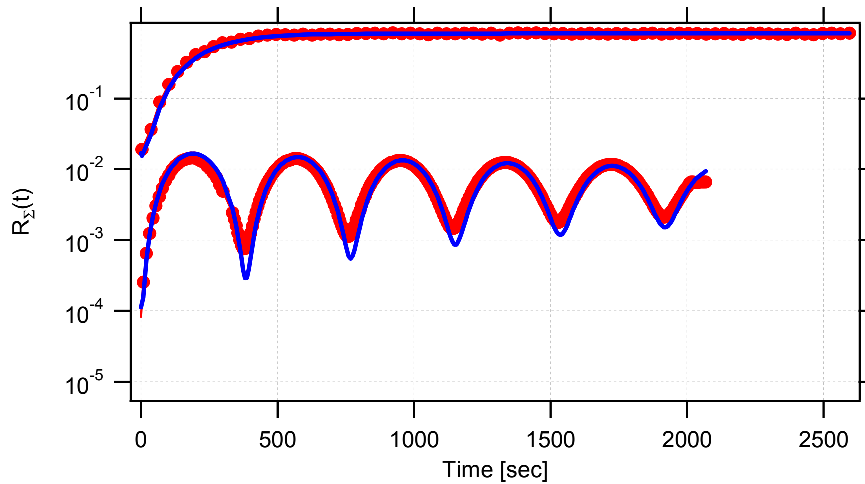

Figure 4-20: Reflectivity versus deposition time for a tungsten film growing onto a Si substrate. The in situ measurements were performed at a grazing angle θ_0 of 0.15° (upper curve) and of 0.5° (oscillating curve). The X-ray energy was E= 17.5 keV.

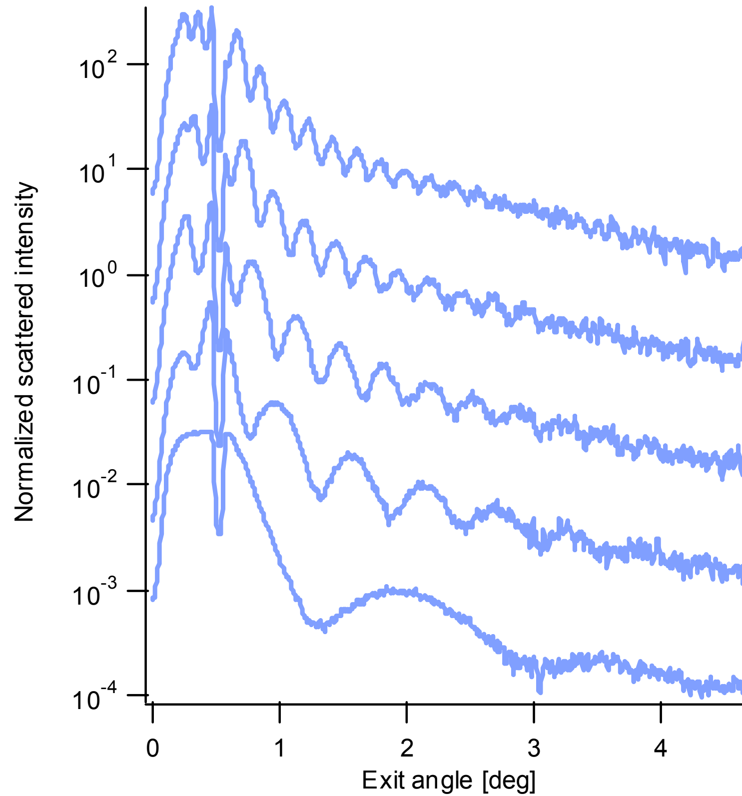

Figure 4-21: Scattering diagrams measured at progressive film thickness and in correspondence of the peaks of $R_\Sigma(t)$ (see OTER measurement in Figure 4-20). The curves are rescaled vertically for clarity.

For each point of the reflectivity curves, see Figure 4-20, a correspondent scattering diagram, see Figure 4-21, was also measured using the procedure presented in the previous sections. For clarity, we show only few of them in Figure 4-21, namely the ones measured in correspondence of each peak of the reflectivity curve. The curves were obtained by horizontal binning of 2D images following the normalization procedure described in section 4.6. The range of measured scattering angles corresponds to a spectral bandwidth extending from 4.6×10^{-2} to 3.1×10^{-4} nm^{-1}.

The appearance of fringes in all the scattering diagrams is a clear indication of the development of correlated roughness at low scattering angles (low spatial frequencies) in all curves. However, this behavior is maintained up to a certain spatial frequency, located in the middle angles region between 2°-3°, and is clearly dependent on the film thickness. This remarkable feature accounts for the evolution of the roughness conformity in according to the film thickness and has been predicted theoretically [14]. Note that the total reflectivity measured in TER cannot be used generally to extract the variation of the film thickness versus time. However, this curve contains precious information. It can be used to identify the presence of high spatial frequency roughness. It can serve as a monitor for the variation of film density occurring during the deposition.

Eventually, the excellent agreement between Fresnel theory and the reflectivity data presented here demonstrates that small-scale roughness is negligibly small. Therefore, the analysis of the scattering diagrams can be performed without any model of film growth and of correlation function but simply obtained using the PT approach.

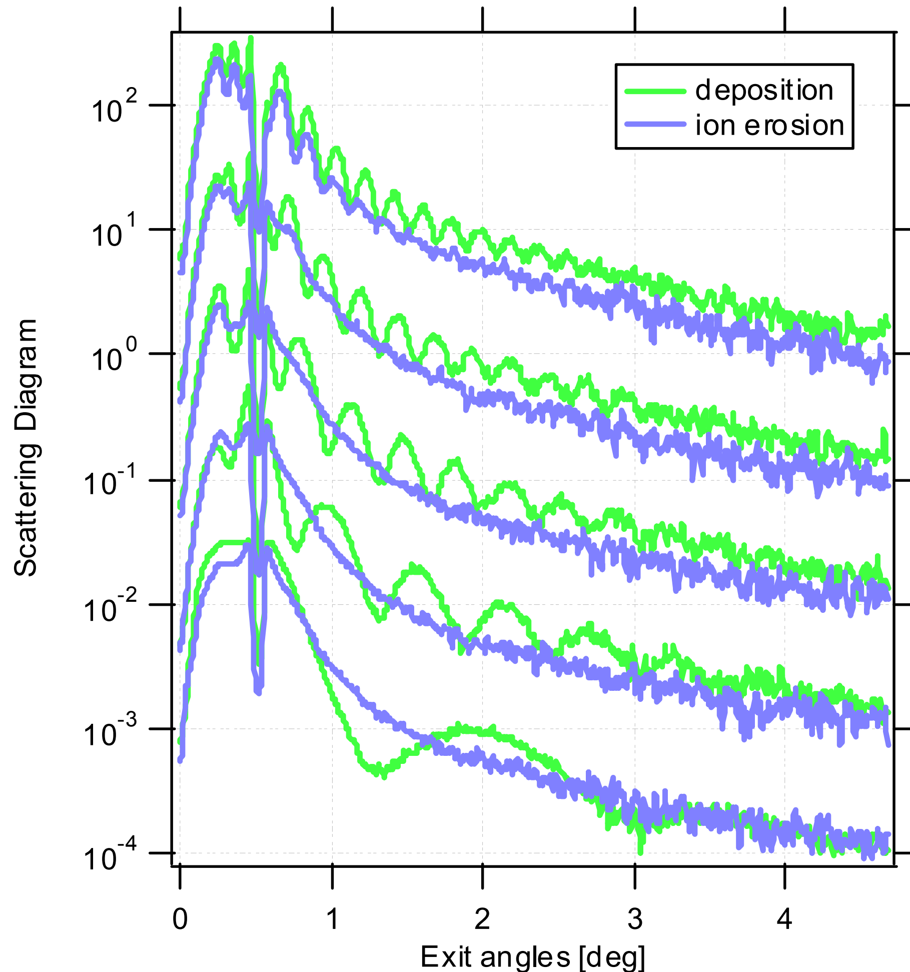

Figure 4-22: Evolution of the scattering diagrams measured during sputter deposition and subsequent erosion of a tungsten thin film

To demonstrate the sensitivity of the instruments to the partial correlation, occurring during different surface processes, we show in Figure 4-22 a comparison between scattering diagrams measured during sputter deposition, the same reported in Figure 4-21, and the ones at correspondent thickness measured during subsequent film erosion[25]. The measurements reveal that the diffuse scattering undergoes a non-symmetrical behavior, which is irrespective of the thickness changes. During deposition,

[25] The film was removed using 1 keV Ar bombarding ions.

the random arrivals of atoms on the substrate lead to the development of roughness that is correlated with the starting topography, while, during erosion of the same film, this correlation disappears rapidly after few monolayers of material. This point will be further discussed in Chapter 6.

In conclusion, this section proved that all the features necessary to evaluate the performance of a synthesis process are accessible in real time and can be used to extrapolate detailed information about the validity of the growth erosion theory presently used. This information includes the evolution of film thickness, conformity, roughness and film density. A detailed comparison of our finding with theory will be given in the following sections.

Chapter 5 Real-time studies on film growth

This section presents examples of studies of tungsten film growth performed using real time reflectometry. These examples illustrate unique characteristics of our instrument: the combined temporal and spatial resolution (vertical and lateral), the sensitivity at controlling roughness and conformity during film deposition.

Finally, after a critical discussion of the method, a strategy of development for optimizing the surface roughness on mirrors for SR applications is presented.

5.1 Substrate characterization

Before performing a real time experiment, a characterization of the morphology of the initial substrate is desirable. As discussed in section 0 rough surfaces can be characterized using various techniques including SPM and XRS. All these techniques proved to give excellent agreement in the regions where their measured PSD would overlap. This was verified for several materials systems and surface roughness distributions. Since an excellent review on this subject can be found in ref. [51], a comparative analysis of these techniques was not been considered as a priority. Thus, for the analysis hereafter, AFM and XRS methods will be assumed exchangeable for substrate characterizations.

The characterization of the substrate is probably one at the major limitations of the work presented here. One reason of this limitation is a very small value of the critical angle for Si: ~0.1 degree at X-ray energy of 17 keV. When operating in the TER region it was difficult to define the incidence angle accurately. When operating in the OTER region, despite a greater angle, the study remained difficult due to a reduced intensity ($\propto 1/\sin(\theta_0)^4$) and to the effect of a transition layer (native oxide) that would complicate the quantitative analysis of the substrate. Moreover, when the intensity is low, the spurious contribution of the polyamide windows to the measured scattered intensity makes the data corrections problematic. Finally, the CCD camera was optimized for an energy range of 17 keV, which makes it difficult to operate at a lower energy, i.e., at larger

critical angles. Therefore, the substrate characterizations were preferably performed using AFM and standard ex-situ reflectometry (using a synchrotron radiation reflectometer).

Two types of samples, which would differ by their surface quality, were used during our experiments:

- Silicon samples cut out of the same wafer, 150 mm diameter, 0.6 mm thick, had a size of ~15 mm x 40 mm, and were, therefore, statistically identical. They were characterized by ex-situ reflectometry and by AFM.
- Highly polished Si crystal, 25x50 mm^2, 7 mm thick, polished together in the same butch by the General Optics (GO) company. They were characterized by AFM using different scanning windows.

In all experiments the silicon samples were used directly, i.e., we did not remove the native oxide layer. Prior to deposition, a nitrogen gas jet blown on the surface removes particles. In both cases, the substrates were characterized prior to deposition to confirm they had identical statistical roughness parameters. PSD calculations were finally carried out on both AFM images and XRS measurements.

When analyzed with AFM, the samples were measured in tapping mode with scanning windows of 8 μm [256 x 256] pixels for sample from GO and 10 μm for the silicon wafers. These measurements were finally combined with other characterizations with smaller windows, 1 μm size, keeping the same number of sampled points.

The AFM topographs of GO sample and Silicon wafers are shown in Figure 5-1 and Figure 5-2, respectively.

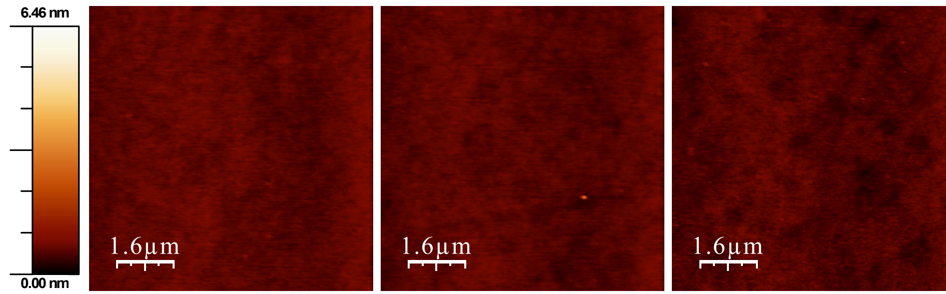

Figure 5-1: AFM topographs for three samples from GO polished following the same procedure. The scanning window is 8 μm with 256x256 points, the area rms roughness is σ=0.16 nm.

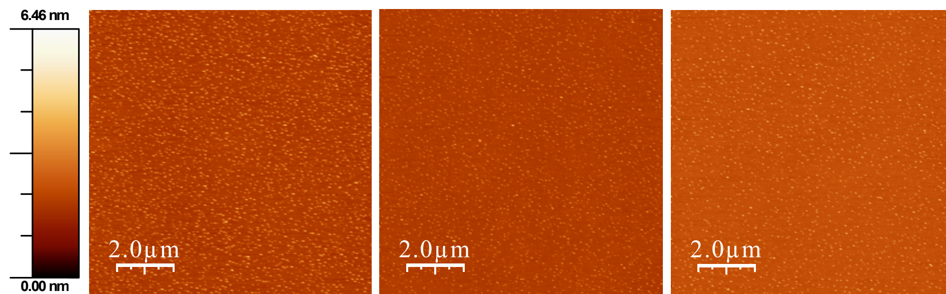

Figure 5-2: AFM topographs for three statistically identical Si wafers. The scanning window is 10 μm with 256x256 sampled points, while the area rms roughness is σ=0.77 nm.

The images were corrected only by a flatten procedure to remove the tilt and offset from the measured data. The rms roughness obtained from a statistical analysis of the three images, i.e., by averaging the roughness values, was of 0.16 nm in the case of the GO substrate and of 0.77 nm for the wafers. The scanning windows were respectively 8 and 10 μm.

From the AFM measurements performed on the GO samples (8 μm and 1μm micron) we could derive the 2D PSDs (after windowing) over a spectral frequency range extending over two order of magnitudes, therefore fully covering the frequencies range obtained with the in situ XRS measurements. The resulting PSD is shown on Figure 5-3. The two PSD curves are superimposed and show a power law behaviour of the form $PSD_{2d} = K / f^{2\alpha+2}$ with roughness exponent α=0.14 and $K = 1.3 \cdot 10^{-4}$ which leads to roughness value of 0.070±0.005 nm[26] within a spectral bandwidth [3.05 10^{-4}, 4.62 10^{-2}] nm^{-1} accessed in the experiments described hereafter.

[26] The roughness error is estimated assuming an error on the estimation of the PSD function of 10%.

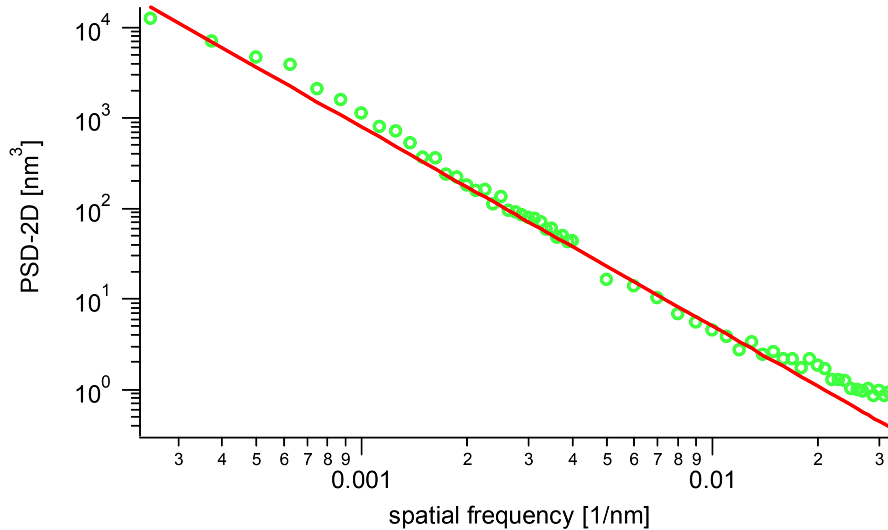

Figure 5-3 PSD_{2D} of the silicon wafer of figure 5.1 measured by XRS.

The substrate parameters of the Si wafer were extracted from scattering measurements performed prior to deposition using a diffractometer installed in the EH1 of the BM5 beamline at an X-ray energy of 17.5 keV. The measurements consisted in performing a 2θ scan using a grazing angle θ_0=0.1 deg. (TER region) and scanning angles θ_s between 0° and 3°. The PSD calculated using formula (3.20) is shown in Figure 5-4 superimposed with a power law with a roughness exponent α=0.4.

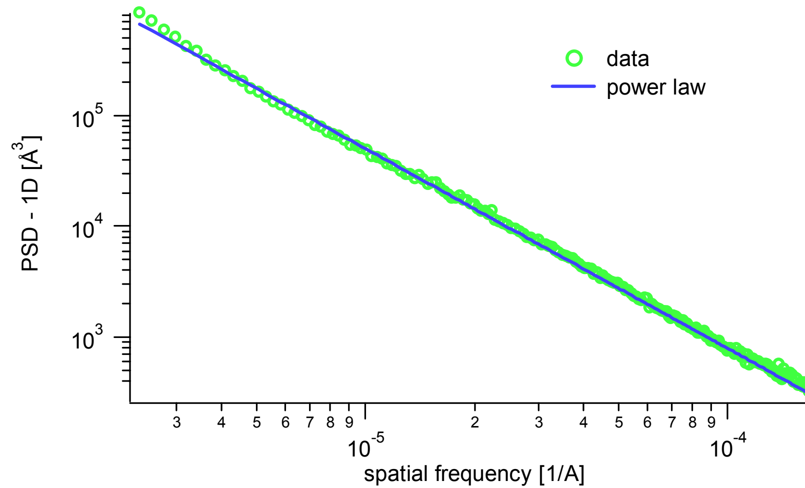

Figure 5-4: PSD_{1D} of the silicon substrate of figure 5.2 measured by XRS.

Therefore, within the measurable spatial frequency range, both samples could be described by a 1-dimensional PSD-function having the form of a fractal power law $PSD(f) \sim 1/f^{2\alpha+1}$, with a Hurst exponent α= 0.4 (wafer) and 0.14 (GO substrate). Moreover, AFM images acquired for different samples clearly showed that they had

identical statistical properties. Finally, the plots in Figure 5-3 and Figure 5-4 proved a power law behaviour and the excellent agreement between measured data sets.

Let us conclude this section with remarks concerning the Si wafer substrate. As one can see from the AFM images of Fig. 5.2, a dot-like structure is present, which is not observed on the GO substrate. This morphology could be due to chemical contamination connected to sample aging and/or exposure to air. While this structure is visible with AFM, it does not appear on scattering measurements, the power law behavior proving this statement. On the other hand, the spectral analysis performed on the AFM topographs results in PSDs that are far from being fractal like or monotone function of the spatial frequency *f*. This type of morphology makes the Fourier analysis complex and probably meaningless. On the other hand, the AFM and XRS method are based on different physical phenomena: attractive and repulsive molecular interactions and the diffraction of electromagnetic radiation by an inhomogeneous interface. These methods provide different experimental information, namely, a two-dimensional surface relief in atomic-force microscopy and an angular distribution of the intensity of scattered radiation in the X-ray scattering method. In the second case, surface features are averaged out over large sample area and the sensitivity to the presence of local defects is weak, i.e., leads to low-density contrast, and insignificant contribution to the scattering intensity.

Therefore, for further data processing on the wafer samples, we only considered the results obtained from XRS measurements, keeping the AFM images for qualitative discussion only.

5.2 Determination of film thickness and optical constants

We determined experimentally the film thickness and the optical constants during each experimental session because this information is needed for the analysis of the scattering data. When analyzing XRS diagrams they enter as parameters in the data processing and during the extraction process of the PSD function. This is why we present this section before discussing the real time scans.

In-situ reflectometry is a technique that can access film thickness, density, and interface roughness independently when roughness is not too large, with pm sensitivity (on film thickness). This method was developed first, by several authors [87-89], who had the necessity of depositing high quality multilayers or thin films. In this case, a thin layer with high-Z layer is grown over another one with dissimilar density, and its reflectivity is monitored (at fixed angle). The high-Z layer is grown until the intensity reaches a maximum value. At this point ideally the low-Z material starts to be deposited until the intensity decreases. The deposition of the low-Z material is stopped at the minimum, then

the growth of the high-Z starts again, and so on. The overall intensity rises up to reach a saturation level, determined by the absorption of the spacer material (see Fig. 1.4).

The method developed during this work follows this simple idea. The only difference is that not only specular reflectivity is measured, but the sum of reflectivity and scattering, i.e., $R_\Sigma(t)$. In the smooth surface limit (SSL), R_Σ is expected to follow the Fresnel behavior. Here, the film thickness and the optical constants (see paragraph 3.1.2) can be easily extracted without having to account for the roughness evolution.

For instance, Figure 5-5 shows a measurement of R_Σ during tungsten deposition onto Si wafer substrate performed at 17 keV and grazing angle θ_0=0.5° (θ_{cr}~0.25°). The sputtering target was placed as usual at 150 mm from the substrate and the sputter gas was pure (99.999%) Argon set at working pressure of 9.3 10^{-3} hPa using a flow rate of 5 sccm. The discharge was realized using a bias voltage of 370 V resulting in a total ion current of 60 mA.

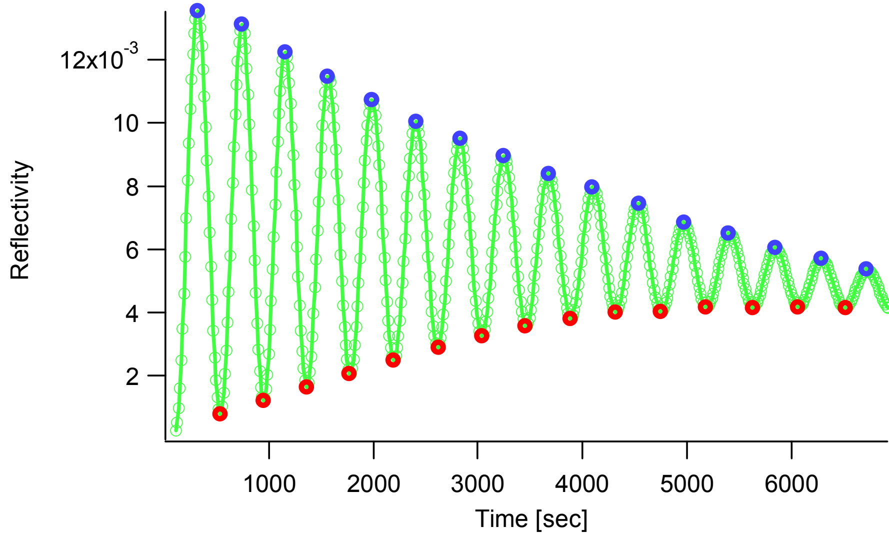

Figure 5-5: In situ reflectivity versus time obtained from a tungsten layer grown onto a Si (100) substrate. The grazing angle of incidence was 0.5. Each dots denotes a well-defined layer thickness.

Figure 5-5 shows intensity oscillations as predicted by Fresnel theory. Each maximum and minimum on this curve, appears when the phase factor appearing in Eq. (3.12) fulfills the following conditions:

$$2k_1(\theta_0)d = 2k\sqrt{\varepsilon_f - \cos(\theta_0)}d = (2M+1)\pi \tag{5.1}$$

for maxima and

$$2k_1(\theta_0)d = 2k\sqrt{\varepsilon_f - \cos(\theta_0)}d = (2m+2)\pi \tag{5.2}$$

for minima. Here the index M,m = 0, 1, …, N-1 and N is the number of maxima and minima in the measured reflectivity curve. This relation suggests a simple graphical method to determine the layer thickness evolution from the measured R(t). Using (5.1) and (5.2), the thickness corresponding to each peak order (M and m) can be plotted as a function of the time at which the peaks are found. Another option consists in fitting the specular reflectivity with the Fresnel formula and considering $h \equiv h(t) = a + vt$ as unknown fitting function (where a and v are fitting parameters), and v is nothing but the deposition rate of material.

The graphical method proposed is only an approximation because the position of the peaks generally depends on the optical constants (ε_f) of the film, which could also vary during deposition. However, in many practical applications, the density variation is negligible and the graphical method can be applied.

As an example, we analyzed Figure 5-5 following this simple procedure. The results are shown in Figure 5-6. The red and blue dots correspond to the thickness extracted from the position of the maxima and minima values, respectively, and calculated using (5.1) and (5.2). A linear fit of the data has been superimposed. From the slopes of this curve, we derive the average deposition rate. The excellent agreement with a linear law denotes the good stability of the deposition system and will allow us to assume a linear deposition rate in further data processing. Notice that, such an assumption is often made without a detailed proof, especially in publications on work performed ex-situ. While this is often the case (first approximation), measurements presented in further sections will show that this is far from being valid for any process. Examples include the ion-assisted deposition of thin film, and the early stage of the deposition (island regime)[27].

[27] It is worth noting that all the values found for the line offset (parameter *a*) during the fitting of R_Σ yield negative value while at thickness h=0 should correspond to time t=0. We conclude that at small thickness the deposition rate cannot be linear.

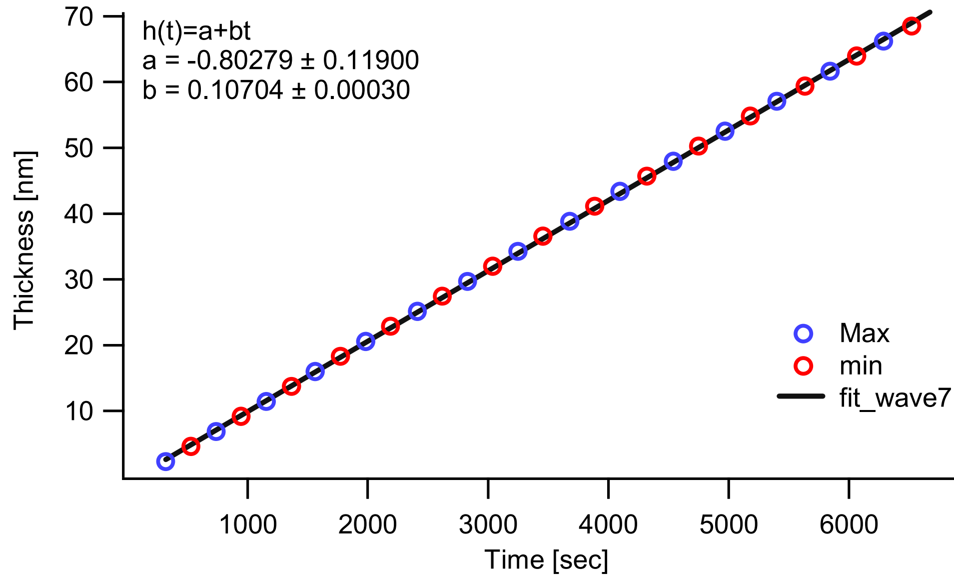

Figure 5-6: Layer thickness versus time extracted from the position of the extrema in the previous graph.

With the procedure described we have studied, for example, the dependence of the deposition or erosion rate and of the film density as a function of the magnetron target current, the bias voltage, the ion energy, etc.

For instance, the results of the analysis of the relation between the deposition rate on a W film and the target current are presented in Figure 5-7. During the same experiment we measured the variation of the reflectivity with time for different magnetron target currents, namely 30 mA, 50 mA and 100 mA. Figure 5-7 shows the increase of the frequency of the oscillations in the reflectivity curve (hence, of the deposition rate) with increasing target current. Basing on Figure 5-7, we additionally derived the relations between film thickness and deposition time and between deposition rate and target current. They are presented in Figure 5-8. The deposition rate proved to vary linearly with increasing target current.

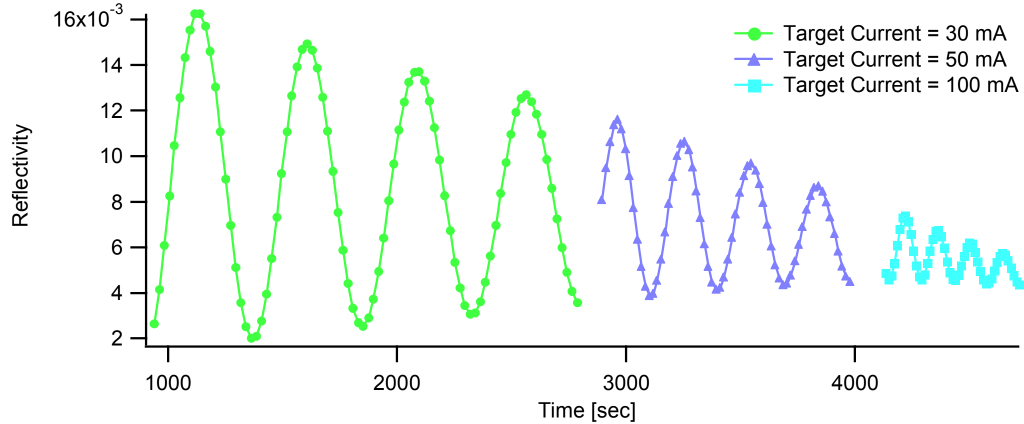

Figure 5-7: Specular reflectivity measured with different target currents onto the Si same substrate

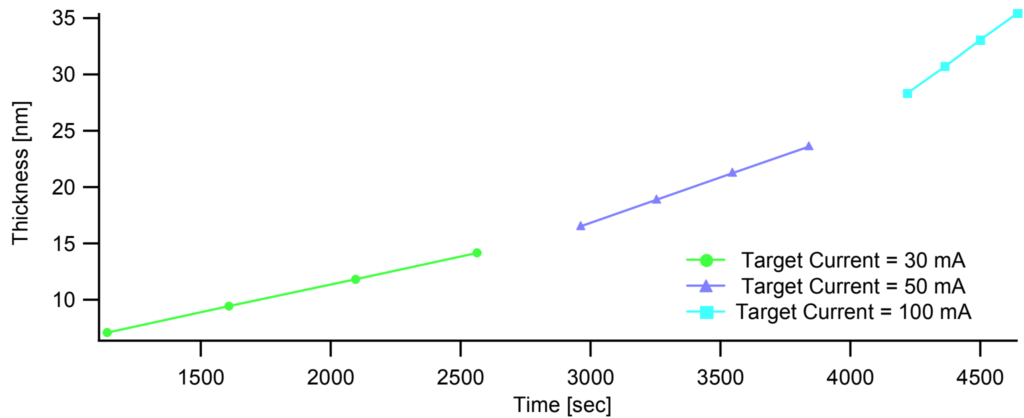

Figure 5-8: Thickness versus time obtained for three different target currents: 30 mA, 50 mA and 100 mA. The calibration curve for the sputtering system obtained from this curve is reported on Figure 4-6.

It is worth noting that, when performed ex-situ, such an analysis would be very labor intensive, as it would require the preparation a set of samples, on which subsequent $\theta/2\theta$ scans would have to be performed. Moreover, its accuracy is determined by the possibility of performing a series of identical experiments.

In Section 5.3 the methods used to extract experimentally the optical constants will be illustrated. The optical constants are generally obtained by measuring the specular reflectivity as a function of the angle θ_0, prior to deposition (bare substrate) and after deposition (thin film).

5.3 Real time analysis in the case of a thick film

As discussed earlier our measurement technique allows to measure in parallel the variation of the differential scattered intensity (DSI) and the specular reflectivity.

Although the DSI can yield the PSD function and, in turn, an accurate description of the roughness of the surface under investigation, the less-sophisticated TIS measurements have still some interest. This method was successfully employed in several contexts, from radio waves (for studying of their reflection by the surface of the earth, the troposphere, the moon and the planets) to visible light (for studying roughness at large spatial scales in optics) [59, 90]. These measurements have the advantage to relate easily to the surface quality and to provide a rapid control of a process. In the following example, we analyze the variation of TIS with time measured simultaneously to R_Σ.

We recall here that for a single surface the TIS is the ratio between scattered power to the totally reflected one. When SSL is valid, this ratio is independent of the surface statistics and particularly by the distribution of the roughness. In this limit, roughness can be related to TIS measurements through the expression $TIS(t)/R_\Sigma(t) \sim (2k\sigma(t)\sin(\theta_0))^2$ where $TIS(t) = \int_0^{\theta_{\max}} \Pi(\theta,t)d\theta$.

The aim of this section is to study how the TIS signal varies over the large range of thicknesses probed, up to ~70 nm. Thus, we will be able to estimate the range of thicknesses where the roughness variation remains small and, in turn, acceptable for the perturbation theory to be valid (SSL). In Figure 5-9, we plot together the Figure 5-5 and the corresponding TIS curve.

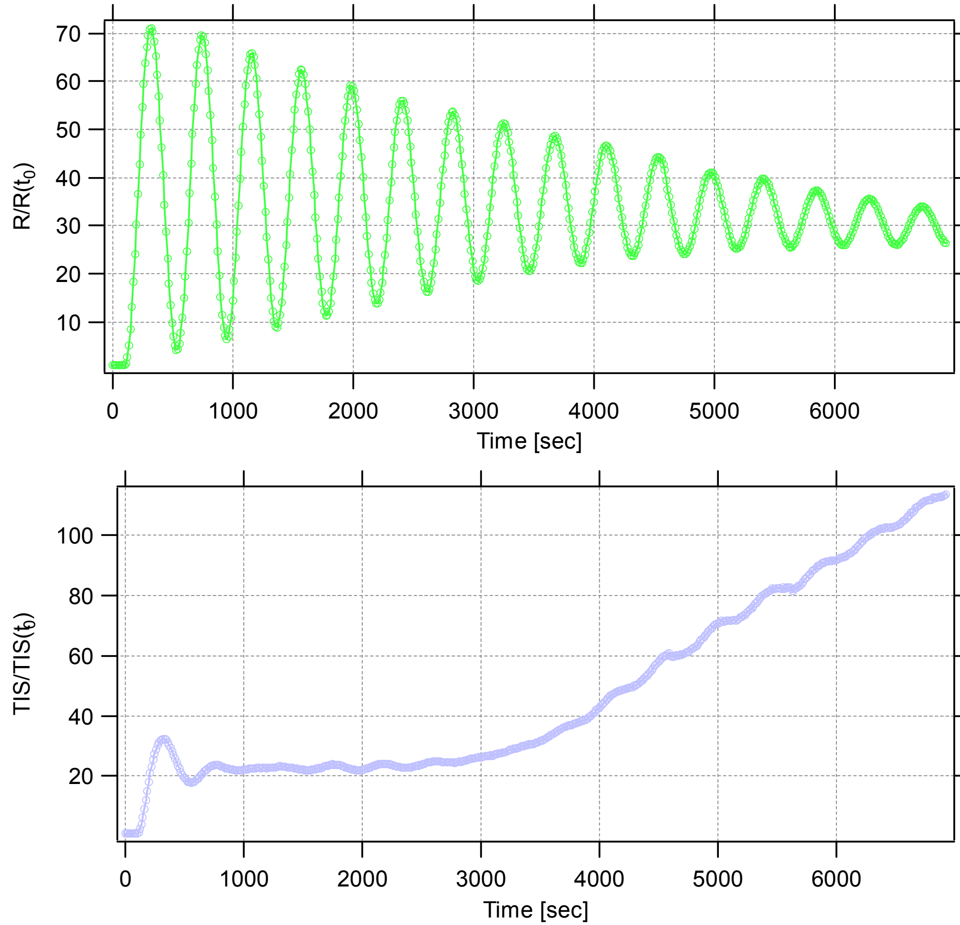

Figure 5-9: $R(t)/R(t=0)$ *(top) and* $TIS(t)/TIS(t=0)$ *- OTER measurements.*

The TIS measurements, normalized to the initial integrated intensity, are plotted as a function of the growth time t in Figure 5-9 (bottom), with the reflectivity acquired simultaneously (Figure 5-9, top). The oscillations appearing in the TIS signal are nothing, but interference effects arising as the fields scattered by the substrate and the film surface mix up during signal integration. These oscillations do not represent a roughness behavior: they only reflect an interference effect. On the other hand, roughness is expected (see sec. 3.2) to follow a similar trend, i.e., to increase with increasing thickness. Two main regimes can be distinguished: before and after a crossover at time τ~3000 sec. For earlier times, the reduction of the scattered intensity seems to be related to a smoothing mechanism while at later time $t>\tau$ a coarsening regime becomes dominant. The behavior at $t<\tau$ is qualitatively similar to the one simulated in paragraph 3.2, Figure 3-17 (blue trace). The difference is that, modeling, was obtained assuming an evolution of the PSDs that would follow the model proposed by Stearns while modeling was done

using parameters leading to roughening since the beginning of growth. However, the specular reflectivity seems to agree with the Fresnel reflectivity as if small-scale roughness would prevent the power to be redirected into the bulk.

To avoid oscillations, which may complicate our interpretation, we have performed measurements in TER region, at θ_0~0.15° using a statistically identical Si wafer and the same process parameters as for the previous film deposition. Results of these measurements, i.e., $R_\Sigma \equiv R_\Sigma(t)$ and $TIS \equiv TIS(t)$, are shown in Figure 5-10. Again, a crossover at the time t~3000 is observed, which confirms the previous observation. In contrast to the measurement performed in OTER region, R_Σ seems to decrease after a knee point at t~1000, just after the TER condition for W is reached.

The physical origin of the coarsening regime could have many causes: crystallization, columnar deposition (non-linear growth) and various types of growth instabilities. Speculations only based on our measurements would be difficult to draw and are probably out of the scope of this study. On the other hand, the reduction of R_Σ will be correlated to the appearance of small-scale roughness on the film surface, probably induced by the starting roughness. This will be detailed in the following paragraphs.

To conclude the analysis of our test case we will now present results on two AFM images of the samples that were analyzed earlier (Figure 5-11). The measurements were performed in tapping mode with a scanning window of 8 μm and 256x256 sampled points. The rms roughness obtained by analyzing the images is of σ=2.55 nm (the deposited film is ~73.82 nm thick) and σ=0.76 nm (the deposited film is 55.43 nm thick). Notice that the two samples were treated for different total time of growth: the difference in the roughness value is probably related to this difference.

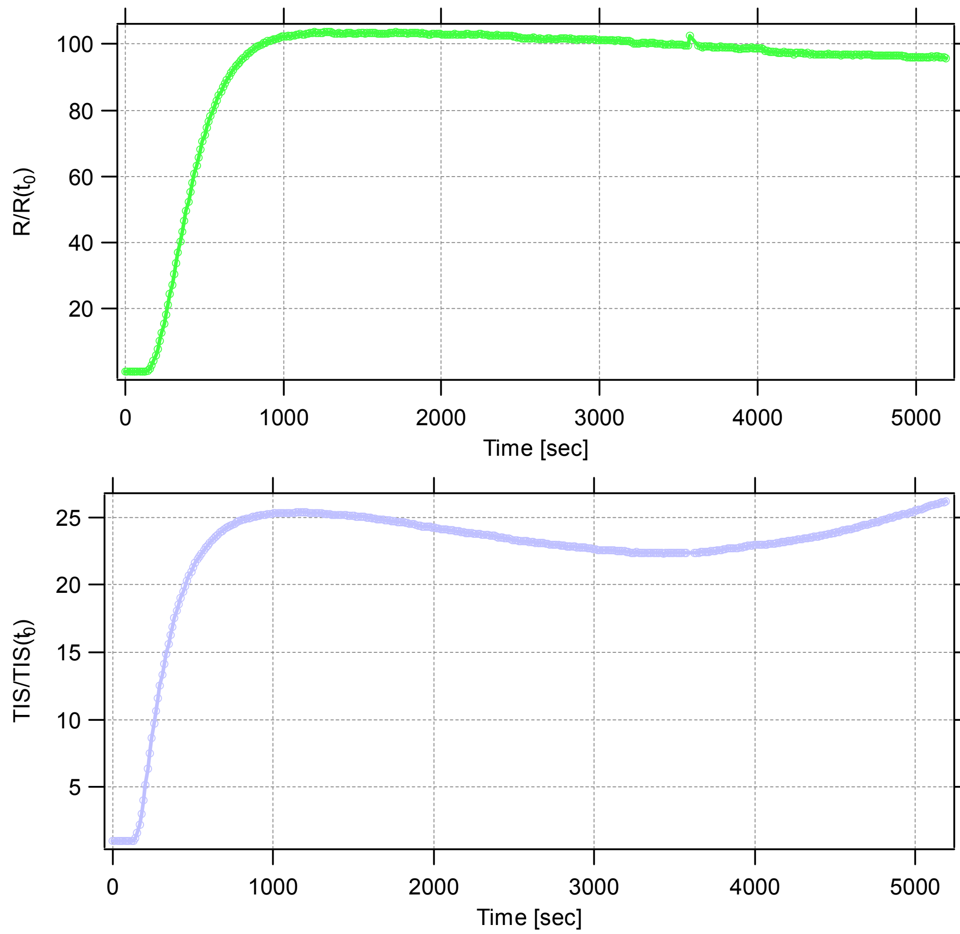

Figure 5-10: $R(t)/R(t=0)$ *(top) and* $TIS(t)/TIS(t=0)$ *- in TER (bottom).*

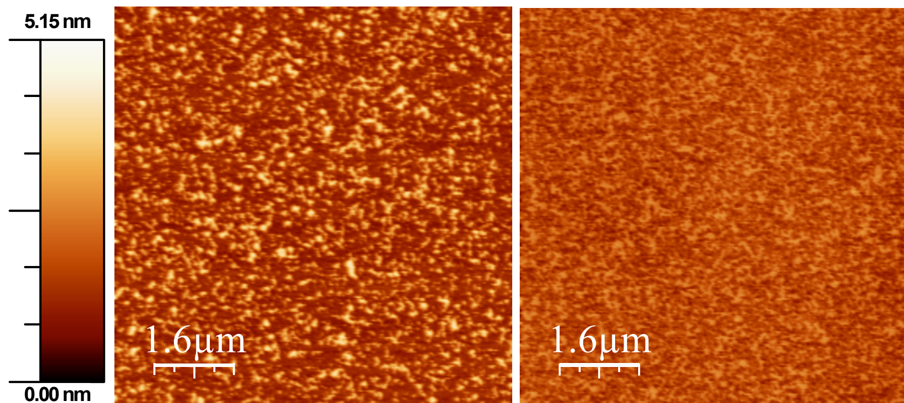

Figure 5-11: AFM topographs of two samples after deposition of 73.82 nm (left) and ~55.43 nm (right). The rms roughness values obtained from images analysis is respectively σ*=2.55 nm and* σ*=0.76 nm.*

In conclusion, we have analyzed the deposition of thin films over a large range of thickness and using the rougher substrates. This allowed us to define criteria for our future experiment and to give us an indication on the parameters for the PT to be applicable. Under the condition we had in our experiment the times of deposition, should be less than 3000 sec, to keep the additional roughness induced by the process itself low. With smoother substrates the film roughness should be greatly reduced and surely lower than 0.76 nm, see figure 5.11 (right). Notice that, in the OTER region, using grazing angle θ_0=0.5° at E=17.5 keV, the upper limits for the applicability of the PT are given by a σ such that the value $g = [2k\sigma \sin(\theta_0)]^2 = 1$, i.e., for σ~0.65 nm. In the TER region (θ_0=0.15°) the same roughness leads to a value of g that is much smaller than 1, i.e., g=0.09. This means that, to be conservative and to operate in both TER and OTER conditions, roughness should be, at least, lower than 0.5 nm ($g_{OTER}=0.614<1$ and $g_{TER}=0.054$), a condition certainly valid before the crossover time, τ=3000 sec.

This example illustrates again that the real time in-situ XRS investigation is a rapid method to control a process.

5.4 Study of tungsten film growth on smooth silicon substrate

In this section we present a quantitative analysis of a tungsten film deposited on super polished Si substrates. Two of these samples were characterized by AFM. Their statistical parameters are given in section 5.1. AFM topographs are also shown in Figure 5-12.

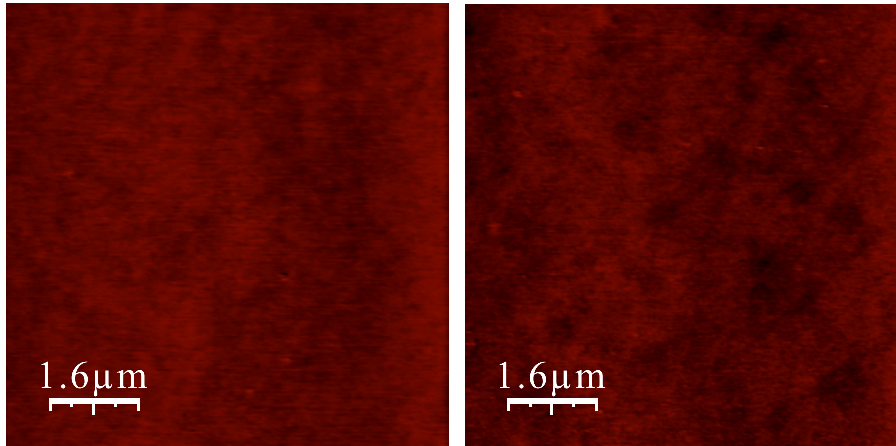

Figure 5-12: AFM topographs of two GO substrates used for real time in-situ XRS studies during tungsten film growth.

The temporal evolution of the total reflectance of tungsten films growing on two identical super polished silicon substrates (General Optics) is shown in Figure 5-13, dots. The two curves in the figure differ by the grazing angle θ_0 set either at $\theta_0 = 0.15°$ (TER) or at $\theta_0 = 0.5°$ (OTER). For comparison, the critical angle of the total external reflection for bulk tungsten is about 0.25° at energy of 17.5 keV. Solid curves in Figure 5-13 were calculated under the following simplifications: (a) an effect of roughness on the reflectivity is negligible, (b) the tungsten density is independent of the film thickness, (c) the presence of an interlayer at the film – substrate interface is neglected. For TER measurements, the penetration depth the wave field does not exceed several nanometers. Therefore, the reflectivity is practically constant once the film thickness gets greater than 5-7 nm. The oscillations in the reflectivity curve measured in the OTER region are caused by the interference of the waves reflected from different film interfaces, the amplitude of these oscillations decreasing with film thickness due to the greater absorption of the radiation in the tungsten film. Both solid curves were fitted to experimental data assuming a tungsten density of 17.04 g/cm^3 (88.3% the bulk density) and a deposition rate of 7.65 pm/s. The last value demonstrates a pm sensitivity of the instrument.

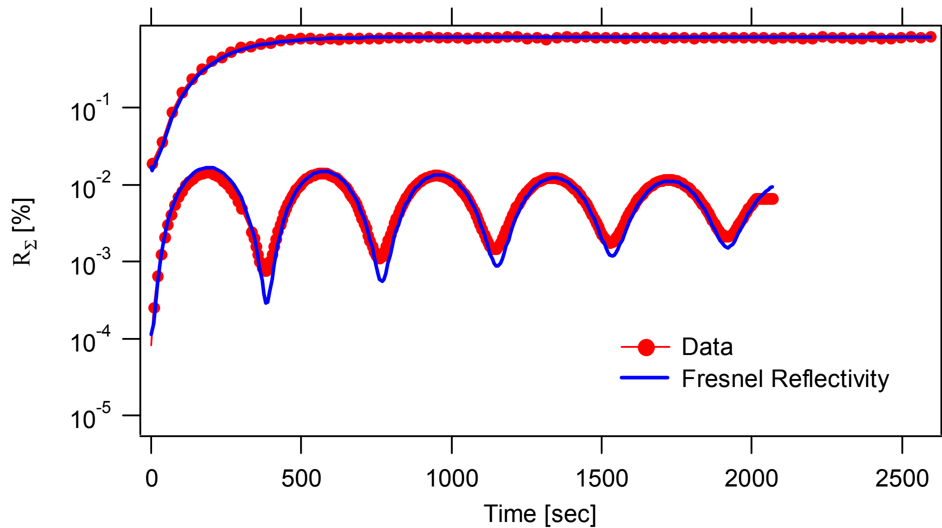

Figure 5-13 Measured (dots) and calculated (solid lines) reflectivity versus deposition time for a tungsten film growing onto the substrate presented in Figure 5-2. The in situ measurements were performed at a grazing angle θ_0 of 0.15°(TER, upper curve) and 0.5°(OTER, lower curve) and an energy of E= 17.5 keV.

To check that the fitted curves resulted in correct values of the film density and of the deposition rate for tungsten, we measured the reflectivity (at 17.5 keV) of the film as a function of the grazing angle θ_0. The measurements were performed in vacuum immediately after deposition of the film. The experimental reflectivity is shown in Figure

5-14, circles. The solid curve was calculated using a film thickness of 24.90 nm, and a tungsten density of 17.04 g/cm^3 derived from analysis of Figure 5-13. As one can see the agreement between experiment and calculation is excellent at grazing angles $\theta_0 < 0.6^o$, while the curves are somewhat different from each other at larger angles. This can probably be explained by the use of a too simplified model, in particular, neglecting the film – substrate interlayer which inevitably formed due to the implantation of W atoms into the Si substrate as well as the interdiffusion and chemical reactions at the boundary between these two different materials. Indeed, it is possible to show that the smoothing of the film – substrate interface results in decreasing amplitude of the interference oscillations in the reflectivity curve [52].

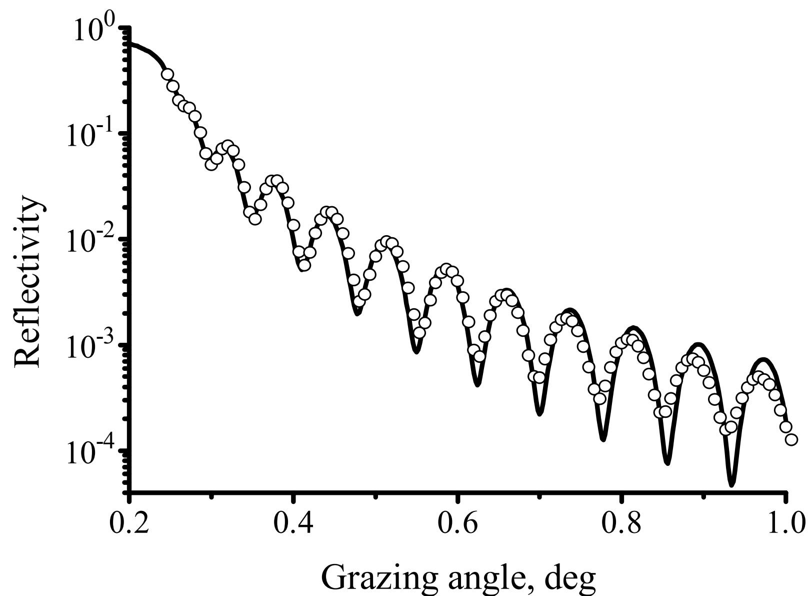

Figure 5-14: Reflectivity (at 17.5 keV) versus grazing angle for tungsten film of 24.9 nm thickness deposited onto silicon substrate compared to the calculated on with optical constants as in the previous image.

Here, it is useful to recall that the information about the fine structure of the interlayers or near surface layers is contained in large grazing angle part of the reflectivity curve. Nevertheless, Figure 5-13 and Figure 5-14 demonstrate that the use of the simplified model of a film is justified at small grazing angles. For further data processing, i.e., analysis of the scattering diagrams with $\theta_0<0.6$, the effect of a transition layer will be neglected. Nevertheless, it is instructive here to push the analysis of these curves as they can yield quantitative information about the interlayer formed at the substrate – layer interface. As explained in section 3.1.5, the asymptotic behavior of $R(\theta)$, i.e., the slope

and the amplitude of the oscillations, can yield information on the type of discontinuity/continuity at the interfaces and, in particular, on the spatial extent L of a transition layer. Kozhevnikov [52] has developed a computational algorithm to solve the inverse problem consisting in a reconstruction of the depth-distribution of the dielectric permeability $\varepsilon(z)$ from intensity reflectivity data obtained in a limited range of incidence angles.

The case of a W film on a Si substrate is a good case to test this approach. Figure 5-15 present the fit obtained on this data using i) the Fresnel formula and assuming a step-like variation of density at the two interfaces (green curve)[28], ii) the method of the inverse problem of reflectometry (blue curve). Figure 5-16 shows the corresponding density profile.

[28] This is the same data as in Figure 5-14 except for the wider angular range shown

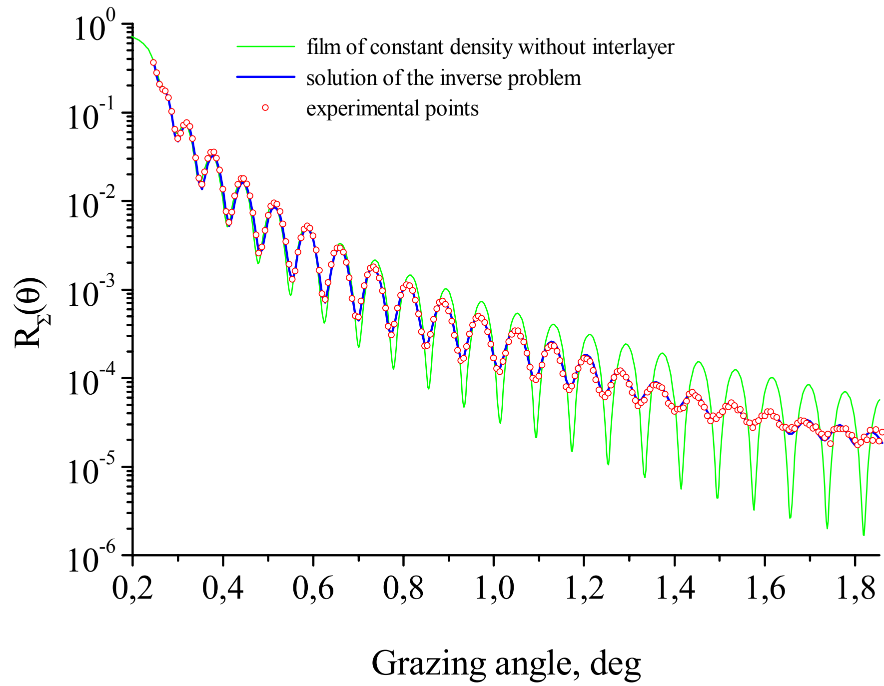

Figure 5-15: Results of the inverse problem of reflectometry obtained minimizing a merit function as explained in the reference [52].

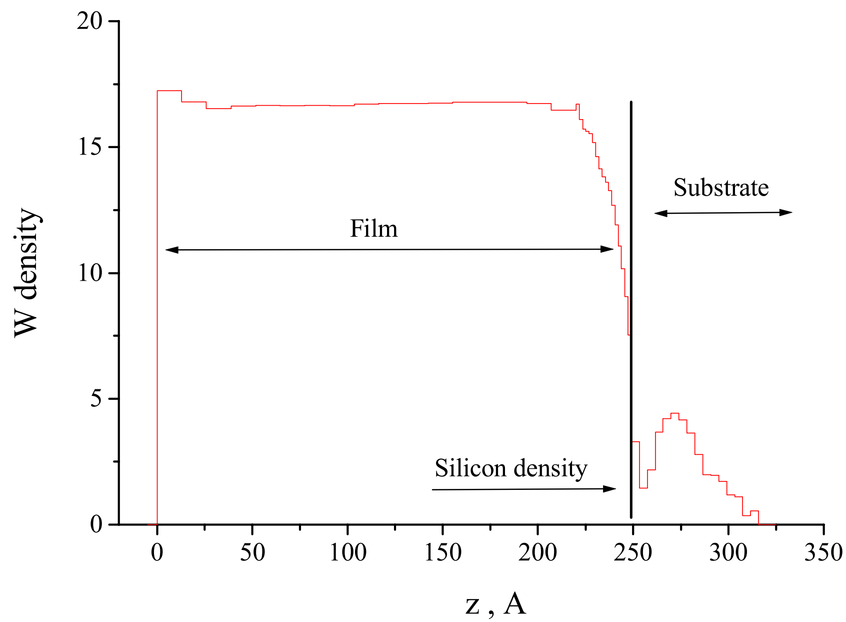

Figure 5-16: Tungsten density profile reconstructed using the refinement procedure [52] on the specular reflectivity data. The substrate is located at a z-value of 24.9 nm.

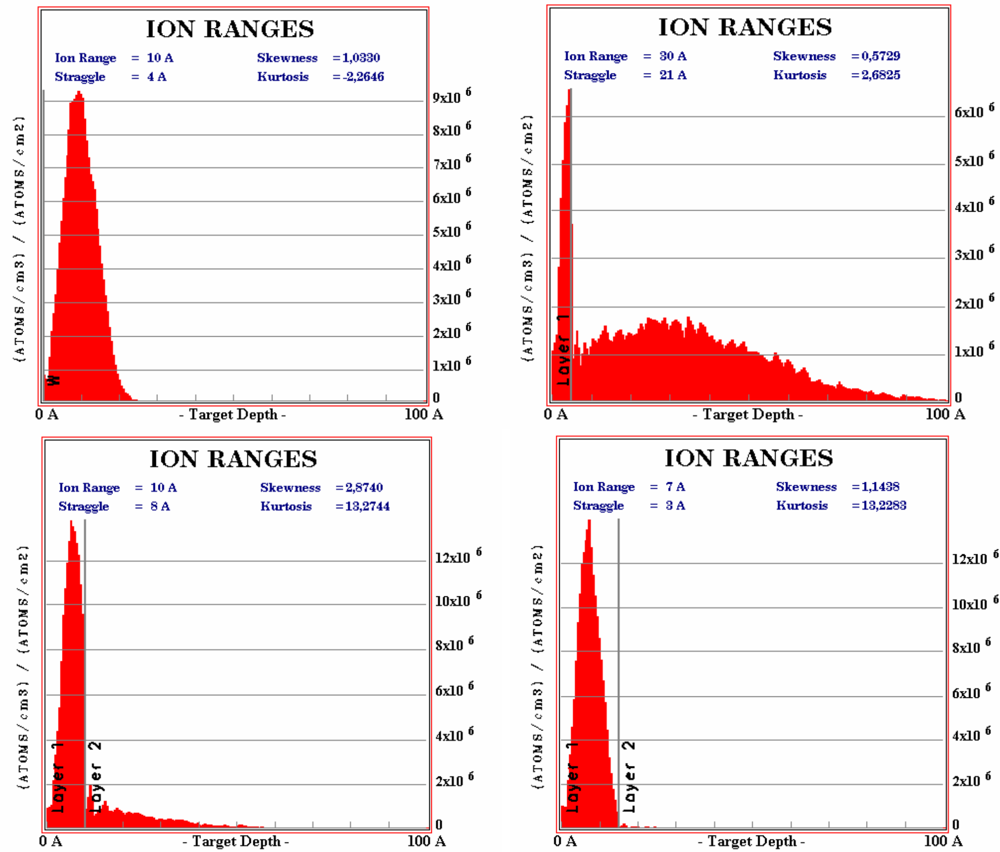

Figure 5-17: Tungsten implantation profile inside a silicon substrate obtained by Monte Carlo simulation. The curves correspond to the case of W thicknesses of 0.01 nm(left top), 0.5 nm, 1 nm and 1.5 nm thick (right bottom). The simulation was performed with 10000 atoms for a run and assuming an ion beam energy of E=0.37 keV impinging at normal incidence.

The reconstruction of the density profile shows a bump in a region that is located below the surface of the Si substrate (altitude z=24.9 nm). This result suggests that, when depositing W atoms, at least in the early stage of the tungsten growth, the atoms are partially implanted in the Si bulk. This interpretation is also confirmed by Monte Carlo simulations obtained with the TRIM code[29]. The simulation performed using the conditions of our particular experiment is presented in Figure 5-17. It shows the distribution of the W atoms present in the depth of silicon sample after the deposition of 0.01 nm, 0.5 nm, 1 nm and 1.5 nm of W. The result fully supports the increase of density below the Si surface obtained by simulation of the reflectometry data.

This suggests a possibility for X-ray reflectometry to study ion-solid interaction from an experimental point of view.

---

[29] This software can be found at the web page http://www.srim.org/.

The depth profile reconstruction presented in Figure 5-16 was also used to model the experimental curve shown in Figure 5-13, obtained in the OTER case. The resulting curve, labeled as “variable density”, is plotted, in Figure 5-18, with the experimental points and the curve calculated assuming a constant W density. The excellent agreement (in linear scale) of the variable density curve with the measured one confirms the correctness of the data procedure.

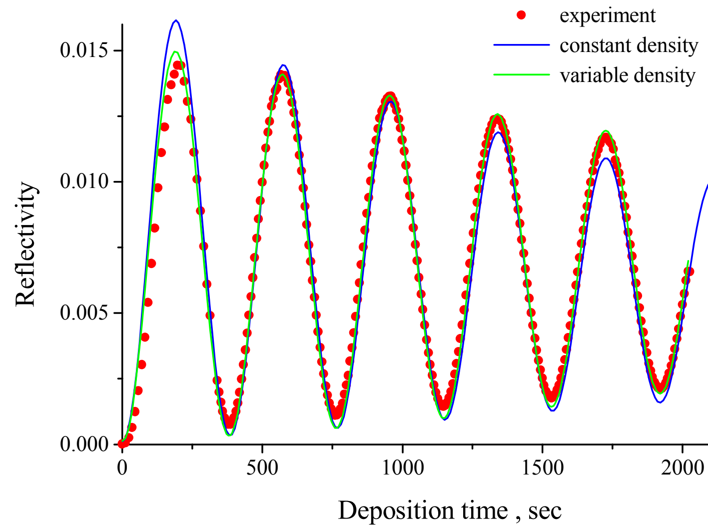

Figure 5-18: Real-time evolution of the total reflectivity for a W film deposited by sputter deposition. The two calculated models differ in the assumption made on depth density profiles.

For each point of the reflectivity curve a scattering diagram was measured using the experimental method presented in the previous chapters. For clarity, we will show only few of these diagrams in Figure 5-19, namely the ones measured at the maximum of each oscillation of the reflectivity curve plotted in Figure 5-18. The curves were obtained by horizontal averaging of the 2D images described in the data correction section (section 4.6.2). The range of measured scattering angles corresponds to a spectral bandwidth extending from [$3.05\ 10^{-4}$, $4.62\ 10^{-2}$] nm^{-1}.

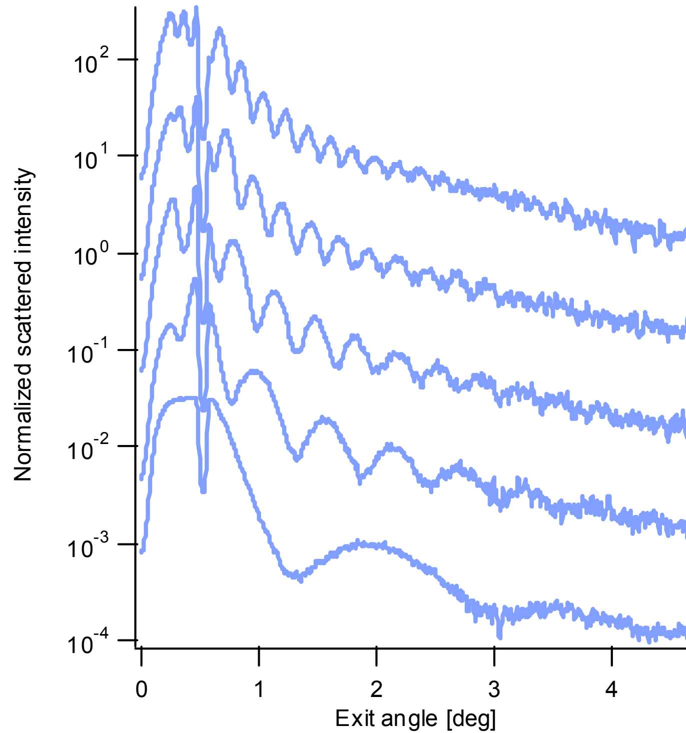

Figure 5-19: Selection of few normalized scattering profiles measured during W deposition. The curves have been selected at equal thickness intervals and correspond to the maximum of each oscillation observed in the reflectivity curve measured in OTER. The curves have been shifted vertically for clarity.

By observing the fringes amplitude and the extension of the oscillations, we notice a roll-off scattering angle where the fringes get damped and which differs for each curve according to the film thickness. The displacement of this angle with film thickness reflects the variation of conformity between the film topography and the substrate topography during film growth.

In the following sections, the quantitative analysis of the scattering diagrams measured during film growth is presented using two different approaches. The aim is to show the possibility, at any time of the growth, to extract the PSDs from the scattering diagrams data, as well as the mutual correlation between film and substrate, i.e., the conformity.

5.5 Roughness analysis: conformity during film growth

The XRS method gives a unique possibility to investigate buried interfaces, to establish the degree of vertical correlation (conformity) between the roughness of the substrate and of the external film surface, and to extract the PSDs of the surfaces contributing to the scattering process. The ability to differentiate features induced by the topography of the substrate from those generated during deposition is an important asset

in the optimization of the growth, allowing eventually, to gain insight into the growth mechanism.

In the following example, we present a quantitative analysis of XRS diagrams measured in-situ and in real time. This study was performed in view of evaluating the variation of conformity of a tungsten film deposited onto a Si substrate. The measurements were carried out using the first setup presented in chapter 4. Therefore, the range of angles was limited to ~2.5 deg. due to the size-distance limitation of the 2D detection system (to be compared to the data of Figure 5-19 obtained with our new setup).

The growth of tungsten films was studied in two experiments, which differed only by the value of the grazing incidence angle θ_0 relatively to the critical angle for tungsten (0.25° at an energy of 17.5 keV). The angle was set either in the total external reflection (TER) with a θ_0 value of 0.125°, or out of it (OTER) with θ_0 value of 0.5°. The scattering intensity distribution was measured *in-situ* as a function of the grazing scattering angle, the sample and the CCD detector both remaining in a stationary position. While tungsten was deposited, a series of scattering diagrams was acquired at 30 s intervals. The integration time of the CCD detector was set to 0.1 s for TER measurements and to 30 s for the less intense OTER measurements. The horizontal beam size was set to 5 mm to favor a high intensity at the detector. As the scattering diagram is very narrow in azimuthal (horizontal) plane, the scattered intensity was integrated in this direction through pixel binning. The vertical beam size was set to 0.1 mm or 0.2 mm for TER or OTER measurements, respectively. The two silicon substrates were cut from the same super-polished silicon wafer. From the scattering diagrams of the substrates measured prior to deposition we confirmed that both substrates had identical statistical parameters of roughness. Within the measurable spatial frequency range, they could be described by a 1-dimensional PSD-function having the form of a fractal power law $PSD_s(p) \sim 1/p^{1+2H}$, with a Hurst exponent H= 0.10, leading to an rms roughness value of 0.18 nm. The range of spatial frequencies, $p \in [0.15, 15]\mu m^{-1}$, was limited experimentally, on the lower side by the size of the beamstop, and on the higher side, by the size of the transmission silicon detector.

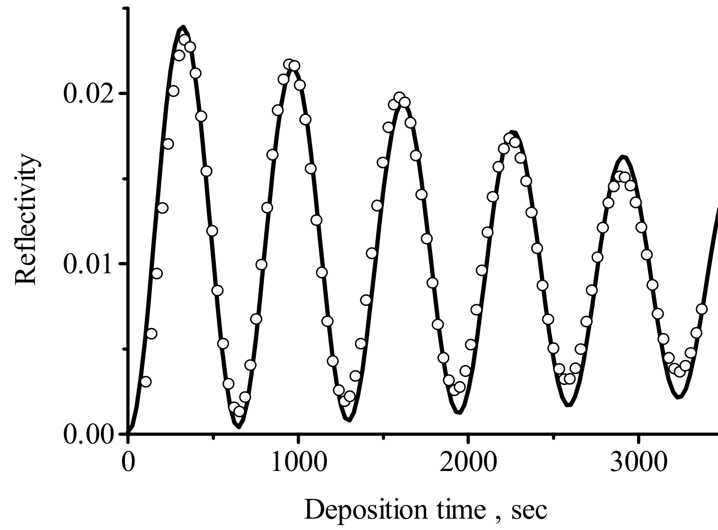

Figure 5-20: Reflectivity of a tungsten film versus deposition time. The in situ measurements were performed at a grazing angle θ_0 of 0.5° and an energy E= 17.5 keV.

The total integrated reflectivity, i.e., the sum of the specular reflectivity and the total integrated scattering, measured in OTER with the diode transmission detector as a function of the deposition time is shown in Figure 5-20, circles. The solid curve is the result of fitting assuming a deposition rate of 7.65 pm/s. The density of the film was found by fitting the reflectivity curve measured after deposition as a function of the grazing angle. Although the fitting model did not account for roughness, a good fit of the experimental reflectivity curve is achieved. This is caused by the long-scale roughness does not influence the total integrated reflectivity measured.

A series of scattering diagrams measured with the CCD camera in TER and OTER is shown in Figure 5-21, circles. The sharp minimum observed on the curves, at the position of the specular peak, is due to the presence of the beamstop.

In the framework of the first-order scalar PT, the scattering diagram integrated over the azimuth scattering angle reads:

$$\Pi(\theta,h) = \frac{1}{W_{inc}}\frac{dW_{scatt}}{d\theta} = \frac{k^3}{16\pi\sin\theta_0}\left[A_f PSD_f(p,h) + A_s PSD_s(p) + A_{sf} PSD_{sf}(p,h)\right] \quad (5.3)$$

in which A_f, A_s, and A_{sf} have the expressions (3.27) given in chapter 3.1.4 and where W_{inc} and dW_{scat} are the radiation powers of the incoming beam impinging under an angle θ_0 and of the beam scattered in the θ direction within an angular interval $d\theta$, respectively. $PSD_f(p,h)$ ($PSD_s(p)$)is the 1-dimensional PSD-function of the external film surface (substrate) and $PSD_{sf}(p,h)$ describes the statistical correlation between film

roughness and substrate roughness. The quantity $p = |\cos\theta - \cos\theta_0| / \lambda$ is the spatial frequency and $k = 2\pi / \lambda$ the wave number.

The expression (5.3) for the scattered intensity is composed of three terms. The first two terms describe the intensity scattered from the film surface and from the substrate, while the third one originates from the interference of the waves scattered by the different interfaces having conformal roughness. By measuring the scattering diagram at two different angles θ_0, one can use (5.3) to form a system of linear algebraic equations. For each value of the spatial frequency p, the two unknown functions $PSD_f(p)$ and $PSD_{sf}(p)$ can then be derived without using of any model of correlation function. However, the solving of this system turns out to be an ill-conditioned problem, when even a small inaccuracy in the measured scattering intensity may lead to a very large error in the PSD-functions extracted. One way of overcoming the problem is described in Ref. [91]

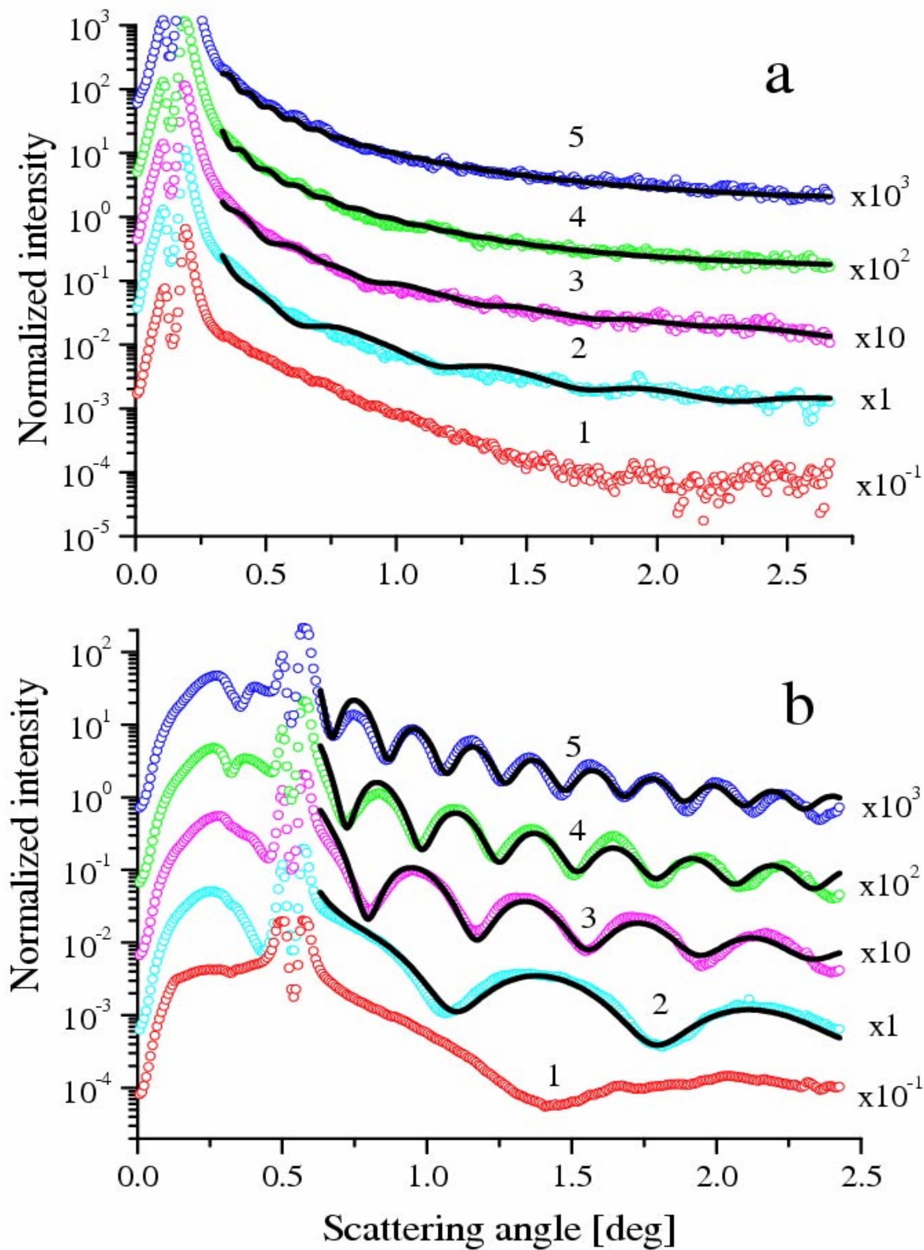

Figure 5-21: Normalized scattered intensity (circles) measured in-situ in TER (θ_0= 0.125°, a) and OTER (θ_0= 0.5°, b) at corresponding film thickness: h= 2.5 nm (1), 5.6 nm (2), 10.2 nm (3), 14.8 nm (4), 19.4 nm (5). For clarity the curves are shifted vertically by a factor 10 with respect to each other so that only curve 2 is set to its real scale (x1). The solid curves have been calculated using the PSD-functions displayed in Figure 5-22.

However, when the films are thick enough, the extraction of the PSD functions is simpler. In this case, when the probe beam falls onto a sample in TER condition, the electrodynamics factors A_s and A_{sf} decrease exponentially with increasing film thickness h. Therefore, when h is of the order of 5–6 nm the scattered intensity is only caused by the surface roughness of the external film. Thus, neglecting the effect of the substrate ($A_s = A_{sf} = 0$), the PSD-function of the external film surface $PSD_f(p)$ can be extracted directly from (5.3). To get rid of the statistical oscillations we approximated the PSD functions using the following expression:

$$\log\left[PSD_f(p)\right] = \sum_{j=0}^{j_{\max}} a_j \left[\log(p)\right]^j \quad j_{\max} = 3 \text{ or } 4 \qquad (5.4)$$

The smoothed PSD-functions are shown in Figure 5-22, solid curves 1-5, for different film thicknesses. For comparison, the smoothed PSD-function of the substrate is also presented (curve 6). The PSD-function of the external film surface increases with film thickness due to the development of intrinsic film roughness. The variation of the PSD-function is more pronounced at high spatial frequencies, as also predicted from the existing theories on film growth[2, 43]. In the measured range of spatial frequency this increase in the PSD corresponds to a slight increase of the rms roughness parameter, from 0.18 nm for the bare substrate up to 0.21 nm after deposition of a 23.5 nm thick film. When the probe beam falls onto the sample in OTER condition, the electrodynamics factor A_{sf} oscillates as a function of the scattering angle θ, the frequency of the oscillations increasing with the film thickness. These oscillations are clearly observed in the measured scattering diagrams presented in Figure 5-21, thus demonstrating the presence of roughness conformity between the film and the substrate underneath. As the functions $PSD_s(p)$ and $PSD_f(p)$ were already obtained from the TER measurement, it is now possible to extract, from Eq. (5.3), the PSD-function for the cross-correlation $PSD_{sf}(p)$. As above, the PSD-functions extracted contained statistical oscillations, which can be large near the spatial frequencies where the factor A_{sf} is equal to zero. To remove them, we used a polynomial approximation of the function $PSD_{sf}(p)$ with coefficients found by the fitting of the scattering diagram in OTER condition. The resulting smoothened functions $PSD_{sf}(p)$ are presented in Figure 5-22, dotted curves 1-5, for different film thickness. The figure demonstrates clearly that conformity of roughness decreases with increasing film thickness and increasing spatial frequency. Finally, using the functions PSD_s, PSD_f, and PSD_{sf} given in Figure 5-22, the scattering diagrams corresponding to the TER and OTER regions were calculated (Figure 5-21, solid curves) and compared to the measured ones (circles). The excellent agreement demonstrates the consistency of our procedure of extraction of the PSD-functions. It is important to

emphasize again that these PSD-functions were obtained from the measured scattering diagrams without any additional assumption about roughness.

To characterize the roughness conformity quantitatively we calculated the replication factor for roughness:

$$K(p,h) = \frac{PSD_{sf}(p,h)}{\sqrt{PSD_f(p,h)PSD_s(p)}} \qquad (5.5)$$

which is shown in Figure 5-23 for different film thicknesses. Let us define the critical spatial frequency $p_c(h)$, for which the replication factor is decreased by a factor e, and the corresponding critical length $L_c(h) = 1/p_c(h)$. The dependence of L_c on the film thickness is shown in the inset of Figure 5-23. Surface features with a lateral size greater than L_c are strongly replicated after deposition of a film of thickness h. Features with a smaller size are smoothened, although additional uncorrelated roughness appears. As one can see, the critical size of a replicated feature increases proportionally to the film thickness. For the tungsten growth process presented here, only surface features with a lateral size about 10 times greater than the film thickness are well replicated.

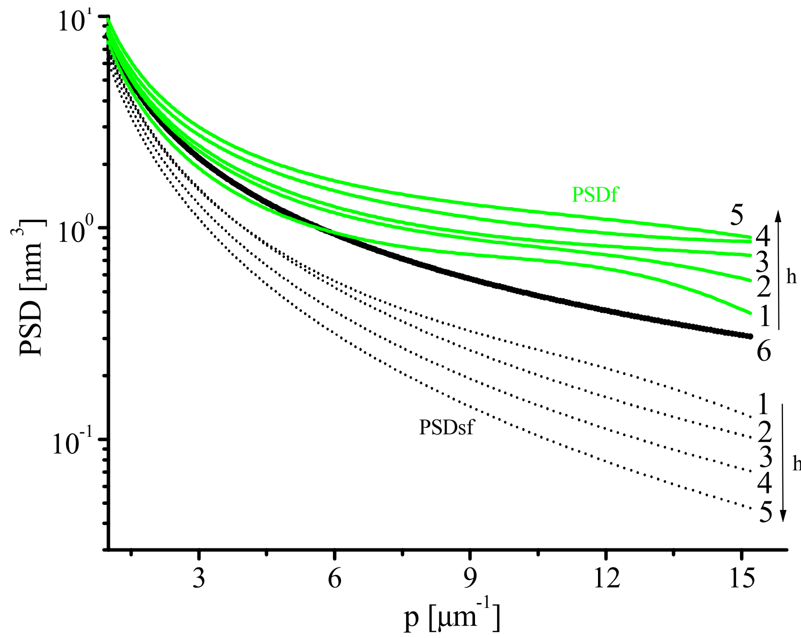

Figure 5-22 : PSD-functions of the external film surface (solid curves) and of cross-correlation (dotted curves) extracted from the measured scattering diagrams as a function of the film thickness h: 5.6 nm (1), 10.2 nm (2), 14.8 nm (3), 19.4 nm (4), and 23.5 nm (5). Curve 6 is the PSD-function of the silicon substrate

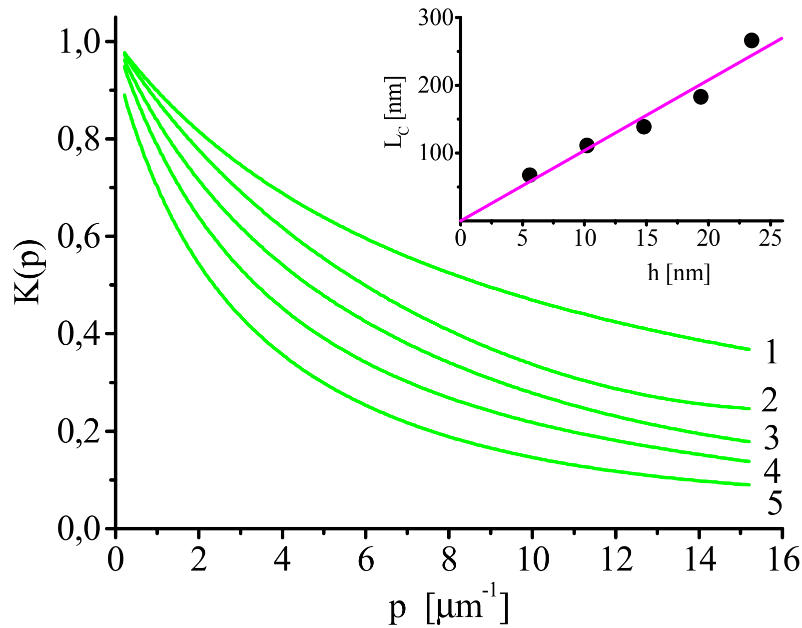

Figure 5-23: Replication factor of roughness for different film thicknesses: 5.6 nm (1), 10.2 nm (2), 14.8 nm (3), 19.4 nm (4), and 23.5 nm (5). The inset shows the dependence on the film thickness on the critical length of the roughness replicated.

Ex-situ analysis by AFM

In the previous analysis, we have only shown the reflectivity curve measured in the OTER region. A deeper analysis of the previous measurements shows an apparent contradiction, which becomes clear representing $R_{\Sigma}(t)$ measured in TER region. The experimental points, shown as red circles in Figure 5-24 are superimposed to calculations (green curve) in which perfectly smooth substrate and film are assumed. The same hypothesis as for the calculations made in the OTER region (see Figure 5-18) provides a good agreement between experimental data and calculation. It is a quite unexpected fact that the calculated reflectivity curve coincides well with experimental data in OTER, while differs strongly on it in TER (see green curve and red points). This behavior may be connected with development of small-scale roughness during film growth.

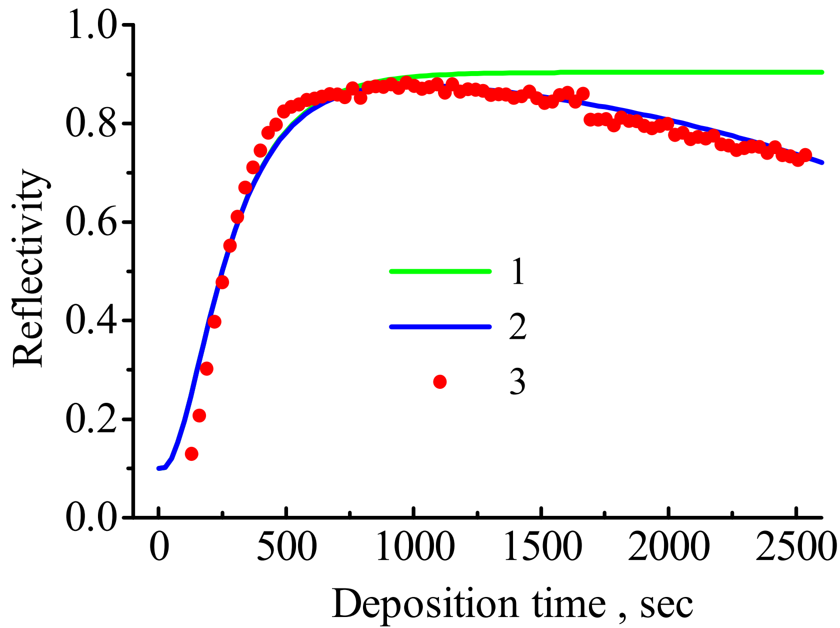

Figure 5-24: Reflectivity of a growing tungsten film versus deposition time. The in situ measurements were performed at a grazing angle q_0 of 0.15° and an energy E= 17.5 keV.

To verify this interpretation, surface roughness was characterized at different time of the growth ex-situ, at the surface science lab of the ESRF, using an atomic force microscope from Digital Instruments, Nanoscope III®. Before deposition, the background pressure of the sputtering chamber was less than 3.6×10^{-7} hPa. The sputtering was conducted with pure (99.999%) Argon gas, using a working pressure of 13.3 10^{-3} hPa. The experimental conditions were realized using a bias voltage of 370 V and a total ion current of 30 mA. The pressure set point was achieved fixing the gas flow rate of 3 sccm. For this purpose 4 different samples were deposited using the same process parameters.

The samples were measured in *tapping mode* using scan windows of 1 μm size with 256x256 sampled points. Results of these measurements are shown in Figure 5-25. When compared to the bare substrate the measurements reveal the appearance of some small-scale features, i.e., the formation of nano-holes with increasing diameter at progressive film thickness. However, the substrate shows a dot-like structure apparently spatially correlated to the holes morphology (see also Figure 5-2).

When the film thickness is varied between 2.7 nm (t=450 sec) up to 21.6 nm, the average depth of formed holes is found to vary from ~1 nm up to ~4 nm.

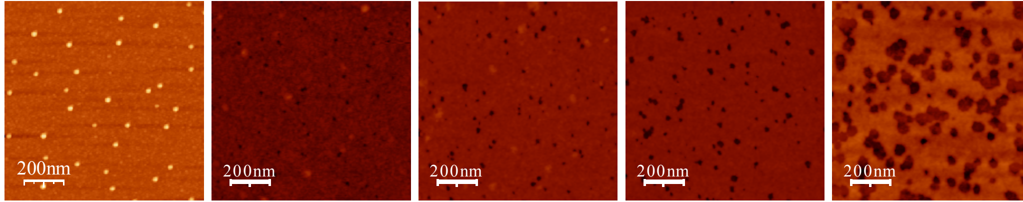

Figure 5-25: AFM topographs of W films at different times of the depositon, from left to right at, 0 s(Si wafer), 450 s, 900 s, 1800 s and 3600 s, respectively.

Furthermore, the roughness of the substrate and the thinnest films (t=450 s), were compared within the 1 μm^2-scanning window of the images in Figure 5-25. The substrate had a roughness σ_{rms} = 0.86 nm while the sample at t=450 s had a roughness σ = 0.25 nm. This proves that smoothing can be achieved using thin sputtered layers. A similar smoothing effect was reported earlier by Spiller [92]. Chemical contamination could be a possible cause of the spikes observed. From the AFM images it is clear that these spikes disappear with further deposition, which may result from be the energetic sputtered atoms impinging onto the surface and eliminating the various chemical components, leaving vacancies (hole) in the film surface. Note also that the holes do not penetrate the whole film, their depth being always lower than the film thickness.

Although the physical origin of these holes is unclear, their formation can be considered as a special case of small-scale roughness. Let us consider shortly the x-ray reflection from a single rough surface. Obviously, the larger is the grazing angle, the greater is the decrease in the specular reflectivity (caused by scattering). Instead of recording the specular reflectivity R_{spec} we measured simultaneously the specular reflectivity and the total integrated scattering $R_{\Sigma}=R_{spec}+TIS$. The variation of R_{Σ} with grazing angle differs essentially from that of $R_{spec.}$

The width of the scattering diagram is equal to $\Delta\theta = \lambda / \pi\xi \sin(\theta_0)$, where ξ is the roughness correlation length and θ_0 is the grazing angle of the probe beam. The width of the scattering diagram increases with decreasing grazing angle, and, if $\Delta\theta$ becomes

greater than θ_0, the scattering diagram "lies" onto the surface. Let us introduce the following the a-dimensional quantity:

$$\mu = \frac{\theta_0}{\Delta\theta} \approx \frac{\pi\xi\theta_0^2}{\lambda} \quad (5.6).$$

Two different cases can be distinguished for the scattered intensity: i) $\mu > 1$ and ii) $\mu \ll 1$. In the first case the decrease in specular reflectivity is equal to the total integrated scattering, so that R_Σ is almost equal to the reflectivity of a perfectly smooth surface. This condition was realized on OTER experiment with a parameter $\mu \sim 1.6$ at $\xi = 0.5\ \mu m$. In the second case, substantial part of the scattered intensity is redirected into the depth of the sample and cannot be detected. As a result, R_Σ is lower than the reflectivity of a perfectly smooth surface. This case was realized in a TER with a parameter $\mu \sim 0.1$ at ξ=0.5 μm. These two situations are illustrated in Figure 5-26.

In OTER measurements the roughness with a correlation length of ξ=0.5 μm should be considered as a small-scale one and should result in an increase of the radiation transmitted into the substrate. At the same time, this roughness is a large scale one for OTER measurements.

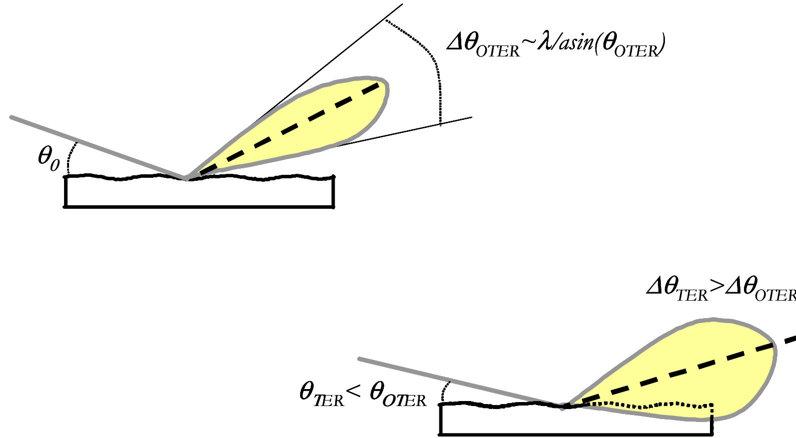

Figure 5-26: Schematic view of the scattering process in presence of small scale roughness (see holes in Figure 5-25) in the TER and OTER regions. The small grazing angle in TER region causes an enlargement of scattering diagram and penetration into the bulk of the layer.

The result is presented in the Figure 5-24 (blue curve). The blue curve was calculated in the framework of the perturbation theory. The blue curve represents the total reflectivity:

$$R_\Sigma = R_0 - \delta R + \int \Phi(\theta,\varphi)d\Omega \quad (5.7)$$

where an integration of the scattering diagram is performed over the aperture of the transmission detector. R_0 is the reflectivity of a perfectly smooth film, δR and Φ are calculated in the first order perturbation theory. The expressions for δR, rather complex, will not be shown here.

During the calculation, the following form of the one-dimensional PSD was assumed:

$$PSD_{1D}(\nu) = \frac{4\sigma^2\xi}{1 + (2\pi\nu\xi)^2} \tag{5.8}$$

using a correlation length ξ = 0.5 μm. For the rms roughness we used the following law

$$\sigma(t) = 2.5\, nm \cdot \left(\frac{t}{2500}\right)^{1.2} \tag{5.9}$$

where the deposition time t is in seconds.

5.6 Alternative approach to extract the PSD

The study of roughness conformity during W growth shows that the spectral analysis requires two different sets of real time scattering data to perform the data analysis. This seems natural, since two unknown functions need to be determined. For similar reasons, since the PSDs are properties of the sample and independent by the measurement itself, ones could obtain the cross correlation between two interfaces by measuring the scattering diagrams at two or more X-ray energies. However, for measuring at two energies simultaneously, the monochromator would have to be tuned on two different Bragg angles. This would require a sophisticated setup where the monochromator switches quickly from one tuning position to the other at any instant of the growth, a solution probably impracticable.

Although the analysis of two independent sets of measurements using the same physical and optical film model would be a convincing argument about the correctness of the procedure, it requires an experimental method that is, practically-wise, particularly demanding: two "identical" experiments, which differ only by the grazing angle, must be performed. In practice, one must reduce as much as possible all causes of instabilities that may occur during a temporal scan (e.g. X-ray beam and/or sputtering stability). Moreover, it is important to have a set of samples with well-defined statistically identical properties.

A careful analysis of formula (5.3) shows some other interesting features, which allow us to improve the experimental method. Let us recall formula (5.3), which represent the scattering diagram of a thin film:

$$\Pi(\theta,h) \propto \left[A_f(\theta,h) PSD_f + A_s(\theta) PSD_s + A_{sf}(\theta,h) PSD_{sf} \right] \qquad (5.10)$$

In (5.10) we have written explicitly the dependence of the electrodynamics factors by θ and *h*. Let us assume that any of the PSDs is a smooth function of the spatial frequency *f* (hence of θ). The dependence on the grazing scattering angle θ of the coefficients A_f, A_s, and A_{sf} entering in Eq. (5.10) is shown in Figure 5-27, for a tungsten film (h = 10 nm) deposited onto a silicon substrate. The probe beam (E = 17.5 keV) was set to an OTER angle θ_0=0.5° (for comparison θ_{cr} = 0.25°). As one can see, the coefficient A_{sf} is an oscillating function of the grazing angle: this behavior is responsible for the oscillations of the scattering diagram. An example is presented in Figure 5-30, showing the scattering diagram from a W film of thickness h = 24.6 nm. The sharp minimum observed on the curves, at the position of the specular peak, is due to the presence of the beamstop in front of the CCD to avoid its saturation.

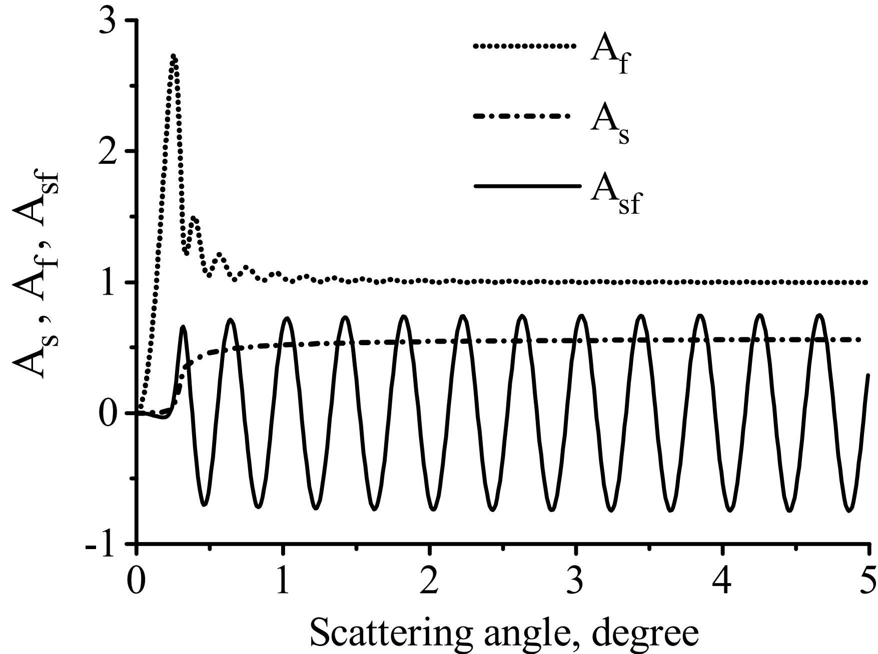

Figure 5-27 Coefficients A_s, A_f, and A_{sf} for a tungsten film 10 nm thick deposited onto a silicon substrate as a function of the grazing scattering angle. Calculations were performed assuming the radiation energy 17.5 keV and a grazing angle of the incident beam of 0.5°.

The behavior of the function A_{sf}/A_f X-ray scattering diagrams is illustrated by Figure 5-28 for different film thicknesses. Figure 5-28 shows the variation of the

coefficient A_{sf} with an increase of the scattering angle θ. This angle is related to the spatial frequency by the grating equation. The coefficient A_{sf} describes the interference of the waves scattered from both interfaces of a thin film. It oscillates with the change of the scattering angle and equals zero for some scattering angles θ_s. Clearly, when A_{sf} is close or equal to zero, it is impossible to determine the PSD_{sf} representing the cross-correlation function of the film. However, since the PSD function of the substrate roughness has been measured earlier, once entered in (5.10), one can use these points to extrapolate the PSD function of the external film surface as a function of θ (or p(θ,η) where A_{sf} equals zero). Let us discuss this procedure in more details.

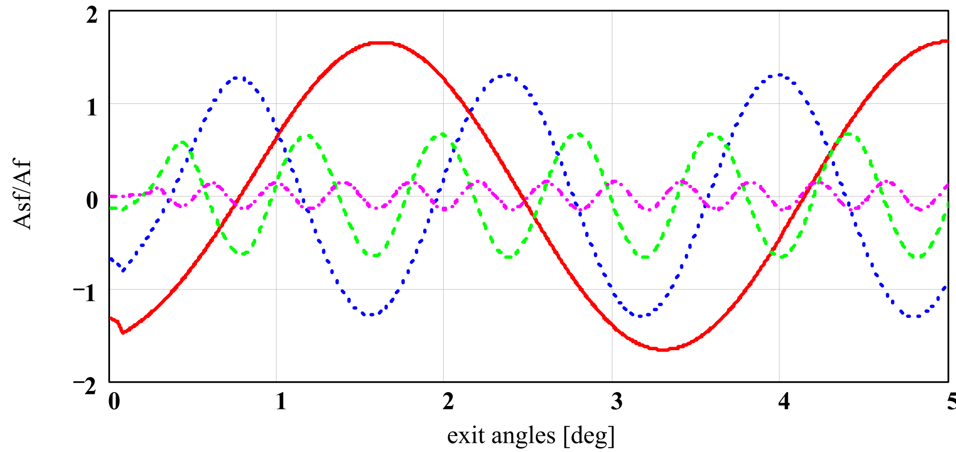

Figure 5-28: Ratio A_{sf} / A_f for different film thicknesses, namely, from the largest oscillation in four different cases, 1,25 nm (red curve), 2.5 nm(blue curve), 5.0 nm (green) and 10 nm (pink curve).

As one can see on Figure 5-28 the number of zeros decreases quickly when the film thickness is reduced. For a film thickness of 1.25 nm there are only three point where Asf=0. As for the analysis of TER XRS diagrams, our procedure encounters difficulties in obtaining direct information on the PSD when the film gets very thin, i.e., less than 1.5-2 nm.

Figure 5-27 shows that the coefficient A_{sf} is equal to zero at particular scattering angles θ_0, i.e., at particular spatial frequencies p = p(θ_0, h). Hence, we can find the PSD function of the external film surface PSD_f at these frequencies from Eq. (5.10) directly. The found values of PSD_f are shown in Figure 5-29, red dots, for a tungsten film of thickness h=24.60 nm. The PSD function of the substrate, measured before deposition, was assumed unvaried during film deposition. As mentioned earlier, the frequency of the oscillations of the coefficient A_{sf} increase with film thickness and, consequently, the number of zeros present within the measurable range of scattering angles. From general physical considerations we can also deduce that PSD_{ff}(p) will be a smooth function of the spatial frequency.

To decrease the experimental errors and to interpolate the PSD function between measured points, we have represented the function PSDf(p) in the following way:

$$PSD_{ff}(p) = PSD_{ss}(p)\left(1 + \sum_{j=1}^{j_{\max}} a_j p^j\right) \tag{5.11}$$

where typically j_{max} = 2 or 3. In addition, the representation (5.11) implies the reasonable physical assumption of roughness conformity at small spatial frequency, i.e., $PSD_{ff}(p) \to PSD_{ss}(p)$ while $p \to 0$, allowing us to extrapolate the PSD function also in the small spatial frequencies range. These conditions are particularly useful for very thin films, i.e., when the number of zeros of the coefficient A_{sf} is small inside the measurable range of spatial frequencies.

The PSDs found are presented in Figure 5-32.

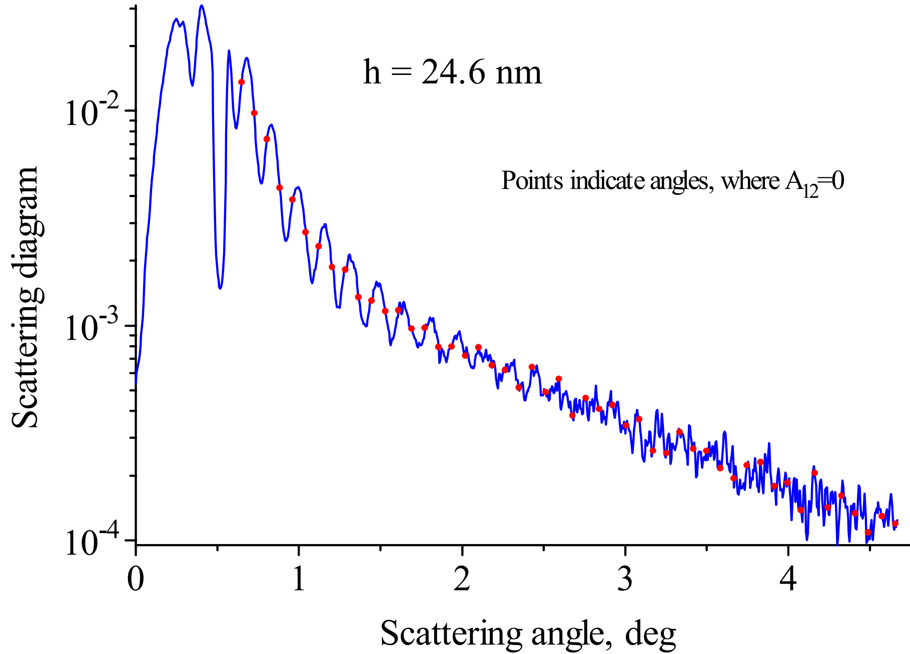

Figure 5-29: Scattering diagram of a 24.6 nm thick film. The points at which A_{sf} is equal to zero are marked on the curve (red points).

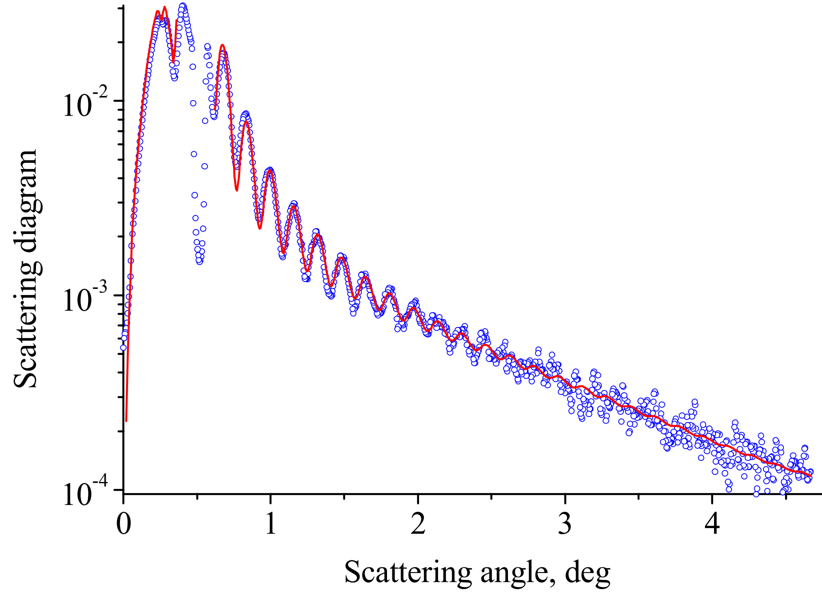

Figure 5-30: The previous XRS diagram (data points) for a W film, 24.6 nm thick superimposed to a XRS diagram calculated with the PSDs extracted.

In the analysis of the conformity using our method, the final step, consists of determining the spectral correlation PSD_{sf} representing the mutual correlation between film and substrate topography. Again, as the PSD function of the external film surface is known, we can deduce the function PSDsf(p) with the help of the representation (5.11). The coefficients a_j in this representation are found by fitting the measured scattering diagram. Notice that the function PSDsf(p) determined directly from (5.10) exhibit large errors at the spatial frequencies where the coefficient A_{sf} is equal to zero (or very small). Therefore, we perform a fitting, using the representation(5.11). The result is shown in Figure 5-32. Notice that the data in the region $\theta_s < \theta_0$ are also modeled. The same procedure was applied to analyze scattering diagrams measured on films of different thicknesses. These are shown in Figure 5-31.

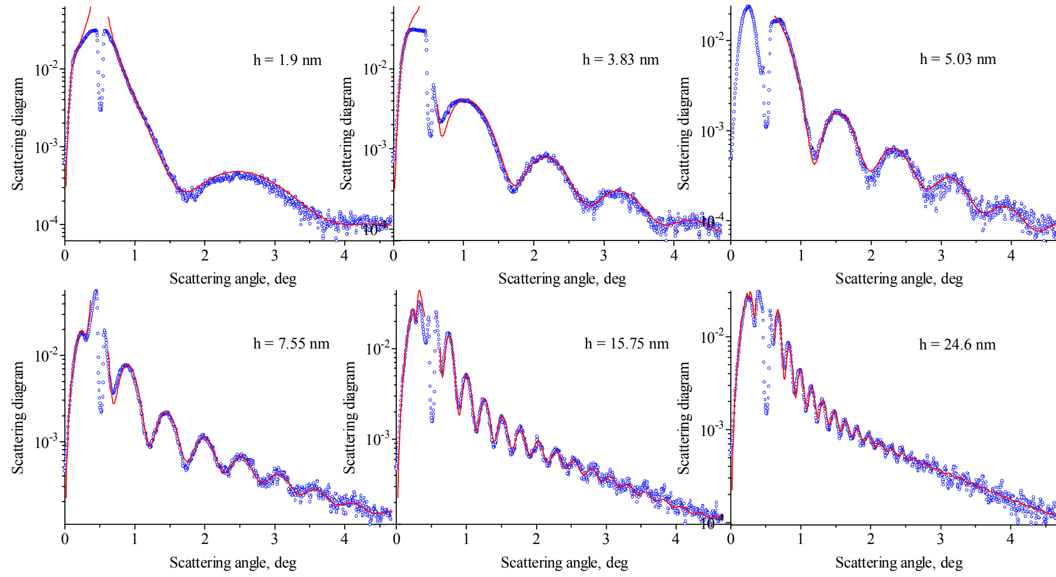

Figure 5-31: Scattering diagrams superimposed to data modeled using the improved spectral analysis. The curves correspond to film thicknesses, h=1.90 (top left) nm, 3.83 nm, 5.03 nm, 7.55 nm, 15.75nm and 24.6 nm (from top left to bottom right).

From a mathematical point of view, Eq. (5.10) can be considered as a system of linear equations of the (unknown) functions PSDff and PSDsf that should be analyzed separately using two sets of spatial frequency. A first set $\{P_0\}$ of denumerable spatial frequencies for which the coefficient A_{sf} = 0 is defined. Then, the system 5.12, only function of PSDf(p), can be solved rather accurately for this set $\{P_0\}$ despite of experimental errors. Assuming PSDff(p) to be a smooth function we can interpolate it using Eq. (5.10) over the whole range of measured spatial frequency. Notice, that the function PSDsf(p) cannot be found at the set $\{P_0\}$.

A second continuous set of spatial frequencies containing all the spatial frequencies except the set $\{P_0\}$. Here, the system (5.10) contains both the functions $PSD_{ff}(p)$ and $PSD_{sf}(p)$. As the function $PSD_{ff}(p)$ has already been interpolated over the whole range of spatial frequency, we can now extract the function $PSD_{sf}(p)$ from the same scattering diagram, using the same representation (5.11) excluding the set $\{P_0\}$. Finally, we can interpolate $PSD_{sf}(p)$ at each point of this second set in a continuous way.

The accuracy of the approach is demonstrated by the solid curves in Fig. 5.31 superimposed to the experimental data (blue dot). All the curves are in excellent agreement with the experimental data and were calculated using the PSDs functions obtained previously and shown in Figure 5-32. These PSDs have a profile already discussed in section 5.5: a power-law at small spatial frequency followed by the development of a bump for large spatial frequency f. This last feature has been

interpreted as the result of the development of intrinsic roughness and was also predicted by existing growth models[43]. Moreover, the roll-off frequency, i.e. the value where the transition between two regimes occurs, gets smaller at greater growth times, while the PSDs at low spatial frequency is nearly unaltered by the deposition process. As seen earlier, the low spatial frequency part of the PSD is related to features of the substrate profile.

The behaviour of the PSD can be understood with the simple analogy of the snow falling onto a morphology with rippled ground (small spatial frequency) covered with grass (large spatial frequency): the small spatial frequencies (ground waviness) will be reproduced even after a thick layer of snow. The large spatial frequencies corresponding to the grass will quickly be blurred, even after a small layer of snow. The development of a snow-induced morphology will then become dominant (intrinsic roughness).

In this section, we demonstrated that two PSD functions of a rough film $PSD_f(f)$ and $PSD_{sf}(f)$ could be uniquely extracted from a single scattering diagram[30] measured in OTER condition. This straightforward procedure greatly simplifies the experimental method and the data analysis enabling the estimation of the PSD_s of a surface at various film thicknesses. In contrast to our earlier analysis, see sec. 5.5, the high quality of the data now available, thanks to the improved 2D detection system, enables accurate measurements in the high spatial frequency region, a region sensitive to the development of intrinsic roughness during film growth.

[30] Assuming the PSD of the substrate known.

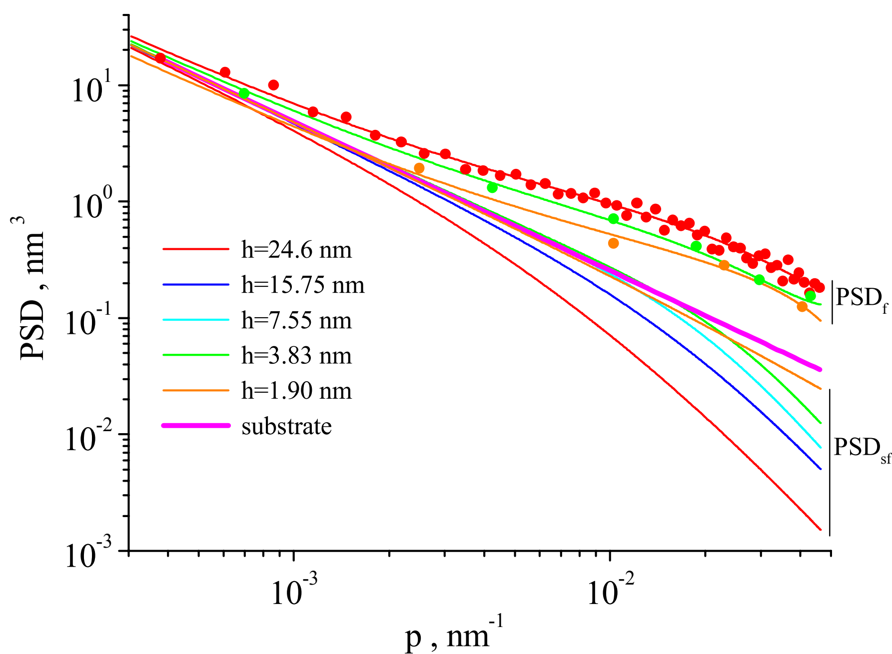

Figure 5-32: PSDs calculated from the previous scattering diagrams at different film thicknesses. The solids lines shows the smoothened PSDs extracted using a logarithmic fit of the measured data.

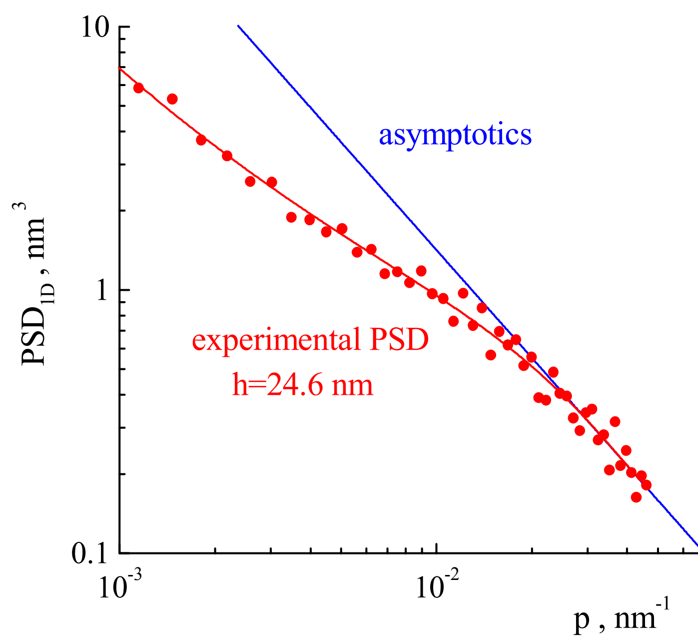

Figure 5-33: PSD obtained on the thickest film made in this work (h=24.6 nm) in comparison with its asymptotic at large spatial frequency showing the development of intrinsic roughness during film deposition.

For instance, the PSD for the thickest film is shown in Figure 5-33 superimposed to an asymptotic axis illustrating the change of slopes of the PSD. In this region, a detailed analysis of the PSD can lead information on the relaxation mechanisms that are responsible for the film morphology.

5.7 Dynamic scaling analysis

In this section, we analyze the scaling behavior of a W film grown onto a Si substrate. This can lead to the identification of a "universal behavior", i.e., a behavior that is independent of the details of the growing system. Notice that, in the literature, several authors [93-97] have performed dynamic scaling analysis on the base of scattering data. However, they always used models to describe the film growth model and the correlation functions at each interface. The motivation for showing this study is to prove that the scattering method proposed is also suited to perform scaling analysis in a model-independent way, and does not invoke numerical fitting procedure to determine the sample related features.

The scaling concept was recalled in section 2.5. Here, we shall test the validity of the data collapse approach by re-plotting the PSD data[31] and to obtain the scaling exponents. When dealing with a PSD, a function accessed through XRS measurements, the data collapse should be performed in the Fourier space. This can be done following the approach described by Barabasi in [2], i.e., in which the data are presented in a plot having a "normalized" spatial frequency as horizontal coordinate:

$$q = h^{\frac{1+2\alpha}{z}} f^{1+2\alpha} \tag{5.12}$$

, and a new "normalized" PSD multiplied by a scaled spatial frequency as y-coordinate:

$$PSD(f,t) = f^{1+2\alpha} PSD_{film}(f,t) \tag{5.13}$$

where as usual the subscript *f* denotes the spectra for the external film surface and h in (5.12) represent the film thickness.

In this way, the PSD curves obtained from measurements at different thickness/time are expected to collapse into a single master curve provided the proper scaling exponents are used. Therefore, the scaling function will behave similarly to the real-space case and will show a saturation regime at the normalized time q_x.

[31] The PSDs were obtained from the analysis performed already in the previous paragraph on the same sample

To check the consistency between data acquired at several film thicknesses, the experimental PSDs measured during the sputter deposition process have been scaled according to (5.12) and (5.13). The rescaled curves are shown in Figure 5-34, and the resulting data collapse definitely supports the scaling hypothesis, i.e., the data from different PSDs collapse into a single master curve, which reproduces the behavior expected in real space analysis. It is important to recall that the various sets of data shown in Figure 5-34 have been scaled using β values obtained independently from TIS measurements versus thickness (see Figure 5-35), without any adjustable parameter. The rescaled PSDs curves saturate when the normalized spatial frequency $q \to \infty$, confirming the existence of a saturation regime. This work brings strong experimental evidence that our method of investigation can be used to identify the universal features of a deposition process without the need of a model of film growth.

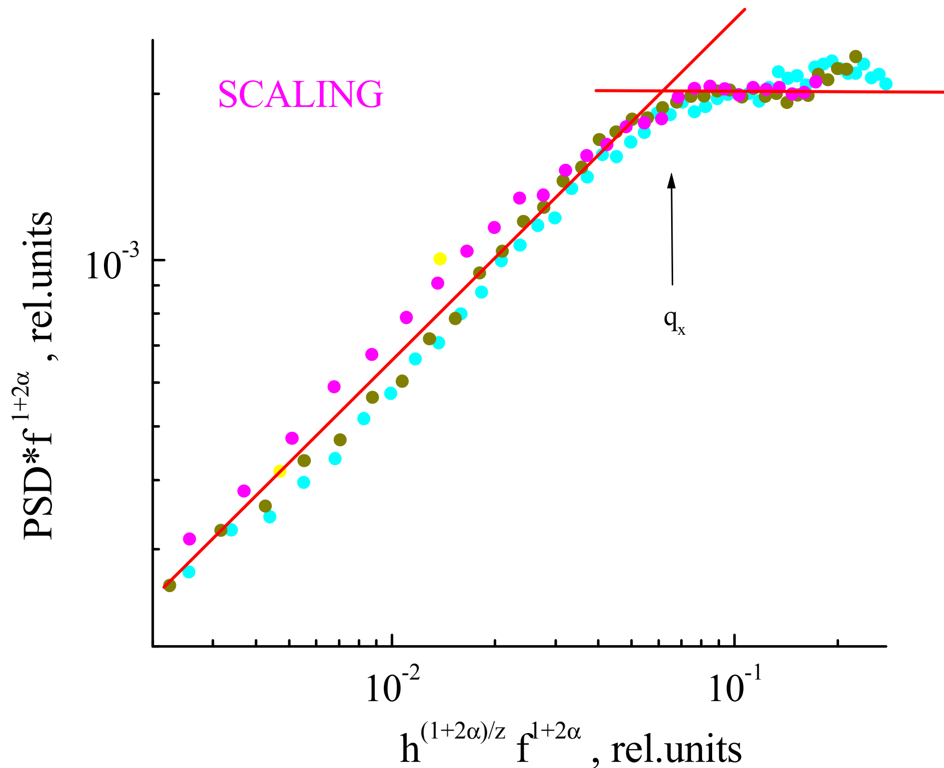

Figure 5-34: Fourier-space data collapse obtained without adjustable parameter. The straight line is a guide to the eye showing the behavior of the scaling function g(u) (see section 2.5) .

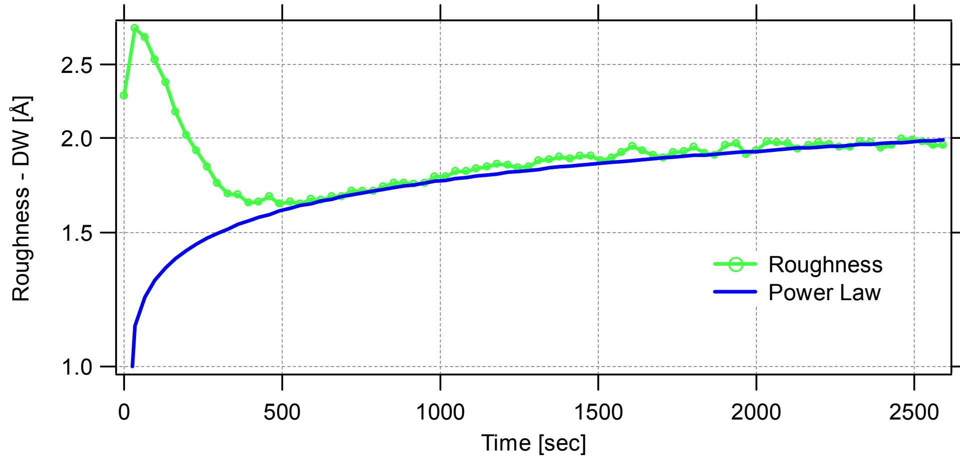

Figure 5-35: Roughness evolution obtained from TIS measurements. The corresponding scaling exponent, β=0.06, agrees with the one obtained from the data collapse.

The scaling exponents used to obtain the data collapse are α=0.18, β=0.06 and z=3. They are consistent with those obtained from independent measurements of β (from TIS analysis) and of α (from the slopes of the PSDs). The set of exponents α, β and z observed in the present work does not conform to any of the presently known universality classes. The discrepancies between the growth theories and the experiments presented so far could be due to the fact that part of the roughness may result from the presence of crystalline grains. Moreover, the scaling theories, strictly speaking, consider deposition on an ideally "flat" substrate. A more realistic substrate was never considered theoretically. Obviously, the ideal substrate cannot be realized in practice. Nevertheless, an ordering parameter, describing the local degree of crystallinity, has been recently considered by Kardar [98], showing that the application of the Kolmogorov energy cascade concept to the Kardar Parisi Zhang equation leads to scaling exponents that are completely different from the one predicted by linear and non-linear theories of film growth. These considerations further emphasize the difficulty for the existing growth models[2] to predict the scaling exponents and conversely, one should be cautious when using growth models purely based on scaling exponents.

The roughness exponents were obtained from independent analysis and indicate the suitability of the proposed method for dynamic scaling analysis, i.e., for the determination of α, β and z. Our scaling analysis method may have important consequences in the study of film growth processes as well as for many future experiments in thin films and multilayers deposition. We are not aware of any other experimental method providing a simultaneous measurement of all the scaling exponents. In particular, it is known that if two of the scaling exponents are measured the third one can be uniquely determined. Therefore, our method could uniquely determine a universal behavior and confirms the existing scaling theories. Such an experiment would require the data-collapse analysis to

be performed for different material systems. If the data collapse is achieved with a unique set of parameters α, β and z the system is said to belong to a certain universality classes, independently of the details of the experimental setup.

5.8 Critical analysis of the scattering method

In this section, we analyze scattering diagrams taken at two different grazing incident angles on the same sample. As mentioned in 5.4, a change in the grazing angle leads to a change in the diffusely scattered intensity and in the width/shape of the angular distribution radiation. At the same time, the PSD function, extracted from the experimental data, should not depend on the grazing incident angles since it describes the properties of the same surface. Therefore, a comparison of the PSDs obtained from measurements made at two different angles is a relevant exercise to verify the consistency of our method.

For this study the sample presented in section 5.3 was characterized by XRS at two grazing incidence angles, namely of θ_0=0.15° and θ_0=0.5°. Unfortunately, as the surface of this sample was particularly rough the comparison of the PSDs extracted from the XRS measurements with the one obtained from AFM data would not coincide. This set of measurements is the only one, presently available to perform such a comparison. Therefore, the proposed comparison will remain qualitative.

When the film was very thick (~70 nm) we have used the formula (3.16) for the scattering diagram $\Pi(\theta,h)$, of a semi-infinite substrate made of tungsten and we obtained the PSDs corresponding to both measurements. The results of these calculations are shown in Figure 5-36.

The PSD functions extracted from the experimental data obtained at various grazing incident angles coincide quite well with each other. Then, the independence of the experimental PSD function from the grazing angle θ_0 of the probe beam supports the validity of our approach, i.e., the possibility of applying the perturbation theory to process the experimental XRS data.

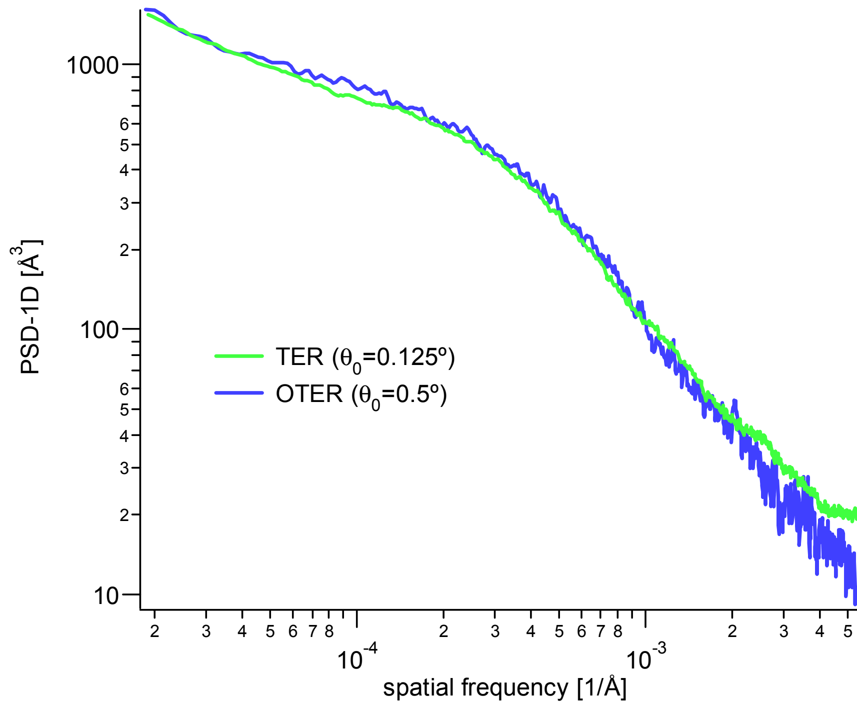

Figure 5-36: PSD spectra obtained from two independent scattering measurements respectively in TER and OTER conditions. The excellent agreement between the two measurements confirms the consistency, the effect of the near surface transition layer on the measurement being negligible.

The topography of the film surface was analyzed by AFM in air after W coating using two scanning windows, 8 and 1 μm. A total of 256x256 points were sampled. The Figure 5-37 shows the scan with the 8 μm window. The PSD obtained by combining the two AFM measurements is also given in Figure 5-37, showing a roll-off in the middle spatial frequency region, around f=4-6 10^{-3} nm^{-1}. At larger frequencies the PSD fall with a very high fractal index, i.e., with a roughness exponent α~1.2.

When compared with AFM, the PSDs would only coincide qualitatively because of the presence of a "knee" in the PSD profile. The PSD obtained from AFM measurement differs by almost one order of magnitude from the XRS one. Moreover, the fractal index is very high for AFM measurements, i.e., larger than 1 (limit for self-affine surfaces). The are numerous possible reasons for this discrepancy, including an effect induced by the FFT processing, a possible inaccuracy of PT to this particular data set, the possible presence of a transition layer formed on the surface after exposure to air.

Undeniably, the most conclusive proof could be provided by a comparison of the XRS data with independent results obtained by other methods, primarily, one of SPM methods illustrated in 0. Comparative analysis based on the data obtained by the XRS and SPM methods, including AFM, were performed by several authors including the author of this manuscript and can be found in Refs. [51, 99].

The AFM and the XRS characterization methods are based on quite different physical phenomena: attractive and repulsive molecular interactions and the diffraction of electromagnetic radiation by an inhomogeneous interface. These methods provide different experimental information, namely, a two-dimensional surface relief in atomic-force microscopy and an angular distribution of the intensity of scattered radiation in the X-ray scattering method. Finally, the technique of extracting the PSD data from the scattering diagram strongly depends on the model of surface used and the theory of interaction between radiation and roughness. Therefore, a comparison of the XRS and AFM data for the same samples is not only of practical importance but also of considerable scientific interest. A detailed analysis of this issue remains incomplete and is envisaged for near future experiments.

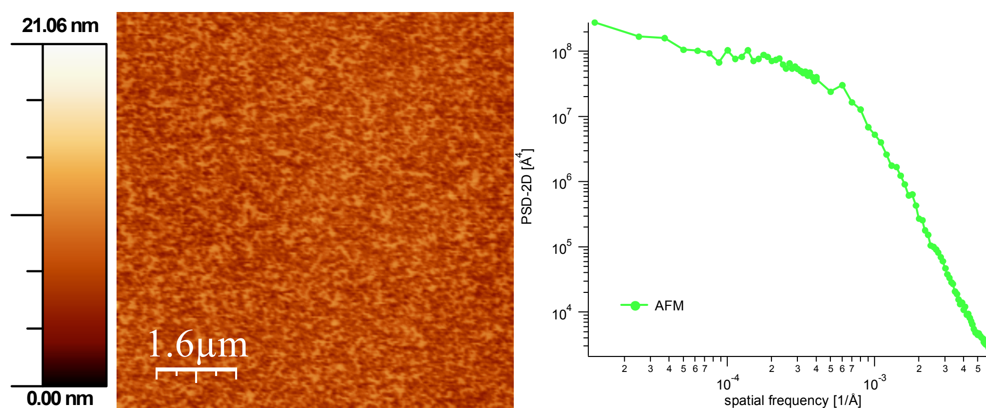

Figure 5-37: AFM topograph of the sample analyzed and its correspondent PSD (right), The PSD was obtained combining two measurements having scanning windows of 8 and 1μm and 256x256 sampled points.

5.9 Minimization of the surface roughness

We have seen that the film deposition is very sensitive to the initial growth condition. The contribution of the substrate to the roughness must be low as compared to the contribution of the deposited layers. Therefore, substrates of high quality, i.e., without local imperfection and/or chemical contaminants, and smooth ($\sigma < 1$ nm), are necessary. So, the minimization of the roughness for X-ray optical applications must start with the specifications on the substrate.

An important parameter, which determines the resulting roughness, is the film thickness: when growing thick films, roughness can become excessive. At large film thickness columnar growth and/or crystallization might play an important role. We have presented several analysis methods that just show their limits in the case of small film thickness. To perform, in this region, an analysis that would not require a model of film growth, measurements would have to be obtained for scattering angles larger than that

obtained with our improved 2D detector. This is, probably, not an easy issue, at least from a technical point of view. Means of improving this situation include the choice of more favorable X-ray energies and/or the use of a less sophisticated TIS data acquisition method[32].

In all cases, even if the extraction of the PSDs is not always possible, the interpretation of the measured data from a physical point of view and based on the experience accumulated can help improving the performance of a fabricated film. The use of a real time method offers a net advantage over a sequential iteration on the process parameters on the base of ex-situ analysis. Using real time analysis one could perform a parametric study of the ultimate parameters controlling the roughness development, and eventually perform a systematic control and optimization. These parameters are the working pressure, the temperature of the substrate, the distance between sample and sputtering target as well as the energy and the angle of the impinging particles.

Despite the high throughput achievable with a real time XRS method, a systematic study of the parameters influencing the roughness development would require labor-intensive experiments as well as intensive data analysis, in a time schedule that would overcome the time of this PhD thesis. These issues remain a challenge for future research in this field and for the author of this manuscript.

[32] for many situation can give a useful and fast process control parameter

Chapter 6 Real time studies on surface etching

Finding a process that could optimize the figure and the finish of a mirror surface is a technological goal that is crucial for the development of hard X-ray optics. The main reason is that present polishing techniques are difficult to apply to curved optics. This situation, convinced us to investigate the ion beam fabrication process, a process already investigated by some authors [100, 101].

In this chapter, experimental measurements acquired either during serial or a parallel mode of deposition will be discussed and compared to the analysis performed for the case of sputter deposition of thin film. To complement the findings, an AFM study will be presented. Finally, the sputtering process of Si crystal surfaces is presented.

6.1 Ion beam sputtering processing

In the previous chapter, we have studied the formation of a layer using a sputter process, in which the material is removed from a target by ion bombardment to get condensed onto a substrate in the form of a layer (favorable case). Now we will study the ion removal process itself using a layer film as a target. As before our attention will be focused on the modification of the film, and, particularly, on its surface topography. When re-deposition of the sputtered material does not occur, the same theory used to describe sputter deposition could be used for ion bombardment. Here, the topography of a film deposited onto an initially smooth surface should be quite similar to an initially flat surface subject to ion bombardment. Thus, a self-affine fractal surface is expected to develop, and its exponents should exhibit a power law dependence by the erosion time t. The interesting point here is that the spatial scale of the impinging particles in use, the ions, falls in the same spatial scale (atomic) as for the roughness that affects the performance of an optical device.

The use of bombarding particles as a tool to obtain highly sharp interfaces was demonstrated in several studies, in particular by Spiller and collaborators [81, 102, 103] in

pioneer activities in the EUV lithography. Here, ions were used either conjointly or consecutively to sputter deposition. The specifications for surfaces used in EUV and X-ray optics are very close to each other, therefore, it would make sense to use ion processing for fabricating high quality X-ray mirrors.

Except for Refs. [81, 102, 103], most of the experimental results on ion bombardment found in the literature can be classified in two main categories. There are results in which ion sputtering can lead to the development of periodic ripples on a sample surface[79-81, 104-106]. Under certain conditions, these ripples could be even straight and ordered. Several recent investigations have provided rather detailed and convincing evidence that, under certain experimental conditions, ion eroded surfaces would become rough, the coarsening effect following the predictions of various scaling theories, see, e.g., [2, 44] and reference therein. Moreover, these investigations did not report any evidence of ripple formation on the surface.

These two morphological tendencies, usually treated separately, have recently been described using a unique theoretical framework proposed by Barabasi and Cuerno [105]. It has been created to discuss the dynamical aspect of the sputtering phenomena including also non-linear effects. The following discussion will be made in the light of the existing physical models [107].

6.2 Ion-induced ripple formation

In this section, following the description given by Chason [108, 109], the theory of ion-induced ripple formation will be briefly presented. The first widely accepted theoretical approach describing the ripple formation on an amorphous substrate was developed by Bradley and Harper (BH) [107]. This (linear instability) theory is rather successful in predicting the ripple wavelength and orientation and agrees with numerous experimental observations. For Bradley and Harper, the ion bombardment acts as a driving force to roughen the surface, while surface diffusion acts to restore the surface to its flat equilibrium state. The competition between these two processes results in the selection of a preferred wavelength that grows faster than any others wavelength. Though the theory is only valid for small-amplitude structures, it has been surprisingly successful as a basic guide to understand ripple formation. However, the BH's theory predicts an unlimited exponential increase of the ripple amplitude in contrast to the saturation of the surface width experimentally observed. Similarly, it cannot account for surface roughening or for alternative ripple orientations. Finally, recent experiments have observed ripples whose wavelength is independent of the substrate temperature, and is proportional to the ion energy, in contrast to the BH's predictions for which the ripple

wavelength depends exponentially on temperature and decreases with the ion energy [110].

In the early stages of ripple formation, as the spatial dependence on the roughening and the smoothing processes is different, instabilities appear, i.e., a spatial periodicity that grows faster than others is favored. The wave vector of the fastest growing Fourier component q* depends on the ratio of the sputter roughening rate ν_{max} and the diffusional relaxation rate, *B*, that is:

$$q_* = \sqrt{\frac{\nu_{\max}}{2B}} \tag{6.1}$$

The ripple amplitude grows exponentially at this wave vector as $\exp(R_* t)$ where $R_* = \nu_{\max}^2 / 4B$. Since the parameter B is related to the surface diffusivity and mobile defect concentration, the surface kinetics are directly linked to the wavelength of the resulting pattern. For longer sputtering times, nonlinear terms become significant so that the amplitude may saturate and the wavelength may not remain fixed.

One of the most important predictions of the BH theory is that ripples should rotate in the surface plane. For normal incidence angles, ripples with an orientation aligned along the perpendicular to the ion beam projection are expected and should rotate as the angle is reduced to grazing condition (see Figure 6-1).

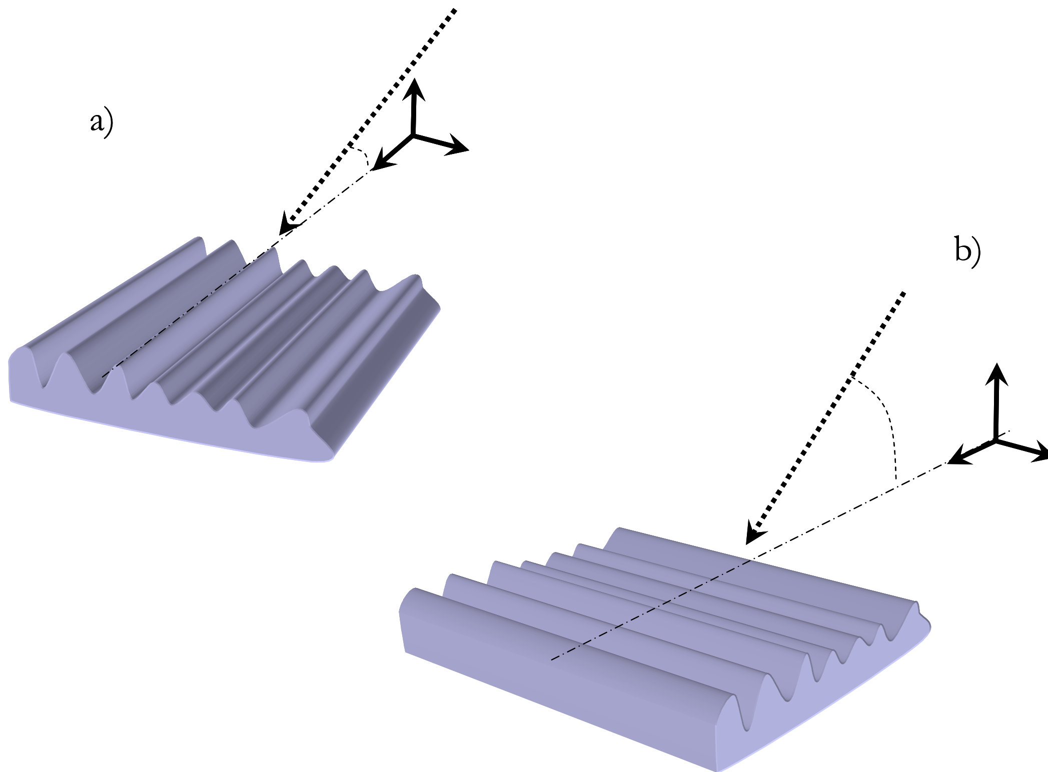

Figure 6-1: Representation of the ripple rotation predicted by the Bradley-Harper theory of ripples: grazing angles sputtering geometry (a, left) and close to normal incidence sputtering geometry (b, rigtht).

In the experiments reported hereafter, the ion incident angle was set to 10 deg. with respect to the sample surface. In this condition the ripples are expected to be generated along a direction parallel to the projection of the ion beam, i.e., perpendicular to the X-ray beam direction. For small amplitude ripples developed by ion bombardment, the scattering theory predicts an increase of the scattered intensity at the angle θ^* according to q* given by the grating equation. With similar arguments, Chason et al. have developed a spectroscopic (energy dispersive) light scattering technique based on the measurement of the spectrum of the light scattered from the surface in a non specular direction during various sample treatments[73]. They have also used this technique to study the evolution of the ripples during ion bombardment and proposed a model to describe the evolution of ripples in terms of their PSD extracted directly from the light scattering data.

In their model, Chason et al. describe the morphology of the surface by considering several smoothing and roughening mechanisms, and the evolution of the roughness height $h(\mathbf{x},t)$ is described in the Fourier space, i.e. in terms of its PSD:

Smoothing mechanism. Viscous flow and surface diffusion are the most important smoothing mechanisms. These two effects lead to an evolution of the PSD given by the following equation:

$$\frac{d}{dt}[PSD(\mathbf{q},t)] = -\left(Fq + Dq^4\right)PSD(\mathbf{q},t) \tag{6.2}$$

where Fq and Dq^4 are respectively the rates of relaxation by viscous flow and by surface diffusion and t is the time of erosion.

Roughening mechanism. The roughening, is associated with the removal of material by sputtering, is a stochastic mechanism caused by the random arrival of the ions at the surface. Assuming a Poisson-like process, this leads to another term α, which is expected to be independent by the spatial frequency and amplitude of the PSD (i.e., assuming absence of shadowing). The last roughening term, proposed first by BH, describes the effect induced by the surface curvature. This leads to a roughening term, also called *curvature term* given by:

$$\frac{d}{dt}[PSD(\mathbf{q},t)] = Sq^2 PSD(\mathbf{q},t) \tag{6.3}$$

where

$$S = J\left(A_1\cos^2(\phi) + A_2\cos^2(\phi)\right) \tag{6.4}$$

Here, J is the ion flux, ϕ is the azimuthal angle of incidence between the ion direction and the surface, the wave vector is $\boldsymbol{q}$ and the terms A_1 and A_2 are the curvature dependent sputtering yields. These last terms result from the fact that ions incident on a peak present on the surface are likely to sputter atoms on the neighboring slopes, while incident ions on a trough are likely sputter atoms near the trough.

By combining these smoothing and roughening mechanisms, we obtain a linear equation that governs the evolution of the PSD:

$$\begin{aligned} \frac{d}{dt}PSD(\mathbf{q},t) &= R_q PSD(\mathbf{q},t) + \alpha \\ R_q &= -Fq + Sq^2 - Dq^4 \end{aligned} \tag{6.5}$$

where R_q is the total rate of relaxation.

By integration of equation (6.5) we obtain the time-dependent behavior of the PSD:

$$PSD(\mathbf{q},t) = PSD_0(\mathbf{q})\exp\left(R_q t\right) + \left(\frac{\alpha}{R_q}\right)\left[\exp\left(R_q t\right) - 1\right] \tag{6.6}$$

where $PSD_0(\boldsymbol{q})$ is the initial roughness spectrum. As noticed by Puik and Schlachtman [102, 111], equation (6.6) is a generalization of the results reported earlier by Stearns. In this model the final surface morphology results from different relaxation mechanisms. It can also be used to predict the existence of a preferred wave vector q^*. We see that if $R_q>0$ the amplitude of the PSD increases exponentially, while in the

opposite case the amplitude reaches a steady state. The maximum value of R_q determines the preferred wave vector and the maximum rate R_*. The evolution of (6.6) during ion erosion, i.e. during the formation of ripples is shown in Figure 6-2. The measured PSD has been normalized to the starting spectrum to observe clearly the dominant frequency.

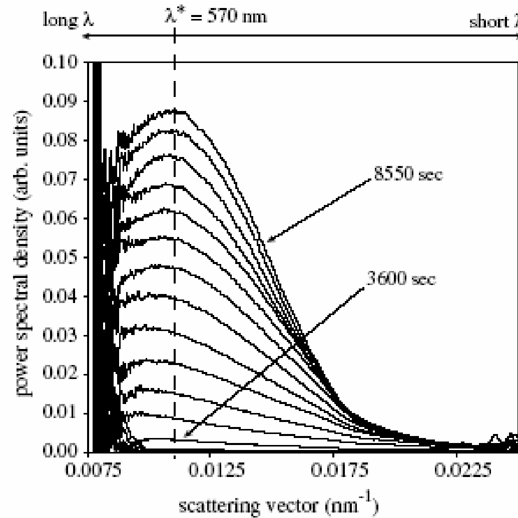

Figure 6-2 Power Spectral Density measured by Chason et al. [108] using a spectroscopic light scattering technique[73]. The displayed spectra are separated by equal intervals of time.

6.3 Ion erosion experiments

A series of samples coated with a tungsten film have been measured, and the results were discussed in chapter 5. After film deposition, they were eroded using our ECR low energy ion source while being characterized by XRS. The main motivation of these experiments was, i) to understand the surface behavior of the grown film when subjected to the action of our specific ion beam, ii) To perform a comparison between erosion and deposition processes.

The ion beam erosion process was monitored by time resolved reflectometry. The samples were irradiated with 1 keV Argon ions using an incidence angle of 10° with respect to the sample surface. The other parameters of the experiment were: extractor voltage $E_{extractor}$.= 0.2 keV and Argon mass flow MF=3 sccm. These parameters yield an ion flux Φ=3.7 10^{13} ions/cm^2/s. The experiments were performed at room temperature and the sputter time, i.e., the ion dose was adjusted to achieve the complete removal of the deposited thickness. All the experiments were performed in vacuum condition directly after the deposition of the film. The sample remained in a fixed position avoiding any movement of the sample/chamber and the specular and diffuse XRS signal were monitored. The morphology of the resulting surface (the bare substrate) was finally characterized ex-situ by AFM.

Before starting an ion etching experiment it is important to choose the amount of material (thickness) to be removed. As already discussed, see section 5.3, sputter deposition results in a very smooth surface only up to a certain critical thickness, less than ~30 nm. Above that thickness level, roughness proved to increase markedly with time (thickness). However, the film should be thick enough for the temporal scan to lead to a quantitative analysis of the external film roughness and of the film thickness evolution and to determine the removal rate. It was shown that both specular and diffuse XRS strongly depend on the interference effects occurring between substrate and film topography. This proved to be also the case for TER measurements, when the penetration depth is of the order of the film thickness. In addition, the speed of growth/erosion can be monitored if $\theta_0>\theta_{cr}$, and a minimum number of fringes appear (at least 5-6) when measuring in OTER condition. Eventually, we decided to process films having a thickness smaller than 20-30 nm, which was a good compromise with respect to the above requirements. Two samples were deposited (see Section 5.4) and subsequently eroded using grazing incidence ion bombardment.

Let us, first, analyze the specular reflectivity and compare it to the case of deposition. The intensity of the signal $R_{\Sigma}(t)$=TIS(t)+R(t)[33] measured during the deposition of a thin tungsten film deposited and the subsequent erosion are shown in Figure 6-3.

---

[33] Here R(t) is the specular reflectivity which is given by $R(t)=R_F(t)-\delta R(t)$.

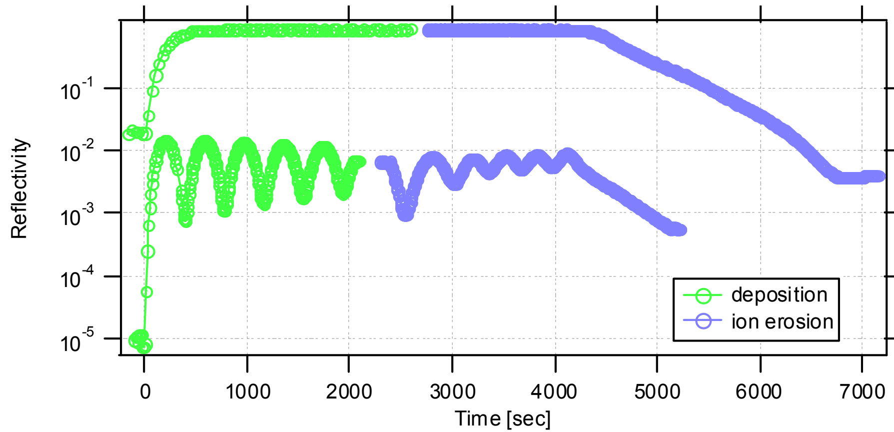

Figure 6-3: Specular reflectivity measured in situ during the deposition of a W thin film followed by its erosion. The oscillating curves on measurements in OTER condition (θ_0=0.5°) while the others are measured in TER condition (θ_0=0.15°).

Let us first discuss several features on the basis of general physical grounds instead of performing an accurate data analysis. The aim is to exploit the advantage of having consecutive measurements, and to make considerations of the general trends observed on the normalized curve.

The first remarkable feature on Figure 6-3 is the variation of film thickness with time. In the case of the deposition, the thickness was varying linearly with time *t*. In the case of erosion, the etching velocity would decrease continuously, particularly when approaching the complete removal of the film. This behavior is visible both on the TER and OTER measurements by simply observing the decay of the specular reflectivity beyond the knee points on the blue curves (representing an exponential intensity decay).

The second feature visible in Figure 6-3 is that, in the OTER condition, the amplitude of the oscillations (contrast) decreases with time, contrary to the expectation (deposition). This can be due to a number of reasons, including:

1. The variation of the optical constants during the measurement
2. The presence of small scale roughness
3. A drift of the erosion velocity along the ion beam footprint.

The first two hypotheses can probably be eluded. As one can see, the corresponding measurements in TER condition, i.e., at the beginning of the erosion process, show a constant density for the tungsten layer and a negligible presence of small-scale roughness. If small-scale roughness was present, in the reflectivity R_Σ, the latter should be further reduced, see, e.g., Section 5.5.1. Other scattering measurements performed in the OTER condition, where the Yoneda peak appears, proved that the position of the critical angle

θ_{cr}, was stabilized around a well-defined position during both deposition and erosion, i.e., the density remained constant. Thus, we conclude that the first two assumptions do not hold in this particular case, the last hypothesis being the most probable cause of the reduction of contrast. Actually, a variation of the film thickness along the footprint could generate this reduction. Let us consider the effect of a parabolic thickness profile, on the reflectivity, distributed along a footprint length L. We can then evaluate the reflectivity at a number of discrete points. If the average thickness is supposed to vary from 0 to h_0 following a linear law, then the beam profile will be described by this simple formula:

$$h(x) = h_0 + \left[q \cdot 10^{-8}(x - L)\right]^2 \tag{6.7}$$

To simplify the calculation we have considered the profile stationary along the x coordinate, as shown in Figure 6-4.

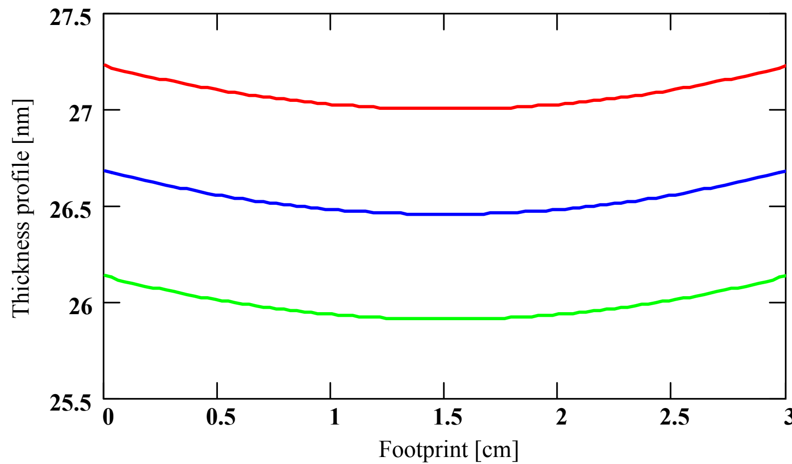

Figure 6-4: Evolution of a stationary parabolic profile, i.e., with constant aperture q.

In Eq. (6.7) the parameter q provides different parabola curvatures, of which, three examples are shown in Figure 6-5. It is possible to calculate the reflectivity of a thin film (see section 0) and to add all the contributions from the different positions x the beam footprint on the surface. Then, the total reflectivity, i.e., the sum of all the contribution from a different position x on the film reads:

$$R(\theta_0, h_i) = \frac{1}{N-1}\sum_j R(\theta_0, h_{i,j}) \tag{6.8}$$

and is shown in Figure 6-6.

As one can see, not only the amplitude of the oscillation is strongly reduced when the curvature of the parabola becomes larger, but the position of the peaks is shifted towards lower film thickness. One would expect the curvature of the parabola to get larger when the film thickness is reduced. Hence, the oscillations would vary as shown on

the experimental measurements, i.e., reducing contrast toward smallest thicknesses, therefore explaining the reflectivity behavior.

In sputtering, the problem of beam non-uniformity is often resolved by employing masks that collimate and level the ion beam flux profile. However, we did not consider this solution that can generate contamination of the film and the substrate when the mask is made of a material different from the one being analyzed. The ion beam could be sputtering material from the mask on the sample, thus complicating the data analysis. Another way of achieving a more uniform beam would consist of varying the sample-source distance or of reducing the X-ray beam footprint on the sample.

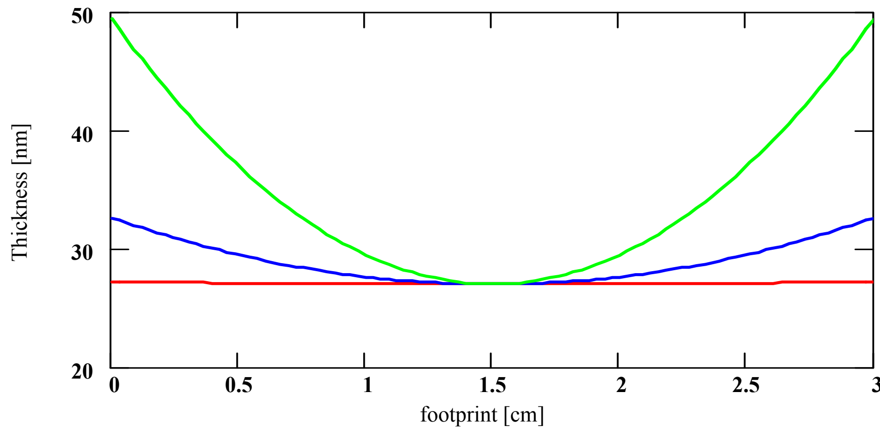

Figure 6-5: Parabolic profile with different curvatures q, i.e., 1 (red) 5 (blue) and 10 (green).

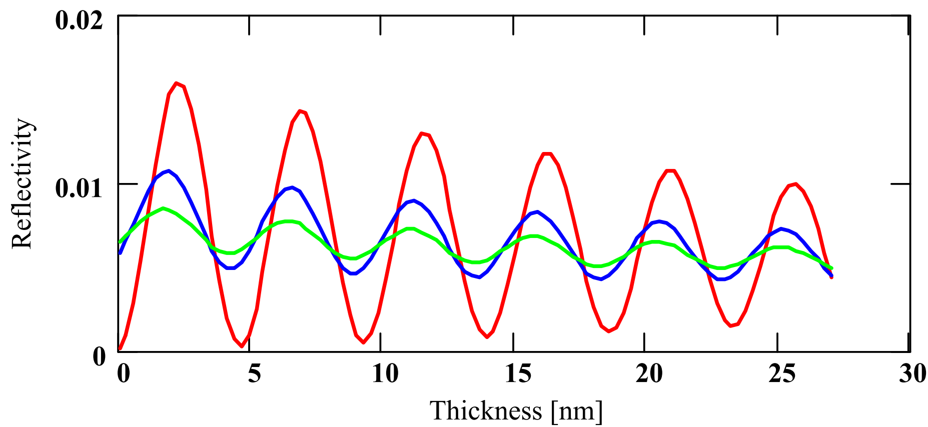

Figure 6-6: Total reflectivity evolution assuming three values for the three values of q, i.e., 1 (red) 5 (blue) and 10 (green) for the profile $h_{i,j}$

Let us now discuss the last and probably most intriguing feature in Figure 6-3: the decreasing of the intensity signal, and the decrease of the erosion rate when approaching the substrate. The possible reasons, will be investigated in the next paragraph:

- The film density increases during the scan
- Part of the sputtered material is kicked inside the bulk, i.e., intermixing occurs, making the definition of film thickness more difficult
- The sputtered material is redistributed differently over the surface. This option would be compatible with the formation of ion-induced ripples.

To answer these questions let us analyze the information contained in the distribution of the diffusely scattered intensity.

6.3.1 Evolution of roughness conformity during ion erosion

In the previous chapter, the roughness conformity during film growth has been studied quantitatively for several film thicknesses. Two main approaches (see 5.5 and 5.6) proved to describe quantitatively the overall evolution of the surface height both in the spatial and temporal domains. In this paragraph, the XRS measurements are discussed in a qualitative manner by comparing the scattering diagrams measured during erosion and deposition of thin films. To do that, we have selected several normalized scattering diagrams and compared them to the ones measured at the corresponding film thickness during deposition phase. We found a simple criterion that consists of selecting XRS diagrams corresponding to the maximum of each oscillation in the reflectivity curve (OTER) shown in Figure 6-3. These measurements are shown in Figure 6-7.

As one can see in Figure 6-7, in contrast to the deposition case, the fringes contrast quickly reduce with increasing grazing angle, while the total amount of diffusely scattered intensity remains comparable. At first glance, one may think the reduction of the contrast to have the same cause as fort the specular reflectivity. Actually, this cannot be the case since the oscillations disappear since the beginning of the erosion, i.e., when the parabola curvature is not yet pronounced. Notice that, as explained earlier, the off-specular fringes have a different physical interpretation than in the specular case, i.e., they are not Kiessig fringes. Their position is related to the film thickness, but their contrast amplitude depends only on the film and substrate conformity. See Eq. (3.26) in Chapter 3.

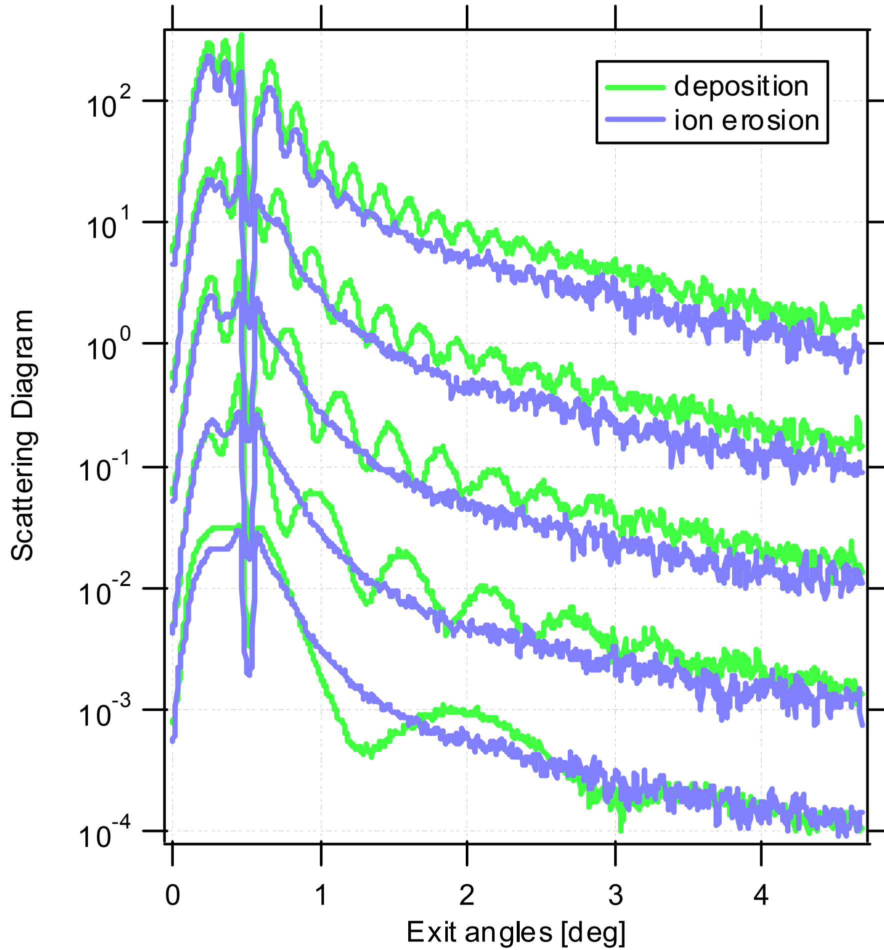

Figure 6-7: Evolution of the scattering diagrams measured during sputter deposition and subsequent erosion of a tungsten thin film at correspondent film thicknesses. The curves are shifted vertically for clarity.

The fact that the conformity is reduced during ion bombardment is quite understandable if we remember that the ion erosion is performed under grazing incidence. Grazing incidence sputtering is expected to etch the external layer only, since the sputtering yield is low in this regime. To prove it, it is possible to evaluate the distribution of Ar ions falling onto a W layer film. Following a procedure similar to that presented in 5.4, we have simulated the ion distribution using the *TRIM* Monte Carlo code. The result of the simulation is presented in Figure 6-8. As one can see, the atoms are mainly distributed within ~1 nm proving our interpretation. Despite this easy explanation, the results show an apparent contradiction with the stochastic model of film growth and ion erosion proposed by Stearns (see section 2.6 and ref. [14]). This model describes the evolution of roughness in terms of its power spectrum but suggests that roughness is replicated that would depend on the thickness h through an exponential function of the type $\exp(-b(q)h)$, where $b(q)$ is a function accounting for the relaxation

processes at the surface and h is the film thickness. In other words, the removal of a layer just after deposition should increase the conformity as the thickness is reduced.

Figure 6-8: Ion distribution inside the tungsten simulated using TRIM. The parameters for the simulation were, the number of atoms 10000, E=1 keV ϕ=80 deg and layer thickness h=27 nm.

The experimental "puzzle" can be interpreted as follows: the small penetration depth of the ions during the bombardment at 10 deg. grazing angle, results in the removal of the externals layers only and does not affect the material underneath. Therefore, the film's roughness variation induces a reduction of the correlation with the surface underneath. Eventually, the Stearns model might be able to describe the behavior observed and explain the results if the external film topography is considered as initial roughness.

6.3.2 TIS and roughness evolution during tungsten ion erosion

The experimental setup developed allows us to measure two independent quantities: the total integrated scattering (TIS) and the total specular reflectivity. The first quantity is obtained by integration of the scattering diagram using a CCD, the second one by counting the overall reflected signal using a transmission detector. As already mentioned (see Section 3.2), these two quantities can be used to estimate the value of the rms roughness (Eq. (3.38)).

As an example, the roughness evolution from TIS measurements is given in Figure 6-9. It shows (top) the time dependence of $R_{\Sigma}(t)$ during the deposition process (green curve) followed by the erosion process (blue curves). The simultaneous measurements of

TIS(t) allowed us to follow the time dependence of the roughness (Figure 6-9, bottom) via expression (3.38).

The representation in Figure 6-9 enables three actions:

1. To correlate the variations of the specular reflectivity to those of the surface roughness
2. To observe the general trends of the system during the dynamical process
3. To carry out a comparison between different processes through a unique control parameter σ calculated from TIS and R_Σ measurements.

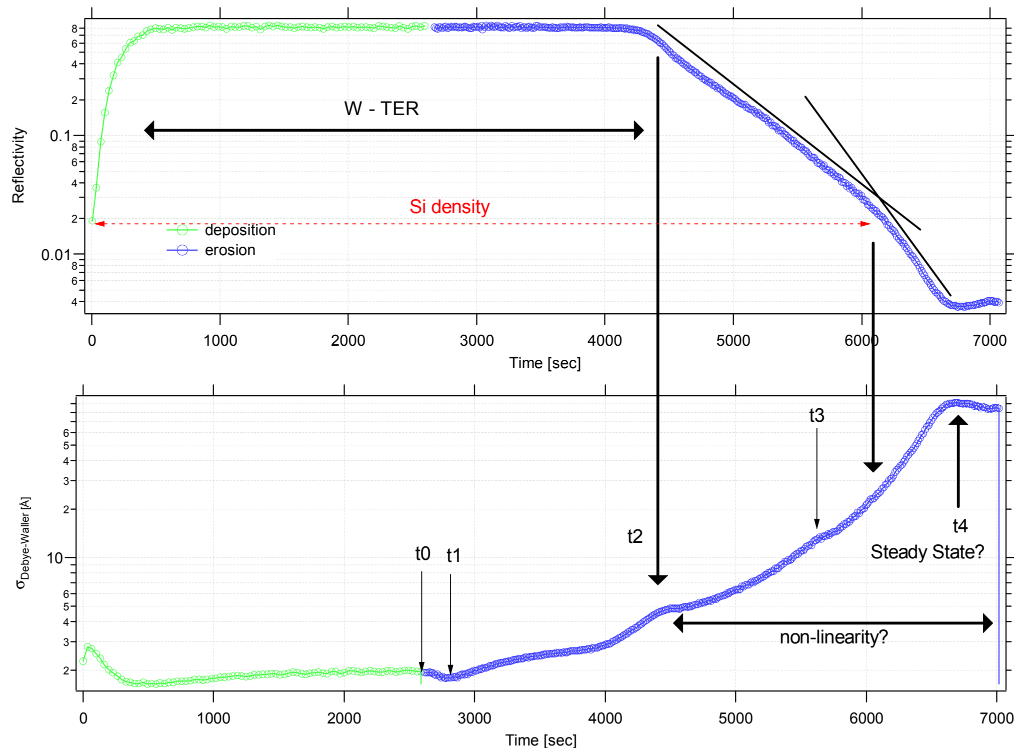

Figure 6-9: Top curve: variation of the reflectivity R_Σ during the deposition of a W film on Si substrate followed by the erosion of this film. The two straight lines are guides to the eye indicating the reflectivity corresponding to the initial Si density. Bottom curve: evolution of the corresponding roughness with time, obtained simultaneously via the acquisition of the TIS signal in (3.38).

Hereafter, the discussion is made by dividing the temporal evolution in Figure 6-9 (bottom) by subsequent intervals of time Δt corresponding to different regimes. As the case of deposition was analyzed earlier, only the erosion process will be detailed here. Before to start the description of each interval Δt is worth noting that under the TER condition (starting from few hundred seconds up to ~4500 sec) the reflectivity is constant

with t and the effect of the small-scale roughness on the measured reflectivity is negligible[34].

Interval [t_0, t1] – Here, a first remarkable feature appears: at the beginning of the erosion process a tiny smoothing effect occurs and the roughness is reduced from 0.2 nm down to 0.17 nm, i.e., by ~11% (see the zoom of this region in Figure 6-10).

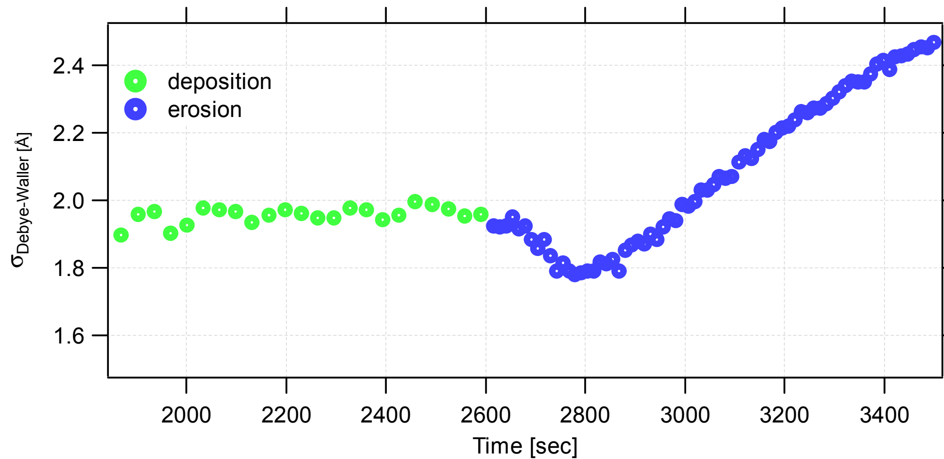

Figure 6-10: Zoom in of the region [t_0, t_1]; the smoothing occurs between 2600 and 3000 s.

At a first glance this effect seems to be very small, however, such a reduction could become extremely important when depositing a multilayer stack and confirms previous works about the growth of multilayer coatings [87, 88]. Here, since a many layers contribute to the reflectivity, a small reduction of the roughness of the deposited layers leads to considerable improvement of the total ML reflectivity. At the same time, the roughness of the upper layers strongly depends on the starting roughness and determines the roughness propagation along the stack.

Interval [t_1, t_2] – In this region the time dependence of the roughness obeys a power law, i.e., $\sigma(t) \propto t^{\beta}$, where β is the dynamic exponent. Figure 6-11 illustrates this statement. The blue line was calculated assuming β=0.25.

[34] In other words, the variation of the specular reflectivity due to small-scale roughness is negligible.

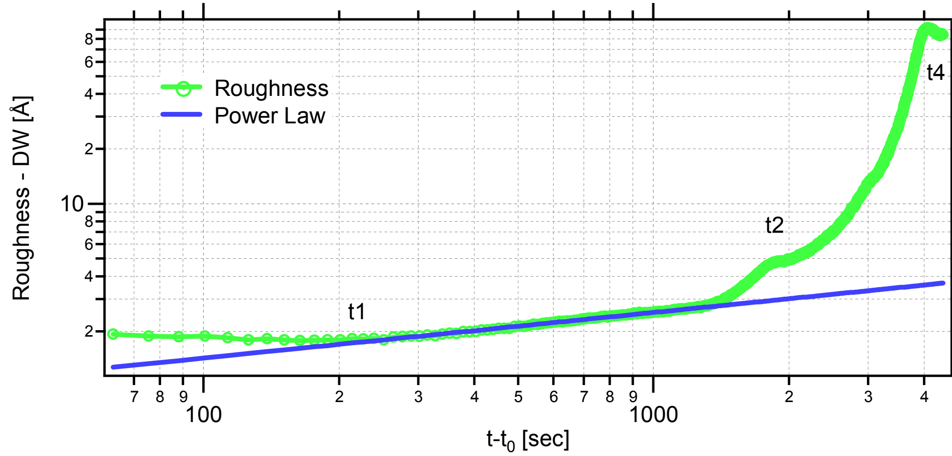

Figure 6-11: Roughness evolution using the DW model (as explained in the text). The solid line (blue) is a power law model with β=0.25).

The value of β=0.25 can be interpreted in the frame of various growth/erosion theories described in [2, 105]. To investigate the evolution of the PSDs within this interval, we first verified whether the PT is applicable. In fact, as the roughness in this region it is still small, i.e., σ<*1 nm,* and comparable to the case of deposition, we can apply the perturbation theory and calculate the PSD of the external films during the evolutions using the formula for a *semi-infinite* substrate, (Eq. (3.20)), in which the substrate is considered to be infinitely thick.

Eq. (3.20) shows that the PSDs can readily be calculated from the scattering data. The PSDs obtained are presented in Figure 6-12.

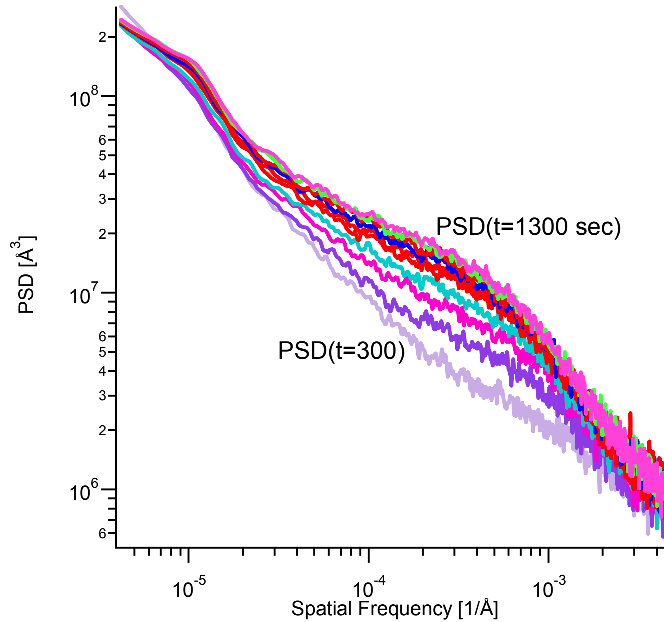

Figure 6-12: 10 PSDs calculated from XRS data and representing the external film's surface. PSDs are separated by equal time intervals in the region [t_1, t_2].

It is worth noting that ion bombardment occurs at grazing incidence, the ion and X-ray beam being placed in planes orthogonal to each other (see Figure 6-14). In this case, the BH model predicts the formation of ripples aligned along the ion beam direction. In this condition, the rippled surface acts as a grating placed perpendicular to the X-ray beam direction and the scattering intensity should be enhanced in some preferred directions (angles) according to the grating equation. The results presented in Figure 6-12 and Figure 6-13 seem to confirm this interpretation. Moreover, this data are very similar with the data reported by Chason et al. [108] and shown in Figure 6-2. To remove the statistical oscillations the PSD_f curves were represented in powers of the variable log (f), i.e., using the representation in Eq. (5.4).

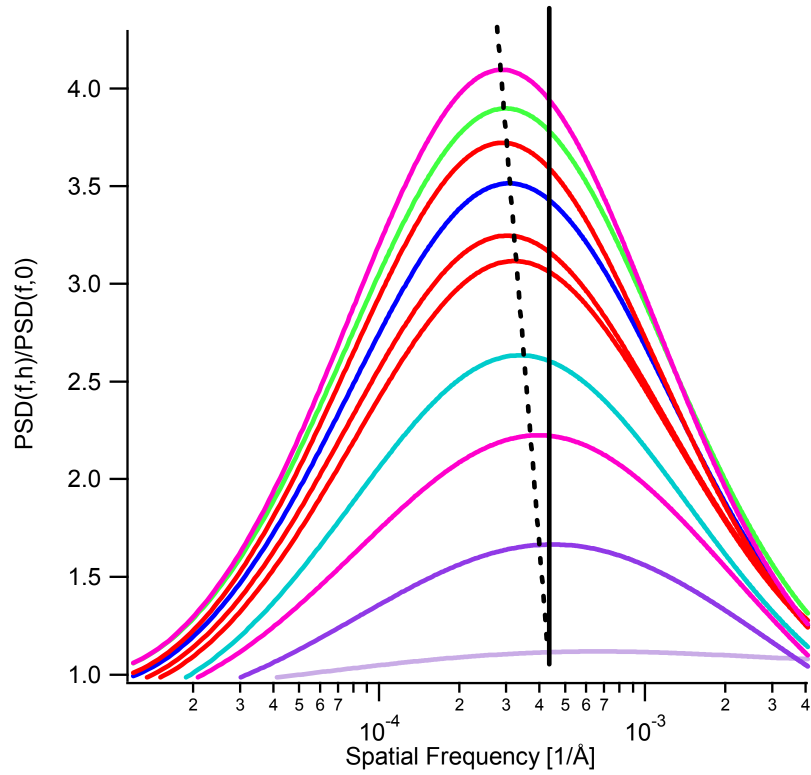

Figure 6-13: The smoothened PSD normalized to the initial spectra following the representation used in the Chason's model [108]. The dashed line is used as a guide to the eye showing the wavelength evolution with time.

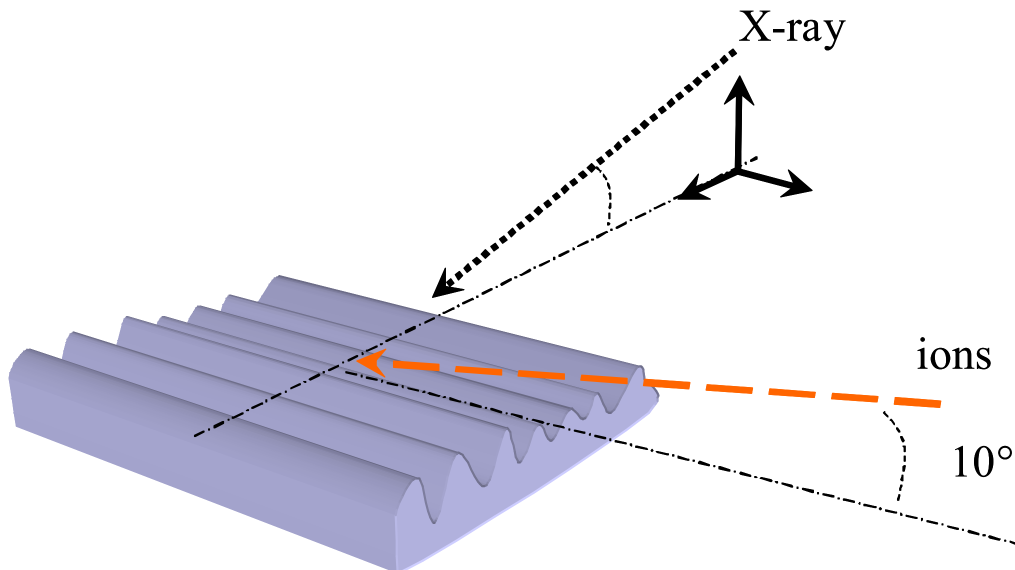

Figure 6-14:X-ray Scattering geometry with ripples formed in accordance to the BH model.

Figure 6-13 shows the evolution of the normalized PSD during erosion at room temperature at ion flux of $\Phi = 3.7\ 10^{13}$ ions/cm^2/s. The peaks of each normalized PSD displayed in Figure 6-13, are located around a spatial frequency f = 3 10^{-3} nm^{-1}. As the erosion proceeds, the typical period of the surface modulation varies from 243 nm up to 454 nm. The dashed line is a guide to the eye and indicates that the ripple periodicity evolves according to a power law (the abscissa f is in a log scale). Although such a behavior is in contradiction with the BH model (see section 6.2), the variation of ripple periodicity was also confirmed by measurements performed by Boragno et al. [80, 104] on other material systems, including semiconductor and metals.

Chason discusses this phenomenon using a linear instability theory, predicting an exponential variation of the ripple amplitude with time. However, in our case the roughness σ, and in turn, the ripple amplitude, follows a power law with exponent β=0.25. A careful inspection of Figure 6-2 shows that the authors of Ref. [108] did not observe the claimed exponential variation (notice the linear scale on both axes of Figure 6-2, and the fact that the PSDs were extracted at equal intervals of times). In conclusion, the analysis in the region [t_1, t_2], reveals the existence of ripples with a well-defined wavelength, periodicity and probably[35] orientation. They were correctly described by the linear theory proposed by Chason.

Interval [t_2, t_4] – This region is very difficult to describe in the frame of the existing models of ion-solid interactions. As one can see, the consecutive slopes of curve presented in Figure 6-11 change continuously up to the time t_4 where the specular intensity and the roughness reach a steady state value. Between t_2 and t_4 there are two knee points, one is visible on the specular curve (top Figure 6-9) and another is the point at time t_3. The former probably correspond to the transition between the tungsten film and the silicon. The point t_3 does not seem to be correlated with any features, neither on specular reflectivity or on the scattering diagrams measured in this region.

The trend observed indicates that roughness undergoes an exponential increase. In this region, further roughness analysis to extract the PSDs spectra from XRS spectra is extremely complex. The reasons are the following:

- The roughness is too large in this region and the perturbation theory cannot be used (σ>>1 nm)
- Out of the TER region an interference contribution is present and scattering is determined by three unknown PSDs that are not easily accessible because of the small film thickness.

[35] We have no direct evidence that ripples are aligned perpendicularly to the X-ray beam.

- When the film is too thin, the ions are likely to be implanted inside the films and reach the substrate further complicating the analysis.

Therefore, we will limit ourselves to a qualitative analysis of the roughness evolution in the light of the model that predicts the non-linear dynamics of a surface under ion sputtering. Since we found only one model (Ref. [105, 112]) to describe (numerically) the coarsening regime, the discussion hereafter will be only speculative.

The first remarkable feature is the dramatic increase of roughness: it is faster than a power law. This observation is probably the main indication that the system undergoes a transition to a non-linear regime where shadowing and roughening play an important role. Numerical simulations in ref. [105, 112] indicate that the non-linear terms should not affect the surface morphology or dynamics until a crossover time τ has been reached. For early times, i.e., for $t < \tau$, the surface morphology and the dynamics are expected to be described by a linear theory (for us this regime correspond to the case [t_1; t_2=τ]). Beyond this crossover time τ, the nonlinear terms become essential. One of the most striking consequences of these terms is that the surface roughness increases abruptly. Furthermore, the ripple pattern generated in the linear region disappears, and the surface exhibits kinetic roughening. A qualitative analysis of the XRS signal beyond the time t_2 shows that the intensity did not exhibit any enhancement of the intensity at scattering angles anymore.

Another quantity that reflects the transition from the linear to the nonlinear region is the erosion velocity. The nonlinear terms tend to decrease the mean height variation. The inspection of the erosion velocity was performed on the base of data acquired in OTER condition. Its rate was proved to vary with the erosion time as seen by inspecting the position of each peak on R_Σ. However, this effect, if existing, would be mixed up with the geometrical effect described in 6.2.1.

After the first crossover time τ the surface roughness should be stabilized, and the ripples should disappear. Here, the system enters a rather long transient region where the surface is rough, and with no apparent spatial ordering.

Interval [$t>t_4$] In this region the sample is consisting of only silicon, as sputtering takes place with a very high ion dose. The real time scan was stopped, and the sample was analyzed ex-situ using an AFM.

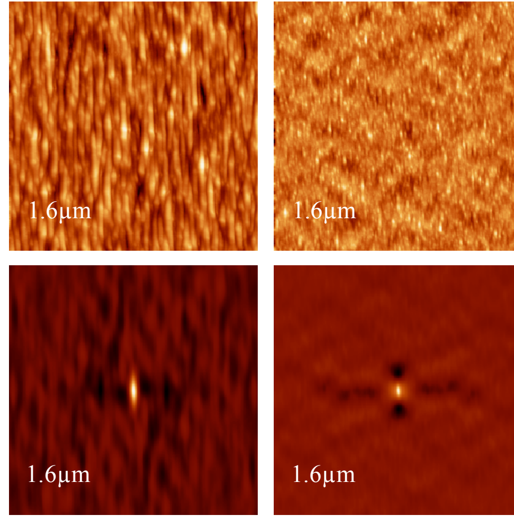

Figure 6-15: Ion sputtered surfaces analyzed with an AFM using 10 μm windows (top, images) accompanied with their self-correlation (bottom). The ripple morphology is aligned along the ion beam direction and is manifested by an elongated correlation peak along the vertical axis (bottom).

Figure 6-15 show the surface morphology of the same sample after ion bombardment at 10° grazing incidence during the two experiments performed with a different ion dose. Two morphologies are clearly observed: small ripples at reduced ion-dose (right, Figure 6-18), and better-defined ripples (sample measured in TER condition, left Figure 6-18). Both structures are oriented parallel to the ion beam projection on the substrate surface, which is consistent with the theoretical predictions of the BH model. According to this model, the ripple amplitude should evolve as the ion dose received during the process is increased. One question that arises is whether the ripple structure was present before reaching the steady state value (time t_4). The answer could be only obtained by analyzing this system with a method capable to analyze a rougher surface. Such a method should be able to differentiate both the dynamic from the morphology aspects. One way of overcoming the smooth surface limit could be to use a speckle based metrology technique. As noticed by Françon [113] measuring the speckle contrast in real time would enable to analyze roughness up to largest value defined by $g = [2k\sigma \sin(\theta_0)]^2 > 1$.

6.4 Ion beam assisted deposition

Several authors [87, 88, 111, 114] motivated by the need to optimize the reflectivity of their multilayer and thin film structures, used ion beam assisted deposition (IBAD) as manufacturing process. Some of them [87, 111] developed methods to control roughness in-situ through the measurement of the specular reflectivity. However, none of these experimental methods were designed to perform diffuse X-ray scattering measurements

that, in turns, can provide additional information such as PSD and conformity between the interfaces.

IBAD can be operated in two different ways: i) successive iteration of a deposition process followed by ion bombardments of a film or ii) simultaneous deposition and partial removing of the growing film by ion bombardment. In a recent work[115], Carter compared theoretically these two modes of deposition. He pointed out that the superiority of one or the other mode of deposition was dependent on the ratio of the growth and erosion rates. Different surface relaxation processes, including viscous flow and surface diffusion, were examined and found to affect both the average surface roughness and the spatial frequency spectrum of the roughness. In the concluding remarks, he made the following observations: "*Unfortunately, no comparative experimental data exists with which to compare the current predictions for both modes but studies of serial mode and parallel mode separately tend to confirm the validity of the approach. It is advocated that structured comparative experimental investigations should be undertaken to further test the predictions made here which would then allow firmly advised choice of optimised process routes for general film deposition requirements. It is also suggested that, where possible, not only surface roughness as determined from the averaging inherent in the variance* σ^2 *but also the power spectral density of the spatial frequencies that comprise the roughness should also be measured since this can illuminate the dominant relaxation mechanism.*"

This comment is meant to show that the instrument and the methods of roughness analysis developed during this thesis would actually allow performing such a comparison. This text also emphasizes that speed of growth and erosion are tunable parameters, and can be adjusted to a desired rate of layer growth.

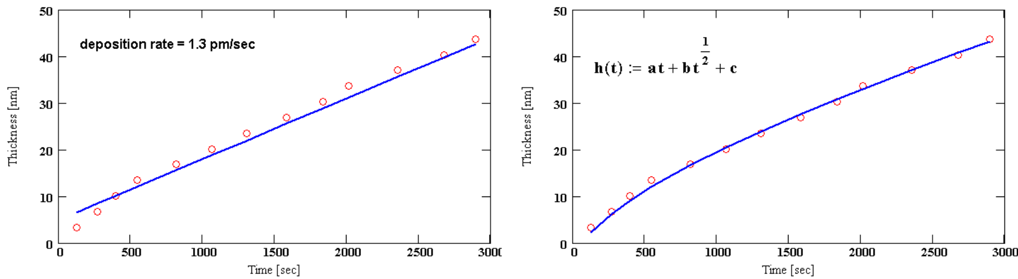

Figure 6-16: Variation of film thickness as a function of time during IBAD. Left: experimental point superimposed to the expected dependence with a deposition rate of 1.3 pm/sec (left). Right: the same data are fitted to another polynomials of the variable t $h(t) = at + b\sqrt{t} + const$.

We have performed XRS measurements during IBAD with an Ar+ conducted at 9.3 10^{-3} hPa pressure, 3 sccm gas flow and 50 mA target current. The ion source was operated in parallel to the deposition and ion parameters were the same as in our previous test case (see 6.2.1.).

The thickness profile obtained from the analysis of the reflectivity curve is shown in Figure 6-16 (dots) and Figure 6-17 presents the evolution of the XRS diagrams at different time of growth. As the deposition system was calibrated before, see Figure 4-6, we selected a target current for the sputter rate v_d to be larger than the measured erosion rate v_e. At 50 mA the deposition rate is typically $v_d \sim 8\ pm/\sec$ while the removal rate is ~6 pm/sec. By combining these two processes, we obtained an effective growth rate $v_d = 1.3\, pm/\mathrm{s}$, a value close to our predictions (see Figure 6-16, blue-line, left). However, the fact that the thickness dependence is somewhat different from a pure linear dependence (Figure 6-16, right), suggests a possible enhancement of the ion-etching rate as the time goes by. This effect was also found by Puik in his thesis [116], and attributed to a high mobility of the atoms.

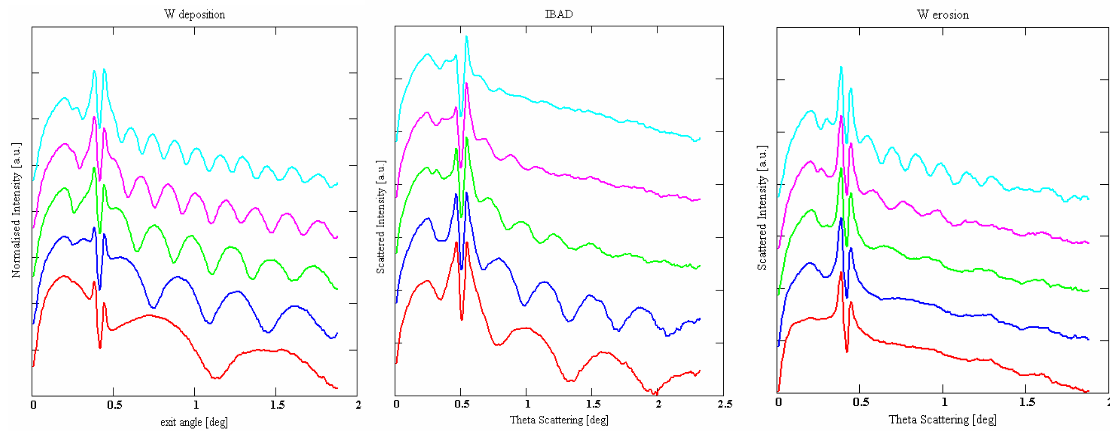

Figure 6-17: Scattering diagrams measured for the same sequence of film thicknesses at different sample treatments. Sputter deposition (left), IBAD (middle) and ion erosion process (right). The curves are shifted vertically, by a factor 10 each, for clarity.

Figure 6-17 shows that the IBAD process can be successfully monitored using our experimental technique and method to extract the PSD. Here we will limit ourselves to the qualitative comparison of the scattering diagrams obtained sputter deposition, IBAD and ion erosion. The most striking feature concerns the conformity arising when the film thickness is evolving. We have already discussed in 6.2.2, the fact that, the conformity of a film is reduced when ion erosion takes place while, during deposition, the degree of conformity is maintained even for large film thickness. The IBAD case is expected to lie between these two regimes and the spatial frequency at which the replication factor decay by a factor e, is expected to reduce more quickly in comparison to sputter deposition. This proved to be the case, see Figure 6-17 center. As one can see in Figure 6-17, the fringes appearing due to the roughness conformity disappear more quickly during IABD than during sputter deposition. Notice that each scattering diagram is measured at correspondent film thicknesses using the criterion explained in 6.2.2.

Another feature concerns the amount of diffuse scattering. Figure 6-17 shows that IBAD results in a higher level of diffusely scattered intensity, in contrast to the cases of sputter deposition and ion erosion. A higher level of disorder induced by the erosion process probably explains this. In the works [87, 88, 111, 114] the ion assistance was used in combination with e-beam evaporation. This is the only combination that proved to reduce the rms roughness. Our previous analysis, see Fig. 6.10, indicates that smoothing can only occur by employing a serial mode of ion irradiation with ion dose reduced to the time intervals (t_0-t_1).

In conclusion, by tuning sputter or erosion rates, one can adjust the speed of growth to the desired level. The measurements shown in Figure 6-17 clearly demonstrate the potentiality of our method to meet the conditions defined by Carter in ref [115]. Moreover, a detailed analysis at the beginning of the deposition process is also possible, opening the possibility of performing a new type of experiments focused, e.g., to the study of deposition at small thicknesses ($h<1$ nm).

6.5 Ion bombardment of silicon

In this section, we present an analysis of the ion beam etching process of Silicon. We processed Si samples in a high-vacuum chamber with a base pressure of 2 10^{-7} hPa. In all our studies, we used single-crystal Si (100) substrates. Notice that, in contrast to the previous analysis, the samples were not coated before etching. Prior to etching, a nitrogen gas jet blown on the surface was used to remove particles. The samples were irradiated with 1 keV Argon ions at an incidence angle of 10° with respect to the substrate surface. The experiments were performed at room temperature and the sputtering time, was varied from several minutes up to several hours. The surface morphology was then characterized by atomic force microscopy (AFM) and by X-ray scattering during experiments performed in air. Figure 6-18 show AFM images of a sample bombarded at 10° grazing incidence for 60 min. Two morphologies are clearly observed: a smaller ripple with a periodicity in the range of 50 nm and an amplitude of 4-5 nm and a larger saw tooth-like structure with period in the order of 400 nm. Both structures are oriented parallel to the ion beam projection on the substrate surface, which is consistent with the theoretical predictions of the BH model. The smaller ripples dominate the surface morphology for sputtering times shorter than several minutes. They appear superimposed to the larger-wavelength saw tooth-like structure for longer sputtering times.

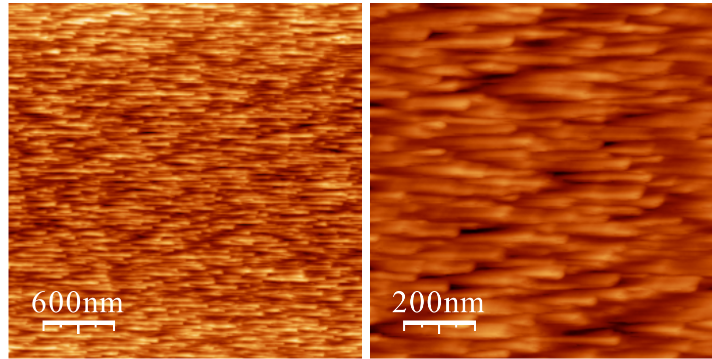

Figure 6-18: Silicon surface after ion bombardment analyzed by AFM with two different magnifications, corresponding to 8 μm and 1 μm AFM window.

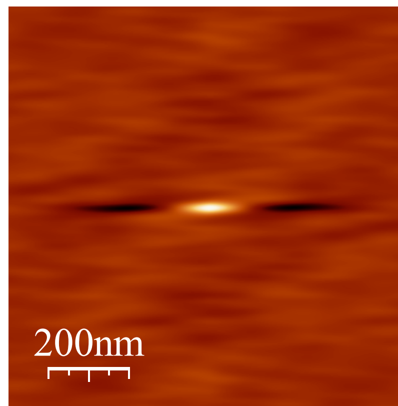

Figure 6-19: Self-correlation function of the 1 μm^2 AFM image (in Figure 6-19). The elongated shape of the correlation peak is an indication of the lateral extent of the ripples.

The AFM images (see Figure 6-20) indicate that, although the saw tooth like morphology becomes predominant, the nano-ripple structure is still present, even after several hours of ion sputtering (>3h). This is evident if we look at the self-correlation function that has an elongated shape in one of the diagonal and the unusual anti-correlation shape. The data indicate that the silicon substrate should be sputtered only for shorter times, less than 60 min, to avoid their formation.

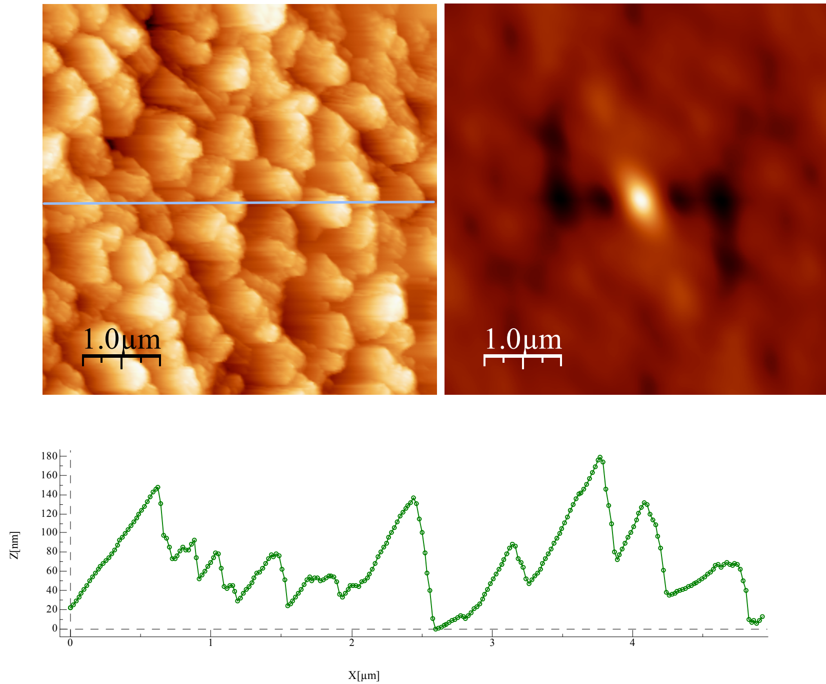

Figure 6-20:The last AFM image of this dissertation is devoted to the first sample processed during all this thesis. Its morphology was visible also by naked eyes due to its periodicity, which diffracted natural light predominantly at the blue wavelength.

Further inspection of the facets showed that their angle is strongly correlated to the ion incidence angle and was around 13° while the local roughness on each facet was extremely reduced, see figure 6.21 bottom. This observation suggests that bombarding at extremely low ion angle could probably lead surface smoothing. Other authors, recently started considering the grazing angle geometry for smoothing semiconductor surfaces and reported experimental evidence that sputtering can be used successfully to obtain surface smoothing [100, 101, 117].

We also measured the effect of this type of morphology on the 2D scattering distribution. We acquired two images, with and without a beam stop, in the plane of incidence. The primary beam was reduced in the horizontal direction to have a symmetrical pencil beam of 0.2 x 0.2 mm^2 size while the surface was probed at a 0.5° grazing angle The recorded scattered intensities were then added, after normalization, to obtain the 2D pattern. The scattered intensity, shown in Figure 6-21 in log scale (arbitrary units) was obtained by summing the two measurements while accounting for different exposure times: 20 s for the in-plane scattering and 500 s for the out of plane.

As one can see the scattered radiation is distributed asymmetrically with respect to the incidence plane. The scattered intensity seen on the left side of the image is enhanced along one diagonal whose direction is probably connected to the inclination of facets

modulating the surface morphology. The existence of a saw-tooth morphology was also reported by other authors [106, 118] and analyzed by XRS [118] using scanning detectors at different times of the erosions process.

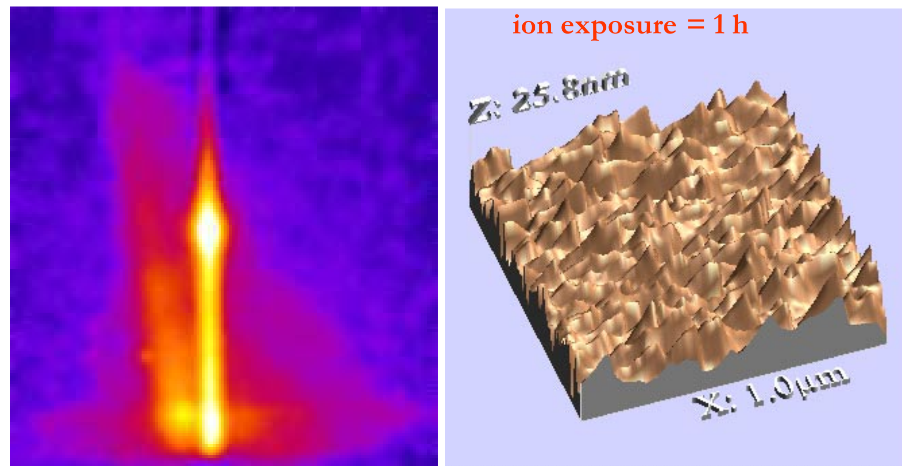

Figure 6-21: 2-D X-ray scattering from rippled surface like the measured with a grazing incidence angle of 0.5 deg.

Notice that the integration time needed to monitor the out-of-plane scattered intensity is of the order of 500 s at BM5 (to reach enough counting statistics), a value larger by a factor 10^2 than the one needed for in-plane scattering. For this type of real-time measurements, an undulator beamline, instead of a bending magnet, would be desirable when scans are to be performed. Alternatively, focusing or using a wide band-pass monochromator placed downstream the source would keep the counting time in the order of the few seconds that are necessary to follow the ripple dynamics.

Conclusion and outlook

The subject of the present dissertation is the development and application of a real time in-situ X-ray scattering apparatus to the study of surfaces and thin films. This thesis work is part of the development of hard X-ray optics for synchrotron radiation carried out in the Optics group of the ESRF. The main results achieved during the thesis period will now be presented:

i) Design and the realization of a real time in-situ XRS apparatus. During half of the thesis period, a temporary setup has been designed and realized. With this setup we could define and test an experimental technique and method, and formulate the requirements for an improved setup. The final apparatus, now available also for external ESRF users, proved to be flexible and suited to the study of a many synthesis processes. These include sputter deposition, IBAD and ion beam etching. The versatility achieved by the setup allows to perform parametric studies on ion beam etching and film growth, on various combinations of materials, to obtain highly smooth thin films. The performance of the instrument for real time analysis has been demonstrated, therefore, achieving the objectives of the research project.

ii) Development of a characterization technique for studying thin films with real time XRS. The methods developed allow to describe quantitatively the deposition process in a model-independent way in a range of thickness extending from 1-2 nm up to 20-30 nm when roughness does not exceed 0.5-0.6 nm. In this thickness range the PSDs can be extracted and provide quantitative information on conformity, scaling exponents and several surface quality attributes, such as the rms roughness, slope error and correlation length of the surface roughness. The PSDs are accessible, in a single CCD frame, over a wide range of spatial frequencies, extending up to two orders of magnitude. The surface attributes are readily available and can be used, for example, to predict the optical performance of a focusing mirror fabricated with the same technology. The conformity arising during growth was, for the first time, analyzed in a quantitative way, defining the extent of the replication process in the direction perpendicular and parallel to the sample surface.

iii) Improvement of the real time scattering technique. A simplified spectral analysis allowed us to improve the experimental method, limiting the number of experiments to a unique temporal acquisition performed out of the total external reflection condition. Using this method, a set of PSDs representing the external surface and its mutual correlation with the substrate could be extracted without the needs of a model of film growth and of the correlation functions at the interfaces. On the base of the high quality data collected by the improved experimental setup, a dynamic scaling analysis was carried out and the scaling exponents were determined. For the first time, all the scaling exponents have been determined simultaneously.

iv) The analysis of the ion beam process using real time XRS. The experimental data have been described and successfully correlated to the experimental results found in the literature on ion-induced smoothening, roughening and ripple formation. The intriguing formation of ripple was also observed and discussed in the framework of the existing theory of ion-solid interaction.

Despite the remarkable achievements obtained with the instrument, several technical difficulties and fundamental questions remain presently unsolved. These are:

i) *The possibility of analyzing very thin films*, i.e., with thicknesses lower than 1-1.5 nm. These films are of great interest for the fabrication of SR multilayer optics. In this case, it is difficult to analyze the X-ray data without using a model of film growth.

ii) *The development of a quantitative metrology technique for rougher films and substrates*. This issue is crucial for the development of ion beam processing as a new tool to control and fabricate state-of-the-art figured and polished optics.

When characterizing ion-induced ripples, the analysis is appropriate only if ripples have a small amplitude, i.e. for short ion exposure. Probably the best tool to analyze these structures in real time consists in the development of a new dedicated metrology technique. Techniques such X-ray near field Scattering [119] and out of plane XRS, whose study started just at the end of this work, are expected to help achieving a suitable metrology in a widest range of surfaces. The study of rougher films constitutes also a challenge for further developments both, theoretically and experimentally.

Future prospects include several technical improvements on the apparatus, e.g., the insertion of in-vacuum slits, the design of a load lock sample transfer system and the integration of a multilayers deposition system into the present setup. The latter will help in understanding the mixing effects at an interface as well as the evolution of roughness along a ML structure during the fabrication process. We also intend to perform a comparative analysis of AFM, in-situ XRS and ex-situ XRS methods as well as the analysis of the dependence of the growth/erosion processes on the initial conditions. We

expect to study new materials combination to be used in X-ray optics. The possibility of smoothing a rough substrate by thin film deposition could lead to lower requirements on X-ray mirror substrates or to X-ray mirrors with a better surface finish than today.

Résumé

Une nouvelle technique basée sur la diffusion des rayons X et un montage adapté ont été conçus et implémentés sur la ligne de lumière BM5 de l'ESRF. L'instrument permet l'étude in situ et en temps réel de la rugosité d'une surface par diffusion en incidence rasante. L'interaction des rayons X avec la surface, analysée dans le cadre de la théorie des perturbations scalaire du premier ordre, permet d'exprimer les paramètres caractérisant une surface par sa densité spectrale de puissance. En final les valeurs de rugosité, de longueur de corrélation, de conformité de la rugosité, et les exposants propres aux processus de synthèse ont été obtenus.

Les potentiels d'un tel instrument ont été vérifiés dans deux cas particuliers: le dépôt de couches minces par pulvérisation magnétron et le décapage par bombardement ionique. Les résultats expérimentaux obtenus ont été discutés par rapport aux modèles actuels décrivant la croissance des films minces et l'interaction des ions avec un solide.

Introduction

Le concept de rugosité est familier à chacun de nous car présent dans la vie courante. Ainsi, la majeure partie de la lumière que notre œil perçoit est de la lumière diffusée par des surfaces rugueuses. En conséquence, il n'est pas nécessaire d'observer un objet selon une direction spéculaire pour qu'il apparaisse à nos yeux. La rugosité est également révélée dans le phénomène de frottement, lorsqu'un corps se déplace relativement à un autre tout en restant en contact. C'est la rugosité qui rend possible, par exemple, la marche d'un individu, en permettant l'adhérence de ses chaussures ou de ses pieds nus au sol.

Une grande variété de surfaces et d'interfaces présentes dans la nature possèdent la caractéristique de rugosité et peuvent être associées au concept de fractale défini par Mandelbrot [1] en termes de mouvement brownien partiel. Dans certain cas, les surfaces apparaissent comme auto affines au lieu de purement fractales. De tels systèmes se rencontrent en optique des rayons X, en microélectronique ou en lithographie EUV, lorsqu'on considère des échelles spatiales de l'ordre de quelques micromètres jusqu'à l'échelle atomique. Le concept de surface auto affine a été créé pour décrire une surface qui se situerait entre une surface purement fractale, c'est-à-dire montrant la même morphologie à différentes échelles d'observation, et une surface non-fractale. Une surface auto affine change de forme en lorsqu'on lui applique un changement d'échelle différent dans les deux directions.

La rugosité est une mesure de la variation topographique d'une surface par rapport à une hauteur moyenne choisie par convention comme niveau zéro. Pour les surfaces synthétisées, la rugosité et sa nature stochastique résultent des processus de fabrication utilisés comme le dépôt de couches minces, le polissage ou la gravure. Même à l'échelle atomique les surfaces sont rugueuses à cause de la présence de plusieurs mécanismes de relaxation. Par exemple, lorsqu'une surface est exposée à un procédé de dépôt, l'évolution de sa topographie est liée à l'arrivée aléatoire de particules et au lissage dû au transport de matière [2]. Dans l'analyse de la rugosité elle-même, le concept de fractale permet de décrire la morphologie d'une surface avec un nombre limité de paramètres statistiques. Ainsi, trois paramètres statistiques sont suffisants pour décrire la topographie d'une surface et la distribution du rayonnement diffusé.

L'étude de la rugosité présente des intérêts à la fois fondamental et pratique. D'un point de vue fondamental, la rugosité est liée à la cinétique de surface. Étudier l'évolution de la rugosité peut donc apporter des informations sur les mécanismes de croissance. D'un point de vue technologique, la rugosité de surface détermine les performances finales des éléments optiques dans le domaine de rayons X ou de la lithographie EUV.

Cette thèse est une contribution au développement de systèmes optiques par réflexion pour rayons X durs pour des sources de rayonnement synchrotron. Les systèmes utilisés pour conditionner le faisceau X issu d'un synchrotron se divisent en trois classes: les miroirs en réflexion totale, les cristaux et les multicouches La longueur d'onde utilisée et les caractéristiques de la source (flux excédant 1013 ph/s et divergence du faisceau inférieure au milliradian) dictent les caractéristiques requises concernant la forme et le fini des surfaces. Pour optimiser la surface des éléments réfléchissants, une métrologie dotée d'une sensibilité spatiale en deçà de l'échelle atomique est nécessaire. Ceci est la motivation première de cette thèse. L'objectif du projet est de réaliser un instrument de mesure de rugosité en temps réel pour des surfaces et des films minces utilisées dans les applications SR. Les techniques de métrologie utilisées pour mesurer la rugosité peuvent, quant à elles, se classer en deux catégories: (i) Les techniques de balayage de sonde comme la profilométrie optique, la microscopie de champ proche, et en particulier, la microscopie de force atomique, (ii) Les techniques basées sur la diffusion diffuse d'un rayonnement, par dispersion en énergie et en angle. En effet, la sensibilité et la résolution optimales de chaque technique sont seulement admissibles dans une certaine bande spatiale et une gamme limitée de tailles dans la direction verticale. La combinaison de mesures obtenues avec différents instruments est indispensable pour une description complète de la morphologie d'une surface. Parmi les techniques utilisées, la réflectométrie permet de déterminer les propriétés des échantillons que sont la densité, l'épaisseur de film et la rugosité de la surface. C'est pour ses caractéristiques uniques que la réflectométrie des rayons X a été choisie pour décrire les surfaces. Le travail expérimental a été effectué sur la ligne de lumière BM5 de l'installation européenne de rayonnement synchrotron (ESRF).

Le chapitre I débutera par une présentation générale des différentes optiques X utilisées sur les lignes de lumière provenant de sources de rayonnement synchrotron et sera illustré de quelques exemples. Cet exposé se limitera aux dispositifs de formation d'image basés sur la réflexion en incidence rasante, dont la qualité est liée aux diverses imperfections des surfaces en jeu. Des processus de déposition et de polissage classiques seront passés en revue et comparés à des approches nouvelles. La diffusion des rayons X constituant l'outil principal de la recherche, les chapitres II et III exposeront les concepts physiques et mathématiques sous-tendant le phénomène de diffusion dans le cas d'une simple surface rugueuse (substrat) et en particulier dans le cas d'un film déposé sur un substrat. Les outils statistiques et les principaux paramètres de rugosité permettant de décrire une surface seront d'abord présentés. Dans le chapitre III, ces paramètres seront liés à la théorie de la diffusion par une surface à travers la théorie des perturbations scalaire au premier ordre. Une attention particulière sera donnée au concept de réflectométrie en temps réel, montrant le potentiel de la méthode par rapport aux

techniques de caractérisation a posteriori. Le premier but de ce travail a été de concevoir et de mettre en application un appareil et une technique permettant de réaliser des études pendant la déposition par pulvérisation cathodique de couches minces. Ceci constitue l'essentiel du chapitre IV. Le chapitre V expose les résultats expérimentaux les plus représentatifs et démontre les performances spatiale et temporelle de l'instrument. Une comparaison entre les résultats obtenus avec les rayons X et avec un microscope à force atomique viendra compléter l'étude. Sur la base de ces résultats, une description plus détaillée de la physique sous-tendant le processus de croissance sera donnée à la fin du chapitre.

Les résultats expérimentaux sont présentés dans le contexte d'une future utilisation de notre méthode pour des processus de fabrication de miroirs en incidence rasante. L'avantage "temps réel" de la méthode pour l'optimisation de la rugosité des surfaces sera mis en valeur. Au cours du chapitre VI l'accent sera mis sur l'étude in situ du processus de décapage par un faisceau d'ions de couches minces et de substrats de silicium. La formation intrigante d'une ondulation de surface pendant les expériences est également présentée et discutée.

Chapitre I

Les sources de rayonnement synchrotron de troisième génération (ESRF-France, APS-USA, Spring8-Japon) fournissent des faisceaux de photon avec des intensités et une qualité sans précédent. La source a une taille de l'ordre de quelques dizaines de microns en largeur à mi-hauteur (FWHM) et une divergence inférieure au milliradian. Par exemple, pour la ligne de lumière ID01 de l'ESRF, le faisceau a une divergence de 0.208 x 0.009 mrad2 et un flux de l'ordre de 1013 ph/s après monochromatisation. Pour ces machines, la gamme d'énergie des photons disponibles s'étend de quelques centaines d'électron-volt (eV) à plusieurs centaines de milliers d'eV. Les longueurs d'onde typiques associées sont de l'ordre de l'Ångström (énergie de 12.4 keV). Des surfaces ayant une forme et un fini presque parfait sont nécessaires pour réfléchir efficacement des rayons X d'énergie entre 1 keV et 100 keV, soit par réflexion totale sur des miroirs (incidence rasante), soit par réflexion de Bragg sur des multicouches (ML) ou des cristaux. À ce jour, la qualité des miroirs disponibles réduit partiellement l'exceptionnelle qualité du faisceau de photons fourni par les sources de rayonnement synchrotron. Les déviations locales de la surface par rapport à la surface réfléchissante idéale, appelées erreur de forme ou erreurs de pente, doivent être maintenues dans la gamme du µrad (RMS) sur la longueur entière de miroir, de l'ordre du mètre, alors que la micro rugosité doit rester dans la gamme de l'échelle atomique (Å-RMS). Parce que les techniques de polissage mécanique traditionnelles ont remarquablement évolué au cours des dernières années, ces conditions

peuvent, de nos jours, être réalisées, et ce, sur une éventail relativement large de matériaux. L'optimisation de la rugosité reste cependant le but, pour une pleine exploitation de la cohérence partielle de la source. Parmi les applications concernées par ce travail, on citera celles de l'imagerie, de la microscopie en contraste de phase, de la spectroscopie de fluctuation des rayons X, et de l'interférométrie des rayons X.

La grande variété des éléments optiques pour le rayonnement synchrotron peut se classer selon 4 familles: les monochromateurs à cristaux, les miroirs en incidence rasante (focalisant ou pas, avec ou sans dépôt multicouches), les lentilles de Fresnel et les lentilles réfractives composites. Dans tous les cas, les imperfections de surface génèrent de la diffusion diffuse qui dégrade la performance optique. Dans cette thèse, seuls les systèmes optiques par réflexion sont présentés. Pour des informations supplémentaires sur les autres types de composants optiques on pourra consulter l'article de revue rédigé récemment par Dhez (voir [3] et référence).

Chapitre II

Le fini des surfaces optiques est une grandeur importante dans le cas des systèmes optiques pour rayons X parce que la présence de rugosité dégrade l'image. Dans ce chapitre, les paramètres principaux affectant le degré de finition d'une surface sont discutés en introduisant la notion de densité spectrale de puissance de la rugosité (PSD), laquelle permet de décrire la qualité d'un système optique en termes de rugosité RMS, de longueur de corrélation et d'exposant de rugosité.

Les techniques de caractérisation donnant l'accès à ces paramètres et la topographie des surfaces sont également décrits. Les différentes méthodes de caractérisation sont comparées selon leur sensibilité spatiale. Le modèle d'échelle et le modèle linéaire de croissance et d'érosion d'un film sont discutés. Ces approches prouvent qu'une description paramétrique de la rugosité, par un modèle physique de la surface, combinée avec la théorie de la diffusion diffuse des rayons X (voir chapitre III), permettent de décrire de manière univoque la morphologie d'une surface dans les domaines spatial et temporal.

Chapitre III

Historiquement, les premières études scientifiques connues sur le comportement optique des couches minces ont été effectuées au dix-septième siècle. Elles apparaissent, avec toute une panoplie d'observations optiques, dans le traité de Sir Isaac Newton intitulé "Optiks" [48]. Bien qu'à cette époque, le mécanisme de la propagation de la lumière ne soit pas encore très clair, Newton fit le lien entre la couleur réfléchie par une

couche mince et son épaisseur s'est révélé être très utile. Cette méthode expérimentale est ce qui s'appelle aujourd'hui une mesure en dispersion d'énergie. Ces résultats sont à la base de certaines des méthodes de mesure d'épaisseur employées de nos jours, y compris le principe et l'appareil décrits dans ce travail. Les propriétés optiques des couches minces sont aussi liées à la rugosité de surface, inévitablement produite pendant tout processus de synthèse. Dans ce chapitre, nous avons étudié la théorie de la diffusion diffuse engendrée par l'éclairement d'une surface rugueuse par un faisceau de rayons X monochromatique et collimaté. Bien que les méthodes dispersives en angle et en énergie soient extrêmement différentes d'un point de vue expérimental, leur concept est toujours identique et basé sur la théorie de l'interaction des rayons X avec une interface non homogène. La section suivante présentera l'interaction d'un faisceau de rayons X monochromatique avec une surface rugueuse dans le cas d'un substrat nu et dans la situation particulière d'un film déposé sur un substrat. Les contraintes sur la cohérence du rayonnement au niveau de l'échantillon sont d'abord discutées. Puis, la diffusion spéculaire et diffuse sont présentées. L'approche théorique discutée dans les paragraphes suivants est basée sur la théorie des perturbations scalaire du premier ordre. Dans ce cas, l'amplitude de la diffusion est exprimée en série de hauteurs de profil de rugosité. Cette théorie constitue la base théorique de l'analyse des données expérimentales effectuée dans cette dissertation. Une telle approche théorique a été largement utilisée pour l'analyse de la dispersion de la lumière visible et s'est avérée applicable dans le domaine de rayon X, comme l'a montré Kozhevnikov au cours des 20 dernières années [34, 49-52].

Chapitre IV

Les parties les plus importantes de cette dissertation ont été la conception, la réalisation, la caractérisation et finalement l'application sur la ligne de lumière BM5 de l'ESRF d'un nouvel appareil expérimental permettant d'effectuer des mesures de réflectométrie sur des couches minces résolues en temps réel. La disposition générale de la ligne et une description des éléments optiques conditionnant le faisceau de synchrotron est présentée. L'appareil développé est décrit, y compris son mode de calibration. En conclusion, une nouvelle méthode expérimentale est présentée avec une attention particulière sur ses performances d'échantillonnage spatial et temporel.

Chapitre V

Cette partie présente des exemples d'études de croissance de films de tungstène effectuées en utilisant la réflectométrie X en temps réel. Ces exemples illustrent les caractéristiques uniques de notre instrument: sa possibilité de combiner résolutions

temporelle et spatiale, dans les deux directions, et sa sensibilité à la conformité résultant de l'évolution temporelle du film. En conclusion, après une discussion critique sur la méthode, une stratégie visant à optimiser la rugosité des miroirs en vue d'applications dans le domaine du rayonnement synchrotron est présentée.

Chapitre VI

La détermination d'un processus permettant d'optimiser la figure et la finition de surface d'un miroir est un but technologique qui est crucial pour le développement des systèmes optiques X. La raison principale est que les techniques de polissage traditionnelles sont difficilement applicables aux systèmes optiques courbes utilisés pour la focalisation d'un faisceau X. Cette situation nous a convaincus d'étudier le processus de fabrication par faisceau d'ions, un processus étudié par ailleurs dans les références [99, 100].

Dans ce chapitre, les mesures expérimentales, enregistrées lors d'acquisitions en série, et aussi en parallèle, au cours du dépôt, seront discutées et comparées à l'analyse effectuée dans le cas d'un dépôt de couche mince. Pour compléter les résultats, une étude ex-situ par AFM sera présentée. En conclusion, le processus de pulvérisation de la surface d'un cristal de silicium est présenté.

Conclusion et perspectives

Le sujet de cette dissertation est le développement et l'application d'un ensemble expérimental permettant des mesures de diffusion diffuse et spéculaire in situ pendant le dépôt de couches minces ou le bombardement ionique de surfaces. Ce travail s'inscrit dans le cadre du développement de systèmes optiques X pour le rayonnement de synchrotron effectué dans le groupe optique de l'ESRF. Les résultats principaux réalisés sont les suivants :

Conception et réalisation d'un ensemble expérimental permettant des mesures in situ et en temps réel de XRS. Pendant la moitié de la période de thèse, une installation provisoire a été conçue et réalisée. Elle a permis de définir et d'examiner une technique et une méthode expérimentales, afin d'estimer les points à améliorer lors de la réalisation d'un montage optimisé. L'appareil final, maintenant accessible aux utilisateurs de l'ESRF, est flexible et convient à l'étude d'un grand nombre de processus de synthèse. Ceux-ci incluent le dépôt par pulvérisation, l'IBAD et le décapage par bombardement ionique. L'installation que nous avons réalisée permet de réaliser des études paramétriques sur la croissance, le décapage, ou la gravure par faisceau d'ions soit de matériaux massifs tels que le silicium soit de couches minces. Il permettra aussi d'optimiser les processus de croissance de film

en vue d'obtenir des couches lisses. L'instrument ad hoc pour effectuer des analyses en temps réel a été réalisé, accomplissant ainsi l'objectif visé par le projet de recherche initial.

Définition d'une technique de caractérisation pour étudier les couches minces avec XRS en temps réel. Les méthodes développées permettent de décrire quantitativement le procédé de dépôt sans avoir recours à un modèle. Ceci est valable dans une gamme d'épaisseur s'étendant de 1-2 nm jusqu'à 20-30 nm et lorsque la rugosité n'excède pas 0.5- 0.6 nm. Dans cette gamme d'épaisseur, les PSDs pouvant être extraites à partir d'une seule image CCD, sur une bande fréquence spatiale couvrant jusqu'à deux ordres de grandeur. Elles fournissent des informations quantitatives sur la conformité, les exposants, et sur certains attributs de la surface externe, comme la rugosité RMS, les erreurs de pente et les longueurs de corrélation de la surface mesurée. Ceci pouvant servir, par exemple, à prévoir la performance optique d'un miroir focalisant, fabriqué avec des procédés identique. L'évolution de la conformité résultant de la croissance a été étudiée et analysée d'une manière quantitative, définissant l'ampleur du processus de réplique dans la direction perpendiculaire et parallèle à l'amélioration de la direction de croissance.

Amélioration de la technique d'analyse en temps réel. Une analyse spectrale simplifiée nous a permis d'améliorer la méthode expérimentale, limitant le nombre d'expériences à une seule acquisition temporelle effectuée en condition de réflexion totale. En utilisant cette méthode, un ensemble de PSDs représentant la surface externe et sa corrélation mutuelle avec le substrat ont pu être extraites sans avoir recours à un modèle de croissance de film et aux fonctions de corrélation aux interfaces. Grâce aux données d'excellente qualité collectées par une installation expérimentale optimisée, une analyse dynamique a été effectuée pour déterminer les exposants d'échelle. Pour la première fois, tous les exposants d'échelle ont pu être déterminés simultanément.

Analyse par XRS en temps réel d'une surface traitée par un processus de décapage par faisceau d'ions. Les données expérimentales ont été décrites et corrélées avec succès avec les résultats expérimentaux trouvés dans la littérature concernant la formation des ondulations et de la rugosité de surface induites par bombardement ionique. La formation intrigante de l'ondulation a été également observée et discutée au moyen de la théorie d'interaction des surfaces par les ions.

En dépit des accomplissements remarquables obtenus avec l'instrument, plusieurs difficultés et questions fondamentales ou techniques restent à résoudre. Celles-ci sont:

i) La possibilité d'analyser des films avec des épaisseurs plus petites que 0.1-0.2 nm. Ces films sont d'un grand intérêt pour la fabrication des systèmes optiques à multicouches pour rayons X durs. Dans cette gamme d'épaisseur, il est difficile d'analyser les données XRS sans recourir à un modèle de croissance de film.

ii) Le développement d'une technique de métrologie quantitative permettant d'analyser des films et des substrats plus rugueux. Cette question est cruciale pour le développement d'un outil utilisant le faisceau d'ions. Celui-ci devrait permettre d'améliorer la figure et le poli optique des systèmes optiques utilisés dans des applications SR.

La caractérisation de l'ondulation induite par les ions n'est possible que lorsque l'ondulation est de faible amplitude, c'est-à-dire dans le cas d'une exposition courte au faisceau ion. Pour analyser ces structures en temps réel il sera probablement nécessaire de développer une nouvelle technique de métrologie. Les analyses de la granularité X en champ proche [118] et de la diffusion diffuse en dehors du plan d'incidence (étude commencée récemment) sont envisagées comme bases d'une métrologie applicable à un large éventail de surfaces. L'étude de films plus rugueux constitue également l'objectif de développements ultérieurs, à la fois théorique et expérimental.

Les perspectives futures incluent plusieurs améliorations techniques concernant l'appareil, comme l'insertion de fentes sous vide, la conception d'un système de chargement et de transfert d'échantillon, et l'intégration d'un système de dépôt de multicouches. Cette dernière option permettra de mieux comprendre les effets de mélange à l'interface de deux matériaux, ainsi que l'évolution de la rugosité le long d'une structure multicouches lors du processus de fabrication. De nouvelles combinaisons de matériaux pourront ainsi être étudiées. Une analyse comparative plus poussée des méthodes AFM, XRS in situ et ex-situ est envisagée, ainsi que l'analyse de l'influence des conditions initiales sur les processus de croissance et d'érosion. Enfin, il sera intéressant d'étudier la possibilité de lisser un substrat rugueux par le dépôt d'une couche mince, ce qui pourrait constituer un moyen économique de réduire les contraintes sur la qualité des miroirs X fabriqués à ce jour.

Bibliography

1. Mandelbrot, B.B., *The fractal geometry of nature*. Rev. ed. 1983, New York: W.H. Freeman. 468.
2. Barabâasi, A.-L. and H.E. Stanley, *Fractal concepts in surface growth*. 1995, Cambridge: Cambridge University Press. xx, 366.
3. Dhez, P., et al., *Instrumental aspects of x-ray microbeams in the range above 1 keV*. Review of Scientific Instruments, 1999. **70**(4): p. 1907-20.
4. Kiessig, H., Ann. Physik, 1931. **10**: p. 769.
5. Compton, A., Phi. Mag., 1923. **45**: p. 1121.
6. Snigirev, A., et al., *A compound refractive lens for focusing high-energy X-rays*. Nature, 1996. **384**: p. 49-51.
7. Spiller, E. *Multilayer Interference Coatings for the Vacuum Ultraviolet*. in *Space Optics, 9th int. cong. of the int. comm. for optics*. 1972. Santa Monica, Cal.: National Academy of Sciences.
8. Kozhevnikov, I.V., I.N. Bukreeva, and E. Ziegler, *Design of X-ray supermirrors*. Nucl. Instr. & Meth., 2001. **A460**: p. 424-43.
9. Takacs, P.Z., Nucl. Instr. & Meth., 1986. **A246**: p. 227.
10. Rommeveaux, A., Private Communication.
11. Ice, G.E., et al., *Elliptical x-ray microprobe mirrors by differential deposition*. Review of Scientific Instruments, 2000. **71**(7): p. 2635-9.
12. Yamauchi, K., et al., *Nearly diffraction-limited line focusing of a hard-X-ray beam with an elliptically figured mirror*. J. Synchrotron Rad., 2002. **9**: p. 313-6.
13. Kirkpatrick, P. and A.V. Baez, J. Opt. Soc. Am., 1948. **38**: p. 766.
14. Jentzsch, F., Phys. Z., 1929. **30**: p. 766.
15. Underwood, J.H., *High-energy x-ray microscopy with multilayer reflectors (invited)*. Review of Scientific Instruments, 1986. **57**(8): p. 2119-23.
16. Buckley, C.J. and A.G. Michette, *X-ray science and technology*. 1993, Bristol: Institute of Physics. x, 369.
17. Angel, J.R.P., *Lobster eyes as X-ray telescopes*. The Astrophysical Journal, 1979. **233**(1): p. 364-73.
18. Aoki, S., A. Takeuchi, and M. Ando, *Imaging X-ray fluorescence microscope with a Wolter-type grazing-incidence mirror*. Journal of Synchrotron Radiation, 1998. **5**(3): p. 1117-8.

19. Citterio, O., et al. *Multilayer optics for hard X-ray astronomy by means of replication techniques*. in *X-ray Optics*. 1999. Denver, CO, USA: SPIE.

20. Citterio, O., et al., *Replication techniques for soft and hard X-ray optics.* S.A.It.-AstroTech Journal, 1999. **2**.

21. Ziegler, E., et al. *X-ray focusing using elliptically bent multilayers*. in *Optics for High Brightness Synchrotron Radiation II*. 1996. Denver: SPIE.

22. Michette, A.G., *Optical systems for soft X rays*. 1986, New York: Plenum Press. 334.

23. Hignette, O., et al. *Submicron focusing of hard x rays with reflecting surfaces at the ESRF*. in *X-ray micro- and nano-focusing: applications and techniques II*. 2001. San Diego: SPIE.

24. Ziegler, E., *Multilayers for High Heat Load Synchrotron Applications.* Opt. Eng., 1995. **34**(2): p. 445-52.

25. Yamauchi, K., et al., *Nearly diffraction-limited line focusing of a hard-X-ray beam with an elliptically figured mirror*. Journal of Synchrotron Radiation, 2002. **9**(5): p. 313-6.

26. Fawcett, S.C. *Production of x-ray optics by diamond turning and replication techniques*. in *Space Instrumentation and Dual-Use Technologies*. 1994: SPIE.

27. Abusafieh, A.A. *Diamond turned composite optics for IR and visible applications*. in *Optical Materials and Structures Technologies*. 2003: SPIE.

28. Haensel, T.J., A. Schindler, and B. Dissing. *Multiple high-period-accuracy gratings fabricated by holographic exposure and ion-beam etching with nanometer depth accuracy in silicon*. in *Optical Manufacturing and Testing V*. 2004: SPIE.

29. Ghigo, M., et al. *Ion beam figuring of nickel mandrels for x-ray replication optics*. in *Advances in X-Ray Optics*. 2001: SPIE.

30. Ghigo, M., et al. *Ion-beam polishing of electroless nickel masters for x-ray replication optics*. in *Grazing Incidence and Multilayer X-Ray Optical Systems*. 1997: SPIE.

31. Church, E.L. and P.Z. Takacs, *Specification of glancing and normal-incidence x-ray mirrors.* Optical Engineering, 1995. **34**(2): p. 353-60.

32. Schmittbuhl, J., J.-P. Vilotte, and S. Roux, *Reliability of self-affine measurements.* Physical Review E (Statistical Physics, Plasmas, Fluids, and Related Interdisciplinary Topics), 1995. **51**(1): p. 131-47.

33. Castelnovo, C., et al., *Fractal analysis of sampled profiles: Systematic study.* Physical Review E (Statistical, Nonlinear, and Soft Matter Physics), 2002. **65**(2): p. 021601-11.

34. Salditt, T., et al., *Non-specular x-ray scattering from thin films and multilayers with small-angle scattering euipement.* J. Phys. D, 1995. **28**: p. A236-40.

35. Kozhevnikov, I.V., *Use of the DWBA and perturbation theory in X-ray control of the surface roughness.* Journal of X-Ray Science and Technology, 2000. **8**: p. 253-75.

36. Church, E.L. and P.Z. Takacs, *The optimal estimation of finish parameters.* SPIE, 1992. **1530**: p. 71-85.

37. Church, E.L. and P.Z. Takacs, *Instrumental effects in surface-finish measurements.* SPIE, 1988. **1009**: p. 46-55.

38. Church, E.L., *Fractal Surface Finish.* Applied Optics, 1988. **27**(8): p. 1518-26.

39. Church, E.L., *Effects of the optical transfer function in surface profile measurements*. SPIE, 1989. **1164**: p. 46-59.

40. Church, E.L. and P.Z. Takacs, *Comments on the correlation length.* SPIE, 1987. **680**: p. 102-11.

41. Bennett, J.M. and L. Mattsson, *Introduction to Surface Roughness and Scattering.* 2nd edition ed. 1999: Optical Society of America;. viii, 308.

42. Spiller, E., D. Stearns, and M. Krumrey, *Multilayer x-ray mirrors: Interfacial roughness, scattering, and image quality.* Journal of Applied Physics, 1993. **74**(1): p. 107-18.

43. Stearns, D.G., *Stochastic model for thin film growth and erosion.* Applied Physics Letters, 1993. **62**(15): p. 1745-7.

44. Family, F. and T. Vicsek, *Dynamics of fractal surfaces.* 1991, Singapore ; London: World Scientific. xi, 480.

45. Stearns, D.G., *The scattering of x rays from nonideal multilayer structures.* Journal of Applied Physics, 1989. **65**(2): p. 491-506.

46. Stearns, D.G., *X-ray scattering from interfacial roughness in multilayer structures.* Journal of Applied Physics, 1992. **71**(9): p. 4286-98.

47. Stearns, D.G., et al., *Nonspecular x-ray scattering in a multilayer-coated imaging system.* Journal of Applied Physics, 1998. **84**(2): p. 1003-28.

48. Spiller, E., *Soft X-Ray Optics.* 1994: SPIE-International Society for Optical Engine (June 1, 1994). 278.

49. Newton, I., *Opticks: or, A treatise of the reflexions, refractions, inflexions and colours of light.* 3rd ed. 1721, London.

50. Asadchikov, V.E., et al., *Application of X-ray scattering technique to the study of supersmooth surfaces.* Nuclear Instruments and Methods in Physics Research Section A: Accelerators, Spectrometers, Detectors and Associated Equipment, 2004. **530**(3): p. 575-95.

51. Asadchikov, V.E., I.V. Kozhevnikov, and Y.S. Krivonosov, *X-ray Investigations of Surface Roughnesses.* Crystallography Reports, 2003. **48**(5): p. 836-50.

52. Kozhevnikov, I.V., *Physical analysis of the inverse problem of X-ray reflectometry.* Nuclear Instruments and Methods in Physics Research Section A: Accelerators, Spectrometers, Detectors and Associated Equipment, 2003. **508**(3): p. 519-41.

53. Kozhevnikov, I.V., *Analysis of X-ray scattering from a rough multilayer mirror in the first-order perturbation theory.* Nucl. Instr. & Meth. A, 2003. **498**(1-3): p. 482-95.

54. Holy, V., U. Pietsch, and T. Baumbach, *High-resolution X-ray scattering from thin films and multilayers.* Springer tracts in modern physics ; 149. 1999, Berlin ; New York: Springer. xi, 256 p.

55. Born, M. and E. Wolf, *Principles of Optics.* 7. ed. 1978, New York: Pergamon Press.

56. Heavens, O.S., *Optical Properties of Thin Films.* 1955, New-York: Dover Publication.

57. Tolan, M., *X-ray scattering from soft-matter thin films : materials science and basic research.* Springer tracts in modern physics ; 148. 1999, Berlin ; London: Springer. viii, 197.

58. De Boer, D.K.G., Phys. Rev. B, 1994. **49**(9): p. 5817-20.

59. Beckman, P. and A. Spizzichino, *The scattering of electromagnetic waves from rough surfaces.* 1963, Oxford: Pergamon.

60. Nevot, L. and P. Croce, Rev. Phys. Appl., 1976. **11**: p. 113.

61. Church, E.L., H.A. Jenkinson, and J.M. Zavada, *Relationship between Surface Scattering and Microtopographic Features.* Optical Engineering, 1979. **18**(2): p. 125-36.

62. Stover, J.C., *Optical scattering : measurement and analysis*. Optical and electro-optical engineering series. 1990, New York: McGraw-Hill. xi, 238.

63. Vinogradov, A.V., et al., *Phenomenon of total external reflection of x rays*. Soviet Physics - JETP, 1985. **62**(6): p. 1225-9.

64. Yoneda, Y., *Anomalous Surface Reflection of X Rays*. Phys. Rev., 1963. **131**(2010).

65. Asadchikov, V.E., et al., *Application of x–ray scattering technique to the study of supersmooth substrates*. Nucl. Instr. & Meth., 2004. **530**(3): p. 575-95.

66. Peverini, L., et al., *Roughness conformity during tungsten film growth: an in-situ X-ray scattering study*. Physical Review B, 2004(submitted).

67. Salditt, T., T.H. Metzger, and J. Peisl, *Kinetic roughness of amorphous multilayers studied by diffuse x-ray scattering*. Physical Review Letters, 1994. **73**(16): p. 2228-31.

68. Schlomka, J.-P., et al., *X-ray diffraction from Si/Ge layers: Diffuse scattering in the region of total external reflection*. Physical Review B (Condensed Matter), 1995. **51**(4): p. 2311-21.

69. Rayleigh, L. Proc. R. Soc. London. Vol. 41. 1886, London. 275.

70. Alaudinov, B.M., et al., *An optical model of a surface in the x-ray range*. Crystallography Reports, 1994. **39**(4): p. 540-50.

71. Artyukov, I.A., et al., *Experimental observation of the near surface layer effects on X-ray reflection and scattering*. Physica B: Condensed Matter, 1994. **198**(1-3): p. 9-12.

72. Artioukov, I.A., V.E. Asadchikov, and I.V. Kozhevnikov, *Effects of a Near-Surface Transition Layer on X-Ray Reflection and Scattering*. Journal of X-Ray Science and Technology, 1996. **6**(3): p. 223-43.

73. Chason, E., et al., *Spectroscopic light scattering for real-time measurements of thin film and surface evolution*. Applied Physics Letters, 1998. **72**(25): p. 3276-8.

74. Luken, E., *Preparation and in-situ Growth characterisation of X-ray Multilayer Structure*. 1997, Hamburg University: Hamburg. p. 168.

75. Ziegler, E., et al. *The ESRF BM05 Metrology Beamline: Instrumentation And Performance Upgrade*. in *Synchrotron Radiation Instrumentation: Eighth International Conference on Synchrotron Radiation Instrumentation*. 2004. San Francisco, California (USA): AIP.

76. Neissendorfer, F., et al., *The energy-dispersive reflectometer/diffractometer at BESSY-I*. Measurement Science and Technology, 1999(5): p. 354-61.

77. Albertini, V.R., et al., *Time-resolved energy dispersive x-ray reflectometry measurements on ruthenium phthalocyanine gas sensing films*. Applied Physics Letters, 2003. **82**(22): p. 3868-70.

78. Peverini, L., T. Bigault, and E. Ziegler. *A real time in-situ X-ray scattering apparatus to monitor surface roughness*. in *Seventh Conference on the Physics of X-ray Multilayer Structures*. 2004. Sapporo, Japan: Tohoku University, Sendai, Japan.

79. Gago, R., et al., *Production of ordered silicon nanocrystals by low-energy ion sputtering*. Applied Physics Letters, 2001. **78**(21): p. 3316-8.

80. Boragno, C., et al., *In situ x-ray scattering study of Ag(110) nanostructuring by ion erosion*. Physical Review B (Condensed Matter and Materials Physics), 2002. **65**(15): p. 153406-4.

81. Carter, G., *The physics and applications of ion beam erosion*. Journal of Physics D-Applied Physics, 2001. **34**(3): p. R1-R22.

82. Kimura, K., et al., Nuclear Instruments & Methods in Physics Research, Section B, 1999. **148**: p. 149.

83. Anton, R., et al. *Design and performance of a versatile, cost-effective microwave electron cyclotron resonance plasma source for surface and thin film processing*. in *The 8th interntaional conference on ion sources*. 2000. Kyoto (Japan): AIP.

84. Gruner, S.M., M.W. Tate, and E.F. Eikenberry, *Charge-coupled device area x-ray detectors.* Review of Scientific Instruments, 2002. **73**(8): p. 2815-42.

85. Barna, S.L., et al., *Calibration procedures for charge-coupled device x-ray detectors.* Review of Scientific Instruments, 1999. **70**(7): p. 2927-34.

86. Moy, J.P., et al., *A Novel Technique for Accurate Intensity Calibration of Area X-ray Detectors at Almost Arbitrary Energy.* Journal of Synchrotron Radiation, 1996. **3**(1): p. 1-5.

87. Spiller, E., *Smoothing of multilayer x-ray mirrors by ion polishing.* Applied Physics Letters, 1989. **54**(23): p. 2293-5.

88. Schlatmann, R., J.D. Shindler, and J. Verhoeven, *Diffuse-x-ray-scattering measurements of roughness on ion-etched multilayer interfaces.* Physical Review B (Condensed Matter), 1995. **51**(8): p. 5345-51.

89. Chason, E. and M. Chason. *In situ x-ray reflectivity measurements of thin film structural evolution*. in *The 40th National Symposium of the American Vacuum Society*. 1994. Orlando, Florida (USA): AVS.

90. Davies, H., *The reflection of electromagnetic waves from a rough surface.* Proc. Inst. Elec. Engrs., 1954. **101**: p. 209.

91. Asadchikov, V.E., et al., *Experimental X-ray study of the correlation of the surface profiles of a film and a substrate.* Crystallography Reports, 1998. **43**(1): p. 110-20.

92. Spiller, E.A., et al. *Smoothing of mirror substrates by thin-film deposition*. in *EUV, X-Ray, and Neutron Optics and Sources.* 1999. Denver, CO, USA: SPIE.

93. Lee, D.R., et al., *Nonspecular x-ray-reflectivity study of partially correlated interface roughness of a Mo/Si multilayer.* Physical Review B (Condensed Matter and Materials Physics), 1998. **57**(15): p. 8786-9.

94. Kim, Y. and S.Y. Yoon, *Scaling properties of self-expanding surfaces.* Physical Review E (Statistical, Nonlinear, and Soft Matter Physics), 2004. **69**(2): p. 027101-4.

95. Krim, J. and G. Palasantzas, *Experimental observation of self-affine and kinetic roughening at submicron lengthscales.* International Journal of Modern Physics, 1995. **9**(6): p. 599-632.

96. Lutt, M., et al., *Kardar-Parisi-Zhang growth of amorphous silicon on Si/SiO[sub 2].* Physical Review B (Condensed Matter), 1997. **56**(7): p. 4085-91.

97. Schlomka, J.-P., M. Tolan, and W. Press, *In situ growth study of NiMnSb films on MgO(001) and Si(001).* Applied Physics Letters, 2000. **76**(15): p. 2005-7.

98. Kardar, M., Physica B, 1996. **221**: p. 60.

99. Peverini, L., *Multilayer mirrors for X-ray astronomy: metrology and characterization of reflecting surfaces - Laurea Thesis*. 2000, University of Milano: Milano, Italy.

100. Horn, K.M., et al., *Hydrogen ion beam smoothening of Ge(001).* Journal of Applied Physics, 1991. **69**(1): p. 243-9.

101. Labanda, J.G.C., S.A. Barnett, and L. Hultman, *Sputter cleaning and smoothening of GaAs(001) using glancing-angle ion bombardment.* Applied Physics Letters, 1995. **66**(23): p. 3114-6.

102. Puik, E.J., et al., *Ion Bombardment of Thin Layers: The Effect on the Interface Roughness and its X-ray Reflectivity.* Review of Scientific Instruments, 1992. **63**(1): p. 1415-19.

103. Spiller, E. *Enhancement of the Reflectivity of Multilayer X-ray Mirrors by Ion Polishing.* in *X-ray/EUV Optics for Astronomy and Microscopy*. 1989. San Diego, USA: International Society for Optical Engineering.

104. Boragno, C., et al., *Time evolution of the local slope during Cu(110) ion sputtering.* Physical Review B (Condensed Matter and Materials Physics), 2003. **68**(9): p. 094102-5.

105. Cuerno, R. and A.-L. Barabasi, *Dynamic scaling of ion-sputtered surfaces.* Physical Review Letters, 1995. **74**(23): p. 4746-9.

106. Gago, R., et al., *Nanopattering of silicon surfaces by low-energy ion-beam sputtering: dependence on the angle of incidence.* Nanotechnology, 2002. **13**: p. 304-8.

107. Bradley, R.M. and J.M.E. Harper, Journal of Vacuum Science & Technology A, 1988. **6**(2390).

108. Erlebacher, J., et al., *Spontaneous Pattern Formation on Ion Bombarded Si(001).* Physical Review Letters, 1999. **82**(11): p. 2330-3.

109. Chason, E., et al., *Roughening instability and evolution of the Ge(001) surface during ion sputtering.* Physical Review Letters, 1994. **72**(19): p. 3040-3.

110. Umbach, C.C., et al., Bull. Am. Phys. Soc., 1999. **44**(1): p. 706.

111. Schlatmann, R., J.D. Shindler, and J. Verhoeven, *Evolution of surface morphology during growth and ion erosion of thin films.* Physical Review B (Condensed Matter), 1996. **54**(15): p. 10880-9.

112. Park, S., et al., *Dynamics of Ripple Formation in Sputter Erosion: Nonlinear Phenomena.* Physical Review Letters, 1999. **83**(17): p. 3486-9.

113. Francon, M., *La granularite laser*, ed. Masson. 1977, Paris: Masson.

114. Heilmann, R.K. and R.M. Suter, *In situ specular and diffuse x-ray reflectivity study of growth dynamics in quench-condensed xenon films.* Physical Review B (Condensed Matter and Materials Physics), 1999. **59**(4): p. 3075-85.

115. Carter, G., *Surface roughening during ion-assisted film deposition.* Thin Solid Films, 1998. **322**.

116. Puik, E.J., *Multilayer X-ray Coatings: progress in deposition, characterization and application.* 1990, Vrije Universiteit Amsterdam. p. 129.

117. Voorma, H.-J., et al., *Angular and energy dependence of ion bombardment of Mo/Si multilayers.* Journal of Applied Physics, 1997. **82**(4): p. 1876-81.

118. Umbach, C.C., R.L. Headrick, and K.-C. Chang, *Spontaneous Nanoscale Corrugation of Ion-Eroded SiO[sub 2]: The Role of Ion-Irradiation-Enhanced Viscous Flow.* Physical Review Letters, 2001. **87**(24): p. 246104-4.

119. Giglio, M., M. Carpineti, and A. Vailati, *Space Intensity Correlations in the Near Field of the Scattered Light: A Direct Measurement of the Density Correlation Function g(r).* Physical Review Letters, 2000. **85**(7): p. 1416-9.